

République Algérienne Démocratique et Populaire  
Ministère de l'Enseignement Supérieur et de la Recherche Scientifique



Université Ibn Khaldoun de Tiaret  
Faculté des Sciences Appliquées  
Département de Génie Mécanique



## MÉMOIRE DE FIN D'ETUDES

Pour l'obtention du Diplôme de Master

**Domaine :** Sciences et Technologie

**Filière :** Génie Mécanique

**Parcours :** Master

**Spécialité :** Énergétique

### Thème

**FLUID FLOW AND MAGNETOHYDRODYNAMIC  
FORCED CONVECTION HEAT TRANSFER  
INVESTIGATION OF OSTWALD DE WAELE  
FLUID THROUGH POROUS MICROCHANNEL IN  
THE PRESENCE OF THE LORENTZ FORCE**

Préparé par :

- OULD MOHAMED Amina
- BEKHTAOUI Belhouari Abd Elkarim

Soutenu publiquement le : 12 / 06 / 2023, devant le jury composé de :

M. ATHMANI Houari	Maître de Assistant "A"	(Univ. Ibn Khaldoun)	Président
M. SAD CHEMLOUL Nordeddine	Professeur	(Univ. Ibn Khaldoun)	Examineur
M. KARAS Abdekader	Professeur	(Univ. Ibn Khaldoun)	Examineur
Mr. CHAIB Khaled	Maître de Conférences "A"	(Univ. Ibn Khaldoun)	Encadrant
Mr. ABDI Mohamed	Docteur	(Univ. Ibn Khaldoun)	Co-Encadrant

Année universitaire : 2022 - 2023

بِسْمِ اللَّهِ الرَّحْمَنِ الرَّحِيمِ

# DEDICATION

---

First and foremost, praises and thanks to Allah for his showers of blessings throughout our research work to complete this thesis successfully.

We are incredibly grateful to our parents for their love, prayers, caring and sacrifices for education and preparing me for our future, and their unlimited support who never stop giving us what is necessary to achieve what we are today. Our God, protect you.

We also dedicate this work to :

Our Brothers for their unbounded support throughout our life. Their reliable emotional, spiritual, and financial support has allowed us to accomplish tasks that would have otherwise been impossible.

Our uncles, our aunts and their family.

All our cousins.

All our friends, our colleagues and all those who value us.

# ACKNOWLEDGMENTS

---

In the Name of Allah, the Most Merciful, the Most Compassionate, Alhamdulillah, all praises belong to Almighty Allah, the Lord of the worlds and prayers and peace be upon Muhammad, His servant and messenger.

We want to express our deep gratitude to our supervisor, [Mr Khaled CHAIB](#), a Professor at the University [IBN KHALDOUN](#) of Tiaret. He helped me throughout this thesis and shared his brilliant intuitions in the context of this work. We want to thank our co-supervisor [Mr Mohamed ABDI](#), for his guidance throughout this project. Our teacher [Mr Slimane BENFERHAT](#), words can hardly describe our thanks and appreciation to him. He has been our source of inspiration, support, and guidance. He has taught us to be unique and determined, believe in ourself, and persevere. We are truly thankful and honoured to have a teacher like him. We are very grateful to them for providing us with their long experience in computational fluid mechanics (CFD) throughout this work. We sincerely thank them for giving us the benefit of their skills during the knowledge of the [ALBERT Team](#).

With all our respect to [Mrs Meryem Ould Rouiss](#), Professor at the [GUSTAVE Eiffel University in Champs sur Marne- 77454- \(France\)](#) and member of the “[Modélisation et de Simulation à Multi-Echelles \(MSME\)](#)” . Thank you for your white heart full of kindness and pure soul, a beacon of minds.

We want to express our sincere thanks to all the jury members for accepting and evaluating this work.

Thanks to all the Laboratory "Modélisation et de Simulation à Multi-Echelles (MSME)" members for their help and for sharing their skills. We also thank all the members of the Laboratory "Laboratoire de génie électrique et des plasmas (LGEP) University of Tiaret, Algeria".

We are highly grateful to my colleagues at "THE ALBERT TEAM" for all the beautiful trips and fond memories. Thank you for your encouragement in all the moments. Your friendship makes our lives just a wonderful experience. They are the spice that made my journey less humdrum. With their support, our progress was much faster.

Last but most importantly, we thank our parents today for their blessings, providing us with unfailing support and continuous encouragement throughout our years of study and through the research process and writing this thesis. There are not enough words to express our gratitude for everything they have done for us. We thank our beloved families for their unceasing, unwavering love and encouragement. They have been instrumental in moulding me into who we are today. It is to them that we dedicate our thesis.

"BELIEVE IN YOURSELF AND BE READY TO LEARN"

"THE ALBERT TEAM"

## ملخص

تسعى هذه الدراسة الحالية إلى تعزيز نقل الحرارة في المشتتات الحرارية ذات القنوات الدقيقة القائمة على الموائع النانوية اعتبارًا خاصًا لإدراك تأثيرات تدفق الانزلاق، وطول مصدر حراري، و عدد (Darcy) ، والمسامية المتوسطة، ومؤشر سلوك التدفق، و عدد (Hartmann) ، وزاوية ميل المجال المغناطيسي ( $\alpha$ ) . على الزخم وخصائص نقل الحرارة من خلال عرض ومناقشة مختلف الكميات الإحصائية مثل عدد (Nusselt) المحلية والمتوسطة، وملاصق السرعة، وتبسيط وتوزيعات متساوية الحرارة بعناية. تتعلق الدراسة الحالية بنقل الحرارة بالحمل الحراري المغناطيسي الهيدروديناميكي المستقر (MHD) داخل قناة متناهية الصغر مملوءة بالكامل وجزئيًا يشغلها، والسوائل شبه البلاستيكية والمتوسعة التي يتخللها مجال مغناطيسي عرضي موحد ( $B_0$ ) وبميل بزاوية ( $\alpha$ ) . يتكون التحقيق الحالي من مجموعة من عمليات المحاكاة لنطاقات واسعة من طول مصدر الحرارة ( $30 \geq B \geq 5$ ) ، و عدد (Knudsen) من ( $0.1 \geq Kn \geq 0.001$ ) ، ومؤشرات سلوك التدفق ( $1.8 \geq n \geq 0.2$ ) ، و عدد (Darcy) من ( $10^{-2} \geq Da \geq 10^{-5}$ ) ، مسامات متوسطة ( $0.9 \geq \varepsilon \geq 0.1$ ) ، عدد (Hartmann) من ( $160 \geq Ha \geq 0$ ) ، وزوايا ميل المجال المغناطيسي ( $90^\circ \geq \alpha \geq 0^\circ$ ) للمعلمات الثابتة التالية : عدد رينولدز،  $Re=50$  تركيز الموائع النانوية  $\varphi = 1\%$  ، نسبة الموصلية الحرارية المسامية،  $Ks=0.613$  .

يتم نمذجة الوسط المسامي من خلال استخدام نموذج (Brinkman-Darcy) مع نهج التوازن الحراري المحلي (LTE) بين سائل العمل والمصفوفة المسامية لنقل الطاقة. أظهرت النتائج المتوقعة توافقًا ممتازًا مع نتائج الأدبيات المتاحة للتحقق من صحتها. النتائج الناشئة تشير إلى أن خصائص الزخم وآلية نقل الحرارة تعتمد بشدة على عدد (Knudsen) وطول مصدر الحرارة ومسامية الوسائط ومؤشر سلوك التدفق و عدد (Hartmann) . يؤدي عدد كنودسن المتزايد إلى زيادة ملحوظة في السرعة المحورية وتقليل معدل القص عند الجدار، مما يؤدي إلى انخفاض ملحوظ في السرعة في مركز القناة الدقيقة وزيادة ملحوظة في السرعة المحورية في جدار القناة الصغيرة. من ناحية أخرى، ينتج عن زيادة مؤشر سلوك التدفق انحراف واضح في توزيع معدل القص للسائل المتوسع، مما يؤدي إلى تباين ملحوظ في لزوجة السائل الظاهرة، مما يؤدي إلى زيادة توزيعات السرعة المحورية على طول القناة الدقيقة العالية. يؤدي أيضًا مؤشر سلوك التدفق المنخفض للشبه البلاستيكي إلى تحريك القيمة القصوى للسرعة المحورية باتجاه جدار القناة الدقيقة العلوي.

الكلمات الرئيسية : القناة الدقيقة ; الحمل الحراري ; عدد (Nusselt)

# ABSTRACT

---

The present study concerns a steady-state laminar magnetohydrodynamic (MHD) flow forced convection heat transfer inside a fully and partially filled microchannel occupied by  $\text{Cu-Al}_2\text{O}_3$ /water hybrid, pseudoplastic and dilatant fluids permeated by a uniform transverse magnetic field ( $B_0$ ) and inclined by an angle ( $\alpha$ ). The present investigation consists of a set of simulations for wide ranges of heat source length ( $5 \leq B \leq 30$ ), Knudsen numbers ( $0.001 \leq Kn \leq 0.1$ ), flow behaviour indices ( $0.2 \leq n \leq 1.8$ ), Darcy numbers ( $10^{-5} \leq Da \leq 10^{-2}$ ), medium porosities ( $0.1 \leq \varepsilon \leq 0.9$ ), Hartmann numbers ( $0 \leq Ha \leq 160$ ), and magnetic field inclination angles ( $0^\circ \leq \alpha \leq 90^\circ$ ) for the following fixed parameters : Reynolds number,  $\text{Re}=50$ ; nanofluid concentration,  $\varphi = 1\%$ ; porous thermal conductivity ratio,  $\text{Ks}=0.613$ . The porous medium is modelled by employing the Brinkman-Darcy model with a local thermal equilibrium (LTE) approach between the working fluid and the porous matrix for energy transfer. The predicted results showed an excellent agreement with the available literature results for validation. The parametric study indicates that the momentum characteristics and heat transfer mechanism strongly depend on the Knudsen number, heat source length, media porosity, flow behaviour index, and Hartmann number. The increased Knudsen number induces a pronounced increase in the axial velocity and a reduction in the shear rate at the wall, resulting in a noticeable decrease of the velocity in the microchannel centre and a marked increase of the axial velocity at the microchannel wall. On the other hand, the increased flow behaviour index results in the apparent deviation in the shear rate distribution of the dilatant fluid, resulting in a marked variation in the apparent

fluid viscosity, which leads to an increase in the axial velocity distributions along the microchannel high. The decreased flow behaviour index of the pseudoplastic also leads to moving the axial velocity's maximum value toward the upper microchannel wall.

**Keywords :** Microchannel ; (MHD) ; Forced convection ; (LTE) ; Nusselt number .



# RESUME

---

La présente étude concerne le transfert de chaleur par convection forcée dans un écoulement laminaire magnétohydrodynamique (MHD) en régime permanent à l'intérieur d'un microcanal entièrement ou partiellement rempli par des fluides hybrides  $\text{Cu-Al}_2\text{O}_3/\text{eau}$ , pseudo-plastiques et dilatants imprégnés d'un champ magnétique transversal uniforme ( $B_0$ ) et incliné d'un angle ( $\alpha$ ). La présente étude consiste en un ensemble de simulations pour de larges gammes de longueur de source de chaleur ( $5 \leq B \leq 30$ ), de nombres de Knudsen ( $0.001 \leq Kn \leq 0.1$ ), d'indices d'écoulement ( $0.2 \leq n \leq 1.8$ ), de nombres de Darcy ( $10^{-5} \leq Da \leq 10^{-2}$ ), de porosités ( $0.1 \leq \varepsilon \leq 0.9$ ), de nombres de Hartmann ( $0 \leq Ha \leq 160$ ), et d'angles d'inclinaison du champ magnétique ( $0^\circ \leq \alpha \leq 90^\circ$ ) pour les paramètres fixes suivants : Nombre de Reynolds,  $\text{Re}=50$  ; concentration de nanofluide,  $\varphi = 1\%$  ; rapport de conductivité thermique poreuse,  $K_s=0.613$ . Le milieu poreux est modélisé en utilisant le modèle Brinkman-Darcy avec une approche d'équilibre thermique local (LTE) entre le fluide de travail et la matrice poreuse pour le transfert d'énergie. Les résultats prédits ont montré une excellente concordance avec les résultats de la littérature disponible pour la validation. L'étude paramétrique indique que les caractéristiques de la quantité de mouvement et le mécanisme de transfert de chaleur dépendent fortement du nombre de Knudsen, de la longueur de la source de chaleur, de la porosité du milieu, de l'indice d'écoulement et du nombre de Hartmann. L'augmentation du nombre de Knudsen induit une augmentation prononcée de la vitesse axiale et une réduction du taux de cisaillement à la paroi, ce qui entraîne une diminution notable de la vitesse au centre du microcanal et une augmentation marquée de la vitesse axiale à la paroi du microcanal. D'autre part, l'augmentation de l'indice d'écoulement entraîne une déviation apparente de

la distribution du taux de cisaillement du fluide dilatant, ce qui se traduit par une variation marquée de la viscosité apparente du fluide, qui entraîne une augmentation des distributions de la vitesse axiale le long de la hauteur du microcanal. La diminution de l'indice d'écoulement du pseudoplastique entraîne également le déplacement de la valeur maximale de la vitesse axiale vers la paroi supérieure du microcanal.

**Mots clés :** Microcanal; (MHD); Convection forcée; (LTE); Nombre de Nusselt .

# CONTENTS

---

<b>DEDICATION</b>	<b>ii</b>
<b>ACKNOWLEDGMENTS</b>	<b>iii</b>
<b>ABSTRACT</b>	<b>vi</b>
<b>RESUME</b>	<b>viii</b>
<b>FIGURES LIST</b>	<b>xviii</b>
<b>TABLES LIST</b>	<b>xxiv</b>
<b>NOMENCLATURE</b>	<b>xxiv</b>
<b>GENERALE INTRODUCTION</b>	<b>2</b>
Industrial problematic . . . . .	2
Aims . . . . .	3
Scientific problematic . . . . .	3
<b>I RHEOLOGY AND NANOFUIDS</b>	<b>6</b>
I.1 Rheological behaviour . . . . .	6

---

I.1.1	Rheology Definition . . . . .	6
I.1.2	Shear rate and shear stress . . . . .	9
I.1.3	Rheometry . . . . .	11
I.1.4	Classification of fluid behaviour . . . . .	12
I.1.5	Simple fluid . . . . .	12
I.1.5.1	Newtonian Fluids . . . . .	13
I.1.6	Complex fluid . . . . .	14
I.1.6.1	Non-Newtonian Fluids . . . . .	15
I.1.6.2	Time-Independent Fluids . . . . .	16
I.1.6.2.a	Power-Law Model . . . . .	17
I.1.6.2.a.a	Shear-thinning or pseudoplastic fluids . . . . .	18
I.1.6.2.a.b	Shear-thickening or dilatant fluid behaviour . . . . .	19
I.1.6.2.b	The Cross model . . . . .	20
I.1.6.2.c	Viscoplastic fluid behaviour . . . . .	21
I.1.6.2.c.a	The Bingham fluid . . . . .	22
I.1.6.2.c.b	The Herschel-Bulkley Model . . . . .	23
I.1.6.2.d	The Carreau Model . . . . .	24
I.1.6.2.e	The Carreau-Yasuda Model . . . . .	24
I.1.6.2.f	The Ellis model . . . . .	25
I.1.6.3	Time-dependent Fluids . . . . .	26
I.1.6.3.a	Thixotropic Behaviour . . . . .	27
I.1.6.3.b	Rheopectic Behaviour . . . . .	28
I.1.6.4	Viscoelastic Fluids . . . . .	28
I.1.6.4.a	Linear viscoelasticity . . . . .	29

I.1.6.4.a.a	Maxwell Model . . . . .	29
I.1.6.4.a.b	Jeffreys Model . . . . .	31
I.1.6.4.b	Non-linear viscoelasticity . . . . .	31
I.1.6.4.b.a	Upper Convected Maxwell (UCM) Model . . . . .	32
I.1.6.4.b.b	Oldroyd-B Model . . . . .	33
I.1.6.4.b.c	Bautista-Manero Model . . . . .	33
I.2	Nanofluids and Hybrid nanofluids . . . . .	37
I.2.1	Nanofluids . . . . .	37
I.2.1.1	Base fluids . . . . .	37
I.2.1.2	Nanofluids and their applications . . . . .	38
I.2.1.3	Thermophysical properties of nanofluids . . . . .	41
I.2.1.3.a	Nanofluid Density . . . . .	41
I.2.1.3.b	Nanofluid Specific Heat . . . . .	41
I.2.1.3.c	Nanofluid viscosity . . . . .	41
I.2.1.3.c.a	Experimental investigation of nanofluid viscosity . . . . .	41
I.2.1.3.c.b	Numerical investigation of nanofluid viscosity . . . . .	43
I.2.1.3.d	Nanofluid thermal conductivity . . . . .	43
I.2.2	Hybrid nanofluids . . . . .	45
I.2.2.1	Natural convection heat transfer . . . . .	47
I.2.2.2	Forced convection heat transfer . . . . .	47
I.2.2.3	Applications of hybrid nanofluids in different fields . . . . .	48
<b>II</b>	<b>PREVIOUS WORK</b>	<b>51</b>
II.1	Previous work . . . . .	51

---

<b>III ENHANCEMENT OF HEAT TRANSFER MECHANISMS</b>	<b>69</b>
III.1 Microchannel	69
III.1.1 Flow channel classification	69
III.1.2 Heat Transfer and Pressure Drop in Channels	70
III.1.2.1 Concept of Fully Developed and Developing Flow	70
III.1.2.2 Navier-Stokes Equations	71
III.1.2.3 Fully Developed Region	72
III.1.2.3.a Hydrodynamic Fully Developed Flow	73
III.1.2.3.b Thermally Fully Developed Flow	74
III.1.2.3.c Fully Developed Flow in Circular Channels	75
III.1.3 Heat Transfer Enhancement Classification	77
III.1.4 Heat Transfer and Fluid Flow in Microchannels	78
III.2 Heat Sink	79
III.2.1 Requirement of Microchannels	80
III.2.2 Applications of Microchannels	80
III.2.3 Enhanced microchannels	81
III.2.3.1 Flow disruption structures	81
III.2.3.2 Reentrant cavity structure	82
III.2.3.3 Porous structure	82
III.2.3.4 Nano structure	82
III.2.3.5 Micro-mechanical cutting process	83
III.2.4 The flow and heat transfer through Microchannels	83
III.2.4.1 Mean Free Path	83
III.2.4.2 Knudsen Number and Regimes of Rarefaction	84

III.2.4.3	Gas flow regimes and main models . . . . .	85
III.2.4.4	Thermal Accommodation Coefficient . . . . .	86
III.2.4.5	Temperature Jump . . . . .	86
III.2.4.6	Slip flow regime . . . . .	87
III.2.4.6.a	Boundary conditions . . . . .	87
III.2.5	Configuration of optimized micro-channel heat sinks . . . . .	89
III.3	Porous media and Magneto Hydrodynamics (MHD) . . . . .	90
III.3.1	Porous media . . . . .	90
III.3.1.1	Introduction . . . . .	90
III.3.1.2	Porosity . . . . .	90
III.3.1.3	Momentum Equation : Darcy's Law . . . . .	91
III.3.1.3.a	Brinkman-Corrected Darcy's Law . . . . .	91
III.3.1.3.b	Forschheimer-Extended Darcy's Law . . . . .	91
III.3.1.4	Darcy's Law : Permeability . . . . .	92
III.3.1.5	Applications . . . . .	92
III.3.1.6	Thermal Equilibrium Model (LTE) . . . . .	93
III.3.1.7	Thermal Non-equilibrium Model (LTNE) . . . . .	93
III.3.2	Magneto Hydrodynamics (MHD) . . . . .	94
III.3.2.1	Magneto Hydrodynamics (MHD) Governing Equations . . . . .	94
<b>IV</b>	<b>NUMERICAL PROCEDURE</b>	<b>97</b>
IV.1	Introduction . . . . .	97
IV.2	Generalities on CFD . . . . .	98
IV.3	Areas of application of CFD . . . . .	98
IV.4	CFD simulation and meshing . . . . .	99

---

IV.4.1	Law of Fluid Motion . . . . .	99
IV.4.2	Conservation of Momentum . . . . .	100
IV.4.3	Energy conservation equation . . . . .	100
IV.4.4	Conservation of Mass . . . . .	101
IV.4.5	Boussinesq approximation . . . . .	101
IV.5	Methodology of CFD . . . . .	102
IV.5.1	The general method . . . . .	103
IV.5.2	Numerical methods . . . . .	104
IV.5.2.1	Finite volume method . . . . .	105
IV.5.2.2	Finite Difference Method . . . . .	106
IV.5.2.3	Finite Element Method . . . . .	106
IV.6	Presentation of Ansys . . . . .	107
IV.6.1	PERFORMING A SIMULATION IN ANSYS : FLUENT . . . . .	109
IV.6.2	Presentation of the GAMBIT software . . . . .	110
IV.7	Mesh . . . . .	111
IV.7.1	Mesh cell types . . . . .	111
IV.7.1.1	Tetra Meshing . . . . .	111
IV.7.1.2	Hexa Meshing . . . . .	112
IV.7.1.3	Hybrid Meshing . . . . .	112
IV.8	Simulation . . . . .	113
IV.8.1	Defining boundary conditions . . . . .	113
IV.8.2	Convergence Criteria . . . . .	114
IV.8.2.1	Evaluation Criteria . . . . .	115
IV.8.3	Solution Algorithms for Pressure-Velocity Coupling Equation . . . . .	115



---

IV.8.3.1 SIMPLE Algorithm . . . . .	116
IV.8.3.2 SIMPLER Algorithm . . . . .	116
IV.8.3.3 SIMPLEC Algorithm . . . . .	116
IV.8.3.4 PISO Algorithm . . . . .	116
IV.8.4 Grid Resolution . . . . .	117
<b>V RESULTS AND DISCUSSIONS</b>	<b>119</b>
V.1 Introduction . . . . .	119
V.2 Problem description . . . . .	120
V.3 Governing Equations . . . . .	121
V.3.1 Fundamental flow equations . . . . .	121
V.3.2 Continuity equation . . . . .	121
V.3.3 Momentum equations . . . . .	122
V.3.4 Energy equation . . . . .	122
V.4 Thermophysical properties of hybrid nanofluid . . . . .	123
V.5 Boundary conditions . . . . .	125
V.6 Results and Discussions . . . . .	126
V.7 Validation . . . . .	126
V.8 Hybrid Nanofluid . . . . .	129
V.8.1 Effects of heat source length B . . . . .	129
V.8.1.1 The Local Nusselt profile . . . . .	129
V.8.1.2 The Average Nusselt profile . . . . .	129
V.8.2 Effects of dimensionless slip coefficient Kn . . . . .	130
V.8.2.1 Velocity profiles . . . . .	131
V.8.2.2 Temperature profiles . . . . .	133

---

V.8.2.3	Local Nusselt number . . . . .	134
V.8.2.4	Average Nusselt number . . . . .	135
V.8.3	Effects of Ha and $\alpha$ . . . . .	136
V.8.3.1	Velocity profile . . . . .	137
V.8.3.2	Temperature profile . . . . .	139
V.8.3.3	Average Nusselt number . . . . .	139
V.8.4	Effects of porosity $\varepsilon$ . . . . .	140
V.8.4.1	Velocity profiles . . . . .	141
V.8.4.2	Average Nusselt number . . . . .	143
V.9	Power law fluid . . . . .	144
V.9.1	Effects of behaviour index n . . . . .	145
V.9.1.1	Velocity profiles . . . . .	145
V.9.2	Effects of behaviour index n . . . . .	145
V.9.3	Effects of Reynolds number Re . . . . .	146
V.9.4	Effects of Knudsen number Kn . . . . .	147
V.9.4.1	Velocity profile . . . . .	147
V.9.4.2	Temperature profile . . . . .	148
V.10	Conclusion . . . . .	149
	<b>GENERAL CONCLUSION</b>	<b>152</b>
	<b>BIBLIOGRAPHY</b>	<b>155</b>

# FIGURES LIST

---

I.1	Particle motion in shear and extensional flows [3]. . . . .	7
I.2	Schematic illustration of viscoelastic polymer rheology [4]. . . . .	7
I.3	Hypothetical layers in shear flow [3]. . . . .	9
I.4	The shear stress - shear rate relationship [4]. . . . .	10
I.5	Some classical types of rheometers. . . . .	11
I.6	Fluid deformation by the application of force, where the applied force per unit area is called stress ( $\sigma = \frac{F}{A}$ ) and the resulting rate of change of deformation is called shear rate ( $\dot{\gamma} = \frac{V}{H}$ ) [7]. . . . .	12
I.7	Simple shear of a Newtonian fluid between two parallel planes. . . . .	13
I.8	Representation of flow curves of different types of fluids : Newtonian, shear-thinning and shear-thickening [10]. . . . .	14
I.9	Flow curve and viscosity curve for Newtonian fluids [7]. . . . .	14
I.10	Classification of fluids. . . . .	16
I.11	Qualitative flow curves for different types of non-Newtonian fluids [13]. . . . .	17
I.12	The bulk rheology of a power-law fluid on logarithmic scales for finite shear rates. . . . .	18
I.13	Schematic representation of shear-thinning behaviour [14]. . . . .	19
I.14	Schematic representation of shear-thickening behaviour [14]. . . . .	20

I.15	Flow curve and viscosity curve for shear thinning fluids (solid line), and shear thickening fluids (dotted line). . . . .	20
I.16	Representative shear stress–shear rate data showing viscoplastic behaviour in a meat extract (Bingham Plastic) and in an aqueous carbopol polymer solution (yield-pseudoplastic) [14]. . . . .	22
I.17	Definition diagram of the Bingham model. . . . .	23
I.18	The bulk rheology of a Carreau fluid on logarithmic scales for finite shear rates ( $\dot{\gamma} > 0$ ). . . . .	24
I.19	Viscosity approximation using the Bird-Carreau-Yasuda model. . . . .	25
I.20	The viscosity function $\eta(\dot{\gamma})$ . . . . .	26
I.21	Shear rate histories. . . . .	27
I.22	Graphical representation of viscosity for thixotropic fluids (solid line), and rheopectic fluids (dotted line) under constant shear rate [7]. . . . .	27
I.23	Mechanical analog to Maxwell model comprised of a spring and dashpot in series [7]. . . . .	30
I.24	Schematic of (NPs) dispersion systems (NFs) as a three-phase suspension system [20]. . . . .	38
I.25	Different applications of NFs [20]. . . . .	40
I.26	Potential of NFs for thermal application. . . . .	40
I.27	Hybrid nanofluids types [28]. . . . .	47
I.28	Forced convective heat transfer in different applications [28]. . . . .	48
I.29	Factors that needed careful consideration while investigating the hybrid nanofluids as a heat transfer media, graphical illustration [28]. . . . .	48
I.30	Major areas of applications of hybrid nanofluids. . . . .	49
II.1	Dimensionless temperature variation profiles along dimensionless length of the microchannel in different cross-sections of the microchannel for $Re=10$ . . . . .	54
II.2	Dimensionless temperature variation profiles along dimensionless length of the microchannel in different cross-sections of the microchannel for $Re=100$ . . . . .	54

II.3	Non-dimensional velocity profile obtained for nanofluid along the perpendicular line passing through the microchannel center at $x=L/2$ , $Re=100$ , $Da=0.001$ , $\varepsilon = 0.4$ , and $\varphi = 0.0012$ . . . . .	60
II.4	Non-dimensional velocity profile obtained for nanofluid at the perpendicular line passing through the microchannel center at $x=L/2$ , $Re=100$ , $Da=0.1$ , $\varepsilon = 0.9$ , and $\varphi = 0.0012$ . . . . .	60
II.5	Effects of magnetic field on dimensionless velocity profile for nanofluid with $\varphi = 0.2\%$ at $B=0$ and $0.1$ . Profiles are plotted at two fully developed regions, $x=0.2L$ and $x=L$ , $Ha=15$ (Top) and $Ha=30$ (Bottom). . . . .	62
II.6	Effects of $Ha$ on $u(y)$ , $\theta(y)$ , $Ns$ , and $Be$ . . . . .	63
III.1	As coolant flows through a channel, the flow pattern changes from "developing" to "fully developed" flow. . . . .	71
III.2	Hydrodynamic entrance length and fully developed region. . . . .	71
III.3	Effects of Prandtl number on the size of hydrodynamic and thermal entrance length [62]. . . . .	73
III.4	Fully developed flow in circular channels [62]. . . . .	75
III.5	Temperature variations for different thermal boundary conditions. . . . .	77
III.6	Different methods of heat transfer enhancement. . . . .	78
III.7	Schematic of studies on micro channel heat sinks. . . . .	81
III.8	Fabrication of enhanced microchannels [67]. . . . .	83
III.9	Gas flow regimes and main models according to the Knudsen number. . . . .	85
III.10	Temperature jump diagram. . . . .	87
III.11	Structure of the Knudsen layer and slip velocity [69]. . . . .	88
III.12	Velocity profile for Slip and No-slip. . . . .	89
III.13	Configuration of different types of micro-channel heat sinks [71]. . . . .	89
III.14	Schematic drawings of applications where porous media modeling is useful for analysis [75]. . . . .	92

---

IV.1	Some areas of application for CFD. . . . .	99
IV.2	Flow chart of CFD simulation . . . . .	103
IV.3	Adjoint methodology. . . . .	103
IV.4	A cell or control volume in three dimensions [83]. . . . .	106
IV.5	Methodology of Simple Method. . . . .	110
IV.6	CFD ANSYS FLUENT Methodology for solving nanofluid DASC enclosure boundary value problem [89]. . . . .	111
IV.7	Main cell types used in CFD mesh generation software [80]. . . . .	112
IV.8	Mesh convergence test. . . . .	113
IV.9	The Grid Resolution. . . . .	117
V.1	The schematic of the studied microchannel. . . . .	121
V.2	The schematic of the studied microchannel of power law. . . . .	121
V.3	Temperature profiles of $\theta$ at $\varphi = 0.0$ , $Re=20$ , $Ha=0$ , $\beta = 0.05$ and $\beta = 0.005$ for different cross sections of the micro-channel. . . . .	127
V.4	Velocity profile of $U$ at $\varphi = 0.0$ , $Re=20$ , $Ha=40$ , $\beta = 0.05$ for different cross sections of the microchannel. . . . .	127
V.5	Temperature profile of $\theta$ at $\varphi = 0.2$ , $Re=10$ , $Ha=0$ , $\beta = 0.08$ for different cross sections of the micro-channel. . . . .	128
V.6	Velocity profile of $U$ at $\varphi = 0.2$ , $Re=10$ , $Ha=0$ , for $\beta = 0.0$ , $\beta = 0.04$ , $\beta = 0.08$ . . . . .	128
V.7	Variations of local Nusselt number along the microchannel wall at different values of heat source length $B=5$ , $B=10$ , $B=20$ at fixed Darcy number $Da = 10^{-1}$ and Reynolds number $Re=50$ for $Kn=0.01$ , $Ha=0$ , $\varepsilon = 0.9$ . . . . .	129
V.8	Variations of Average Nusselt number at different values of heat source length $B=5$ , $B=10$ , $B=20$ at fixed Reynolds number $Re=50$ for $Kn=0.01$ , $\varepsilon = 0.9$ . . . . .	130
V.9	Velocity profile of $U/U_b$ for different values of Knudsen numbers at fixed Darcy number $Da = 10^{-1}$ and $B=20$ , for $X=20$ . . . . .	132

V.10	Velocity profile of $U/U_b$ for $Kn=0.05$ , $Kn=0.1$ at fixed Darcy number $Da = 10^{-1}$ and $B=20$ , for different cross sections of the micro-channel. . . . .	133
V.11	Temperature profile of $\theta$ for $Kn=0$ , $Kn=0.1$ at fixed Darcy number $Da = 10^{-1}$ and $B=20$ for different cross sections of the micro-channel. . . . .	134
V.12	Variations of local Nusselt number along the microchannel wall at different values of Knudsen numbers $Kn=0$ , $Kn=0.05$ , and $Kn=0.1$ at fixed Darcy number $Da = 10^{-1}$ and $B=5$ . . . . .	135
V.13	Variations of Average Nusselt number at two values of Darcy numbers $Da = 10^{-1}$ , $Da = 10^{-3}$ for $B=5$ , $B=20$ at fixed Reynolds number $Re=50$ , $\varepsilon = 0.9$ . . . . .	136
V.14	Velocity profile of $U/U_b$ for different magnetic field inclination angles and Hartmann numbers at fixed Darcy number $Da = 10^{-1}$ and $B=20$ . . . . .	138
V.15	Temperature profile of $\theta$ for two values of heat source length ( $B=5$ , $B=20$ ) at fixed Darcy number $Da = 10^{-1}$ and Hartmann number $B=160$ for different cross sections of the micro-channel. . . . .	140
V.16	Variations of Average Nusselt number at two heat source length $B=5$ , $B=20$ with fixed Reynolds number $Re=50$ , $\varepsilon = 0.9$ for different magnetic field inclination angles. . . . .	141
V.17	Velocity profile of $U/U_b$ for different values of porosities at two Darcy number $Da = 10^{-1}$ , $Da = 10^{-3}$ for fixed heat source length $B=20$ and $Kn=0.01$ . . . . .	142
V.18	Velocity profile of $U/U_b$ for three values of porosities at two Darcy number $Da = 10^{-1}$ , $Da = 10^{-3}$ for fixed heat source length $B=20$ , $Kn=0.01$ , $Re=20$ . . . . .	143
V.19	Variations of Average Nusselt number at two Darcy numbers $Da = 10^{-1}$ , $Da = 10^{-3}$ with fixed Reynolds number $Re=50$ , $Kn=0.01$ , $Ha=0$ at two heat source length $B=5$ , $B=20$ . . . . .	144
V.20	Velocity profile of $U/U_b$ for different values of flow behaviour index at Darcy number $Da = 10^{-1}$ , for fixed Knudsen number $Kn=0.1$ , $Re=100$ , $\varepsilon = 0.5$ . . . . .	146
V.21	Velocity profile of $U/U_b$ for different Reynolds numbers at flow behaviour index $n=1.7$ , Darcy number $Da = 10^{-1}$ , for fixed Knudsen number $Kn=0.1$ , $Re=100$ , $\varepsilon = 0.5$ . . . . .	147
V.22	Velocity profile of $U/U_b$ for different Knudsen numbers at flow behaviour index $n=0.2$ , Darcy number $Da = 10^{-1}$ , $Re=100$ , $\varepsilon = 0.5$ . . . . .	148

V.23 Temperature profile of  $U/U_b$  for different Knudsen numbers at flow behaviour index  $n=0.2$ , Darcy number  $Da = 10^{-1}$ ,  $Re=100$ ,  $\varepsilon = 0.5$ . . . . . 149



# TABLES LIST

---

I.1	Overview of different kinds of rheological behaviour [2]. . . . .	7
I.2	Typical shear rate ranges of various physical operations [3]. . . . .	10
I.3	flow curve models [16]. . . . .	35
I.4	The various types of non-Newtonian fluids [9]. . . . .	36
III.1	Channel classification scheme [63]. . . . .	70
V.1	Effective thermal conductivity and dynamic viscosity of Cu- $Al_2O_3$ /water hybrid nano-fluid [91]. . . . .	125

# NOMENCLATURE

---

## SYMBOLS

$B_0$	Magnetic field strength	[T]
$B$	Heat source length	[m]
$C$	The consistency factor	
$C_p$	Specific heat capacity	[J/kgK]
$H$	Microchannel high	[m]
$F$	Force	[N]
$H_S$	Dimensionless microchannel hight $H_S = h/h$	
$h_p$	Power law height	[m]
$k$	Thermal Conductivity	[W/mK]
$K$	Consistency index	[Pa.s <sup>n</sup> ]
$l$	Microchannel length	[m]
$L$	Dimensionless microchannel length $L = 1/l$	
$m$	Dimensionless	
$M$	Consistency coefficient	
$n$	Flow behaviour index	
$P$	Pressure	[Pa]
$q$	Heat flux	[W/m <sup>2</sup> ]
$q_w''$	Constant heat flux	[W/m <sup>2</sup> ]

$Q$	Buckingham-Reiner	
$X, Y$	Dimensionless Cartesian coordinates	[ $m$ ]
$U, V$	Velocity Components in x- and y-directions, respectively	
$t_c$	Characteristic time	[ $s$ ]
$T$	Temperature	[ $K$ ]
$T_h$	Hot temperature	[ $K$ ]
$T_c$	The temperature of the cold inflow nanofluid	[ $K$ ]
$\Delta T$	Temperature difference	[ $K$ ]
$u$	Horizontal velocity (m s <sup>-1</sup> )	[ $ms^{-1}$ ]
$u_c$	Inlet nanofluid velocity	[ $ms^{-1}$ ]
$U$	Dimensionless horizontal velocity $U = u/u_b$	
$u_s$	Slip velocity of nanofluid	[ $ms^{-1}$ ]
$U_s$	Dimensionless slip velocity	
$\nu$	Vertical velocity	[ $ms^{-1}$ ]
$V$	Dimensionless vertical velocity $V = \nu/u_i$	
$x$	Horizontal axis	[ $m$ ]
$X$	Dimensionless horizontal axis $X = x/h$	
$y$	Vertical axis	[ $m$ ]
$Y$	Dimensionless vertical axis $Y = y/h$	

### GREEK SYMBOLS

$\alpha^\circ$	Enclosure inclination angle (Angle of inclintion)	
$\gamma$	Shear	
$\dot{\gamma}$	Shear rate	
$\beta$	Slip coefficient	[ $m$ ]
$\beta^*$	Dimensionless slip coefficient $\beta^* = \beta/h$	
$\alpha$	Thermal diffusivity $\alpha = k/\rho C_p$	
$\varepsilon$	Porosity	
$E_v$	Vertical eccentricity	

$E_h$	Horizontal eccentricity	
$\rho$	Density of fluid	$[kgm^{-3}]$
$\eta$	Shear stress viscosity	
$\eta_\infty$	Infinite shear rate viscosity	
$\theta$	Dimensional temperature	$[K]$
$\lambda$	Characteristic viscous relaxation time	
$\mu$	Dynamic viscosity	$[(Ns\ m^{-2})]$
$\mu_0$	Limit viscosity at the low shear rate	$[(Ns\ m^{-2})]$
$\mu_\infty$	Limit viscosity at the high shear rate	$[pas]$
$\sigma$	Resulting rate	
$\sigma_s$	Stress in the spring	
$\sigma_d$	Stress in dashpot respectively	
$\tau$	Ratio of stresses	
$\tau_0$	Zero-shear stress	
$\phi$	Volume fraction of nanoparticles	
$\varphi$	Concentration of Hybrid nanoparticles	
$\delta$	Thickness of the Newtonian slip layer	
$\nu$	Kinematic viscosity	$(m^{-2}\ s^{-1})$

### DIMENSIONAL NUMBERS

$Da$	Darcy Number $Da = \frac{K}{d^2}$
$Nu$	Nusselt Number $Nu = hD/k$
$Pr$	Prandtl number $Pr = \mu C_p/k = \nu/\alpha$
$Re$	Reynolds number $Re = \frac{\rho_{bf} u_b h}{\mu_{bf}}$
$Ha$	Hartman nubber $Ha = B_0 h \left( \frac{\sigma_{bf}}{\mu_{bf}} \right)^{0.5}$

### INDEXES

$b$	Base fluid
$C$	Cold
$c$	Core

---

<i>L</i>	Laminaire
<i>f</i>	Base fluide
<i>h</i>	Hot
<i>m</i>	Mean value
<i>p</i>	Nanoparticle
<i>nf</i>	Nanofluid
<i>hnf</i>	Hybrid nanofluid
<i>S</i>	Solid
<i>s</i>	Shell

**ABREVIATIONS**

CFD Computational Fluid Dynamics

CPU Central Processing Unit

LMTD Log Mean Temperature Difference

(*K*)

MCHS Microchannel Heat Sink

SIMPLE Semi-Implicit Method for Pressure-Linked Equations

MHD Magnetic fields flow

UCM Upper Convected Maxwell

NFs Nanofluids

CHT Convection heat transfer

HyNF Hybrid Nanofluids

MQL Minimum quantity lubrication

PCM Phase change materials

FMWCNT Water/functional multi-walled carbon nanotube nanofluid

MWCNTs Multi-walled carbon nanotubes

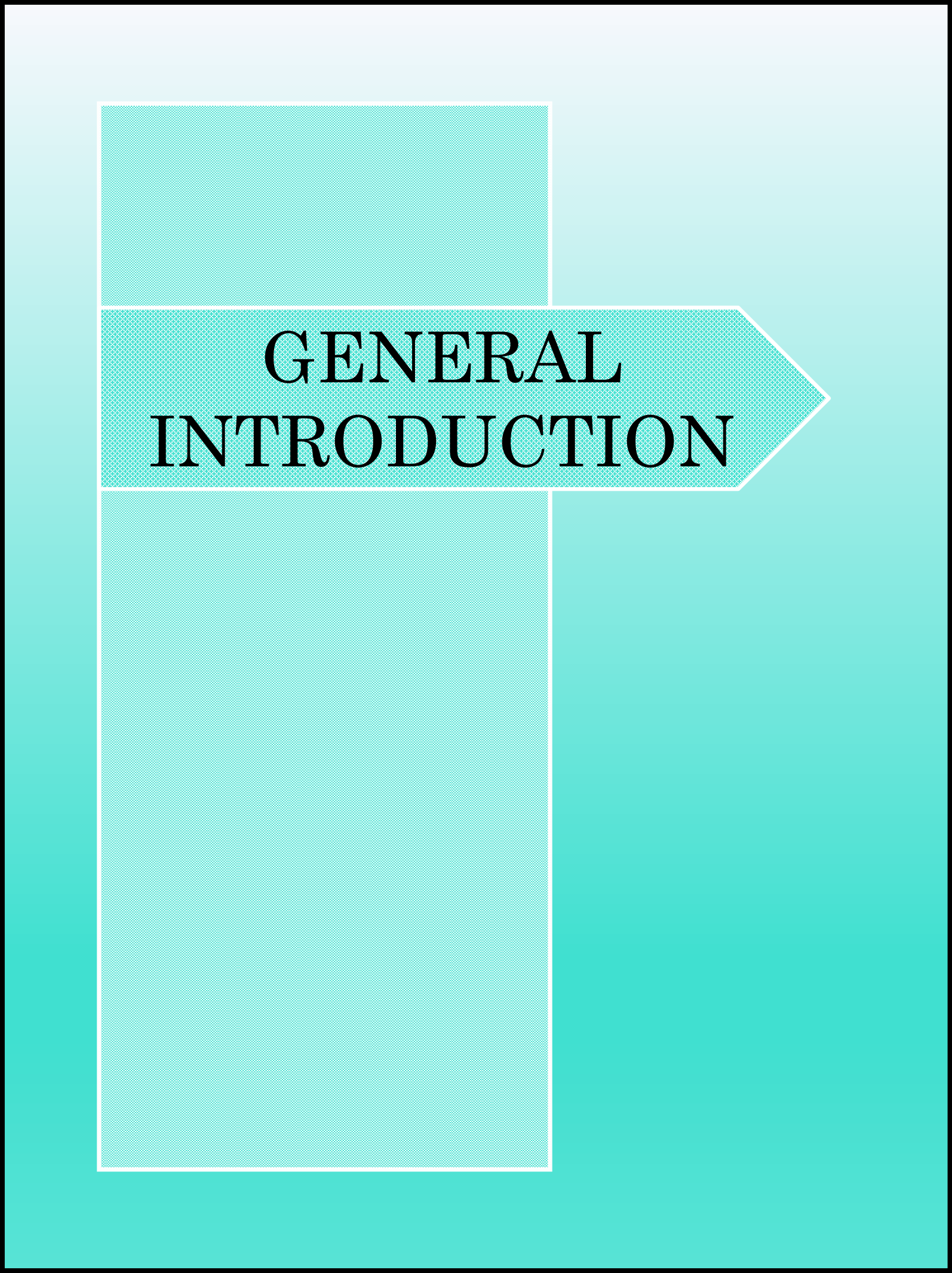
NEPCMs Nano-enhanced phase change materials

EGM Entropy generation minimisation

LTE Local Thermal Equilibrium

LTNE Local Thermal Non-Equilibrium

UNF Used Nuclear Fuel



**GENERAL  
INTRODUCTION**

# GENERALE INTODUCTION

---

## Industrial problematic

Energy has been assumed as the factor for the advancement of the industry for a long time ago, and following to improvement of the industry, employing heat transfer techniques with high thermal efficiency and potential for transfer of a high quantity of energy along with small dimensions are deemed as one of the essential needs in many modern industries and equipment. This issue is crucially important in various industrial tools and processes such as cooling and heating of thermal sources, production processes and industries, e.g. transportation, pharmacology, electronics, automotive and microelectromechanical and nanoelectromechanical systems.

Microchannel heat sinks constitute an innovative cooling technology for removing a large amount of heat through a small area. It is one of the potential alternatives for replacing conventional finned tube heat exchangers. Microchannel heat exchangers have applications in several important and diverse fields, including aerospace; automotive; bioengineering; cooling of gas turbine blades, power and process industries; refrigeration and air conditioning; infrared detectors and powerful laser mirrors and superconductors; microelectronics; and thermal control of film deposition.

In fluid mechanics, fluid flow through porous media is how fluids behave when flowing through a porous medium. The concept of porous media is used in many areas of applied science and engineering. The study of the flow of non-Newtonian fluids in porous media has a wide variety of practical applications in processes such as enhanced oil recovery from underground reservoirs, filtration of polymer solutions and soil remediation through the removal of liquid pollutants.

Heavy oils, foams, polymer solutions and viscoelastic surfactants are some non-Newtonian fluids commonly found in porous media in oil fields.

## Aims

The primary purposes of the present investigation are to look for the best heat transfer efficiency configuration of the heat sink microchannel. This research also seeks to determine and reveal the effects of heater length ( $B$ ), Knudsen number ( $Kn$ ), Darcy number ( $Da$ ), medium porosity ( $\varepsilon$ ), flow behaviour index ( $n$ ), Hartmann numbers ( $Ha$ ), and magnetic field inclination angle ( $\alpha$ ) on the momentum and heat transfer characteristics via offering and discussing the different statistical quantities such as the local and average Nusselt numbers, velocity profiles, streamline and isotherm distributions carefully. The second study gives special consideration to examining the effects of the rheological properties of the Ostwald de Waele fluid on heat transfer characteristics and rheological and hydrodynamic behaviour.

## Scientific problematic

The present study concerns a steady-state laminar magnetohydrodynamic (MHD) flow forced convection heat transfer inside a fully and partially filled microchannel occupied by Cu- $Al_2O_3$ /water hybrid, pseudoplastic and dilatant fluids permeated by a uniform transverse magnetic field ( $B_0$ ) and inclined by an angle ( $\alpha$ ). The present investigation consists of a set of simulations for wide ranges of heat source lengths ( $5 \leq B \leq 30$ ), Knudsen numbers ( $0.001 \leq Kn \leq 0.1$ ), Darcy numbers ( $10^{-5} \leq Da \leq 10^{-2}$ ), medium porosities ( $0.1 \leq \varepsilon \leq 0.9$ ), Hartmann numbers ( $0 \leq Ha \leq 160$ ), and magnetic field inclination angles ( $0^\circ \leq \alpha \leq 90^\circ$ ) for the following fixed parameters : Reynolds number,  $Re=50$ ; nanofluid concentration,  $\varphi = 1\%$ ; porous thermal conductivity ratio,  $Ks=0.613$ . The porous medium is modelled by employing the Brinkman-Darcy model with a local thermal equilibrium (LTE) approach between the working fluid and the porous matrix for energy transfer.

The second investigation of this thesis is based on the slip flow and non-Newtonian fluid through a porous metal foam, with a two-dimensional steady laminar flow forced convection heat transfer of Ostwald de Waele fluid through a partial microchannel heat sink. These investigations were performed for the following parameters : flow behaviour in-



dices (0.2, 0.4, 0.6, 0.8, 1, 1.2, 1.4, 1.6, 1.7), Reynolds numbers (10, 25, 50, 75, 100), Darcy number ( $10^{-1}$ ,  $10^{-3}$ ), at fixed porosity  $\varepsilon = 0.5$ .

## Outline of the Thesis

This thesis is structured into five chapters and is organised as follows :

Chapter I reviews the literature on non-Newtonian fluids, covering fluid classification based on different rheological models ; this chapter presents the relevant fluid mechanics equations for each material type.

Chapter II presents a comprehensive literature review on the experimental and theoretical studies of Newtonian and non-Newtonian flowing through microchannels.

Chapter III presents the various techniques and configurations used in innovative industrial engineering applications.

Chapter IV presents the governing equations, the mathematical formulations, and the physical boundary conditions. In addition, the numerical procedure is also described in this chapter.

Chapter V devotes to the laminar fluid of hybrid nanofluid and Ostwald de Waele fluid through a heat sink microchannel.

Finally, the conclusions are drawn from the findings of the research work and recommendations for future work are made. Additional details and information relevant to the research work conducted are presented in the appendices.

# CHAPTER I

## Rheology and Nanofluids

- Rheology
- Nanofluids

# RHEOLOGY AND NANOFUIDS

# I

## I.1 Rheological behaviour

### I.1.1 Rheology Definition

The term rheology was invented in 1920 by Professor Eugene Bingham at Lafayette College in Indiana USA. A colleague, Martin Reiner, a professor in classical languages and history, inspired him. Bingham, a professor of chemistry, studied new materials with strange flow behaviour, particularly paints [1]. Rheology is the science of deformation and flow. It is a branch of physics and physical chemistry since the most important variables come from the field of mechanics : forces, deflections and velocities. The term "rheology" originates from the Greek : "rhein" meaning "to flow". Thus, rheology is literally "flow science". However, rheological experiments reveal information about liquids' flow behaviour and solids' deformation behaviour. The connection here is that a large deformation produced by shear forces causes many materials to flow [2].

All kinds of shear behaviour, which can be described rheologically scientifically, can be viewed as being between two extremes : the flow of ideally viscous liquids on the one hand and the deformation of ideally elastic solids on the other. The behaviour of all real materials is based on the combination of a viscous and an elastic portion ; therefore, it is called viscoelastic. For example, wallpaper paste is a viscoelastic liquid, and a gum eraser is a viscoelastic solid [3].

There are two basic kinds of flow with relative movement of adjacent liquid particles : shear and extensional flows. In shear flows, liquid elements flow over or past each other. In contrast, in extensional flow, adjacent elements flow towards or away from each other ; see Figure I.1 for illustrations of shear and extensional deformation and flow, respectively [4].

Liquids		Solids	
(ideal-) viscous	Viscoelastic	Viscoelastic	(ideal-) elastic
Flow behaviour	Flow behaviour	Deformation Behaviour	Deformation Behaviour
Newton's law	Maxwell's law	Kelvin/Voigt's	Hooke's law
Flow/Viscosity curves		Creep tests,relaxation tests,oscillatory tests	

**Table I.1** – Overview of different kinds of rheological behaviour [2].

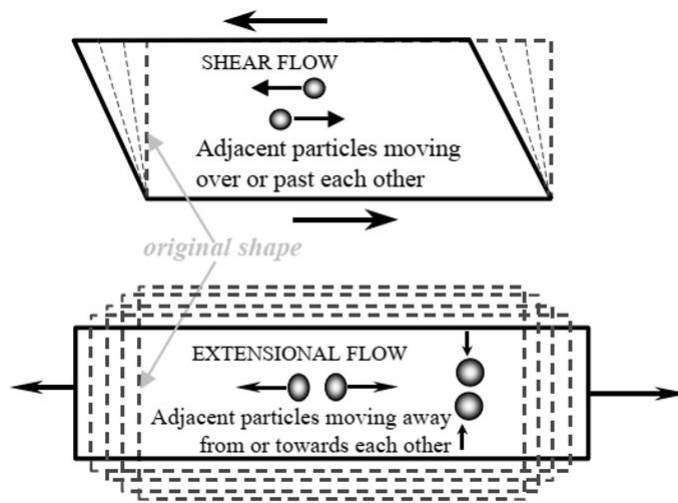


**Figure I.1** – Particle motion in shear and extensional flows [3].

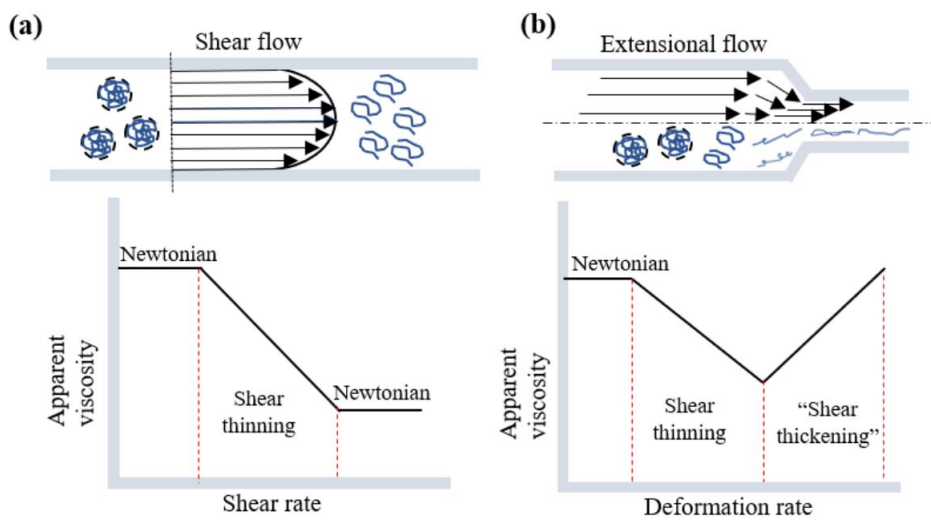


**Figure I.2** – Schematic illustration of viscoelastic polymer rheology [4].

(a) shear flow, such as in rotational rheometers and capillary rheometers showing shear thinning where a relaxation of the largest polymer chain occurs (b) extensional flow, such as in porous media with converging-diverging geometry showing shear thickening, where polymer coils are stretched due to extensional flow [4].

Many industries frequently work with products in a liquid phase during all or some of the industrial operations carried out (concentration, evaporation, pasteurisation, pumps, and those in between), thus a good design of each process installation is indispensable for good operation. In the design of all processes, it is necessary to know the individual physical characteristics differentiating each process. One characteristic is the rheological behaviour of the fluid processed. Knowledge of its rheology can avoid possible excess dimensions of pumps, pipes, evaporators, etc., all of which could cause a negative rebound in the economy of the process [5].

Rheology is very important in the following area of the food industry [5] :

1. Mixing-Two or more materials are blended manually or mechanically.
2. Flow Control-Flowability of material varies from very thin to highly viscous.
3. Dispensing- Material comes out easily or with difficulty.
4. Settling/ Floating – Material with different specific gravity either settle or float depending on viscosity of the material.
5. Pumping- Liquids or semi-solids are forced through the pipe.
6. Coating- Spreading of one material as thin layer over other.
7. Cleaning – Soil removal from the surface of the equipments and pipeline.
8. Control of processing parameters- velocity, magnitude of pressure drop, piping design, pumping requirement for fluid transport system, power requirement of agitation, power requirement of mixing and blending, amount of heat generated during extrusion etc.
9. Influence on unit operations – Heat transfer, Mass transfer, mixing, grinding, sedimentation, separation, filtration, evaporation and drying etc.
10. Study of rheology helps to select proper method of harvesting and sorting of raw materials.
11. Study of rheology helps to select proper ingredients to manufacture processed foods.
12. Study of rheology helps to select proper technology/equipment to manufacture processed foods.with desirable sensory and rheological properties.
13. Study of rheology helps in newer product development (e.g. dietetic ice cream, paneer, low fat mozzarella cheese etc.)

14. Study of rheology helps in designing processing equipment, packaging machines, transportation system etc.
15. Study of rheology helps to improve sensory quality of the products.
16. Study of rheology helps in marketing the products.

### I.1.2 Shear rate and shear stress

As we have seen in Figure I.2, simple shear flow is the continual movement of liquid particles over or past each other, while extensional (or elongational, or stretching) flows are where particles of liquid flow towards or away from each other (see below). In Figure I.3 we visualise shear flow alternatively as the movement of hypothetical layers sliding over each other. In the simplest case the velocity of each layer increases linearly with respect to its neighbour below so that layers twice the distance from any stationary edge move at the double the speed, etc. The velocity gradient in the direction at right angles to the flow is called the shear rate (sometimes called the velocity gradient or strain rate), and the force per unit area creating or producing by the flow is called the shear stress. In our simple example, the shear rate is  $V/h$  and is described by the symbol  $\dot{\gamma}$  (pronounced 'gamma dot'), while the shear stress is given by  $F/A$  and is given the symbol  $\sigma$  [3].

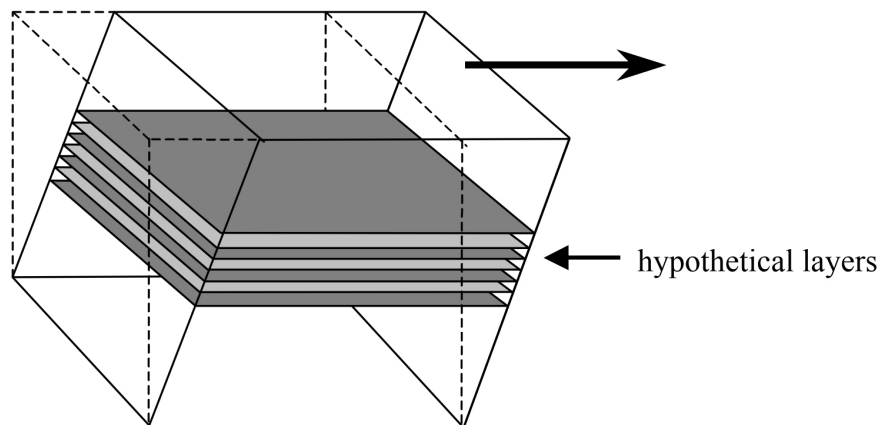


**Figure I.3** – Hypothetical layers in shear flow [3].

The shear rate has the units of velocity divided by distance, i.e., metres per second / metres, leaving us with the units of reciprocal (i.e., one over) seconds, or  $s^{-1}$ . Shear stress force per unit area has the units of newtons per square metre,  $N m^{-2}$  but in the SI system, stress, like pressure, it is given in units of pascals, Pa, in honour of the famous French scientist. For

reference, standard atmospheric pressure, previously known to many as 14.7 pounds per square inch (psi), is  $10^5$  Pa [3].

The approximate value of the shear rate encountered in a wide variety of circumstances found in everyday life or in industrial situations is shown in Table I.2 Readers may relate these numbers to their own field of interest by simply dividing a typical velocity in any flow of interest by a typical dimension [3].

Situation	Shear Rate Range /s <sup>-1</sup>	Examples
Sedimentation of Fine Powders in liquids	10 <sup>-6</sup> – 10 <sup>-3</sup>	Medecines, paints, salad, dressing
Levelling due to surface tension	10 <sup>-2</sup> – 10 <sup>-1</sup>	Paints, printing inks
Draining off surfaces under gravity	10 <sup>-1</sup> – 10 <sup>1</sup>	Toilet bleaches, paints, coatings
Extruders	10 <sup>0</sup> – 10 <sup>2</sup>	Polymers, foods soft solids
Chewing and swallowing	10 <sup>1</sup> – 10 <sup>2</sup>	Foods
Dip coating	10 <sup>1</sup> – 10 <sup>2</sup>	Paints, confectionery
Miwing and stirring	10 <sup>1</sup> – 10 <sup>3</sup>	Liquids manufacturing
Pipe flow	10 <sup>0</sup> – 10 <sup>3</sup>	Pumping liquids, blood flow
Brushing	10 <sup>3</sup> – 10 <sup>4</sup>	Painting
Rubbing	10 <sup>4</sup> – 10 <sup>5</sup>	Skin creams, lotions
High-speed coating	10 <sup>4</sup> – 10 <sup>6</sup>	Paper manufacture
Spraying	10 <sup>5</sup> – 10 <sup>6</sup>	Atomisation, spray drying
Lubrication	10 <sup>3</sup> – 10 <sup>7</sup>	Bearings, engines

Table I.2 – Typical shear rate ranges of various physical operations [3].

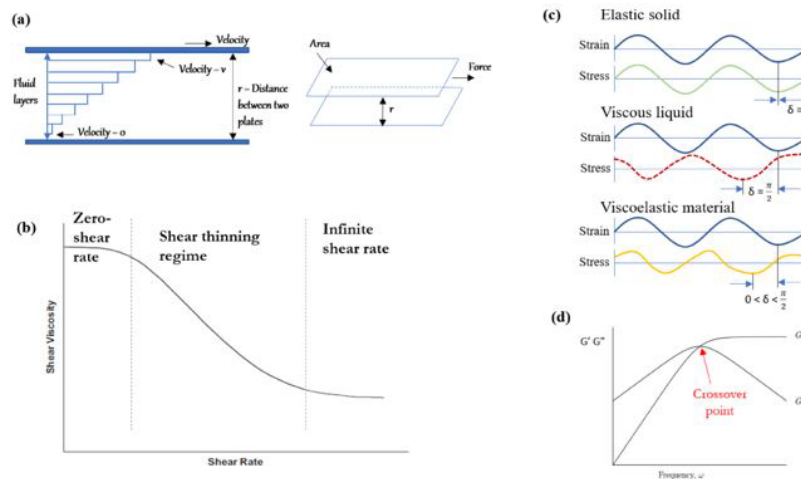


Figure I.4 – The shear stress - shear rate relationship [4].

(a) Schematic representation of fluid flow in simple shear flow (b) Rheogram curve of shear viscosity versus shear rate (c) Illustration of the stress response during oscillatory rheology for elastic, viscous and viscoelastic material (d) Storage and loss modulus as a function of frequency, showing the intersection point of the modulus [4].

### I.1.3 Rheometry

The term "rheometry" is usually used to refer to a group of experimental techniques for investigating the rheological behaviour of materials. It is of great importance in determining the constitutive equation of a fluid or in assessing the relevance of any proposed constitutive law. Most of the textbooks on rheology deal with rheometry. The books by Coleman et al (1966), Walters (1975), and by Bird et al (1987) provide a complete introduction to the viscometric theory used in rheometry for inferring the constitutive equation. The book by Coussot & Ancy (1999b) gives practical information concerning rheometrical measurements with natural fluids. Though primarily devoted to food processing engineering, Steffe's book presents a detailed description of rheological measurements, (Steffe, 1996) [6].

Rheometry is the measuring technology used to determine rheological data. The emphasis here is on measuring systems, instruments, and test and analysis methods. Both liquids and solids can be investigated using rotational and oscillatory rheometers. Rotational tests which are performed to characterise viscous behaviour. In order to evaluate viscoelastic behaviour, creep tests, relaxation tests and oscillatory tests are performed [2].

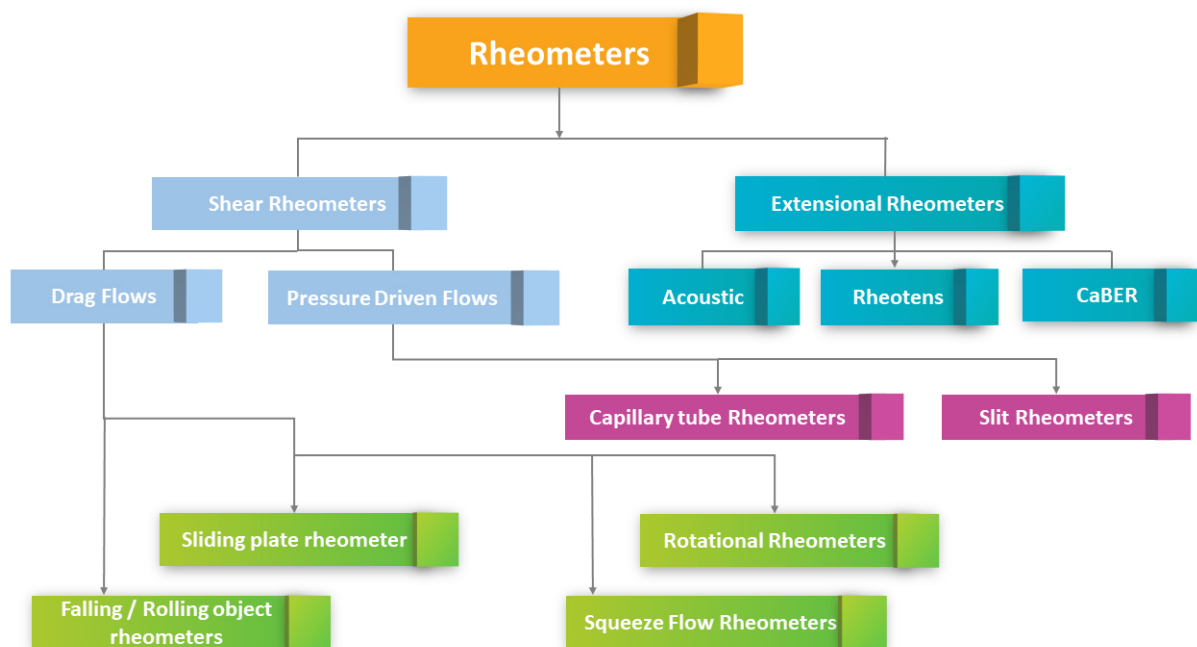
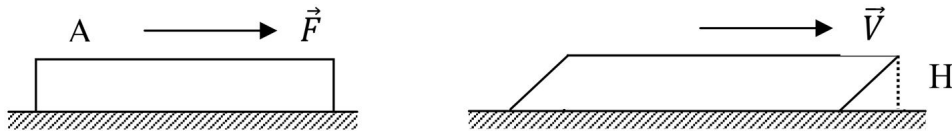


Figure I.5 – Some classical types of rheometers.



### I.1.4 Classification of fluid behaviour

A fluid is a substance that deforms continuously when subjected to a shear stress or tangential force [Figure I.6](#), even if the applied shear stress is very small. In simple words, a fluid is a substance capable of flowing and conforming to the containing vessel. A real fluid is one that has some finite viscosity (resistance to flow) and thus can exert a tangential (shearing) stress on a surface with which it is in contact. The flow of real fluids is called a viscous flow. A real fluid can be further subdivided into Newtonian fluids and non-Newtonian fluids [\[7\]](#).



**Figure I.6** – Fluid deformation by the application of force, where the applied force per unit area is called stress ( $\sigma = \frac{F}{A}$ ) and the resulting rate of change of deformation is called shear rate ( $\dot{\gamma} = \frac{V}{H}$ ) [\[7\]](#).

### I.1.5 Simple fluid

A simple fluid is defined to be a fluid that exhibits only a single type of behaviour. In the case of a simple viscous fluid, which is by far the most relevant to real fluid models, the fluid has a linear response to stress. Called Newtonian fluids, the viscous response follows Newton's law for fluids, a simple linear relationship between stress and strain rate. More rigorously, a fluid is considered to be Newtonian if the stress tensor is constant. If the stresses throughout the fluid may be considered isotropic, then the stress tensor is diagonalisable under the transformation  $T : E \rightarrow E_0$  Where  $E_0 = \{\hat{n}, e'_2, e'_3\}$  is defined in terms of the surface normal. This means that the viscosity can be completely reduced two terms, the shear and normal viscosities since only 1 of the 3 principal viscosities will be normal and the other two will be in the plane of the surface. Under the assumption of incompressibility, normal stresses may be neglected. Therefore, the shear viscosity is the sole parameter of interest for Newtonian fluids [\[8\]](#).

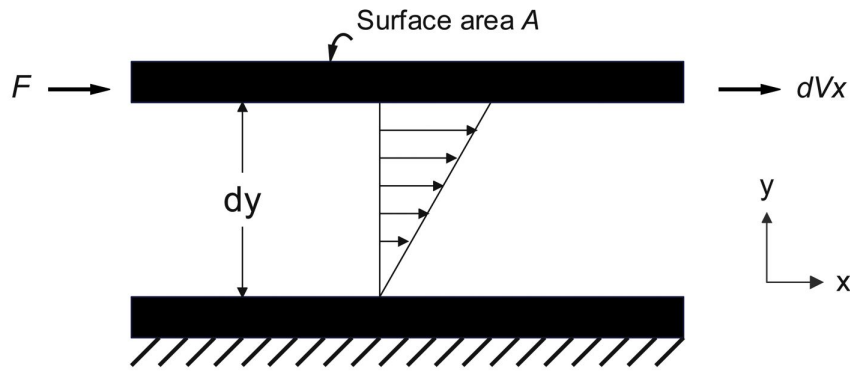


**Figure I.7** – Simple shear of a Newtonian fluid between two parallel planes.

### I.1.5.1 Newtonian Fluids

Fluids that show a departure from Newtonian behaviour are termed as non-Newtonian fluids. When the flow behaviour of a material follows the basic law of viscosity proposed by Isaac Newton, then it is said to depict Newtonian behaviour. The constitutive equation for Newtonian fluids, which show constant viscosity without any yield stress and/or elastic component, is given as [9] :

$$\tau = \mu \dot{\gamma} \quad (I.1)$$

where  $\tau$  is the shear stress,  $\dot{\gamma}$  is the shear rate, and the constant  $\mu$  is termed as the Newtonian viscosity. In general, for determining velocity distributions and stresses, incompressible Newtonian fluids at constant temperature can be characterised by two material constants, namely, the shear viscosity  $\mu$  and the density  $\rho$ . Once these quantities are measured, the velocity distribution and the stresses in the fluid, in principle, can be found for any flow situation. In other words, different isothermal experiments on a Newtonian fluid would yield a single constant material property, namely, its viscosity  $\mu$  whose units are milliPascals seconds . Some examples of the commonly known Newtonian fluids are water ( $\mu \approx 1 \text{ mPa s}$ ), coffee cream ( $\mu \approx 10 \text{ mPa s}$ ), olive oil ( $\mu \approx 10^2 \text{ mPa s}$ ), and honey ( $\mu \approx 10^4 \text{ mPa s}$ ).

The graphical representation of shear stress versus shear rate is a straight line, which passes through the origin as shown in Figure I.8. The slope of the straight line gives the value of viscosity for the given fluid. Thus, the viscosity is constant for Newtonian fluid at a given temperature and pressure. Newtonian's fluids can be represented by rheogram as shown in Figure I.9 given below [7].

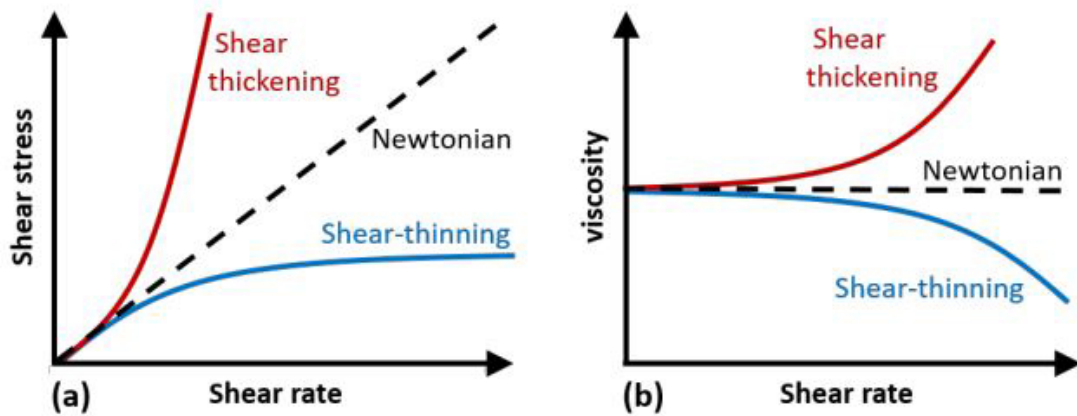


**Figure I.8** – Representation of flow curves of different types of fluids : Newtonian, shear-thinning and shear-thickening [10].

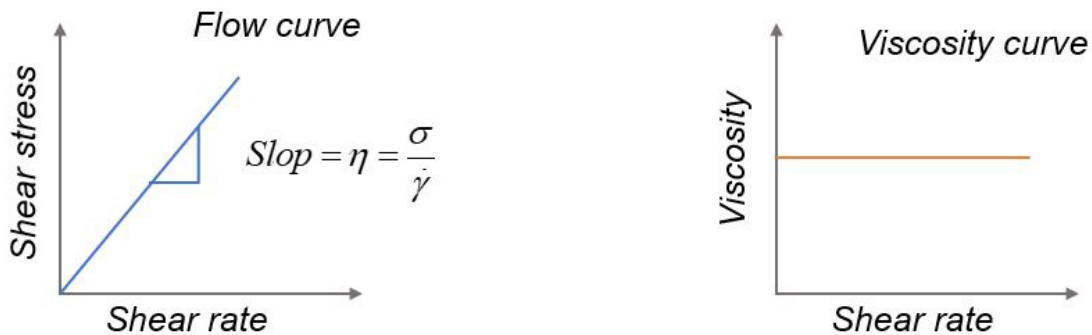


**Figure I.9** – Flow curve and viscosity curve for Newtonian fluids [7].

Examples of Newtonian fluids are air, steam, milk, vegetable oils, fruit juices, sugar solutions, salt solutions, almost all gases and water.

### I.1.6 Complex fluid

Much more often in nature, a fluid will possess more than a single type of stress response. A fluid is deemed complex if it exhibits multiple types of behaviours. While this definition is largely vague, most complex fluids can be regarded as twofold ; a complex fluid usually exhibits two types of behaviours, such as a solid-liquid mixture, or liquid-gas mixture. Modelling the dynamics of flow in complex fluids is convoluted due to the coexistence of multiple matter phases, and non linear effects may arise from the interaction between matter phases. In optical microrheology, microparticles are used to track flows in complex fluids to better understand

the microfluidics created by the interaction of multiple matter phases. This paper will restrict the scope to non-Newtonian fluids, which are a special type of complex fluid resulting from a mixture of liquid and solid behaviours [8].

### I.1.6.1 Non-Newtonian Fluids

A non-Newtonian fluid can be described as a fluid whose rheogram is non-linear and/or does not pass through the origin (Steffe, 1996). The viscosity Eq I.2 of a non-Newtonian fluid is not constant. It is referred to as the apparent viscosity (Perry, 1997) and is dependent on the shear rate. Several mathematical equations have been derived to describe the rheograms of non-Newtonian fluids, some of which are discussed below [11].

$$\mu = \frac{\tau_{yx}}{\dot{\gamma}_{yx}} \quad (\text{I.2})$$

Non-Newtonian fluids are commonly divided into three broad groups, although in reality these classifications are often by no means distinct or sharply defined [12] :

1. **Time-independent fluids** are those for which the strain rate at a given point is solely dependent upon the instantaneous stress at that point.
2. **Viscoelastic fluids** are those that show partial elastic recovery upon the removal of a deforming stress. Such materials possess properties of both viscous fluids and elastic solids.
3. **Time-dependent fluids** are those for which the strain rate is a function of both the magnitude and the duration of stress and possibly of the time lapse between consecutive applications of stress.

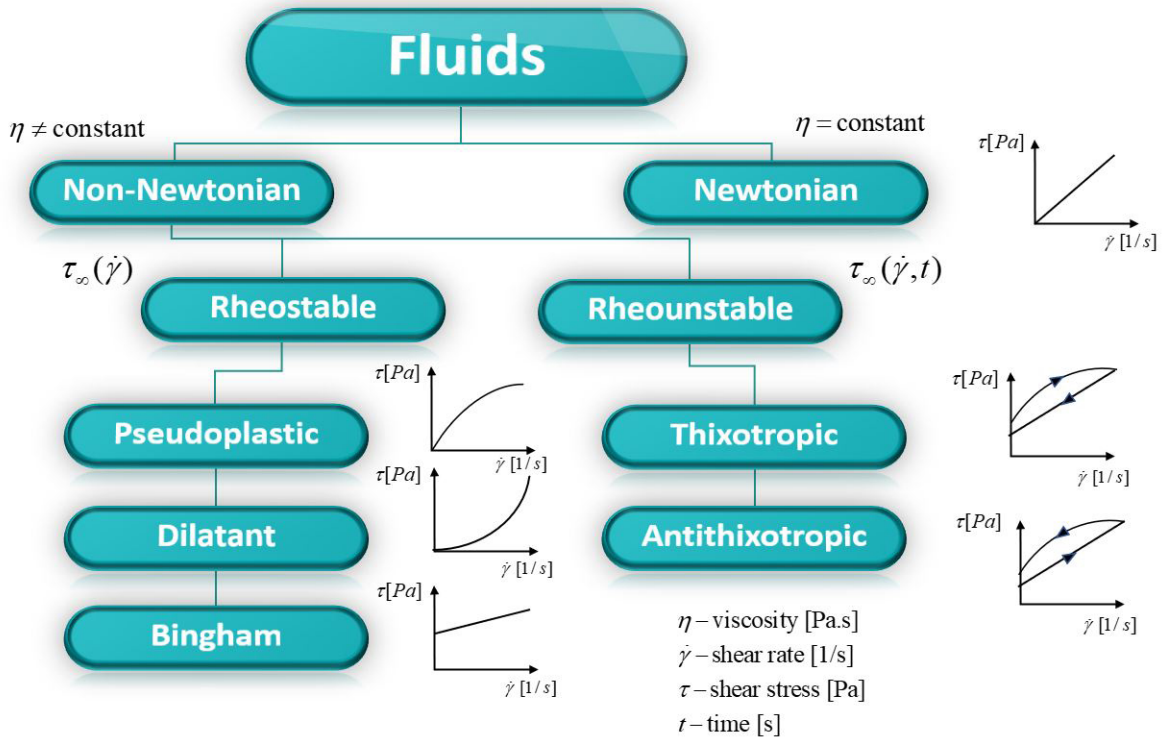
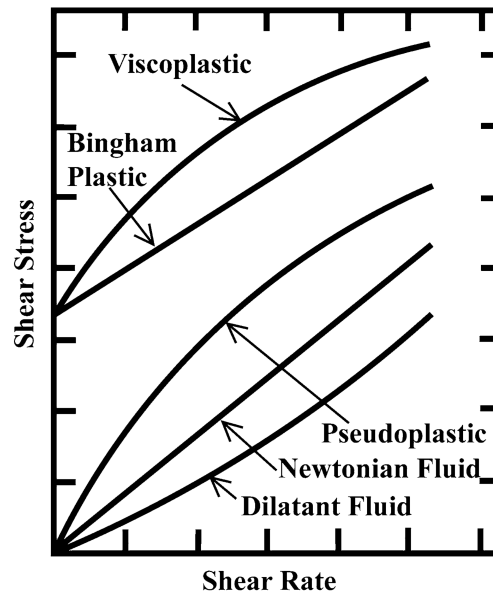


Figure I.10 – Classification of fluids.

**I.1.6.2 Time-Independent Fluids**

Shear rate dependence is one of the most important and defining characteristics of non-Newtonian fluids in general and time-independent fluids in particular. When a typical non-Newtonian fluid experiences a shear flows the viscosity appears to be Newtonian at low shear rates. After this initial Newtonian plateau, the viscosity is found to vary with increasing shear rate. The fluid is described as shear-thinning or pseudoplastic if the viscosity decreases, and shear-thickening or dilatant if the viscosity increases on increasing shear rate. After this shear-dependent regime, the viscosity reaches a limiting constant value at high shear rate. This region is described as the upper Newtonian plateau. If the fluid sustains initial stress without flowing, it is called a yield-stress fluid. Almost all polymer solutions that exhibit a shear rate dependent viscosity are shear-thinning, with relatively few polymer solutions demonstrating dilatant behavior. Moreover, in most known cases of shear-thickening there is a region of shear-thinning at lower shear rates [12].



**Figure I.11** – Qualitative flow curves for different types of non-Newtonian fluids [13].

#### I.1.6.2.a Power-Law Model

The power-law, or Ostwald-de Waele model, is one of the simplest time-independent fluid models as it contains only two parameters. The model is given by the relation [12] :

$$\mu = K\dot{\gamma}^{n-1} \quad (\text{I.3})$$

where  $\mu$  is the viscosity,  $K$  is the consistency factor,  $\dot{\gamma}$  is the shear rate and  $n$  is the flow behavior index. In Figure I.12, the bulk rheology of this model for shear-thinning case is presented in a generic form as viscosity versus shear rate on log-log scales.

The power-law is usually used to model shear-thinning though it can also be used for modeling shear-thickening by making  $n > 1$ . The major weakness of power-law model is the absence of plateaux at low and high shear rates. Consequently, it fails to produce sensible results in these shear regimes.

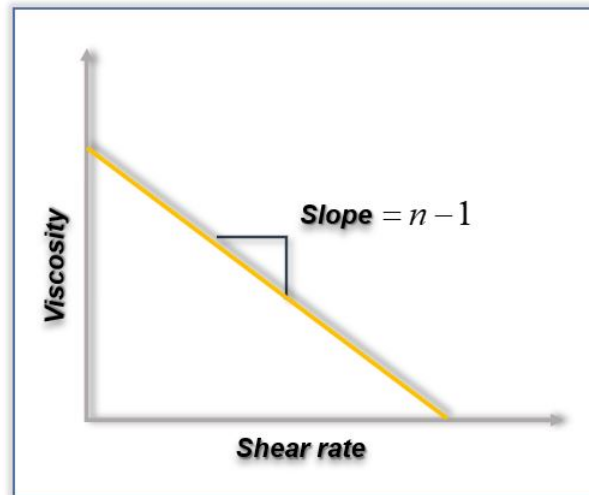


**Figure I.12** – The bulk rheology of a power-law fluid on logarithmic scales for finite shear rates.

#### I.1.6.2.a.a Shear-thinning or pseudoplastic fluids

The most common type of time-independent non-Newtonian fluid behaviour observed is pseudoplasticity or shear-thinning, characterised by an apparent viscosity which decreases with increasing shear rate. Both at very low and at very high shear rates, most shear-thinning polymer solutions and melts exhibit Newtonian behaviour, i.e., shear stress–shear rate plots become straight lines, as shown schematically in Figure I.13 and on a linear scale will pass through origin. The resulting values of the apparent viscosity at very low and high shear rates are known as the zero-shear viscosity,  $\mu_0$ , and the infinite shear viscosity,  $\mu$ , respectively. Thus, the apparent viscosity of a shear-thinning fluid decreases from  $\mu_0$  to  $\mu$  with increasing shear rate. Data encompassing a sufficiently wide range of shear rates to illustrate this complete spectrum of pseudoplastic behaviour are difficult to obtain, and are scarce. A single instrument will not have both the sensitivity required in the low shear rate region and the robustness at high shear rates, so that several instruments are often required to achieve this objective [14].

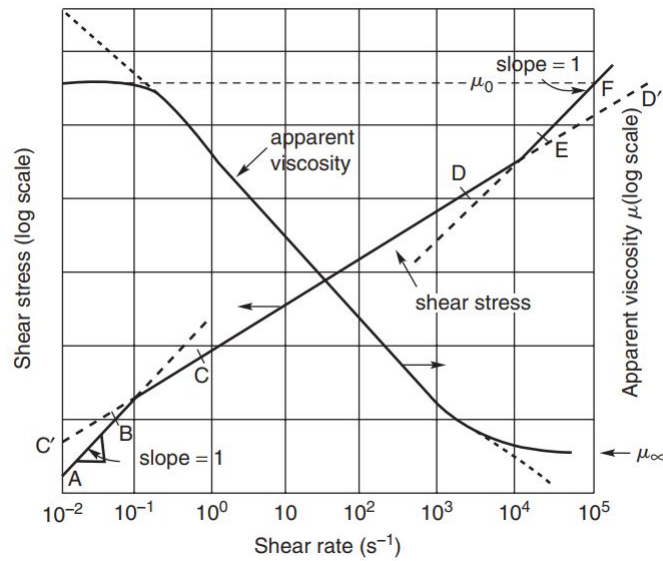


**Figure I.13** – Schematic representation of shear-thinning behaviour [14].

#### I.1.6.2.a.b Shear-thickening or dilatant fluid behaviour

Dilatant fluids are similar to pseudoplastic systems in that they show no yield stress but their apparent viscosity increases with increasing shear rate; thus, these fluids are also called shear-thickening. This type of fluid behaviour was originally observed in concentrated suspensions and a possible explanation for their dilatant behaviour is as follows: At rest, the voidage is minimum and the liquid present is sufficient to fill the void space. At low shear rates, the liquid lubricates the motion of each particle past others and the resulting stresses are consequently small. At high shear rates, on the other hand, the material expands or dilates slightly (as also observed in the transport of sand dunes) so that there is no longer sufficient liquid to fill the increased void space and prevent direct solid–solid contacts which result in increased friction and higher shear stresses (as shown schematically in Figure I.14) This mechanism causes the apparent viscosity to rise rapidly with increasing rate of shear. The term dilatant has also been used for all other fluids which exhibit increasing apparent viscosity with increasing rate of shear. Many of these, such as starch pastes, are not true suspensions and show no dilation on shearing. The above explanation therefore is not applicable but nevertheless such materials are still commonly referred to as dilatant fluids. Of the time-independent fluids, this sub-class has received very little attention; consequently, very few reliable data are available. Until recently, dilatant fluid behaviour was considered to be much less widespread in the chemical and processing industries [14].



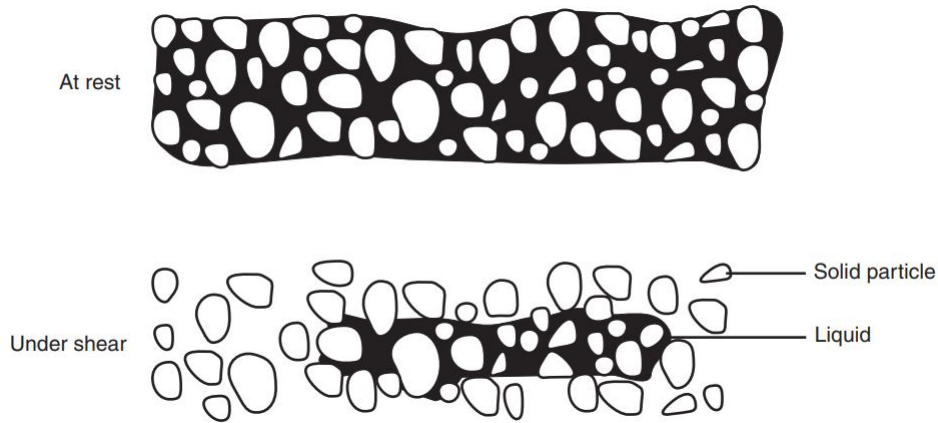


**Figure I.14** – Schematic representation of shear-thickening behaviour [14].

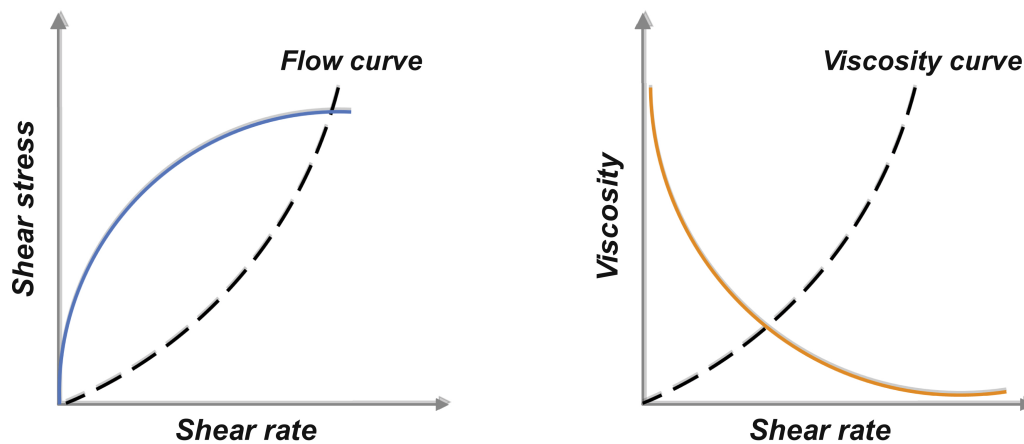


**Figure I.15** – Flow curve and viscosity curve for shear thinning fluids (solid line), and shear thickening fluids (dotted line).

#### I.1.6.2.b The Cross model

First, we will consider one equation that describes the whole curve : this is called the Cross model, named after [Malcolm Cross](#), an ICI rheologist who worked on dyestuff and pigment dispersions. He found that the viscosity of many suspensions could be described by the equation of the form [3] :

$$\frac{\eta - \eta_{\infty}}{\eta_0 - \eta_{\infty}} = \frac{1}{1 + (K\dot{\gamma})^m} \quad (\text{I.4})$$

where, written in this particular way,  $K$  has the dimensions of time, and  $m$  is dimensionless. When this model is used to describe non-Newtonian liquids, the degree of shear thinning is dictated by the value of  $m$ , with  $m$  tending to zero describes more Newtonian liquids, while the most shear-thinning liquids have a value of  $m$  tending to unity. If we make various simplifying assumptions, it is not difficult to show that the Cross equation can be reduced to Sisko, power-

law and Newtonian behaviour, see below. There is another Cross-like model which uses the stress rather than the shear rate as the independent variable, it has been called the Ellis or sometimes the Meter model, and for some specific values of the exponent, it has been given other names : for an exponent of unity, it has been called the [Williamson](#) or [Dougherty](#) and [Krieger model](#), while for an exponent of two it has been called the Philippoff model, etc.

The Carreau model is very similar to the Cross model, but with the whole of the bottom line within brackets, i.e.,  $(1 + (K\dot{\gamma})^2)^{m/2}$  : the two are the same at very low and very high shear rates, and only differ slightly at  $K\dot{\gamma} \sim 1$ .

### I.1.6.2.c Viscoplastic fluid behaviour

This type of fluid behaviour is characterised by the existence of a yield stress  $\tau_0$  which must be exceeded before the fluid will deform or flow. Conversely, such a material will deform elastically (or flow en masse like a rigid body) when the externally applied stress is smaller than the yield stress. Once the magnitude of the external stress has exceeded the value of the yield stress, the flow curve may be linear or non-linear but will not pass through origin. Hence, in the absence of surface tension effects, such a material will not level out under gravity to form an absolutely flat free surface. One can, however, explain this kind of fluid behaviour by postulating that the substance at rest consists of three-dimensional structures of sufficient rigidity to resist any external stress less than  $\tau_0$ . For stress levels greater than, however, the structure breaks down and the substance behaves like a viscous material.

A fluid with a linear flow curve for  $|\tau_{yx}| > |\tau_0|$  is called a Bingham plastic fluid and is characterised by a constant plastic viscosity (the slope of the shear stress versus shear rate curve) and a yield stress. On the other hand, a substance possessing a yield stress as well as a non-linear flow curve on linear coordinates (*for*  $|\tau_{yx}| > |\tau_0|$ ), is called a 'yield-pseudoplastic' material. [Figure I.16](#) illustrates viscoplastic behaviour as observed in a meat extract and in a polymer solution [14].

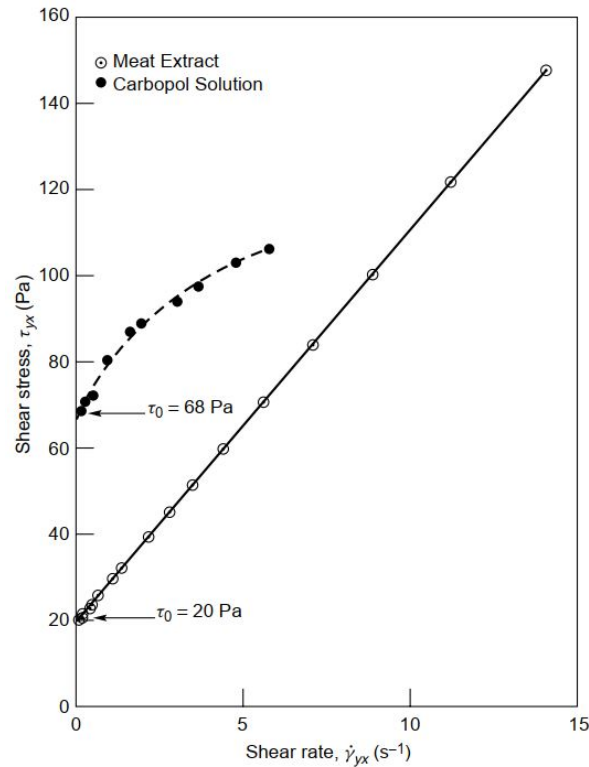


**Figure I.16** – Representative shear stress–shear rate data showing viscoplastic behaviour in a meat extract (Bingham Plastic) and in an aqueous carbopol polymer solution (yield-pseudoplastic) [14].

#### I.1.6.2.c.a The Bingham fluid

The Bingham fluid model is characterized by a yield stress  $\tau_0$  which, if exceeded, makes the material flow like a viscous Newtonian fluid or else behave like a solid at all values below critical stress. Hence, the equations for this fluid are as follows [9] :

$$\begin{aligned} \tau &= \tau_0 + \mu'(\dot{\gamma}) & \text{for } |\tau| > |\tau_0| \\ \dot{\gamma} &= 0 & \text{for } |\tau| < |\tau_0| \end{aligned} \quad (\text{I.5})$$

Here, is called plastic viscosity.

Figure I.17 shows the typical form of the results that would normally have been measured and plotted graphically over the last 50 years. Over a reasonable range of shear rates, the shear stress seemed to be a linear function of shear rate, but now displaced upwards by a constant value, which is called the yield stress. This was found by extrapolation to where the shear rate was zero. This seemed to show that there would be no flow at all unless the stress was higher than this critical value. Bingham investigated systems like this, and this simple straight-line-with-intercept-type behaviour bears his name, and such liquids are called Bingham plastics, and as we have said above, the intercept is called the Bingham yield stress and the slope of the

straight line is called the plastic viscosity,  $\eta_p$  [3].

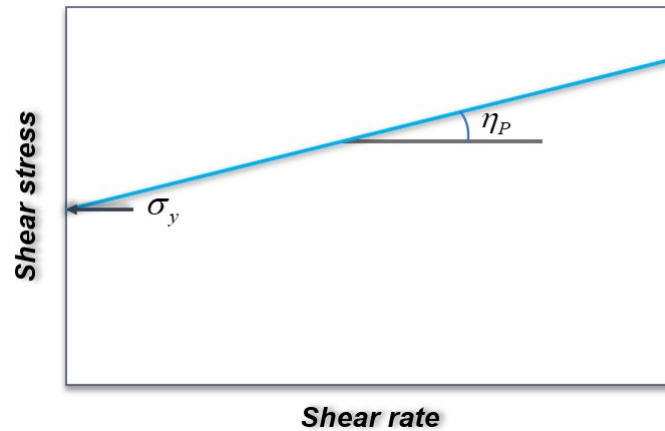


Figure I.17 – Definition diagram of the Bingham model.

#### I.1.6.2.c.b The Herschel-Bulkley Model

The Herschel-Bulkley is a simple rheological model with three parameters. Despite its simplicity it can describe the Newtonian and all main classes of the time independent non-Newtonian fluids. It is given by the relation [12] :

$$\begin{aligned} \tau &= \tau_0 + \mu'(\dot{\gamma})^n & \text{for } |\tau| > |\tau_0| \\ \dot{\gamma} &= 0 & \text{for } |\tau| < |\tau_0| \end{aligned} \quad (\text{I.6})$$

Where  $\tau$  is the shear stress,  $\tau_0$  is the yield-stress above which the substance starts to flow,  $\mu'$  is the consistency factor,  $\dot{\gamma}$  is the shear rate and  $n$  is the flow behavior index. The Herschel-Bulkley model reduces to the power-law when  $\tau_0 = 0$ , to the Bingham plastic when  $n=1$ , and to the Newton's law for viscous fluids when both these conditions are satisfied.

There are six main classes to this model [12] :

1. Shear-thinning (pseudoplastic) [ $\tau_0 = 0, n < 1$ ]
2. Newtonian [ $\tau_0 = 0, n = 1$ ]
3. Shear-thickening (dilatant) [ $\tau_0 = 0, n > 1$ ]
4. Shear-thinning with yield-stress [ $\tau_0 > 0, n < 1$ ]
5. Bingham plastic [ $\tau_0 > 0, n = 1$ ]
6. Shear-thickening with yield-stress [ $\tau_0 > 0, n > 1$ ].

### I.1.6.2.d The Carreau Model

This is a four-parameter rheological model that can describe shear-thinning fluids with no yield-stress. It is generally praised for its compliance with experiment. The distinctive feature of this model is the presence of low- and high-shear plateaux [12].

The Carreau fluid is given by the relation [12] :

$$\mu = \mu_{\infty} + \frac{\mu_0 - \mu_{\infty}}{\left[1 + (\dot{\gamma}t_c)^2\right]^{\frac{1-n}{2}}} \quad (\text{I.7})$$

Where  $\mu$  is the fluid viscosity,  $\mu_{\infty}$  is the viscosity at infinite shear rate,  $\mu_0$  is the viscosity at zero shear rate,  $\dot{\gamma}$  is the shear rate,  $t_c$  is a characteristic time and  $n$  is the flow behavior index. A generic graph demonstrating the bulk rheology is shown in Figure I.18.

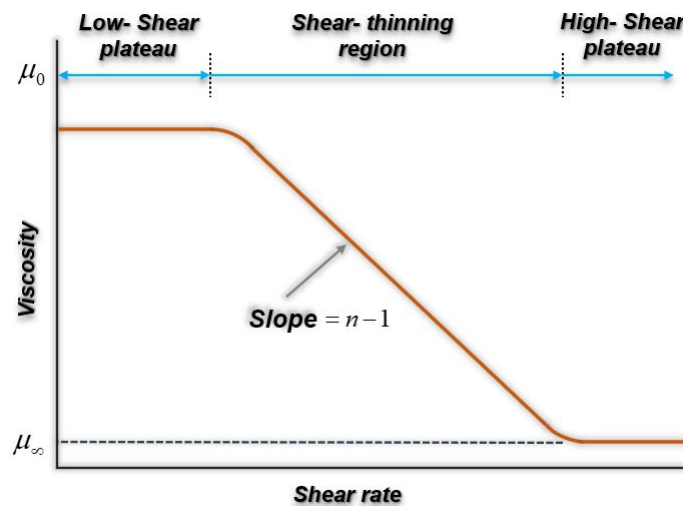


**Figure I.18** – The bulk rheology of a Carreau fluid on logarithmic scales for finite shear rates ( $\dot{\gamma} > 0$ ).

### I.1.6.2.e The Carreau-Yasuda Model

Carreau and Yasuda developed a model that accounts for the observed Newtonian plateaus and fits a wide range of strain rates (Osswald and Rudolph, 2014)[15] :

$$\frac{\eta\dot{\gamma} - \eta_{\infty}}{\eta_0 - \eta_{\infty}} = (1 + (\lambda\dot{\gamma})^2)^{\frac{n-2}{2}} \quad (\text{I.8})$$

Where  $\eta_0$  is the zero-shear rate viscosity,  $\eta_{\infty}$  is an infinite shear rate viscosity of the second Newtonian plateau,  $\lambda$  is a time constant, and  $n$  is the Power Law index, which accounts for the shear thinning behavior, see Figure I.19.

Some features of these Generalised Newtonian Fluid Models (Shogin, 2019) [15] :

- . Predict shear thinning.
- . Worked for steady shear flow.
- . Fail when flow is unsteady.
- . Don't predict the normal stress.

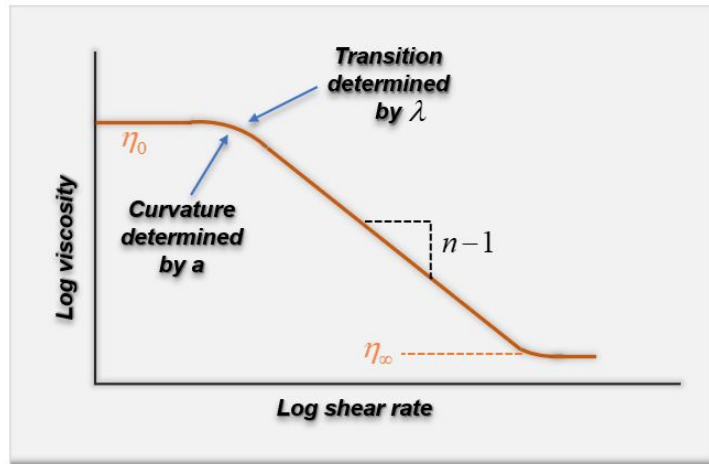


**Figure I.19** – Viscosity approximation using the Bird-Carreau-Yasuda model.

#### I.1.6.2.f The Ellis model

When the deviations from the power-law model are significant only at low shear rates, it is perhaps more appropriate to use the Ellis model. The three-constant Ellis model is an illustration of the inverse form, namely. In simple shear, the apparent viscosity of an Ellis model fluid is given by [14] :

$$\mu = \frac{\mu_0}{1 + \left(\tau/\tau_{1/2}\right)^{\alpha-1}} \quad (\text{I.9})$$

In this equation,  $\mu_0$  is the zero-shear viscosity and the remaining two constants  $\alpha(> 1)$  and  $\tau_{1/2}$  are adjustable parameters. While the index is a measure of the degree of shear-thinning behaviour (the greater the value of  $\alpha$ , greater is the extent of shear-thinning) represents the value of shear stress at which the apparent viscosity has dropped to half its zero-shear value. Eq I.9 predicts Newtonian fluid behaviour in the limit of  $\tau_{1/2} \rightarrow \infty$ . This form of equation has advantages in permitting easy calculation of velocity profiles from a known stress distribution, but renders the reverse operation tedious and cumbersome.

### I.1.6.3 Time-dependent Fluids

These are the fluids for which viscosity of the fluid does not depend only on shear rate but also on the time during which shear rate is applied [7] :

$$\eta = \eta (\dot{\gamma}, t) \quad (\text{I.10})$$

These fluids are very difficult to model. Their behavior is such that for a constant shear rate  $\dot{\gamma}$  and at constant temperature the shear stress  $\tau$  either increases or decreases monotonically with respect to time, towards an asymptotic value  $\tau(\dot{\gamma})$ , see Figure I.20 The fluids regain their initial properties sometime after the shear rate has returned to zero.

The time dependent fluids are divided into two subgroups [1] :

1. **Thixotropic fluids** : At a constant shear rate the shear stress decreases monotonically.
2. **Rheopectic fluids** : At a constant shear rate the shear stress increases monotonically. These fluids are also called antithixotropic fluids. There is another fascinating feature with these fluids. When a thixotropic fluid is subjected to a shear rate history from to a value and back to , the graph for the shear stress as a function of shows a hysteresis loop, see Figure I.21.

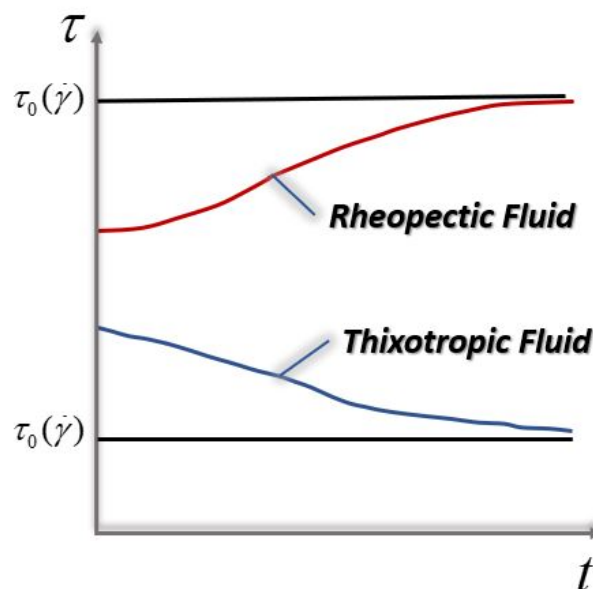


**Figure I.20** – The viscosity function  $\eta(\dot{\gamma})$ .

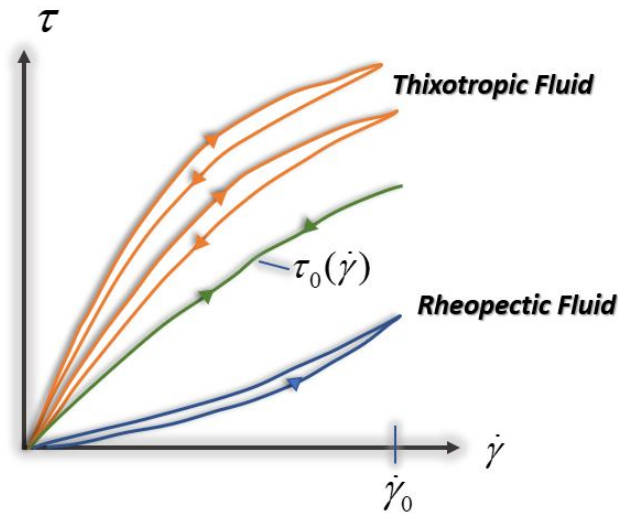


Figure I.21 – Shear rate histories.

### I.1.6.3.a Thixotropic Behaviour

Thixotropic fluids as drilling muds, paints, cosmetics, pharmaceuticals and grease exhibits a decrease in viscosity with time under a constant shear rate, whereas rheopectic fluids are the fluids that exhibit an increase in viscosity with time under a constant shear rate. They are also called negative thixotropic or anti-thixotropic fluids. The graphical representation of these fluids can be seen in Figure I.22 [7].

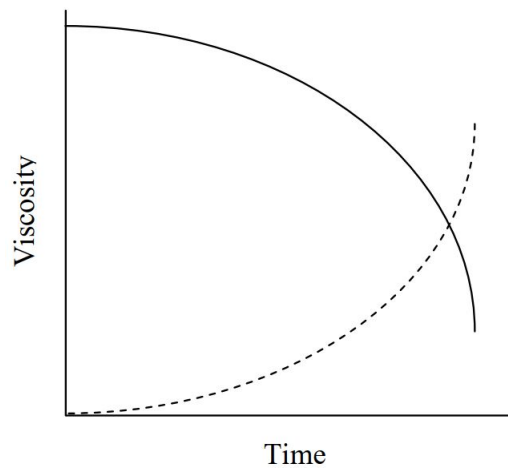


Figure I.22 – Graphical representation of viscosity for thixotropic fluids (solid line), and rheopectic fluids (dotted line) under constant shear rate [7].

Thixotropic behaviour is characterised by shear rate-dependent and time-dependent viscosity. For a well-rested sample (that is, one that has been allowed to rest for a time to recover from the effects of previous shear) when a step increase in shear rate or shear stress is applied the viscosity decreases with the time of shear. Thixotropic behaviour is generally associated with



particulate systems (that is, solid/liquid suspensions, colloids, slurries, pastes and emulsions) [16].

#### I.1.6.3.b Rheopectic Behaviour

The deformation process in some systems may lead, not to a decrease but to an increase in viscosity. This is called “antithixotropy” or “rheopexy”. Sometimes, these effects are distinguished. Both terms are related to a continuous increase of viscosity with time at a constant shear rate, and/or thickening of material with increase in shear rate, and the difference between them lies in the time scale. Both effects are much more rare than thixotropy, but they occur in some materials, especially in systems containing active chemicals, e.g., ionic or polar groups. Deformation may enhance the intermolecular interaction, resulting in viscosity increase [17].

#### I.1.6.4 Viscoelastic Fluids

When an undeformed material, solid or fluid, is suddenly subjected to a state of stress history, it deforms. An instantaneous deformation is either elastic, or elastic and plastic. The initial elastic deformation disappears when the stress is removed, while the plastic deformation remains as a permanent deformation. If the material is kept in a state of constant stress, it may continue to deform, indefinitely if it is a fluid, or asymptotically towards a finite configuration if it is a solid. This phenomenon is called creep. When a material is suddenly deformed and kept in a fixed deformed state, the stresses may be constant if the material behaves elastically, but the stress may also decrease with respect to time either toward an isotropic state of stress if the material is fluid-like or toward an asymptotic limit anisotropic state of stress if the material is solid-like, this phenomenon is called stress relaxation. Creep and stress relaxation are due to a combination of an elastic response and internal friction or viscous response in the material, and are therefore called viscoelastic phenomena. If the material exhibits creep and stress relaxation, it is said to behave viscoelastically. When the material is subjected to dynamic loading, viscoelastic properties are responsible for damping and energy dissipation. Propagation of sound in liquids and gases is an elastic response. Fluids are therefore in general both viscous and elastic, and the response is viscoelastic. However, the elastic deformations are very small compared to the viscous deformations [1].

Broadly speaking, viscoelasticity is divided into two major fields : linear and nonlinear.

#### I.1.6.4.a Linear viscoelasticity

Linear viscoelasticity is the field of rheology devoted to the study of viscoelastic materials under very small strain or deformation where the displacement gradients are very small and the flow regime can be described by a linear relationship between stress and rate of strain. In principle, the strain has to be sufficiently small so that the structure of the material remains unperturbed by the flow history. If the strain rate is small enough, deviation from linear viscoelasticity may not occur at all. The equations of linear viscoelasticity are not valid for deformations of arbitrary magnitude and rate because they violate the principle of frame invariance. The validity of linear viscoelasticity when the small-deformation condition is satisfied with a large magnitude of rate of strain is still an open question, though it is widely accepted that linear viscoelastic constitutive equations are valid in general for any strain rate as long as the total strain remains small. Nevertheless, the higher the strain rate the shorter the time at which the critical strain for departure from linear regime is reached [12].

The linear viscoelastic models have several limitations. For example, they cannot describe strain rate dependence of viscosity or normal stress phenomena since these are nonlinear effects. Due to the restriction to infinitesimal deformations, the linear models may be more appropriate for the description of viscoelastic solids rather than viscoelastic fluids. Despite the limitations of the linear viscoelastic models and despite being of less interest to the study of flow where the material is usually subject to large deformation, they are very important in the study of viscoelasticity for several reasons [12] :

1. They are used to characterise the behavior of viscoelastic materials at small deformations.
3. They serve as a motivation and starting point for developing nonlinear models since the latter are generally extensions to the linears.
3. They are used for analysing experimental data obtained in small deformation experiments and for interpreting important viscoelastic phenomena, at least qualitatively.

##### I.1.6.4.a.a Maxwell Model

Maxwell model consists of a spring connected in series with a dashpot as shown in Figure I.23 [7].

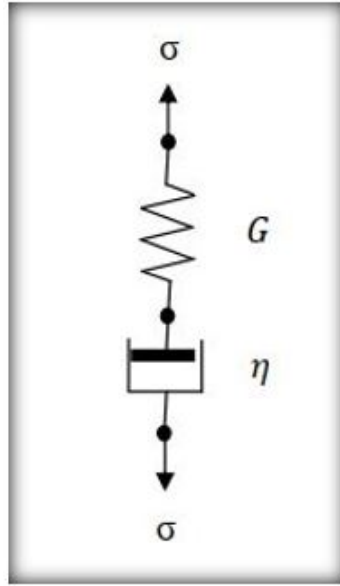


**Figure I.23** – Mechanical analog to Maxwell model comprised of a spring and a dashpot in series [7].

In Maxwell model, the stress is the same in both elements i.e.

$$\sigma = \sigma_s = \sigma_d \quad (\text{I.11})$$

Where  $\sigma_s$  and  $\sigma_d$  represent the stress in the spring and dashpot respectively. The deformation (strain) of the Maxwell model is equal to the sum of the individual deformations of spring and dashpot.

$$\gamma = \gamma_s + \gamma_d \quad (\text{I.12})$$

Where  $\gamma_s$  and  $\gamma_d$  represent the strain in the spring and dashpot respectively.

Again, from equation we get

$$\dot{\gamma} = \dot{\gamma}_s + \dot{\gamma}_d \quad (\text{I.13})$$

By putting the values of  $\dot{\gamma}_s = \frac{\dot{\sigma}}{G}$  and  $\dot{\gamma}_d = \frac{\sigma}{\eta}$  in equation, we will have :

$$\begin{aligned} \dot{\gamma} &= \frac{\dot{\sigma}}{G} + \frac{\sigma}{\eta} \\ \Leftrightarrow G\dot{\gamma} &= \dot{\sigma} + \frac{\sigma}{\eta}G \end{aligned} \quad (\text{I.14})$$

This is the standard form of Maxwell model showing the relationship between stress and strain, and clearly is an ordinary differential equation. This equation appears to be the first attempt to obtain a viscoelastic constitutive equation [7].

#### I.1.6.4.a.b Jeffreys Model

This is a linear model proposed as an extension to the Maxwell model by including a time derivative of the strain rate, that is :

$$\tau + \lambda_1 \frac{\partial \tau}{\partial t} = \mu_0 \left( \dot{\gamma} + \lambda_2 \frac{\partial \dot{\gamma}}{\partial t} \right) \quad (\text{I.15})$$

Where  $\lambda_2$  is the retardation time that accounts for the corrections of this model and can be seen as a measure of the time the material needs to respond to deformation. The Jeffreys model has three constants : a viscous parameter, and two elastic parameters,  $\lambda_1$  and  $\lambda_2$ . The model reduces to the linear Maxwell when  $\lambda_2 = 0$ , and to the Newtonian when  $\lambda_1 = \lambda_2 = 0$ . As observed by several authors, the Jeffreys model is one of the most suitable linear models to compare with experiment [12].

#### I.1.6.4.b Non-linear viscoelasticity

Non-linear viscoelasticity is the field of rheology devoted to the study of viscoelastic materials under large deformation, and hence it is the subject of primary interest to the study of flow of viscoelastic fluids. Nonlinear viscoelastic constitutive equations are sufficiently complex that very few flow problems can be solved analytically. Moreover, there appears to be no differential or integral constitutive equation general enough to explain the observed behavior of polymeric systems undergoing large deformations but still simple enough to provide a basis for engineering design procedures [12].

As the linear viscoelasticity models are not valid for deformations of large magnitude because they do not satisfy the principle of frame invariance, Oldroyd and others tried to extend these models to nonlinear regimes by developing a set of frame-invariant constitutive equations. These equations define time derivatives in frames that deform with the material elements. Examples include rotational, upper and lower convected time derivatives. The idea of these derivatives is to express the constitutive equation in real space coordinates rather than local coordinates and

hence fulfilling the Oldroyd's admissibility criteria for constitutive equations. These admissibility criteria ensures that the equations are invariant under a change of coordinate system, value invariant under a change of translational or rotational motion of the fluid element as it goes through space, and value invariant under a change of rheological history of neighboring fluid elements. There is a large number of rheological equations proposed for the description of nonlinear viscoelasticity, as a quick survey to the literature reveals. However, many of these models are extensions or modifications to others. The two most popular nonlinear viscoelastic models in differential form are the Upper Convected Maxwell and the Oldroyd-B models [12].

#### I.1.6.4.b.a Upper Convected Maxwell (UCM) Model

To extend the linear Maxwell model to the nonlinear regime, several time derivatives (e.g., upper convected, lower convected and corotational) have been proposed to replace the ordinary time derivative in the original model. The most commonly used of these derivatives in conjunction with the Maxwell model is the upper convected. On purely continuum mechanical grounds there is no reason to prefer one of these Maxwell equations to the others as they all satisfy frame invariance. The popularity of the upper convected form is due to its more realistic features [12].

The Upper Convected Maxwell (UCM) is the simplest nonlinear viscoelastic model and is one of the most popular models in numerical modeling and simulation of viscoelastic flow. Like its linear counterpart, it is a simple combination of the Newton's law for viscous fluids and the derivative of the Hook's law for elastic solids. Because of its simplicity, it does not fit the rich variety of viscoelastic effects that can be observed in complex rheological materials. However, it is largely used as the basis for other more sophisticated viscoelastic models. It represents, like the linear Maxwell, purely elastic fluids with shear-independent viscosity, i.e., Boger fluids. UCM also predicts an elongation viscosity that is three times the shear viscosity, like Newtonian, which is unrealistic feature for most viscoelastic fluids. The UCM model is obtained by replacing the partial time derivative in the differential form of the linear Maxwell with the upper convected time derivative, that is [12] :

$$\tau + \lambda_1 \overset{\nabla}{\tau} = \mu_0 \dot{\gamma} \quad (\text{I.16})$$

Where  $\tau$  is the extra stress tensor,  $\lambda_1$  is the relaxation time,  $\mu_0$  is the low-shear viscosity,  $\dot{\gamma}$  is the rate of strain tensor, and  $\overset{\nabla}{\tau}$  is the upper convected time derivative of the stress tensor. This

time derivative is given by :

$$\overset{\nabla}{\tau} = \frac{\partial \tau}{\partial t} + v \cdot \nabla \tau - (\nabla v)^T \cdot \tau - \tau \cdot \nabla v \quad (\text{I.17})$$

#### I.1.6.4.b.b Oldroyd-B Model

The Oldroyd-B model is a simple form of the more elaborate and rarely used Oldroyd-B constant model which also contains the upper convected, the lower convected, and the corotational Maxwell equations as special cases. Oldroyd-B is the second simplest nonlinear viscoelastic model and is apparently the most popular in viscoelastic flow modeling and simulation. It is the nonlinear equivalent of the linear Jeffreys model, as it takes account of frame invariance in the nonlinear regime [12].

Oldroyd-B model can be obtained by replacing the partial time derivatives in the differential form of the Jeffreys model with the upper convected time derivatives.

$$\tau + \lambda_1 \overset{\nabla}{\tau} = \mu_0 (\dot{\gamma} + \lambda_2 \overset{\nabla}{\dot{\gamma}}) \quad (\text{I.18})$$

Where  $\overset{\nabla}{\dot{\gamma}}$  is the upper convected time derivative of the rate of strain tensor given by [12] :

$$\overset{\nabla}{\dot{\gamma}} = \frac{\partial \dot{\gamma}}{\partial t} + v \cdot \nabla \dot{\gamma} - (\nabla v)^T \cdot \dot{\gamma} - \dot{\gamma} \cdot \nabla v \quad (\text{I.19})$$

#### I.1.6.4.b.c Bautista-Manero Model

This model combines the Oldroyd-B constitutive equation for viscoelasticity and the Fredrickson's kinetic equation for flow-induced structural changes which may be associated with thixotropy. The model requires six parameters that have physical significance and can be estimated from rheological measurements. These parameters are the low and high shear rate viscosities, the elastic modulus, the relaxation time, and two other constants describing the buildup and break down of viscosity [12].

The kinetic equation of Fredrickson that accounts for the destruction and construction of structure is given by [12] :

$$\frac{d\mu}{dt} = \frac{\mu}{\lambda} \left(1 - \frac{\mu}{\mu_0}\right) + k\mu \left(1 - \frac{\mu}{\mu_\infty}\right) \tau : \dot{\gamma} \quad (\text{I.20})$$

Where  $\mu$  is the viscosity,  $t$  is the time of deformation,  $\lambda$  is the relaxation time upon the cessation of steady flow,  $\mu_0$  and  $\mu_\infty$  are the viscosities at zero and infinite shear rates respectively,  $k$  is a parameter that is related to a critical stress value below which the material exhibits primary creep,  $\tau$  is the stress tensor and  $\dot{\gamma}$  is the rate of strain tensor. In this model  $\lambda$  is a structural relaxation time whereas  $k$  is a kinetic constant for structure breaks down. The elastic modulus  $G_0$  is related to these parameters by  $G_0 = \mu/\lambda$ .

Model	Constitutive Equation	Viscosity	Rheological Parameters
<b>Newtonian</b>	$\tau = \mu \dot{\gamma}$	$\mu = \mu_N$	$\mu_N$ (Pa s)
<b>Ostwald de Waele</b>	$\tau = K \dot{\gamma}^n$	$\mu = K \dot{\gamma}^{n-1}$	$K$ (Pa s <sup>n</sup> ) $n$ dimensionless
<b>Bingham Plastique</b>	$\tau = \tau_{yB} + \mu_B \dot{\gamma}$	$\mu = \frac{\tau_{yB}}{\dot{\gamma}} + \mu_B$	$\tau_{yB}$ (Pa) $\mu_B$ (Pa s)
<b>Herschel-Bulkley</b>	$\tau = \tau_{yHB} + K \dot{\gamma}^n$	$\mu = \frac{\tau_{yHB}}{\dot{\gamma}} + K \dot{\gamma}^{n-1}$	$\tau_{yHB}$ (Pa) $K$ (Pa s <sup>n</sup> ) $n$ dimensionless
<b>Casson</b>	$\sqrt{\tau} = \sqrt{\tau_{yC}} + \sqrt{\mu_C \dot{\gamma}}$	$\mu = \frac{[\sqrt{\tau_{yC}} + \sqrt{\mu_C \dot{\gamma}}]^2}{\dot{\gamma}}$	$\tau_{yC}$ (Pa) $\mu_C$ (Pa s)
<b>Vocadlo</b>	$\tau = (\tau_{yV}^{1/n} + K \dot{\gamma})^n$	$\mu = \frac{(\tau_{yV}^{1/n} + K \dot{\gamma})^n}{\dot{\gamma}}$	$\tau_{yV}$ (Pa) $K$ (Pa s <sup>n</sup> ) $n$ dimensionless
<b>Prandtl-Eyring</b>	$\tau = a \sinh^{-1}(b \dot{\gamma})$	$\mu = \frac{a \sinh^{-1}(b \dot{\gamma})}{\dot{\gamma}}$	$a$ (Pa) $b$ (s)
<b>Powell-Eyring</b>	$\tau = c \dot{\gamma} + a \sinh^{-1}(b \dot{\gamma})$	$\mu = c + \frac{a \sinh^{-1}(b \dot{\gamma})}{\dot{\gamma}}$	$a$ (Pa) $b$ (s) $c$ (Pa s)
<b>Cross</b>	$\tau = \left\{ \mu_\infty + \frac{\mu_0 - \mu_\infty}{1 + a \dot{\gamma}^m} \right\} \dot{\gamma}$	$\mu = \mu_\infty + \frac{\mu_0 - \mu_\infty}{1 + a \dot{\gamma}^m}$	$\mu_0$ (Pa s) $\mu_\infty$ (Pa s) $a$ (S <sup>m</sup> ) $m$ dimensionless
<b>Sisko</b>	$\tau = \{ \mu_\infty + K \dot{\gamma}^{n-1} \} \dot{\gamma}$	$\mu = \mu_\infty + K \dot{\gamma}^{n-1}$	$\mu_\infty$ (Pa s) $K$ (Pa s <sup>n</sup> ) $n$ dimensionless
<b>Carreau</b>	$\tau = \left\{ \mu_\infty + \frac{\mu_0 - \mu_\infty}{[1 + (a \dot{\gamma})^2]^{m/2}} \right\} \dot{\gamma}$	$\mu = \mu_\infty + \frac{\mu_0 - \mu_\infty}{[1 + (a \dot{\gamma})^2]^{m/2}}$	$\mu_0$ (Pa s) $\mu_\infty$ (Pa s) $a$ (S) $m$ dimensionless
<b>Van Wazer</b>	$\tau = \left\{ \mu_\infty + \frac{\mu_0 - \mu_\infty}{1 + a \dot{\gamma} + b \dot{\gamma}^m} \right\} \dot{\gamma}$	$\mu = \mu_\infty + \frac{\mu_0 - \mu_\infty}{1 + a \dot{\gamma} + b \dot{\gamma}^m}$	$\mu_0$ (Pa s) $\mu_\infty$ (Pa s) $a$ (S) $b$ (S <sup>m</sup> ) $m$ dimensionless
<b>Williamson</b>	$\tau = \left\{ \mu_\infty + \frac{\mu_0 - \mu_\infty}{1 + a \tau} \right\} \dot{\gamma}$	$\mu = \mu_\infty + \frac{\mu_0 - \mu_\infty}{1 + a \tau}$	$\mu_0$ (Pa s) $\mu_\infty$ (Pa s) $a$ (Pa <sup>-1</sup> )
<b>Reiner-Philippoff</b>	$\tau = \left\{ \mu_\infty + \frac{\mu_0 - \mu_\infty}{1 + a \tau^2} \right\} \dot{\gamma}$	$\mu = \mu_\infty + \frac{\mu_0 - \mu_\infty}{1 + a \tau^2}$	$\mu_0$ (Pa s) $\mu_\infty$ (Pa s) $a$ (Pa <sup>-2</sup> )
<b>Meter</b>	$\tau = \left\{ \mu_\infty + \frac{\mu_0 - \mu_\infty}{1 + a \tau^m} \right\} \dot{\gamma}$	$\mu = \mu_\infty + \frac{\mu_0 - \mu_\infty}{1 + a \tau^m}$	$\mu_0$ (Pa s) $\mu_\infty$ (Pa s) $a$ (Pa <sup>-m</sup> ) $m$ dimensionless
<b>Ellis</b>	$\tau = \left\{ \frac{\mu_0}{1 + a \tau^{m-1}} \right\} \dot{\gamma}$	$\mu = \frac{\mu_0}{1 + a \tau^{m-1}}$	$\mu_0$ (Pa s) $a$ (Pa <sup>1-m</sup> ) $m$ dimensionless

Table I.3 – flow curve models [16].



Fluid type	Definition	Typical examples
<b>Pseudoplastic</b>	Fluids that depict a decrease in viscosity with increasing shear rate and hence often referred to as shear-thinning fluids.	Blood Filled polymer systems Polymer melts Printing inks
<b>Dilatant</b>	Fluids that depict an increase in viscosity with increasing shear rate and hence often referred to as shear-thickening fluids.	Aqueous suspension of titanium dioxide Gum solutions Wet sand
<b>Bingham plastics</b>	Fluids that do not flow unless the stress applied exceeds a certain minimum value referred to as the yield stress and then show linear shear stress versus shear rate relationship.	Certain asphalts and bitumen Jellies Sewage sludges Thickened hydrocarbon greases Tomato ketchup Toothpaste
<b>Pseudoplastic with a yield stress</b>	Fluids that have non-linear shear stress versus shear rate relationship in addition to the presence of yield stress.	Heavy crude oils with high wax content Filled polymer systems
<b>Thixotropic</b>	Fluids that exhibit a the reversible decrease in shear stress with time at a constant rate of shear and fixed temperature. The shear stress, of course, approaches some limiting value.	Coal-water slurries Crude oils Drilling muds Filled polymer systems Mayonnaise Salad dressing Yoghurt
<b>Rheopectic</b>	Fluids exhibit a reversible increase in shear stress with time at a constant rate of shear and fixed temperature. At any given shear rate, the shear stress increases to approach an asymptotic maximum value.	Some clay suspensions
<b>Viscoelastic</b>	Fluids that possess the added feature of elasticity apart from viscosity. These fluids exhibit process properties which lie in-between those of viscous liquids and elastic solids	Filled polymer systems Polymer melts Polymer solutions

**Table I.4** – The various types of non-Newtonian fluids [9].

## I.2 Nanofluids and Hybrid nanofluids

### I.2.1 Nanofluids

Cooling is one of the most important technical challenges facing numerous industries such as electronics, automobiles and manufacturing. New technologies, with their increased thermal loads, are the driving mechanism behind the demand for faster and better cooling techniques. The conventional methods to increase the cooling rate such as fins and microchannels are stretched to their limits. Hence, there is an urgent need for new and innovative coolants to achieve this high-performance cooling. Thermal conductivities of traditional heat transfer fluids, such as engine coolants and water, are very low. It increasing global competition, industries have a strong need to develop energy efficient heat transfer fluids with significantly higher thermal conductivities than the available fluids. Nanofluids offer us novel and truly innovative solutions; heat transfer fluids containing suspended nanoparticles, have been developed to meet such cooling challenges [18].

#### I.2.1.1 Base fluids

Water, glycols (in particular ethylene glycol) and mixtures of both, as well oils are the common heat transfer fluids employed in heating and cooling applications. So, they are logically the most used fluids to produce nanofluids. Some important properties about water and propylene glycol liquids, that compose the commercial base fluid used in this study, are provided in the following. Water ( $H_2O$ ), molecules consist of hydrogen and oxygen atoms joined by covalent bonds, is an inorganic compound. At atmospheric conditions, it does not have any color, odor or taste. As its molecules create hydrogen bonds with other molecules easily, and because of its strong polarity, water was identified as a good solvent. Besides, water can be freely mixed with other liquids (alcohols for example). Regarding its physical properties, water presents some unusual behaviors. At atmospheric pressure, its density decreases with temperature in the majority of the liquid-state range, as usual, while it increases from the freezing point to 277 K. While heat capacity usually increases with temperature, a minimum value occurs in case of water at around 308 K. Furthermore, most liquids under higher pressures become more viscous while the viscosity of water shows a minimum as a function of pressure [19].

### I.2.1.2 Nanofluids and their applications

Nanofluids are a new class of solid/liquid mixtures engineered by dispersing nanometer size particles (NPs) or any nanostructures in conventional base liquids. According to the literature, NPs could be metallic/intermetallic compounds (such as Ag, Cu, Ni, Au, Fe, etc.), ceramic compounds such as oxides, sulfides and carbides. Among the ceramics,  $Al_2O_3$ ,  $MoS_2$ ,  $Fe_2O_3$ ,  $Fe_3O_4$ ,  $CuO$ ,  $TiO_2$ ,  $SiO_2$ ,  $CeO_2$ ,  $ZnO_2$ , mesoporous  $SiO_2$ ,  $SiC$ , and  $WS_2$  are some nanostructured ceramic materials reported in the literature. Nanostructured materials can be also carbon-based compounds, such as carbon nanotube, graphene, graphene oxide, graphite, etc. Base liquids are selected from water, ethylene glycol (EG), mixture of water and EG (W/EG), diethylene glycol (DEG), polyethylene glycol, engine oil, vegetable oil, paraffin, coconut oil, gear oil, kerosene, pump oil, etc. This new dispersion can be considered a suspension with three phase system as Figure I.24 shows : solid phase (NPs), solid/liquid interface and the liquid phase. From more than a decade ago since the introduction of NF concept was originated, the potentials of NFs applications in different area have attracted increasing attention. For this reason, many researchers are working in NF area for different aims and applications [20].

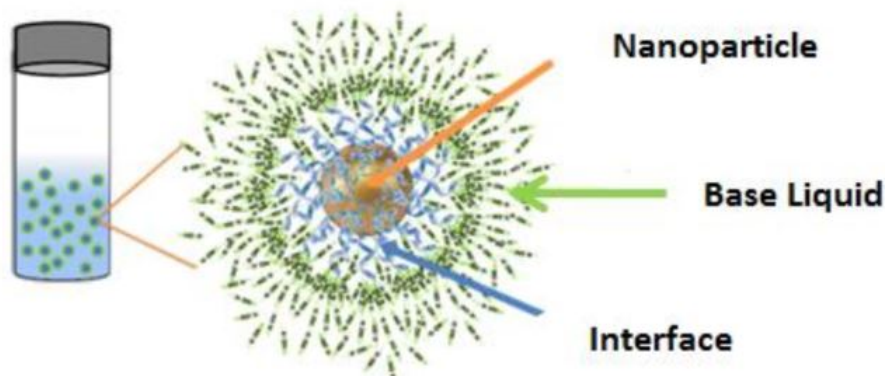


**Figure I.24** – Schematic of (NPs) dispersion systems (NFs) as a three-phase suspension system [20].

According to Boutin adding nano-spherical particles to a conventional fluid can improve heat transfer up to 40%. Choi envisions using these kinds of nanofluids to cool miniaturised high heat flux devices such as supercomputer circuits and high-power microchips. In the past, microparticles were used to enhance heat transfer, but these particles were so large that they quickly settled out of the fluid, and sank to the bottom of the pipe or tank. Additionally, as these particles flow through tubes they might damage the inner surface of the tubes. Because nanoparticles operate with Brownian motion, adding nanoparticles solved this problem. These

particles are permanently suspended in Brownian motion and when they are in equilibrium with no flow, they are distributed in a balance between buoyant weight and thermal agitation [20].

A wide range of applications for NFs in different areas such as biomedical applications, lubrication, surface coating, and petroleum industry have been reported in the literature. Figure I.26 displays some of NFs potential applications in different areas. As literature reports NFs have been used in several biomedical and nano-medicine applications such as nanodrug delivery, cancer therapeutics and sensing and imaging and Nano-cryosurgery. For instance, there are numerous applications that involve magnetic NFs such as hyperthermia, magnetic cell separations and contrast improvement in magnetic resonance imaging. About application of NFs in non-renewable energy fields such as petroleum industry, some reports can be found in the literature. For example, recent experiments have exposed that some NFs have successfully been formulated and applied in enhanced oil recovery (EOR) process, anticorrosive coatings, wettability alteration and drilling technology are other applications of NFs concerning oil and petroleum industry. Recently, NFs systems prepared by dispersing NPs (such as  $MoS_2$ ,  $TiO_2$  and copper oxide) in the conventional lubricating oil have successfully enhanced as anti-wear properties and friction-reduced. These features exhibit the potential of NFs applications as effective lubricants. Several reports in the literature also show the remarkable potential of NFs for use in surface coating, environmental remediation (for example soil remediation), inkjet printing and as fuels additives [20].



Figure I.25 – Different applications of NFs [20].

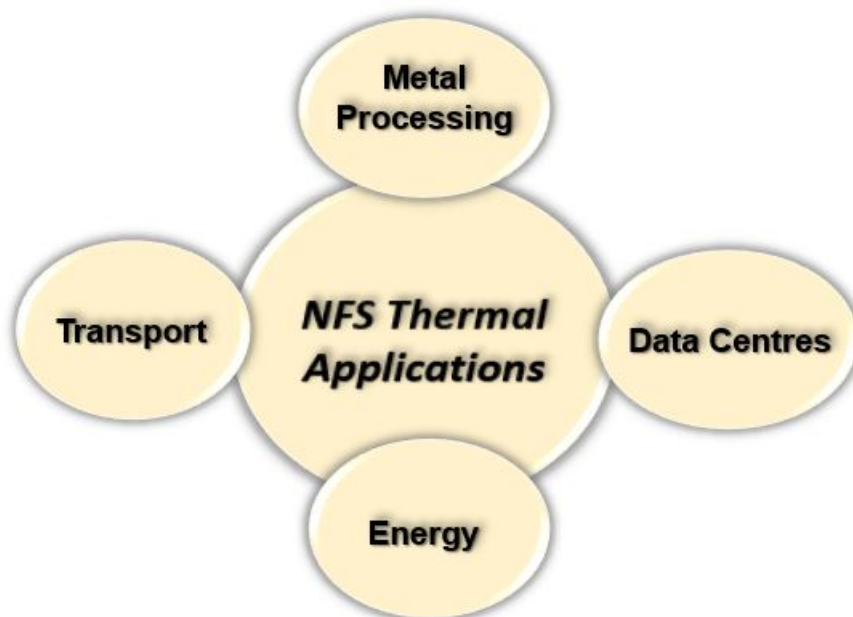


Figure I.26 – Potential of NFs for thermal application.

### I.2.1.3 Thermophysical properties of nanofluids

#### I.2.1.3.a Nanofluid Density

The nanofluid density based on nanofluid volume fraction can be obtained from [21] :

$$\rho_{nf} = \phi\rho_p + (1 - \phi)\rho_f \quad (\text{I.21})$$

The density of the  $Al_2O_3$ /propanol nanofluid at room temperature was obtained, then the measured and calculated densities were compared and indicated that the differences between both densities was found to be less than 5% when the weight concentration is up to 5%.

#### I.2.1.3.b Nanofluid Specific Heat

Two expressions were commonly used to determine the specific heat of nanofluids based also on nanofluid volume fraction [20] :

$$c_{p,nf} = \phi c_{p,p} + (1 - \phi) c_{p,f} \quad (\text{I.22})$$

And :

$$(\rho c_p)_{nf} = \phi(\rho c_p)_p + (1 - \phi)(\rho c_p)_f \quad (\text{I.23})$$

#### I.2.1.3.c Nanofluid viscosity

Nanofluid pressure drop in forced convection is affected by nanofluid viscosity, so the experimental measurements and the numerical investigations can be performed. Generally, increasing in the viscosity by adding nanoparticles to base fluids is significant. The viscosity also depends on particle volume fractions, particle sizes, temperatures, and extents of clustering [20].

##### I.2.1.3.c.a Experimental investigation of nanofluid viscosity

The viscosities of nanofluids were investigated experimentally, which showed some different viscosities between base fluids and nanofluids. The viscosity correlations were also proposed for different nanoparticles and base fluids. An expression for determining the dynamic viscosity of

dilute suspensions that contain spherical particles can be considered with neglecting particles interactions, the well-known Einstein's formula [20] :

$$\mu_{nf} = (1 + 2.5\phi) \mu_f \quad (\text{I.24})$$

and Einstein's equation was extended by Brinkman as :

$$\mu_{nf} = \frac{1}{(1 - \phi)^{2.5}} \mu_f \quad (\text{I.25})$$

Einstein's equation was extended by taking Brownian motion of the nanoparticles and the interaction between them into account by Batchelor model :

$$\mu_{nf} = (1 + C_1\phi + C_2\phi^2) \mu_f \quad (\text{I.26})$$

And by taking the influence of liquid layering into account to calculate volume fraction as in Ward model and renewed Ward model :

$$\mu_{nf} = (1 + C_1\phi + C_2\phi^2 + C_3\phi^3) \mu_f \quad (\text{I.27})$$

where  $C_1$ ,  $C_2$ , and  $C_3$  are constant from the experimental studies. The correlations proposed for the viscosity of the nanofluids were introduced as for 36 nm Al<sub>2</sub>O<sub>3</sub>/water nanofluid :

$$\mu_{nf} = (1 + 2.5\phi + 150\phi^2) \mu_f \quad (\text{I.28})$$

For 19.4 vol.%. Al<sub>2</sub>O<sub>3</sub>/water nanofluid :

$$\mu_{nf} = (1.125 - 0.007T) \mu_f \quad (\text{I.29})$$

For 19.4 vol.%. CuO/water nanofluid :

$$\mu_{nf} = (2.1275 - 0.0215T - 0.0002T^2) \mu_f \quad (\text{I.30})$$

For 47 nm Al<sub>2</sub>O<sub>3</sub>/water nanofluid :

$$\mu_{nf} = (0.904e^{0.148\phi}) \mu_f \quad (\text{I.31})$$

For 06 vol.%.  $Al_2O_3$ /water nanofluid :

$$\begin{aligned}\mu_{nf} &= (1 + 7.3\phi + 123\phi^2) \mu_f \\ \mu_{nf} &= (0.904e^{4.91\phi/0.2092-\phi}) \mu_f\end{aligned}\tag{I.32}$$

And, for 40 nm  $MgO$ /water nanofluid :

$$\mu_{nf} = (1 + 11.61\phi + 109\phi^2) \mu_f\tag{I.33}$$

### I.2.1.3.c.b Numerical investigation of nanofluid viscosity

Most of the viscosity studies obtained viscosity enhancement with the dispersion of nanoparticles in the base fluid and with the increase of volume fraction, no exact theoretical mechanism or common empirical correlations with effect of volume fraction, size, and temperature were available for nanofluid viscosity estimations [21].

The rheological behavior of nanofluids was categorised into four groups as (1) dilute nanofluids (volume concentration less than 0.1 vol.%) whose viscosity fits the Einstein equation and there is no visible shear-thinning behavior; (2) semi-dilute nanofluids (with 0.15 vol.%) with aggregation of nanoparticles, whose viscosity fits the modified  $K - D$ . Equation and there is no obvious shear-thinning behavior; (3) semi-concentrated nanofluids (with 510 vol.%) with aggregation of nanoparticles whose viscosity fits the modified  $K - D$  equation and there is noticeable shear-thinning behavior; and (4) concentrated nanofluids (volume concentration more than 10 vol.%) with interpenetration of aggregation and this is out of the normal concentration range of nanofluids [20].

### I.2.1.3.d Nanofluid thermal conductivity

Nanofluid thermal conductivities were investigated theoretically and experimentally to find the conductivity enhancements, which can also affect the convective enhancements. Many theoretical models were compared with experimental data available in their literatures [22].

The nanofluid thermal conductivity can be measured using techniques as summarised by Paul et al. In three main measurement techniques : transient techniques (transient hot-wire, thermal constant analyser, temperature oscillation, and  $3\omega$  technique), steady state technique



(steady state parallel plate and cylindrical cell), and thermal comparator. The transient hot-wire technique was carried out dominantly. The most attractive advantages of this method were its capacity for experimentally eliminating the error due to natural convection, its fast results, and its simple conceptual design compared to other techniques [22].

The earlier empirical correlations of nanofluid thermal conductivity, Maxwell model, Hamilton and Crosser model, Brownian motion model, clustering model, liquid layering model, Yamada and Ota model for carbon nanotube were concluded in previous review works. Maxwell offered the model that expressed an effective thermal conductivity equation for nanofluids containing spherical nanoparticles [22] :

$$k_{nf} = \frac{k_p + 2k_f + 2(k_p - k_f)\phi}{k_p + 2k_f + (k_p - k_f)\phi} k_f \quad (\text{I.34})$$

Note that the effect of the size and shape of the particles and particle interactions were not included in Maxwell's equation.

Hamilton and Crosser model represented the model for non-spherical particles with the shape factor ( $n$ ) as experimental parameters for different types of nanoparticles [23]

$$k_{nf} = \frac{k_p + (n-1)k_f - (n-1)\phi(k_f - k_p)}{k_p + (n-1)k_f + \phi(k_f - k_p)} k_f \quad (\text{I.35})$$

where  $n$  is defined as :

$$n = \frac{3}{\psi} \quad (\text{I.36})$$

where  $\psi$  is the sphericity. Sphericity is the ratio of the surface area of a sphere with the same volume as the particle to the surface area of the particle, so  $n = 3$  for a sphere.

Brownian motion model focused on Brownian motion which was the random motion of particles suspended in nanofluids. Brownian dynamics simulation was used to determine the effective thermal conductivity of nanofluids as :

$$k_{nf} = \phi k_p + (1 - \phi) k_f \quad (\text{I.37})$$

Note that  $k_p$  includes the effect of the Brownian motion of the nanoparticles on the thermal conductivity.

Koo and Kleinstreuer model proposed the combination model of two thermal conductivity parts as [24] :

$$k_{nf} = k_{static} + k_{Brownian} \quad (I.38)$$

Where  $k$  static represents the thermal conductivity enhancement due to the higher thermal conductivity of the nanoparticles such as the Maxwell model,  $k$  Brownian represents the effect of Brownian motion, which the effect of nanoparticles moving around the nanofluid was taken into account as :

$$k_{Brownian} = 5 \times 10^4 \beta \phi \rho_f c_{p,f} \sqrt{\frac{k_B T}{\rho_p d_p}} f \quad (I.39)$$

Where :

$T$  represents the temperature in  $k$  .

$C_{p,f}$  represents specific heat capacity of base fluid .

$\beta$  represents a constant obtained from their experiment .

### I.2.2 Hybrid nanofluids

The suspension of metallic nanoparticles in base fluid also caused the enhancement in pumping power. In other words, while dealing with forced convection of nanofluids no one can decide the effectiveness of unitary and hybrid nanofluids on the basis of heat transfer only. It is the trade-off of advantages (heat transfer enhancement) and disadvantages (cost and pumping power), as shown in Fig I.27 [25]. One of the advantages of hybrid nanofluid is that the rate of heat transfer can be controlled by varying the particle concentration or altering the combination of nanoparticles. Qin et al investigated the performance of direct absorption solar collector employing plasmonic nanofluid [26].

Hybrid nanofluid is a very new type of nanofluids that contains two or more various nanoparticles. Turcu et al. is one of the first researchers who have begun studies on hybrid nanoparticles

[27]. But the main step in the way of introducing hybrid nanofluids taken by Hemmat Esfe research group. Also, they worked on a new field about controlling the viscosity of hybrid nanofluids in comparison to pure base fluid. The use of hybrid nanofluids is aimed at simultaneously using the physical and chemical properties of two or more different types of nanoparticles, while improving fluid properties, such as water. Studies show the growth of thermophysical and rheological properties of hybrid nanofluids compared to conventional nanofluids [28].

The composition of the nanoparticles used to make the hybrid nanofluids can be divided into three different categories, depending on their type :

1. Metal compounds such as  $Al_2O_3/Cu$ ,  $Al_2O_3/Ni$ ,  $MgO/Fe$ , and  $Al/CNT$
2. Ceramic compounds such as  $Al_2O_3/Cu$ ,  $Al_2O_3/Ni$ ,  $MgO/Fe$ , and  $Al/CNT$
3. Polymer compounds such as  $polymer/CNT$  and  $polymer/TiO_2$ .

Obviously, the issue of choosing the right combination of nanoparticles and their relative proportions has a significant effect on the efficiency and enhancement of the thermophysical properties of nanoparticles, and this issue can be considered as one of the considerations that need to be studied. In composite of results of many studies, the results of some studies show a decline in the thermal properties of hybrid nanofluids compared to conventional ones that could be because of the following reasons [28] :

1. Non compatibility of the used nanoparticles with each other.
2. The size of the used nanoparticles.
3. Base fluid type.
4. Fluid temperature and working temperature of fluid.
5. Stability.

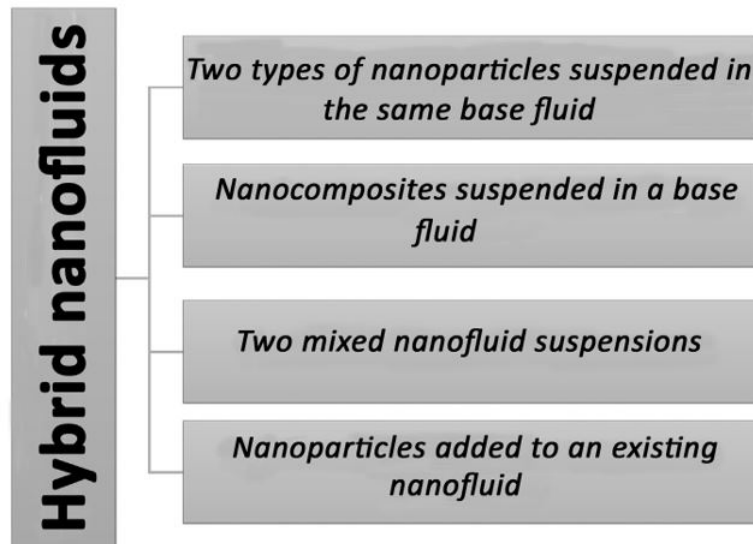


Figure I.27 – Hybrid nanofluids types [28].

### I.2.2.1 Natural convection heat transfer

Natural convection is the phenomenon most frequently occur in many engineering applications. During the past few decades, investigators compiled a number of research articles on natural convection in closed and open cavities. The suspension of nanoparticles in base fluid found to be an effective technique to augment the rate of heat transfer. Abu-Nada and Oztop [29] numerically investigated the effect of fluid flow and natural convective heat transfer inside a two-dimensional enclosure filled with water-based copper (Cu) nanofluid varying the inclination angle (0 – 120 degrees) and particle concentration. Finite volume method was used to solve the governing equations and found that the augmentation in Nusselt number (Nu) was more prominent at low particle volume fraction than that of high concentration. In addition, inclination angle was found to be a good control parameter for pure water and nanoparticles suspended fluid filled enclosure [28].

### I.2.2.2 Forced convection heat transfer

Investigators analysed the forced CHT of unitary and hybrid nanofluids in many application areas such as : in manufacturing industry as a coolant, electronic industry to maintain the temperature of electronic components like microprocesses in a combination of heat sinks, automotive industry, refrigeration and air conditioning, and solar energy. Figure I.28 shows the graphical illustration of the application of hybrid nanofluid in different arenas. Hybrid nanofluid is the advanced class of nanofluids and devised few years ago that is why limited studies are

available on hybrid nanofluids [28].

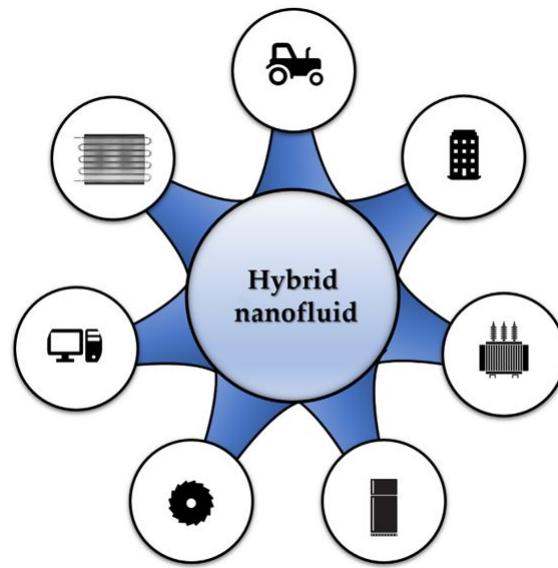


Figure I.28 – Forced convective heat transfer in different applications [28].

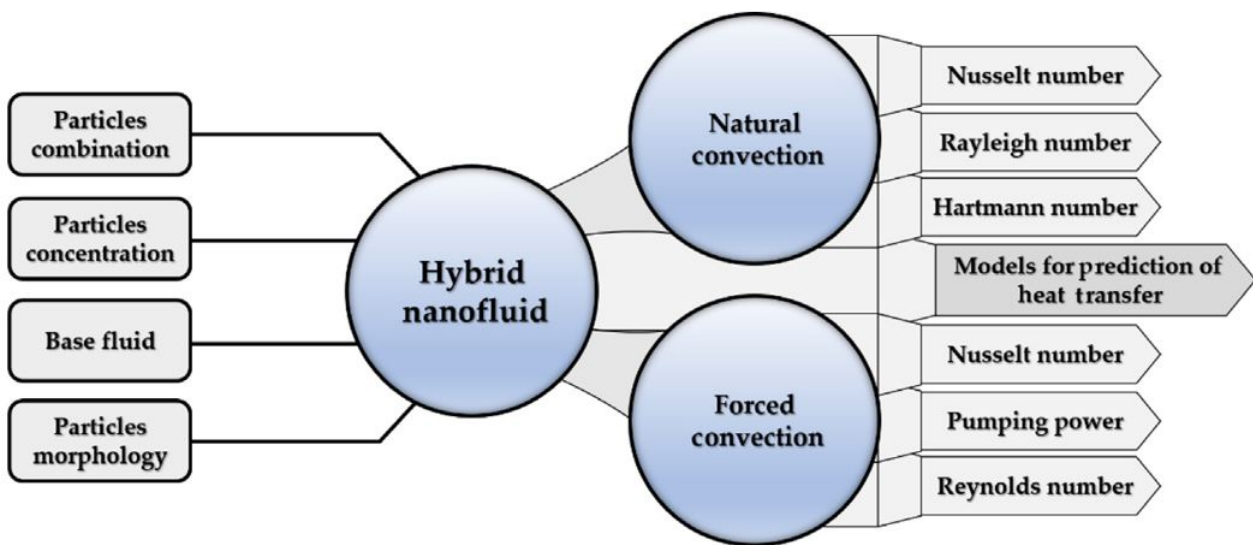
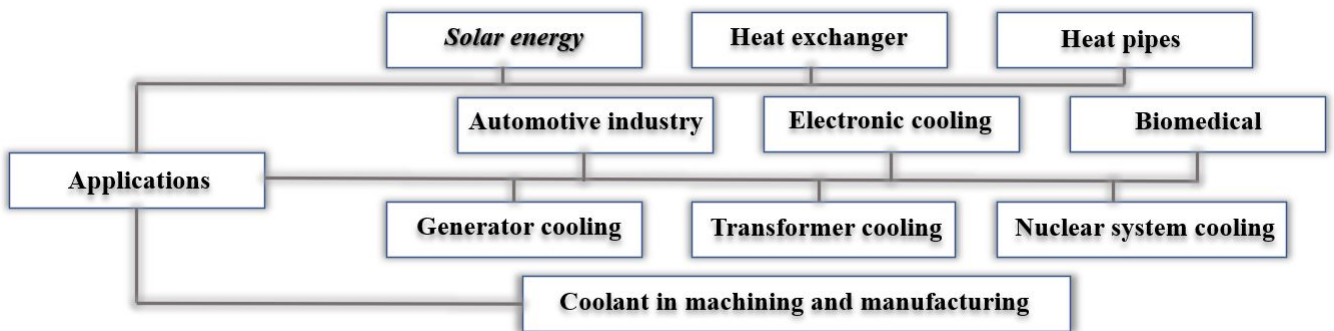


Figure I.29 – Factors that needed careful consideration while investigating the hybrid nanofluids as a heat transfer media, graphical illustration [28].

### I.2.2.3 Applications of hybrid nanofluids in different fields

Hybrid nanofluid can be synthesized using single-step or two-step technique and TC is the main parameter for HT enhancement of hybrid nanofluids. The efficiency of hybrid nanofluid (HyNF) affects by several parameters such as synthesis of NPs, level of purity of NPs, and dispersion of NPs. HT through fluid is due to convection which largely depends on convective HT coefficient. The expected results are hybrid nanofluids that can be performed better compared to

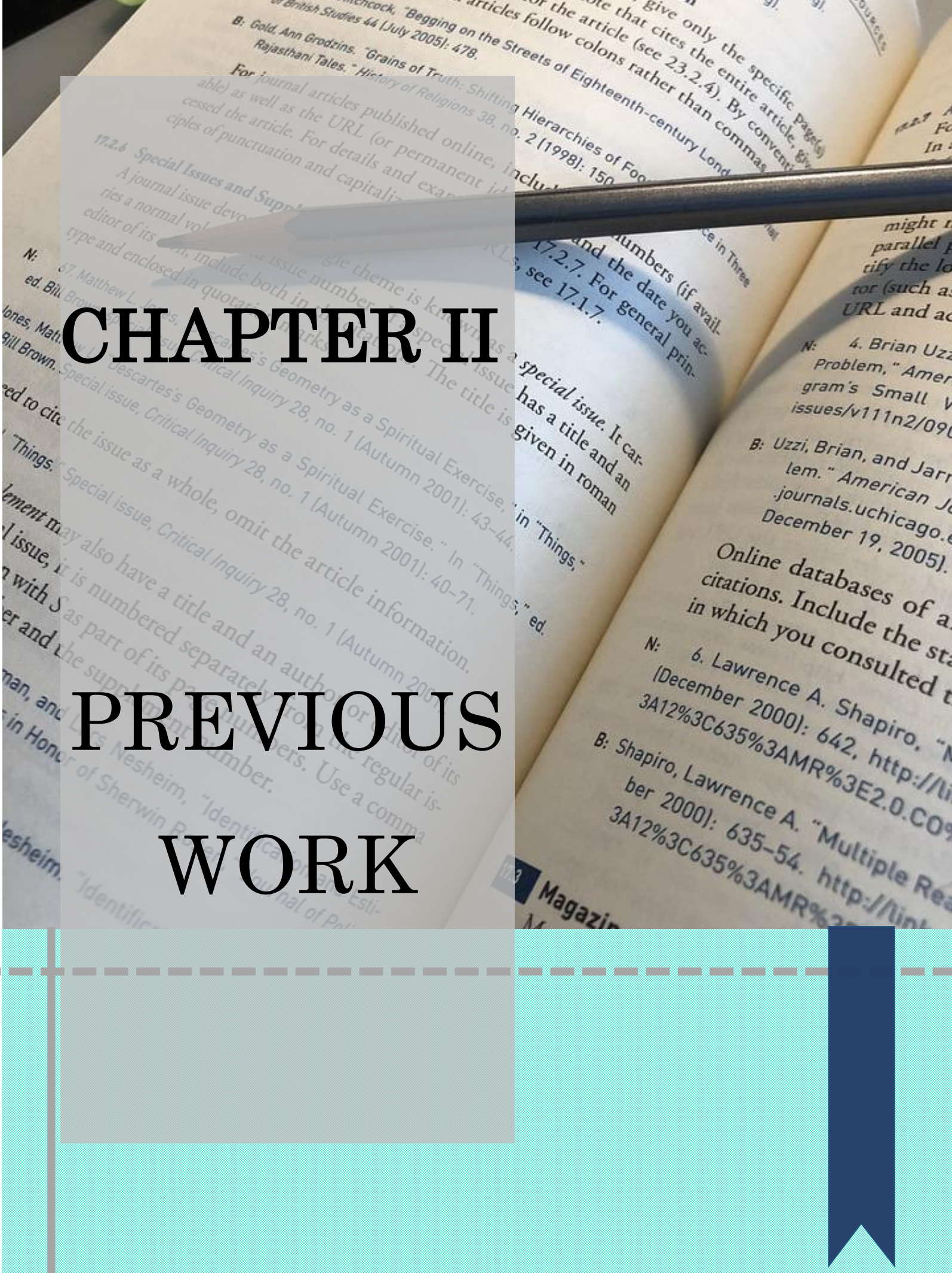
nanofluids in same type of applications. Nanotechnology has been used in many applications that make more efficient in working. This results in decrement in cost of construction, maintenance, and repair [28].



**Figure I.30** – Major areas of applications of hybrid nanofluids.

# CHAPTER II

# PREVIOUS WORK



# PREVIOUS WORK

---

# II

## II.1 Previous work

Fluid mechanics is the branch of physics that studies the flow of fluids, how fluids move, and the forces that develop as a result. The concept of liquids and gases is when they are subjected to efforts or stresses, and fluid flow can be either laminar or turbulent.

Heat transfer is the movement of heat across the system's border due to a temperature difference between the system and its surroundings. It is classified into various mechanisms, such as thermal conduction, thermal convection, thermal radiation, and energy transfer by phase changes. Convection is the process of heat transfer by the bulk movement of molecules within fluids such as gases and liquids. The initial heat transfer between the object and the fluid occurs through conduction, but the bulk heat transfer happens due to the motion of the fluid.

A nanofluid is a fluid containing nanometer-sized particles called nanoparticles. These fluids are engineered colloidal suspensions of nanoparticles in a base fluid. The nanoparticles used in nanofluids are typically made of metals, oxides, carbides, or carbon nanotubes. Common base fluids include water, ethylene glycol, and oil. It can be considered the future of heat transfer fluids in various heat transfer applications. They are expected to give better thermal performance than conventional fluids due to the presence of suspended nanoparticles with high thermal conductivity. Lately, numerous investigations have revealed the enhancement of thermal conductivity and higher heat transfer rate of nanofluids. Significant enhancement in the heat transfer rate with the use of various nanofluids in various applications compared to conventional fluids has been reported by several researchers [35], [36], [37], [38], [39].



Heat exchangers play an important part in energy conservation, conversion and recovery. Several studies have focused on direct transfer type (recuperator) heat exchangers, where heat transfer between fluids occurs through a separating wall or into and out of a wall in a transient manner. Two important phenomena happen in a heat exchanger : fluid flow in channels and heat transfer between fluids and channel walls. Thus, heat exchangers can be improved by improving the processes occurring during those phenomena. Firstly, the heat transfer rate depends on the surface area to volume ratio, which means the smaller channel dimensions provide a better heat transfer coefficient. Secondly, improving the properties of the heat transfer fluids (nanofluids) can yield a higher heat transfer coefficient in a heat exchanger. Heat transfer and fluid flow in microchannels have been topics of intense research in the past decade. Increased heat transfer and cost reduction have been significant challenges facing large industries and factories [40], [41], [42].

Microchannel heat sinks constitute an innovative cooling technology for removing a large amount of heat through a small area. It is one of the potential alternatives for replacing conventional finned tube heat exchangers, mainly used in industries such as automobiles, air conditioning and refrigeration. The heat sink is usually made from a high thermal conductivity solid such as silicon or copper. The microchannels are fabricated into their surface using precision machining or micro-fabrication technology. Micro-channel heat sinks typically contain a large number of parallel microchannels. Coolant is forced to pass through these channels to remove heat from a hot surface. In Microchannel heat exchangers, flow is typically laminar, and heat transfer coefficients are proportional to velocity. Micro-channel heat sinks provide a very high surface area-to-volume ratio, significant convective heat transfer coefficient, small mass and volume, and small coolant inventory [43], [44], [45], [46].

In recent decades, microchannels have been presented as a solution to this problem. The microchannel heat exchanger is used in industries such as microelectronics, aerospace, biomedical, robotics, telecommunications and automotive. These microscale devices, commonly known as MEMS (Micro Electromechanical Systems), are getting more advanced and complex as microfabrication technology progresses well with the trend. However, two factors limit the heat transfer coefficients in a micro heat exchanger : the reduction in the channel dimensions was accompanied by a higher pressure drop, and the amount of heat transfer was limited by the heat transfer fluid used.

Singh et al. (2012) [35] studied experimentally and numerically the hydrodynamics of nanofluids in microchannels. They used three microchannels of hydraulic diameters of 130, 211 and  $300\mu\text{m}$ , the nanofluid of this study was Alumina base fluid water and Ethylene Glycol prepared with three values of concentrations 0.25 vol.%, 0.5 vol.% and 1.0 vol.%, stabilised and characterised with the help of TEM and zeta potential. It was found nanofluids do not behave as single-phase liquids in a microchannel. The friction characteristics of nanofluids in microchannels depend on channel size, particle concentration and viscosity and are visible in turbulent regimes. An early transition phenomenon is observed for  $211\mu\text{m}$  and  $301\mu\text{m}$  channels, probably due to high surface roughness. As well as the numerical simulation was done by considering the mixture rule and discrete phase approach, and the discrete phase modelling were found to be more accurate at higher Reynolds number.

Nikkhah et al. (2015) [36] performed a forced convective heat transfer of water/functionalised multi-walled carbon nanotube (FMWCNT) nanofluid in a two-dimensional microchannel. Walls of the microchannel are under a periodic heat flux, and slip boundary conditions along the walls have been considered. The effect of different values of shear forces, solid nanoparticles concentration, slip coefficient, periodic heat flux of the flow and temperature fields, and heat transfer rate has been evaluated. The Reynolds number was in the range of 1 and 100, 0 – 25% for the weight percentage of solid nanoparticles and 0.001 – 0.1 for the velocity slip coefficient. Results of the current study showed a good agreement with the numerical and experimental studies of other researchers. Results showed that local Nusselt numbers along the length of the microchannel change in a periodic manner and increase with the increase in Reynolds number. The rise in slip coefficient and weight percentage of nanoparticles leads to an increase in Nusselt number, which is greater in higher Reynolds numbers.

Akbari et al. (2016) [37] studied a forced convection heat transfer of water- $\text{Al}_2\text{O}_3$  nanofluid in a two-dimensional microchannel with two rectangular ribs according to the finite volume methods. Boundary conditions include the insulated upper wall and bottom wall being subjected to a constant temperature. The Reynolds number for the laminar flow was selected to be 10 and 100. The volume fractions of solid particles were 0, 2% and 4%. The results marked in this investigation show that heat transfer rate can be enhanced by increasing the rib height and volumetric percentage of nanoparticles and Reynolds number. However, the existence of ribs within the path causes a velocity gradient and enhanced contact between the fluid/microchannel surfaces, which engenders an increase in the average friction factor. Furthermore, the existence

of nanoparticles does not have a major effect on hydrodynamic parameters such as fluid velocity and causes mere variations in the streamlines through the inlet section of the microchannel. In lower Reynolds numbers, the heat transfer rate between the surface and the fluid increases, and fluid has more opportunity for thermal exchange with the surface; on the other hand, more contact of the fluid with the surface causes an increase in friction factor. Among the studied cases, case (2), with the greatest rib height, has the maximum heat transfer due to better mixing of the fluid layers, and case (1), with the lowest rib height, owns the lowest Nusselt number.

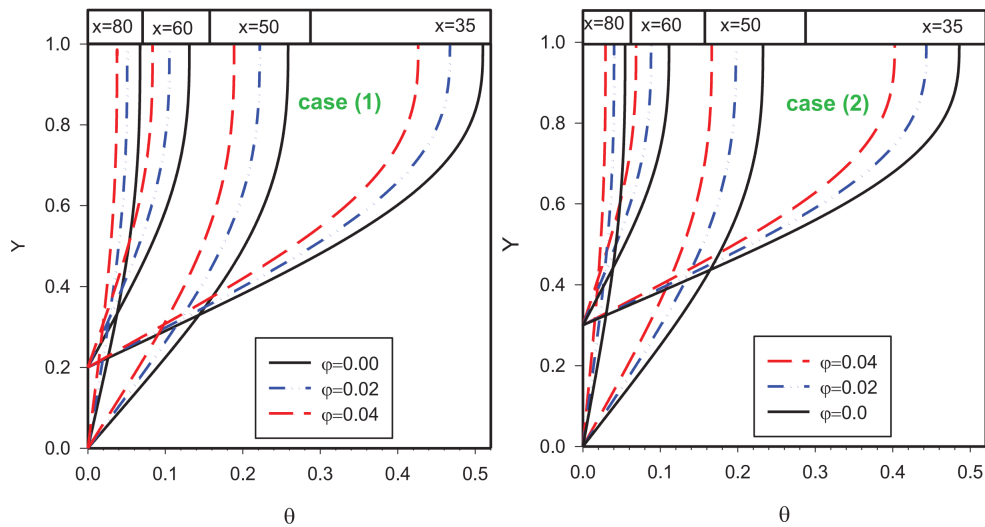


**Figure II.1** – Dimensionless temperature variation profiles along dimensionless length of the microchannel in different cross-sections of the microchannel for  $Re=10$ .

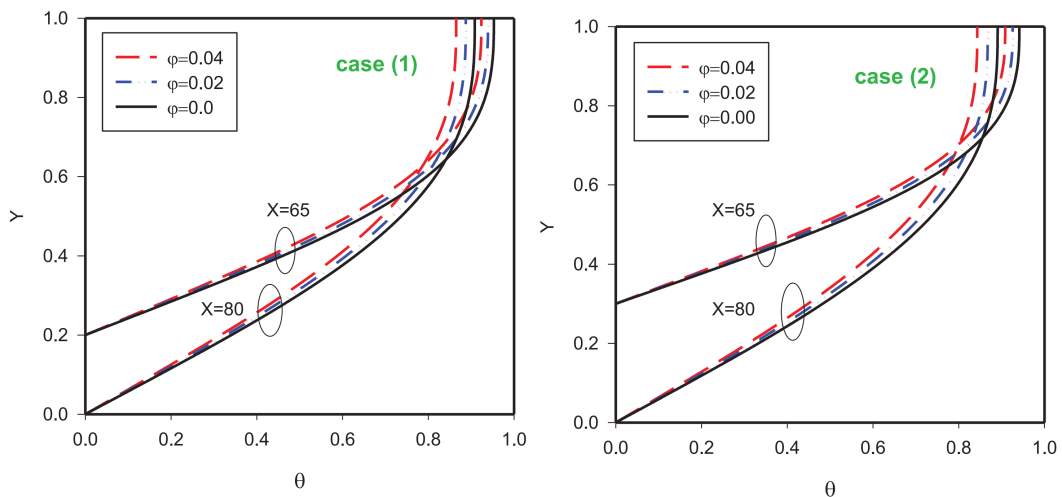


**Figure II.2** – Dimensionless temperature variation profiles along dimensionless length of the microchannel in different cross-sections of the microchannel for  $Re=100$ .

The numerical investigation of the turbulent flow and heat transfer of nanofluid inside a wavy microchannel with different wavelengths has been simulated by Bazdar et al. (2019) [38]. This investigation aims to reveal the effects of changing the wavelength of the sinusoidal microchannel

and CuO nanoparticle concentration on flow and heat transfer properties. Reynolds numbers are assumed to be 3000, 4500, 6000, and 7500 with volume fractions of 0, 1.5, and 3% in three different geometries. The present results validated the previous results, and it showed that there is an excellent agreement between them. Such as, at a lower Reynolds number, the Nusselt number was not changed, but at  $Re = 7500$ , the Nusselt number increases. Also, the change in wavelength increases heat transfer, and the maximum wall temperature of microchannel (b) is lower than other microchannels.

Yang and Du (2019) [39] carried out numerically a forced convective heat transfer of water/alumina nanofluid in a rectangular microchannel, this study investigated the effect of three techniques on heat transfer and pressure drop. In the first technique, three top and three bottom injections (six injections) were added to the base microchannel. In the second technique, the nanofluid was added to the base geometry, and the heat transfer improvement was investigated. In the last technique, the fluid injection was added to a microchannel containing nanofluid. Therefore, all three techniques entailed both a positive effect (increased heat transfer) and a negative effect (increased pressure drop). In the most effective technique, the pressure drop was 30% higher than the base microchannel at the point with maximum heat transfer.

Karimipour et al. (2011) [40] investigated the gravity effects on the mixed convection heat transfer in a microchannel using lattice Boltzmann method. And to include these effects, hydrodynamic boundary condition equations were modified. The present results are compared with previously available results for validation, and computations were performed for a wide range of inlet Knudsen number  $Kn$ . It was observed that with the increase of  $Kn$ , the slip velocity and temperature jump were increased, and  $Nu$  and  $Cf$  were reduced. The maximum value of these parameters occurs at the inlet, and they approach asymptotically to the corresponding constant value along the microchannel. Moreover, the effects of gravity generate buoyancy motions, particularly in the entrance region that has the largest temperature gradient between the fluid and the walls, and thus increases the entrance length.

Tavakoli et al. (2018) [41]. provided a study of mixed convection heat transfer inside a vertical microchannel with a two-phase approach numerically. In their research, they used the finite volume method in two-dimensional coordinates. Because most of the miniature equipment's affected by the oscillating heat flux, The present research has been carried out in Reynolds numbers of 150 – 1000 and Ag nanoparticles volume fractions of 0 – 4% by applying slip and no-slip boundary conditions. Also, in order to estimate the heat transfer behaviour and the com-

putational fluid dynamics, the two-phase mixture method was employed. Results were analysed and presented as the contours of Nusselt number, friction coefficient, pressure drop, thermal resistance and temperature. As well as, applying slip boundary conditions on microchannel walls and enhancing fluid velocity, Grashof number, and volume fraction of nanoparticles cause the improvement of Nusselt number, reduction of thermal resistance and total entropy generation and the augmentation of pressure drop. Additionally, the presence of oscillating heat flux affects the changes in the Nusselt number significantly. In comparison with the pure water fluid with Reynolds numbers of 1000, 700 and 400, in Grashof number of 1000 with no-slip boundary condition on microchannel walls, the enhancement of average Nusselt number in volume fraction of 4% in the same Reynolds numbers is 45%.

D’Orazio and Karimipour (2019) [42] demonstrated a mixed air convection inside a two-dimensional microchannel numerically by using the lattice Boltzmann method. This study conducted the effect of buoyancy forces on slip velocity, and temperature profiles were presented while the microchannel side walls were under a constant heat flux boundary condition. Three states were considered as having no gravity, and the value of the Knudsen number was chosen as  $Kn=0.005$ ,  $Kn=0.01$  and  $Kn=0.02$ , respectively; while Reynolds number and Prandtl number were kept fixed at  $Re=1$  and  $Pr=0.7$ . Density-momentum and internal energy distribution functions were used to simulate the hydrodynamic and thermal domains in the lattice Boltzmann method approach. As a result, it was shown that suitable models for slip velocity and heat flux boundary conditions in terms of LBM’s hydrodynamic and thermal distribution functions were developed to consider both the effects of gravity and velocity inlet. Additionally, Larger  $Kn$  led to larger  $Us$ ; Although the influence of  $Kn$  on  $Us$  decreased at higher amounts of  $Gr$ . Moreover, the negative slip velocity phenomenon due to the buoyance forces was observed for the first time at the present work. Also, Lower  $Kn$  corresponded to higher  $Nu$ . Moreover, the amplitude and number of fluctuations of  $Nu$  increased severely with  $Gr$  because of the strong cell generated by buoyancy forces.

Thansekhar and Anbumeenakshi (2017) [43] investigated the effectiveness of the nanofluids  $Al_2O_3$ / water and  $SiO_2$  water experimentally in enhancing the heat transfer performance of a microchannel heat sink having 25 numbers of rectangular microchannels of 0.42 mm width, 4.2 mm depth and 100 mm length. Nanofluids of  $Al_2O_3$ /water and  $SiO_2$ /water with a volume concentration of 0.1% and 0.25% and deionised water were used as heat transfer fluids. The nanofluid and its volume concentration were the key parameters affecting the thermal perfor-

mance of the microchannel heat sink. Nanofluid  $Al_2O_3$ / water exhibits better heat transfer performance than  $SiO_2$ / water due to the higher thermal conductivity. This makes  $Al_2O_3$ / water a suitable fluid for cooling of photovoltaic cells. And The heat transfer performance of the microchannel heat sink was affected significantly by the volume concentration of nanofluids. Nanofluids with higher volume concentration exhibit higher heat transfer enhancement, which was attributed to the stronger thermal dispersion and thermophoresis. Moreover, the additional pressure drop caused by the nanofluids was not so large that nanofluids are viable cooling fluids for the microchannel heat sink. [44] (2017) They also examined the collective effect of nanofluid and non-uniform heating on the cooling enactment of a MCHS. Three individual heaters of identical dimensions were placed at the bottom of the microchannel heat sink. Nanofluid of  $Al_2O_3$ /water of volume concentration 0.25% and 0.1% and deionised water were used as working fluids. And they publicised that the position of heater has a noteworthy influence on the maximum temperature of the heat sink. The maximum surface temperature of the MCHS is the lowermost when the heaters are located at the upstream of the flow.

Through conducting numerical analysis on heat transfer and laminar flow of kerosene/ multi-walled carbon nanotubes (MWCNTs) nanofluid in the microchannel heat sink with slip boundary condition Arabpour et al [45] (2018), the considered microchannel is two layers in which the length of bottom layer was truncated and was equal to half of the length of the bottom layer. The results evidenced that in different Reynolds numbers, applying oscillating heat flux considerably influences the profile figure of Nusselt number, and this impressionability is obvious in Reynolds numbers of 100 and 10. Also, by enhancing the slip velocity coefficient on the solid surfaces, the amount of minimum temperature of the surface decreases significantly which causes a remarkable increase in heat transfer. Furthermore, the friction coefficient decreases remarkably by enhancing the dimensionless slip velocity coefficient and depreciation. The amount of average friction coefficients in the Reynolds number of 1 is more significant in each of the studied Reynolds numbers. Increasing the Reynolds number and volume fraction of nanoparticles and due to better mixture of fluid flow and heat transfer enhancement and augmentation of convection heat transfer reduces the maximum temperature factor.

Ho et al. (2020) [46] examined the effects of dispersing  $Al_2O_3$  nanoparticles and nanoencapsulation PCM particles in the working fluid on the heat transfer improvement in the mini-channel heat sink, separately. In addition, the contributions of  $Al_2O_3$  nanoparticles and nanoencapsulation PCM particles to boost the thermal efficiency of the coolant in the mini-channel heat sink

were presented. Several important factors in the system were investigated at various concentrations of  $Al_2O_3$  nanoparticles and nanoencapsulation PCM particles, flow Reynolds numbers, and heat fluxes. The numerical results clearly reveal that the maximum thermal resistance reduction of 1.2% and 6.9% can be observed by adding the nanoencapsulation PCM suspension with 2% and 10% concentrations, respectively. For the water-based suspension of  $Al_2O_3$  nanoparticles, the heat transfer coefficient ratios are larger than unity for all heat flux values and Reynolds numbers. The usage of  $Al_2O_3$  nanoparticles provides better cooling performance as compared with the case of nanoencapsulation PCM particles. As a result, the beneficial effect of  $Al_2O_3$  nanoparticles is much greater as compared with that of nanoencapsulation PCM particles.

Metal foam is a particular kind of porous medium that can absorb significant heat from the solid by conducting and rejecting it to the fluid by convection. Metal foam shows different attractive features in comparison with its solid material counterparts. Its advantages include low volume, low density, high thermal conductivity, high effective heat transfer surface area, high flow-mixing capability, and low manufacturing cost. It is used in several thermal systems, such as heat exchangers, heat sinks, fuel cells, and solar collectors. It was shown that metal foam insertion could enhance thermal performance significantly up to 40 times. The solid/fluid thermal conductivity was observed to be an important parameter in increasing the heat dissipation by coolants. Researchers observed a high-pressure drop penalty accomplished to the thermal performance enhancement with the existence of metal foam. Microchannel heat sinks embedded in porous media can be considered as micro pin-fin heat sinks in which the pins act as grains, and the area between the pins accounts for the pore space in the porous media.

The enhanced heat transfer mechanism and thermal energy storage, optimised energy and energy efficiency in these innovative applications have reached the point where they are of significant interest and have become one of the greatest heat transfer performance challenges. Many attractive passive enhancement techniques have been employed to improve heat transfer performance effectiveness and efficiency, including porous metal foams [47], [48], [49], nano-additive nanoparticles, encapsulated phase change materials (NEPCMs), enclosure shape change, grooved surfaces, dimpled surfaces, surfaces with arrays of protrusions, plane fins, pin fins, and artificial surface roughness.

Ghazvini and Shokouhmand (2009) [47] numerically investigated the influence of NFs on the cooling of a heat sink microchannel using fins and a porous medium. They showed that a porosity coefficient increment can enhance the dimensionless temperature and Nuave.

Nojoomizadeh et al. (2018) [48] studied numerically investigated the forced heat-transfer and laminar flow in a two-dimensional microchannel whose lower half was filled with a porous medium. They used the nanofluid  $Fe_3O_4$ /water which contains nanoparticles  $Fe_3O_4$  and the water as based fluid, this nanofluid flow was modelled employing the Darcy–Forchheimer equation. It is hypothesised that there was a thermal equilibrium between the solid phase and nanofluid for energy transfer, and the walls of the microchannels were assumed at a constant temperature higher than the inlet fluid temperature. Also, the slip boundary condition was assumed along the walls. The effects of Darcy number, porosity and slip coefficients, and Reynolds number on the velocity and temperature profiles and local Nusselt number were presented in both porous and non-porous regions. In this work, the Darcy number was assumed to be  $Da=0.1$  and  $0.01$  with three values of Reynolds number  $Re=25$ ,  $50$ , and  $100$ , slip coefficient  $B=0.1$ ,  $0.01$ , and  $0.001$ , the porosity  $\varepsilon = 0.5$  and  $0.9$ , and the volume percentage of the nanoparticles  $\varphi = 0\%$ ,  $2\%$ , and  $4\%$ . The result obtained in this investigation showed that with the increase of Reynolds number, the nanofluid velocity increased, thus increasing the local Nusselt number. In addition, the presence of a velocity difference at the same cross-section of the microchannel due to the presence of a porous medium in the lower half of the microchannel, led us to be witnessing an increase in the slip velocity in the upper half and a decrease in the slip velocity in the lower half of the microchannel as the Darcy number was decreasing.

A numerical study of water/FMWCNT nanofluid forced convection in a microchannel filled with porous material under slip velocity and temperature jump boundary conditions was discussed by Gholamalizadeh et al [49] (2019), for the study parameters, they considered the following ranges : slip factor  $B=0.001$ ,  $0.01$ , and  $0.1$  ; The  $Re$  and solid nanofluid concentrations ranges were  $10 - 100$  and  $0.0012 - 0.0025$ , respectively ; A Darcy number between  $0.001$  and  $0.1$  and a porosity coefficient range of  $0.4 - 0.9$  solid nanoparticle mass fraction rang  $0.0012 - 0.0025$ . In addition, the thermophoresis and Brownian effects were disregarded. Consequently, it was discovered that the existence of a porous medium in microchannels has a very interesting impact, such as increasing the Darcy number had a more pronounced effect on the velocity profile than increasing the Reynolds number. However, increasing porosity was less pronounced at the growth rate of the velocity profile.

The magnetohydrodynamic MHD phenomenon has received considerable attention from engineers and scientists over the last two decades owing to its relevance in many MHD applications like MHD generators, MHD accelerators, electric transformers and cooling of the metallic plate



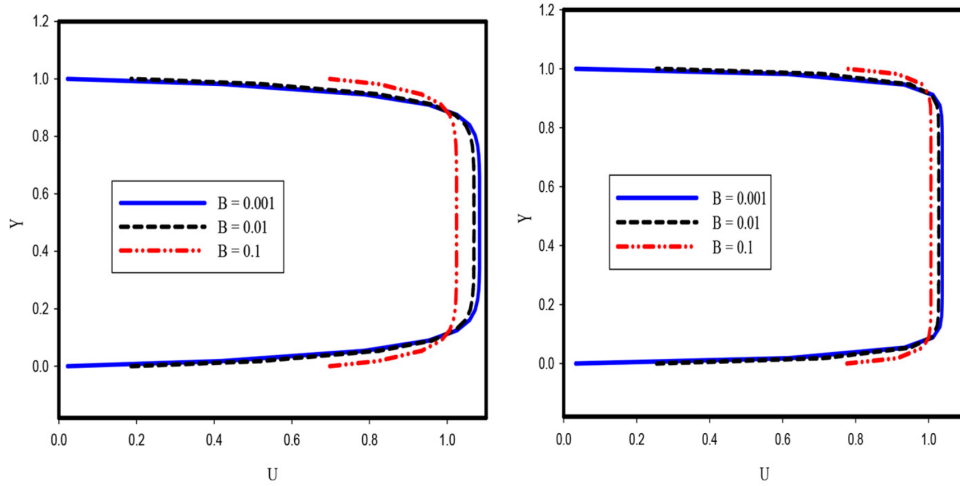


**Figure II.3** – Non-dimensional velocity profile obtained for nanofluid along the perpendicular line passing through the microchannel center at  $x=L/2$ ,  $Re=100$ ,  $Da=0.001$ ,  $\varepsilon = 0.4$ , and  $\varphi = 0.0012$ .

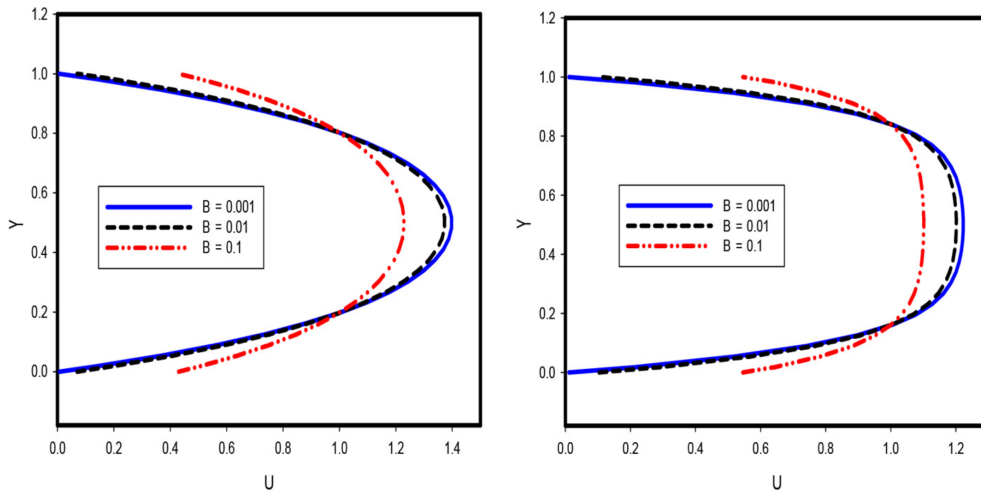


**Figure II.4** – Non-dimensional velocity profile obtained for nanofluid at the perpendicular line passing through the microchannel center at  $x=L/2$ ,  $Re=100$ ,  $Da=0.1$ ,  $\varepsilon = 0.9$ , and  $\varphi = 0.0012$ .

in a cooling bath. Magnetohydrodynamic MHD pumps are already used in chemical energy technology for pumping electrically conducting fluids at some atomic energy centers. For such modern applications, figuring out properly the effects of magnetic fields and the behaviour of the Newtonian fluids, even in narrow ducts, acquired a great importance : miniaturised applications, several experiments and tests started to be performed along with numerical and theoretical evaluations [50], [51], [52], [53], [54].

Afrand et al. (2016) [50] studied the forced convection heat transfer of water/FMWCNT nanofluid in a two-dimensional microchannel under a magnetic field. The effects of Hartmann number, Reynolds number, slip coefficient and solid volume fraction on velocity, temperature and Nusselt number were investigated. They observed that increasing the strength of the ma-

agnetic field led to a significant increase in the amount of slip velocity. And at higher Hartmann numbers, the effects of the slip coefficient on the slip velocity were more than that at lower Hartmann numbers. Higher values of  $Nu$  were achieved at larger amounts of Hartman number and volume fraction at higher Reynolds numbers  $Re=200$ .

Karimipour et al. (2016) [51] numerically investigated on laminar forced convection of nanofluids in the microchannels by using a FORTRAN code. A novel mixture of water and FMWNT carbon nanotubes as the working fluid. The mixture of FMWNT carbon nanotubes suspended in water was considered as the nanofluid. Slip velocity was supposed as the hydrodynamic boundary condition while the microchannel's lower wall was insulated and the top wall was under the effect of a constant heat flux; the flow field was subjected to a magnetic field with a constant strength. Here, the effects of pertinent parameters were explained. It was indicated that increasing the Hartmann number reduced the maximum velocity in the centerline of the microchannel and increased the velocity near the walls. Furthermore, it was marked that imposing the magnetic field was very effective at the thermally developing region, In contrast, the magnetic field effect at the fully developed region is insignificant, especially at a low Reynolds number.

Karimipour et al. (2016) [52] reported The effects of different nanoparticles of  $Al_2O_3$  and Ag on the MHD nanofluid flow and heat transfer in a microchannel, including slip velocity and temperature jump. Microchannel domain is under the influence of a magnetic field with the strength of  $B_0$  Reynolds number chosen as  $Re=10$  and  $Re=100$ . Slip velocity and temperature jump boundary conditions were simulated along the microchannel walls at different slip coefficient values :  $B=0.05$ , and  $0.1$  for different amounts of Hartmann numbers  $Ha=0, 20$ , and  $40$ . And Different types of nanoparticles, such as  $Al_2O_3$  and Ag are examined while the base fluid was considered as water. It was found that the Slip coefficient ( $B$ ) has significant effects on  $U$  profiles from  $B=0.01$  to  $B=0.1$  at a range of  $Y=0.1$  and  $Y=1$ , with various axial positions. Therefore, it is seen that the Magnetic field makes the Lorentz force in the opposite direction of fluid flow ; Hence larger Hartmann number ( $Ha$ ) leads to a smaller  $U_{max}$  at  $Y=0.5$  and also generates a core of uniform flow from  $Y \approx 0.15$  to  $Y \approx 0.85$ . Moreover, larger  $Ha$  leads to larger  $Num$  at higher values of  $Re$ , also, It was recommended to use  $Al_2O_3$ –water nanofluid instead of Ag water to increase the heat transfer rate from the microchannel walls at low values of  $Re$ . However, the nanofluid composed of nanoparticles with higher thermal conductivity works better at larger amounts of  $Re$ .

Alipour Lalami et al. (2019) [53], hydrodynamics and heat transfer of FMWCNT–water nanofluid flow in the hydrophobic microchannel were comprehensively studied for a range of magnetic field intensities ( $Ha=0,15,30$ ), dimensionless slip coefficients  $0 \leq B \leq 0.1$  and suspension volume fractions ( $\varphi = 0, 0.1\%, 0.2\%$ ) at a fix Reynolds number ( $Re=100$ ) and a uniform external heat flux  $q''$ . The adjustable parameter of  $\gamma$  was appropriately selected in the range of 0.5 to 0.8. It was concluded that with magnetic field presence and realistic temperature jump, the surface material of superhydrophobic walls should be chosen properly to avoid inevitable and uncontrolled reduction in heat transfer, such that the highest hydrophobicity was not always the best choice.

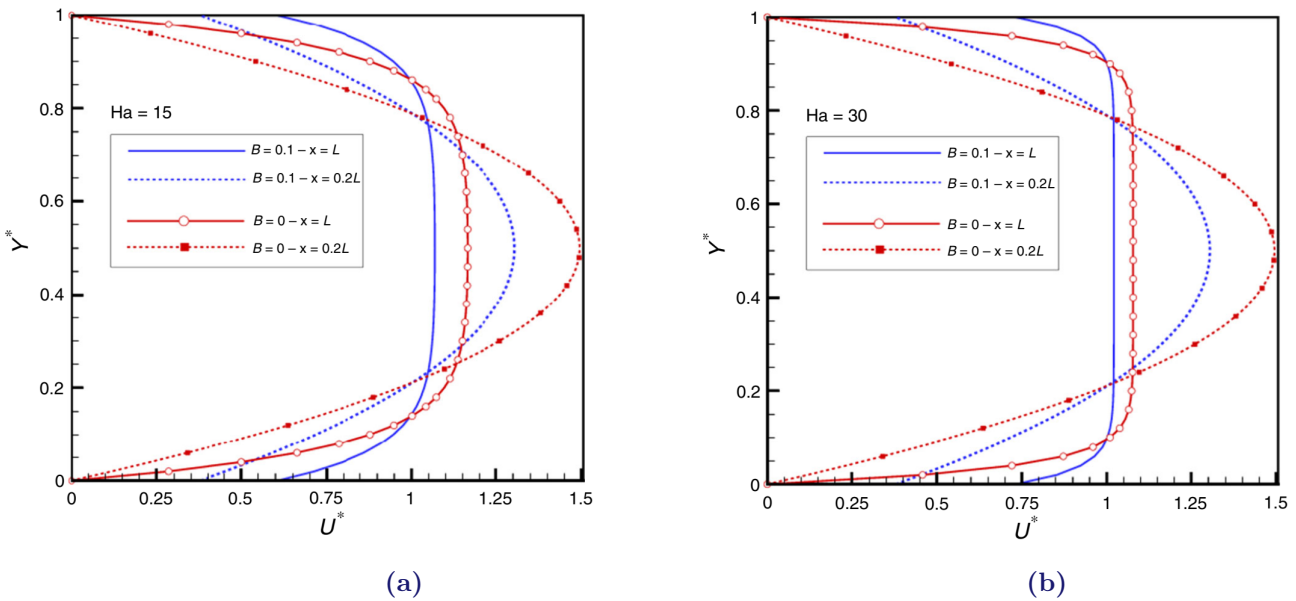


**Figure II.5** – Effects of magnetic field on dimensionless velocity profile for nanofluid with  $\varphi = 0.2\%$  at  $B=0$  and  $0.1$ . Profiles are plotted at two fully developed regions,  $x=0.2L$  and  $x=L$ ,  $Ha=15$  (Top) and  $Ha=30$  (Bottom).

Madhu et al. (2019) [54] analysed The entropy generation and heat transfer characteristics of magnetohydrodynamic (MHD) third-grade fluid flow through a vertical porous microchannel with a convective boundary condition. Entropy generation due to the flow of MHD Non-Newtonian third-grade fluid within a microchannel and temperature-dependent viscosity was studied using the entropy generation rate and Vogel’s model. An appropriate comparison was made with the previously published results in the literature as a limiting case of the considered problem. The comparison confirms excellent agreement. The effects of the Grashof number, the Hartmann number, the Biot number, the exponential space, and the viscous dissipation parameter on the temperature and velocity were studied and presented graphically. The entropy generation and the Bejan number were also calculated, so the main results of the problem were

summarised. In the case of  $Ha$  and  $Bi$ , the temperature profile heightens at the left plate and declines at the right plate. The temperature profile enhanced with larger values of  $A$  and  $\lambda_1$ , and declined with larger values of  $\lambda_2$ ,  $A$  and  $Bi$ . Also, The Bejan number heightens on increasing values of  $\lambda_1$ ,  $A$ , and  $\lambda_2$ , and lessens by increasing  $A$ ,  $Gr$ , and  $Bi$ . The profile of  $Be$  showed an increasing behaviour at the right plate and a decreasing behaviour at the left plate for increasing values of  $Ha$ . Together with  $Ns$  increased with increasing values of  $A$ ,  $Gr$ , and  $Bi$ , and deteriorated by increasing values of  $\lambda_1$  and  $\lambda_2$ . The profile of  $Ns$  increased at the right wall and declined at the left wall with higher values of  $Ha$ .

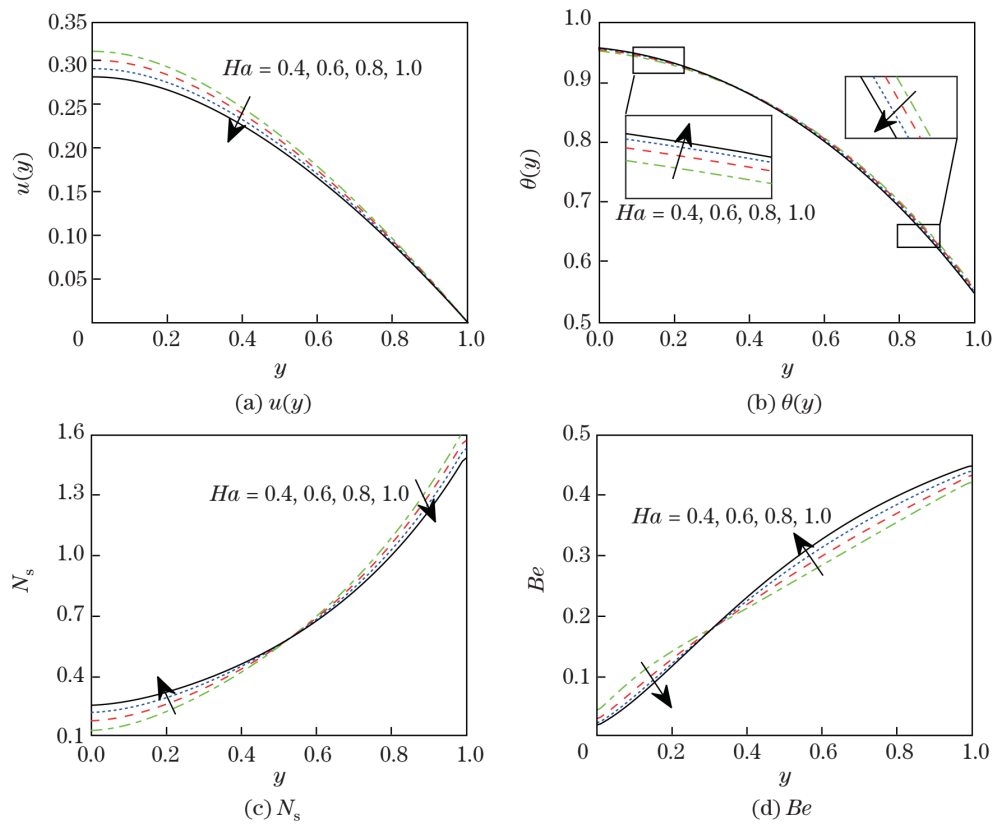


**Figure II.6** – Effects of  $Ha$  on  $u(y)$ ,  $\theta(y)$ ,  $Ns$ , and  $Be$ .

Many fluids of interest in industrial practice exhibit non-Newtonian fluid behaviour; several rheological models, such as power-law and Bingham and Herschel Bulkley models, can characterise these industrial fluids of the non-Newtonian type. Materials that exhibit a shear-thinning non-Newtonian behaviour include slurries, pastes, suspended solids in liquids, and emulsions. The shear-thinning materials are frequently encountered in industries dealing with composite materials, rubber, pharmaceuticals, biological fluids, plastics, petroleum, soap and detergents, cement, food products, paper pulp, paint, light and heavy chemicals, oil field operations, fermentation processes, plastic rocket propellants, electrorheological fluids, ore processing, printing,

and radioactive waste [55], [56], [57], [58], [59], [60], [61].

A Numerical study on the heat transfer performance of non-Newtonian fluid flow in a manifold microchannel heat sink was done by Li et al. (2017) [55], this study presented a three-dimensional simulation, and concerning the non-Newtonian fluid, they described the power law. They investigated the effect of the non-Newtonian fluid on the heat transfer performance, including the heat transfer efficiency and uniformity of temperature distribution, as well as the influence of inlet/outlet configurations on fluid flow and heat transfer, Compared with Newtonian fluid flow. For the heat transfer performance, introducing pseudoplastic fluid flow greatly improved the heat transfer efficiency due to the generation of secondary flow due to the shear thinning property. So, the heat transfer enhancement in pseudoplastic fluid flow can be attributed to the emergence of secondary flow therein, which disturbs the flow and thus promotes the mixing of the cold and heat fluid. However, in dilatant fluid flow, the heat transfer is dominated by conduction, and the shear-thickening property of the dilatant fluid has little contribution to the generation of secondary flow. Moreover, as for the heat transfer performance of non-Newtonian fluid flow, it was found that the application of dilatant fluid has little change in the heat transfer efficiency compared to that of Newtonian fluid. However, the introduction of pseudoplastic fluid flow can significantly improve heat transfer efficiency.

Laminar flow of the non-Newtonian fluid in a rectangular microchannel with triangular ribs has been numerically studied by Shamsi et al. (2017) [56], for the best non-Newtonian, solid nanoparticles of Aluminum Oxide have been added to the non-Newtonian fluid in volume fractions of 0 – 2% with 25, 45 and 100 nm diameters. The power law has been used to speculate the dynamic viscosity of the cooling nanofluid. The field of the numerical solution is simulated in the Reynolds number range of  $5 < Re < 300$ . A constant heat flux of  $10,000 W/m^2$  is exercised on the lower walls of the studied geometry. The effect of triangular ribs with the angle of attacks of  $30^\circ$ ,  $45^\circ$  and  $60^\circ$  have been marked flow parameters and heat transfer due to the fluid flow. The results were analysed for three different angles of attacks of the triangular ribs. Regarding the analyses, it can be said that an increase in the volume fraction of solid nanoparticles in the non-Newtonian fluid causes improved heat transfer which is due to the increase in the micron surface and boosting of the heat transfer mechanisms. Furthermore, the increase in Nusselt number was more significant when there were solid nanoparticles in higher Reynolds numbers and smaller nanoparticle diameters. Additionally, the changes in mean friction coefficient in lower Reynolds numbers were significant and were a result of the total contact between the cooling fluid and all the rib surfaces reaching its maximum level in the angle of attack  $30^\circ$  and

Reynolds number of 5. In higher Reynolds numbers, the mean friction coefficient is almost independent of the nanoparticle diameter and the triangular rib's angle of attack. In the analysis of the changes of the pressure drop, because pressure changes in the input and output of the channel were considered, the changes of the solid nanoparticle diameters make relatively few changes across the entire flow.

Kiyasatfar (2018) [57] examined hydrodynamically a convective heat transfer and thermally fully developed slip flow of power-law fluids through microfluidic channels with parallel-plate and circular cross-sections. In order to verify the analytical model proposed in this study, the analytical results were compared with the related experimental and numerical results available in the literature. The effects of key parameters such as slip coefficient, power-law index and Brinkman number on the flow, heat transfer and entropy generation characteristics have been discussed. And the following major conclusions were presented that the effects of slip and viscous dissipation on heat transfer and entropy generation are considerable and should not be neglected, particularly for dilatant fluids. Nusselt number has a decreasing trend with both  $n$  and  $Br$ , where the effect of  $Br$  becomes stronger for dilatant fluids. Together, at the same conditions, parallel-plate microchannel has a lower Bejan number and tends to produce more entropy than circular microchannel.

Tanveer et al. (2020) [58] simulated a non-Newtonian blood flow in a theoretically microchannel according to the Bingham fluid induced by applied electrostatic potential. The transformed equations for electroosmotic flow were solved to seek values for the nanofluid velocity, concentration and temperature along the channel length. The effects of key parameters like Brinkmann number, Prandtl number, Debye Huckel parameter, thermophoresis parameter, and Brownian motion parameter were plotted on velocity, temperature and concentration profiles were discussed briefly. They concluded that the nanofluid temperature was found an increasing function of electro-osmotic parameter  $\kappa$  if  $U$  is positive while it is a decreasing function if  $U$  is negative. A completely reverse response was seen in the case of the concentration profile. The thermophoresis parameter  $Nt$ , the Brownian motion parameter  $Nb$  and Brinkman number  $Br$  cause an enhancement in temperature.

Javidi Sarafan et al. (2020) [59] treated heat and mass transfer and thermodynamic analysis of power law fluid flow in a porous microchannel. The considered configuration was assumed to be geometrically and thermally asymmetric. The power-law behaviour was assumed for the fluid, and the porous medium was set under local thermal non-equilibrium. The resultant nonlinear

system of partial differential equations was then solved numerically by using a finite volume solver. This led to the developing of two-dimensional solutions for the temperature concentration and local entropy generation fields and evaluating Nusselt number and total entropy generation. It was concluded that for the Newtonian fluids. It was shown that increases in the power-law index value reduce the heat transfer rate and thus drop the value of the Nusselt number. Hence, the local and total generations of entropy are both strongly affected by the value of the power-law index in which increases in this parameter highly enhance the local and total irreversibilities. The other qualitative characteristics of the investigated system were found to remain consistent with those reported for the Newtonian fluids.

A density-based topology optimisation method for thermal-fluid systems has been developed by Dong and Liu (2021) [60] to reduce pressure drop (energy dissipation) and enhance heat transfer. The non-Newtonian fluid effects on the optimal structures of the flow channels and heat transfer performance were studied. In the numerical method, the interpolation term in the density-based topology optimisation method was modified, while the filtering method was used to solve the problems of grayscale and the flow channel discontinuity. When the thermal conductivity of fluid is smaller than that of solid, the heat sources were surrounded by solid material, increasing the multi-objective coefficient  $\omega$ . Therefore, better heat dissipation performance can be obtained by placing materials with a higher thermal conductivity around the heat sources. As well as, the optimal results for Newtonian and non-Newtonian fluids were compared. The differences between the optimal structures of the two fluids were more obvious with  $Re=0.01$  in the dual terminal system. The optimal designs of heat transfer performance for non-Newtonian fluid are better than that for Newtonian fluid while consuming more energy. In biochemical thermal-fluid devices, better heat transfer performance can be obtained by changing water to blood, but at the same time, a more powerful pump is needed to drive the flow.

The thermal and entropy generation nature in magneto Carreau non-Newtonian material induced by convectively heated microchannel has been addressed by Shehzad et al. (2021) [61], finite element-based numerical scheme was adopted for the solutions of the physical model. The application of EGM in microchannel heat sink design was reviewed and discussed in this paper, entropy generation minimisation EGM as a new optimisation theory, stated that the rate of entropy generation should also be optimised. Dimensionless variables were executed for the simplicity of basic equations. The subsequent system was treated by using the finite element method. Behaviours of effective parameters on velocity, Bejan number, entropy generation rate and temperature were interpreted, as well as the Reynolds number with four values  $Re=0.5, 1,$

1.5, 2. The results of various quantities were addressed by plotting graphs. It was noted that the Bejan number  $Be$  and rate of local entropy generation  $Ns$  have sinusoidal nature for increasing values of magnetic field constraint  $M(1.5, 2, 2.5, 3)$ . Furthermore, the velocity  $f$  of liquid was reduced first, but it starts to boost up after  $\eta = 0.6$  for increasing trend of Reynolds number  $Re$ . The behaviors of  $Ns$  and  $Be$  for increasing  $Re$  are similar in a qualitative way. Both quantities decreased firstly and then boost up when the values of  $\eta$  increased from 0.7.





# CHAPTER III

## ENHANCEMENT OF HEAT TRANSFER MECHANISMS

# ENHANCEMENT OF HEAT TRANSFER MECHANISMS

---

# III

## Why Enhancing Heat Transfer Rate Is Crucial ?

For the past century, reducing energy consumption has attracted considerable attention from engineers and scientists. Whether it is energy saving, energy conservation, or energy efficiency, many efforts have created more professional equipment. Other factors like space limitations and economic incentives have accelerated this concept in heat exchange equipment. Firstly, the focus was on boosting the heat transfer coefficient by improving the thermal properties. This has enabled us to solve other significant problems, such as lowering the maximum temperature of surfaces and reducing the mass and size of heat exchangers [62].

### III.1 Microchannel

#### III.1.1 Flow channel classification

Channel classification based on hydraulic diameter is intended as a simple guide for conveying the dimensional range under consideration. Channel size reduction has different effects on different processes. Deriving specific criteria based on the process parameters may seem to be an attractive option, but considering the number of processes and parameters that govern transitions from regular to microscale phenomena (if present), a simple dimensional classification is generally adopted in the literature. The classification proposed by Mehendale et al. (2000) divided the range from 1 to 100  $\mu m$  as microchannels, 100  $\mu m$  to 1mm as meso-channels, 1 to 6mm as compact passages, and greater than 6mm as conventional passages [63].

In biological systems, the flow in capillaries occurs at very low Reynolds numbers. A different modelling approach is needed in such cases. Also, the influence of electrokinetic forces begins

to play an important role. Two-phase flow in channels below  $10 \mu m$  remains unexplored. The earlier channel classification scheme of Kandlikar and Grande (2003) is slightly modified, and a more general scheme based on the smallest channel dimension is presented in Table III.1 [63].

In Table III.1,  $D$  is the channel diameter. In the case of non-circular channels, it is recommended that the minimum channel dimension; for example, the short side of a rectangular cross-section should be used in place of the diameter  $D$ . We will use the above classification scheme for defining minichannels and microchannels. This classification scheme is essentially employed for ease in terminology; the applicability of continuum theory or slip flow conditions for gas flow must be checked for the actual operating conditions in any channel.

Conventional channels $> 3 mm$
Minichannels $3 mm \geq D > 200 \mu m$
Microchannels $200 \mu m \geq D > 10 \mu m$
Transitional Microchannels $10 \mu m \geq D > 1 \mu m$
Transitional Nanochannels $1 \mu m \geq D > 0.1 \mu m$
Nanochannels $0.1 \mu m \geq D$

**Table III.1** – Channel classification scheme [63].

## III.1.2 Heat Transfer and Pressure Drop in Channels

### III.1.2.1 Concept of Fully Developed and Developing Flow

Developing and fully developed flow are basic concepts in fluid flow and heat transfer through channels. These concepts divide the flow into free streams and a boundary layer near the surface. Since the fluid stream is surrounded by the channel walls, the formed boundary layers at the walls may run parallel to each other for a significant length of the channel. After this length, known as the hydrodynamic or thermal entrance length, the flow becomes fully developed. In the fully developed region, hydrodynamic or thermal boundary layers arrive at the same point and travel unaffected through the channel. This concept is shown in Figure III.1 [62].

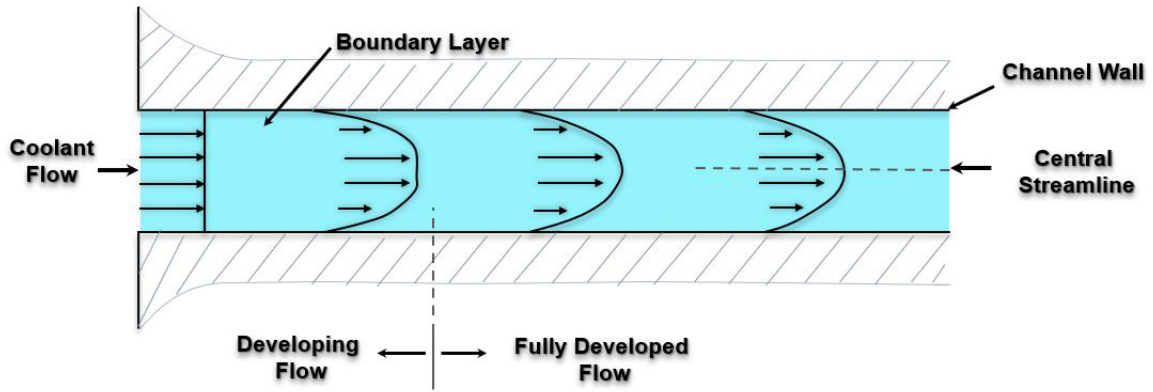


**Figure III.1** – As coolant flows through a channel, the flow pattern changes from "developing" to "fully developed" flow.

The distinctive feature of developing flow is a change in the velocity profile of the coolant. The profile vectors change in the region of developing flow, but remain constant in the fully developed region.

### III.1.2.2 Navier-Stokes Equations

The laminar and incompressible fluid flow in channels that obey the well-known Navier Stokes equations is as follows [62] :

$$\partial_t \rho + \partial_i(\rho u_i) = 0 \tag{III.1}$$

$$\partial_t(\rho u_i) + \partial_j(\rho u_i u_j) = -\partial_i \rho + \partial_j \mu(\partial_i u_j + \partial_j u_i) \tag{III.2}$$

$$\partial_t(\rho c T) + \partial_i(\rho c u_i T) = \partial_i(k \partial_i T) \tag{III.3}$$

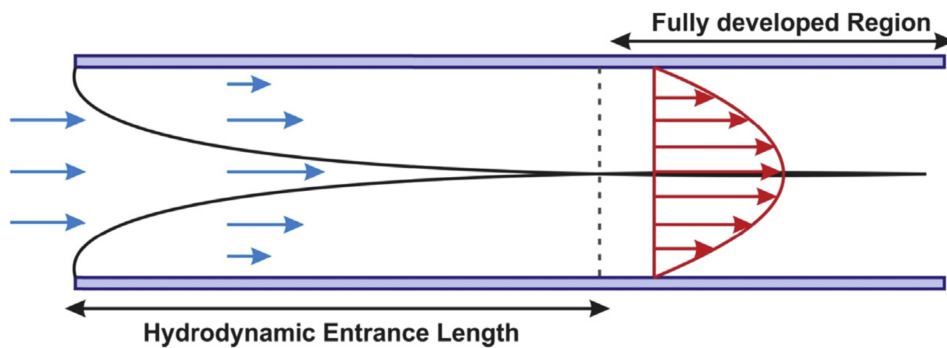


**Figure III.2** – Hydrodynamic entrance length and fully developed region.

where  $u_i$  represents the velocity components;  $T$  represents local temperature, and  $p$  will be pressure. Eq III.1 represents the continuity equation, whereas Eq III.2 considers the momentum, and Eq III.3 is the energy equation. These equations are solved many times by different researchers for special geometries and conditions. However, the similarity among all the equations is that they first divide the equations into developing and fully developed regions. For the fully developed region, the governing equations can be reduced to simplified equations. In some cases, they can be solved analytically. The following subsection will explain the fully developed concept.

### III.1.2.3 Fully Developed Region

Fully developed regions are defined for both hydrodynamic and thermal boundary layers. The first is called the hydrodynamic fully developed flow and the latter is called the thermally fully developed flow. Providing the hydrodynamic boundary layer (velocity profile) does not change flow direction, this flow is called hydrodynamic fully developed flow. Likewise, provided that the thermal boundary layer (nondimensional temperature profile) does not change flow direction, this flow is called thermally fully developed flow. Based on the Prandtl number, (the ratio of momentum diffusivity to thermal diffusivity), either condition may occur first, shown in Figure III.3; small values of the Prandtl number,  $Pr \ll 1$ , show the thermal diffusivity dominates, whereas, with the large values,  $Pr \gg 1$ , the momentum diffusivity dominates the behavior [62].

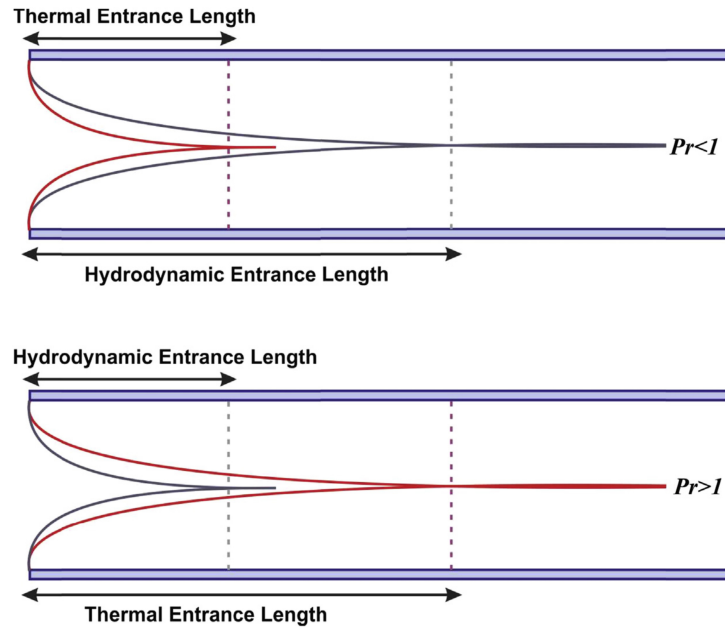


**Figure III.3** – Effects of Prandtl number on the size of hydrodynamic and thermal entrance length [62].

### III.1.2.3.a Hydrodynamic Fully Developed Flow

The hydrodynamic entrance region refers to the portion of the pipe prior to the velocity profile reaching full development. When fluid enters the pipe at a uniform velocity, the fluid particles in the layer in contact with the surface of the pipe come to a complete stop due to the nonslip condition. Due to the fluid's viscosity, the layer in contact with the pipe surface resists the motion of adjacent layers and gradually slows them down. For the conservation of mass to hold true, the velocity of the middle layers of fluid in the pipe increases (since the layers of fluid near the pipe surface have reduced velocities). This develops a velocity gradient across the cross-section of the pipe. However, with hydrodynamic fully developed conditions, the hydrodynamic boundary layers converge with each other, and the velocity profile becomes constant. Thus, the hydrodynamic fully developed region has the following flow limitations [62].

$$\partial \vec{u} / \partial s = 0 \quad (\text{III.4})$$

Where  $s$  represents the flow stream direction.

### III.1.2.3.b Thermally Fully Developed Flow

On thermal fully developed conditions, the hydrodynamic boundary layers clash into each other, and the temperature profile remains constant. The thermal fully developed condition is not similar to the hydrodynamic condition [62].

For instance, the bulk mean fluid temperature ( $T_b$ ) is defined to refer the axial convected thermal energy rate as follows [62] :

$$\dot{m} c T_b = \int_A \rho u c T \, dA \quad (\text{III.5})$$

where  $u$  represents the streamwise velocity,  $c$  represents specific heat capacity, and  $A$  signifies the surface cross-section. If the non-dimensional temperature is defined in terms of wall temperature ( $T_w$ ), the bulk mean fluid temperature ( $T_b$ ), and the nondimensional temperature profile is invariant to the flow direction. This will result in the following relation.

$$\frac{\partial}{\partial s} \left( \frac{T_w - T}{T_w - T_b} \right) = 0 \quad (\text{III.6})$$

Which can be written in the following form :

$$\frac{\partial T}{\partial s} = \frac{\partial T_w}{\partial s} - \left( \frac{T_w - T}{T_w - T_m} \right) \frac{\partial T_w}{\partial s} + \left( \frac{T_w - T}{T_w - T_m} \right) \frac{\partial T_b}{\partial s} \quad (\text{III.7})$$

The temperature gradient in  $s$  direction will not vanish and will strongly depend on wall temperature (thermal boundary condition).

Let us consider two possible conditions and simplify Eq III.7 For the case of constant wall heat flux, the convection rate can be written as [62] :

$$q''_W = h (T_w - T_b) = \text{constant} \quad (\text{III.8})$$

Since  $h$  is a constant

$$(T_w - T_b) = \text{constant} \quad (\text{III.9})$$

So, from Eq III.7 it can be written

$$\begin{aligned}\frac{\partial T_W}{\partial s} - \frac{\partial T_b}{\partial s} &= 0 \\ \frac{\partial T}{\partial s} &= \frac{\partial T_W}{\partial s} = \frac{\partial T_b}{\partial s}\end{aligned}\quad (\text{III.10})$$

For the case of constant wall temperature, the following relation can be obtained from Eq III.7 :

$$\begin{aligned}\frac{\partial T_W}{\partial s} &= 0 \\ \frac{\partial T}{\partial s} &= \left( \frac{T_W - T}{T_W - T_b} \right) \frac{\partial T_b}{\partial s}\end{aligned}\quad (\text{III.11})$$

### III.1.2.3.c Fully Developed Flow in Circular Channels

To further explain, an analytical solution for the fully developed flow and heat transfer of a steady and incompressible fluid is presented in Figure III.4 Axial conduction is assumed to be small (high Pecklet number). For the hydrodynamic fully developed flow, the governing equations can be reduced to [62] :

$$\frac{dp}{dx} = \frac{1}{r} \mu \frac{d}{dr} \left( r \frac{du}{dr} \right) = \text{constant} \quad (\text{III.12})$$

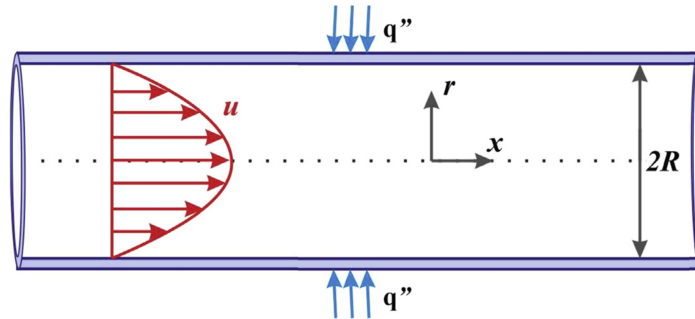


**Figure III.4** – Fully developed flow in circular channels [62].

Solving Eq III.12 subjected to the nonslip condition at the walls

$$\begin{aligned}r = R : u &= 0 \\ r = 0 : \frac{du}{dr} &= 0\end{aligned}\quad (\text{III.13})$$

Results in the well-known Hagen Poiseuille solution

$$\begin{aligned}u &= 2U \left[ 1 - \left( \frac{r}{R} \right)^2 \right], \\ U &= -\frac{R^2}{8\mu} \frac{dp}{dx}\end{aligned}\quad (\text{III.14})$$



Where  $U$  symbolizes mean velocity. The shear stress at the wall can be evaluated from the velocity gradient as follows :

$$\tau_W = \mu \left. \frac{du}{dr} \right|_{r=R} = -\frac{4\mu U}{R} \quad (\text{III.15})$$

Thus, the local friction coefficient can be expressed as :

$$\begin{aligned} c_f &= \frac{\tau_W}{(1/2)\rho U^2} = \frac{16}{\text{Re}}, \\ \text{Re} &= \frac{2\rho U R}{\mu} \end{aligned} \quad (\text{III.16})$$

To consider the thermally fully developed flow as well as the hydrodynamic, the thermal boundary condition should reflect upon. For the constant wall heat flux, substituting Eq III.10 into Eq III.2, we may have

$$\frac{u}{\alpha} \frac{dT_b}{dx} = \frac{1}{r} \mu \frac{d}{dr} \left( r \frac{dT}{dr} \right) = \text{constant} \quad (\text{III.17})$$

and for the constant wall temperature, equating Eq III.11 into Eq III.2 leads to :

$$\frac{u}{\alpha} \left( \frac{T_W - T}{T_W - T_b} \right) \frac{dT_b}{dx} = \frac{1}{r} \mu \frac{d}{dr} \left( r \frac{dT}{dr} \right) = \text{constant} \quad (\text{III.18})$$

Substituting the fully developed velocity profile Eq III.14 into Eq III.17 and Eq III.18, the fully developed temperature profile can be written as :

Constant wall heat flux :

$$T = T_b - \frac{2U}{\alpha} \frac{dT_b}{dx} \left[ \frac{3R^2}{16} + \frac{r^4}{16R^2} - \frac{r^2}{4} \right], \quad (\text{III.19})$$

Constant wall temperature :

$$\frac{T_W - T}{T_W - T_b} = \sum_{n=0}^{\infty} C_{2n} \left( \frac{r}{R} \right)^{2n}, \quad \begin{cases} C_0 = 1 \\ C_2 = -\frac{1}{4} \lambda_0^2 \\ C_{2n} = \frac{\lambda_0^2}{2n} (C_{2n-4} - C_{2n-2}) \\ \lambda_0 = 2.704364 \end{cases} \quad (\text{III.20})$$

It can appear that for the constant wall temperature, the bulk mean fluid temperature increases exponentially to obtain the wall temperature. However, for constant wall heat flux, both

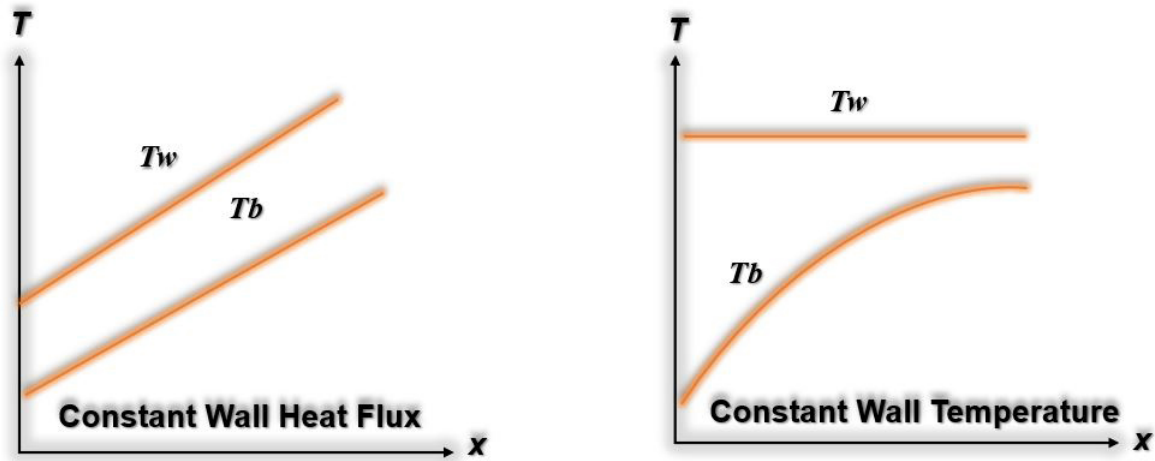


**Figure III.5** – Temperature variations for different thermal boundary conditions.

wall temperatures ( $T_w$ ) and bulk mean fluid temperature ( $T_b$ ) increase gradually with equal rates such that  $(T_b T_w)$  is constant [62].

### III.1.3 Heat Transfer Enhancement Classification

Heat transfer enhancement methods can be classified into two main groups : passive and active techniques. Passive techniques are those which do not require direct application of external power, while active techniques require external power. Except for extended surfaces like fins, which enhance the effective heat transfer surface area, the passive techniques improve the heat transfer coefficients by disturbing or altering the existing flow behaviour which is usually accompanied by a rise in the pressure drop. In the case of active techniques, on the other hand, the addition of external power essentially facilitates the desired flow modification and the concomitant improvement in the rate of heat transfer. As shown in Figure III.6, the various ways of passive and active heat transfer enhancement are as follows [62].

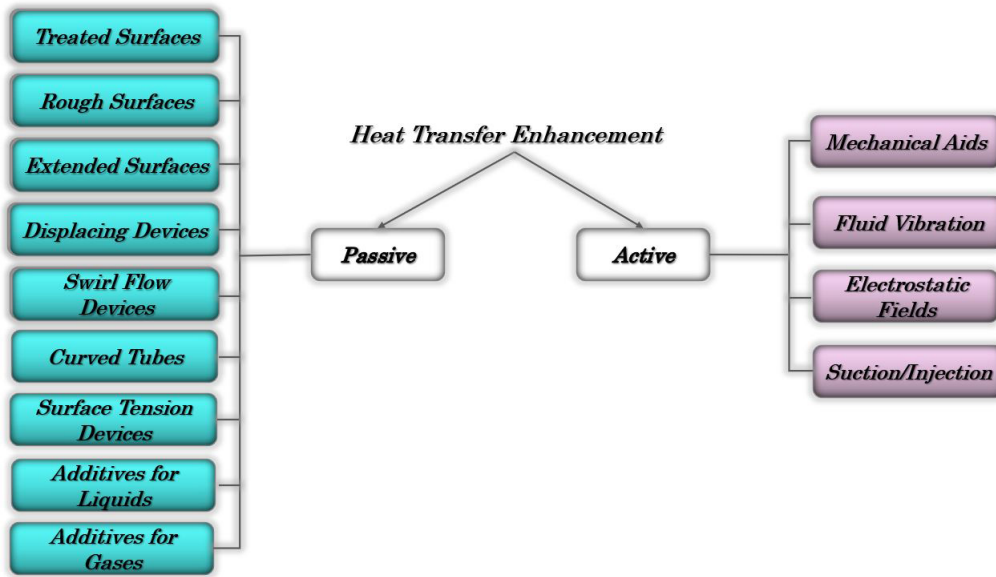


Figure III.6 – Different methods of heat transfer enhancement.

### III.1.4 Heat Transfer and Fluid Flow in Microchannels

Fluid flow inside channels is at the heart of many natural and man-made systems. Heat and mass transfer is accomplished across channel walls in biological systems, such as the brain, lungs, kidneys, intestines, and blood vessels, as well as in many man-made systems, such as heat exchangers, nuclear reactors, desalination units, and air separation units. In general, transport processes occur across the channel walls, whereas bulk flow takes place through the cross-sectional area of the channel. The channel cross-section thus serves as a conduit to transport fluid to and away from the channel walls.

A channel serves to accomplish two objectives : (i) to bring a fluid into intimate contact with the channel walls, and (ii) to bring fresh fluid to the walls and remove fluid away from the walls as the transport process is accomplished. The rate of the transport process depends on the surface area, which varies with the diameter  $D$  for a circular tube, whereas the flow rate depends on the cross-sectional area, which varies linearly with  $D^2$ . Thus, the tube surface area to volume ratio varies as  $1/D$ . Clearly, as the diameter decreases, the surface area to volume ratio increases. In the human body, two of the most efficient heat and mass transfer processes occur inside the lungs and the kidneys, with the flow channels approaching capillary dimensions of around  $4 \mu\text{m}$  [63].

## III.2 Heat Sink

The challenge of heat removal has been a challenge for most of the engineering applications irrespective the kind of application whether it is electronics, microelectronics, thermal plants etc. whether the application is micro or macro the heat removal was always challenging for the engineers as the heat removal comes with a cost i.e., increasing the surface area thereby increasing the space. One such technique of increasing heat dissipation rate from microelectronics is the provision of microchannels heat sink. The microchannel heat sink can be single phase or two phases depending upon the amount of heat to be dissipated [64].

The microchannels were introduced in early 1980 which were able to enhance heat transfer than conventional channels as they had good surface area to volume ratio and high heat transfer coefficient. Microchannels could easily handle heat flux of about  $100 \text{ W/cm}^2$ . The microchannels generally have hydraulic diameter below  $1 \text{ mm}$ . The heat sink is usually made of materials which have high thermal conductivity viz copper. The miniaturisation of electronic gadgets is the trend of the day and more miniaturisation has led to the overheating of devices due to accumulation of high heat fluxes in a small space which demands of a device to remove high heat fluxes within a confined space without compromising the thermal performance. The cross section of the heat sink serves as a passage for the liquid so that heat transfer can occur between the source of heat flux and fluid. The study of microchannel is gaining importance due to the necessity of dissipating large amount of heat with space as a great constraint [64].

However, dissipation of increased heat load has been a problem for simple microchannel heat sink due to high pressure penalty and temperature gradient along the flow. Various studies have been done on graded microchannel heat sinks to overcome the difficulties encountered in simple microchannel heat sink. For example, heat sink with pillars of various shapes, heat sink involving flow boiling (two phase) heat sink with pillars with jet impingement etc. are some of the graded microchannel heat sink that are the hot topics in the study of microchannels.

As with other heat-dissipation analyses, thermal and fluid performance for microchannel heat sinks can be modeled with Reynolds numbers, apparent friction factors, Nusselt numbers. And parameters that describe the thermal and fluid performance of the coolant. The thermal performance depends, in part, on whether the coolant flow is laminar or turbulent. As coolant enters a channel, a boundary layer develops within the coolant. This boundary layer separates the uniform-velocity core from the stationary coolant at the wall (the "no-slip" boundary

condition). The boundary layers will increase in thickness as the coolant flows through the channel. until the velocity profile achieves a "fully developed" profile, which does not change with downstream distance. The flow upstream from that point is said to be "developing"; the flow downstream is "fully developed" [64].

### III.2.1 Requirement of Microchannels

The microchannel heat sink is gaining importance due to two main reasons [64] :

1. Enhancement in heat transfer rate.
2. High heat flux removal required for microelectronics.

Increase in heat generation rates from micro electronic systems demand smart cooling techniques. The development of such thermal systems has been a challenge to micro fluidic industries and academicians. Microchannel coolers have number of coolant channels through which fluid is passed. Depending upon the thermo physical properties of fluid and amount of heat to be dissipated, the appropriate fluid with suitable dimension of heat sink is selected. Many studies had been done on microchannel coolers with different dimensions and with different coolants with varying thermo physical properties. The studies had demonstrated the pros of single-phase microchannel heat sink like handling of large heat load with small surface area, large heat transfer coefficient and minimum cooling inventory. The only purpose of these studies was to optimise the geometry of the heat sink.

### III.2.2 Applications of Microchannels

Micro-channel heat sinks are used for variety of cooling applications. These applications include cooling of components in computer (CPUs, memory storage devices and GPUs etc.), cooling of high-powered electronic components (IGBTs), cooling of proton exchange membrane fuel cells, cooling laser diode arrays, cooling of combustors and evaporator/condenser in miniature refrigerator. Major applications of the MCHS are found in the field of thermal management electronics. The existing conventional cooling methods cannot dissipate the huge amount of heat releases from modern high powered electronic components effectively [65].

Microchannel heat sinks can be used in a wide variety of applications, including microelectronics, diode laser arrays, and high-energy-laser mirrors. Heat sinks that can be used to cool diode laser arrays have been fabricated in indium phosphide with a thermal resistance as low as  $0.072^\circ\text{C}/(\text{W}/\text{cm}^2)$ , which allows these devices to dissipate loads in excess of  $1,000 \text{ W}/\text{cm}^2$ . This thermal resistance is nearly two orders of magnitude lower than that achieved by the methods presently used in the microelectronics industry. A heat- : sink thermal- and fluid-performance model is presented ; microchannel fabrication techniques are described for aluminum [66].

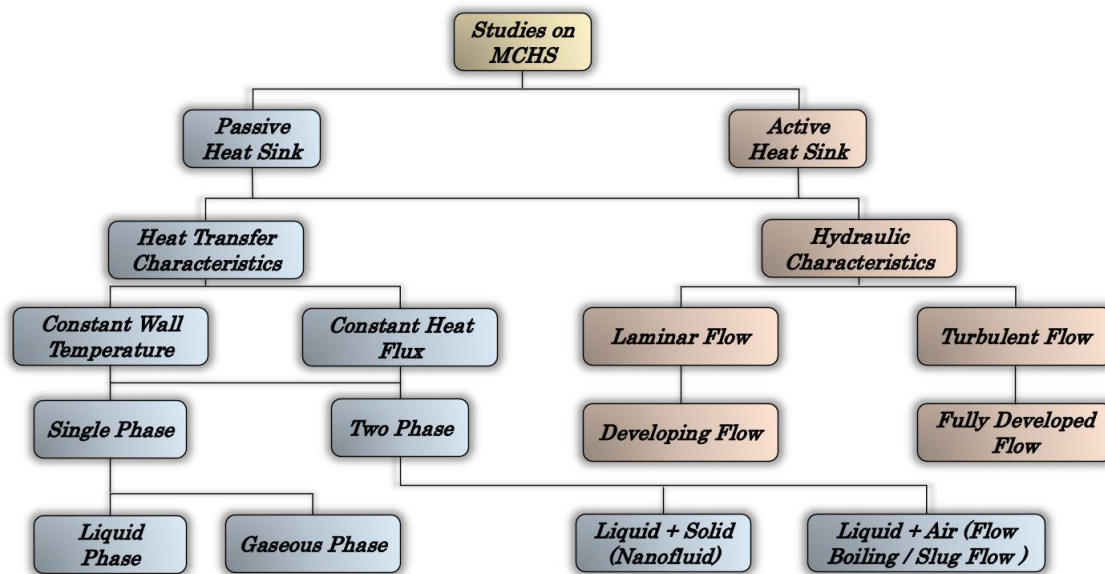


Figure III.7 – Schematic of studies on micro channel heat sinks.

### III.2.3 Enhanced microchannels

#### III.2.3.1 Flow disruption structures

Flow disruption structures enhance heat transfer by disrupting the normal development of thermal and flow boundary layers, reducing the thickness of thermal boundary layer, and preventing bubbles from blocking in two-phase boiling flow. In recent years, a large number of flow disruption structures have been developed to enhance heat transfer in microchannel heat sinks. They can be roughly divided into two means, i.e., micro pin fins and crosslinked microchannels [67] :

### III.2.3.2 Reentrant cavity structure

Reentrant cavity structures have been widely known to promote boiling nucleation as a vapor trap in pool boiling systems. The merits of reentrant cavity structures can be also extended to the flow boiling in microchannels. They enlarge the heat transfer area, and increase active bubble nucleation density by providing artificial nucleation sites in microchannels. Therefore, the reentrant cavity structures help to initiate nucleation earlier at smaller wall superheat, enhance boiling heat transfer performance and mitigate two-phase flow instability. In recent years, three types of reentrant cavity structures, i.e., reentrant cavity structures on the sidewall, artificial nucleation cavity structures on the bottom, and reentrant flow passages of microchannels, have been proposed for flow boiling enhancement in microchannels [67].

### III.2.3.3 Porous structure

Porous structures, such as porous coating, porous powder matrix, porous foams, provide numerous tiny pores for bubble nucleation, which supply as ideal spaces for bubble growth. Besides, the heat transfer area can be significantly increased. Therefore, they are excellent structures to reduce the wall superheat for boiling initiation, and improve both flows boiling heat transfer and CHF. In recent years, two types of porous structures have been reported to enhance the boiling heat transfer, i.e, porous surface structures and porous microchannels [67].

### III.2.3.4 Nano structure

Nano structures feature a series of unique properties, such as extraordinary high thermal conductivity, large specific surface area, wettability manipulation and etc. Therefore, the introduction of nano structures onto microchannels helps to enlarge heat transfer surface areas, modify the surface wettability and flow behaviors, and enhance capillary wicking for liquid rewetting. Many reports have been documented in recent years on microchannels with nano structure. Nanowires, carbon nanotubes (CNTs) and nano coating are the most common nano-structures in enhanced microchannels [67].

### III.2.3.5 Micro-mechanical cutting process

With the advancement of micromachining and high-precision machining, micro-mechanical cutting process has been widely utilized to fabricate microchannels and microstructures. By using the ultra-precision machine tools, it is able to process microstructures with high machining speed, high level of machining accuracy, and good surface finish. A wide range of materials, such as steel, aluminum, brass, plastic and polymer, can be processed by micromechanical cutting process. Moreover, it does not require expensive and complicated fabrication equipments like laser beam machining and etching techniques [67].

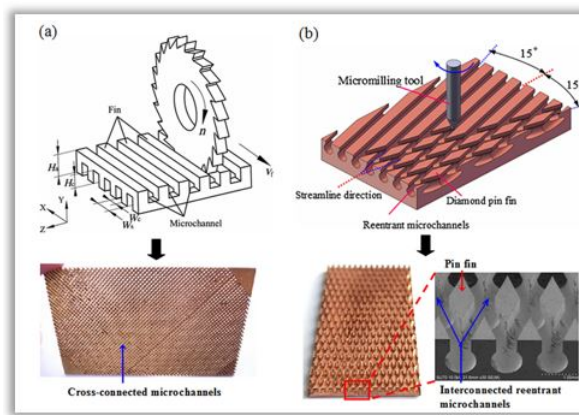


**Figure III.8** – Fabrication of enhanced microchannels [67].

Micro-mechanical cutting process (a) cross-connected microchannels by micromilling with a thin slotting cutter, (b).

## III.2.4 The flow and heat transfer through Microchannels

### III.2.4.1 Mean Free Path

The mean free path,  $\lambda$  is defined as the average distance traveled by gas molecules between successive collisions and is expressed as [68] :

$$\lambda = \frac{\mu}{p} \sqrt{\frac{2k_b T}{m}} \quad (\text{III.21})$$

Where  $\mu$  is the dynamic viscosity,  $P$  is the pressure,  $(K_b)$  is the Boltzmann constant ( $k_B = 1.38 \times 10^{-23} \text{ J/K}$ ),  $T$  is the temperature, and  $m$  is the mass of the gas molecule.

The temperature dependent dynamic viscosity can be determined as :



$$\mu = \mu_0 \left( \frac{T}{T_0} \right)^\omega \quad (\text{III.22})$$

Where  $T_0$ , is the reference temperature and  $\mu_0$  is the reference viscosity at the reference temperature ( $\mu_0 = 1.86 \times 10^{-5} \text{ Pa}\cdot\text{s}$  at  $T_0 = 273.15 \text{ K}$ ). The exponent  $\omega$  in Eq III.22 depends on the gas nature for the Variable Hard Sphere VHS intermolecular collision model. In this work, the Hard Sphere HS model will be used, leading to  $\omega = 0.5$  regardless of the gas nature.

### III.2.4.2 Knudsen Number and Regimes of Rarefaction

To determine the level of rarefaction of a gas, the Knudsen Number [68] :

$$Kn = \frac{\lambda}{L_c} \quad (\text{III.23})$$

defined as the ratio of the mean free path,  $\lambda$ , to the characteristic length of a system,  $L_c$ , is often employed. The characteristic length is typically the smallest length within the system. As the Knudsen Number increases, the gas becomes more rarefied. This can be achieved by decreasing the pressure (which increases the mean free path, see Eq III.23 and/or the characteristic length of the system.

Using the Knudsen number, four regimes of rarefaction can be characterized as shown in Fig III.9 These four regimes as follows [68] :

1. Continuum Regime ( $Kn \leq 10^{-3}$ ), where the Navier-Stokes and Convective Energy equations may be used with no-slip boundary conditions. In this regime, the number of collisions between molecules is high enough to assume equilibrium of the macroscopic properties (temperature, velocity, and pressure) between the gas and the wall at the interface.
2. Slip Regime ( $10^{-3} \leq Kn \leq 10^{-1}$ ), where the Navier-Stokes and Convective Energy equations still apply for gas far from the wall but slip boundary conditions should be employed at the gas-solid interface. In this regime, the number of collisions between the gas molecules and the walls is not sufficient to reach equilibrium, which causes a discontinuity in velocity, temperature, and partial pressure at the gas-solid interfaces.
3. Transitional Regime ( $10^{-1} \leq Kn \leq 10$ ), where the collisional Boltzmann equation must be used. The Navier-Stokes equation, even with slip boundary condition, is no longer capable of solving the flow and heat transfer in this regime. The mean free path and

characteristic length are of the same order of magnitude in this regime, which means that the number of molecule-molecule collisions is almost equal to the number of molecule-wall collisions. This is the most computationally expensive regime to model since there is still a large number of molecules to be solved using the Boltzmann equation.

4. Free Molecular Regime ( $Kn > 10$ ), where the collisionless Boltzmann equation can be used to solve for flow and heat transfer. At this high level of rarefaction, the flow is driven by molecule-wall collisions, since the mean free path is at least ten times larger than the characteristic length, which implies molecule-molecule collisions are rare to occur. Based on the internal pressure and characteristic length of UNF casks, Vacuum drying occurs in the slip regime. At this regime of rarefaction, the Navier-Stokes equation subjected to the slip boundary conditions can be used to model heat transfer.

### III.2.4.3 Gas flow regimes and main models

Usually, according to the range of the Knudsen number  $Kn$ , the gas microflows may be classified into four regimes : the continuum regime, the slip flow regime, the transitional regime and the free molecular regime. The appropriate models must be chosen according to the value of the Knudsen number. Figure III.9 presents the gas flow regimes and their main related models [69].

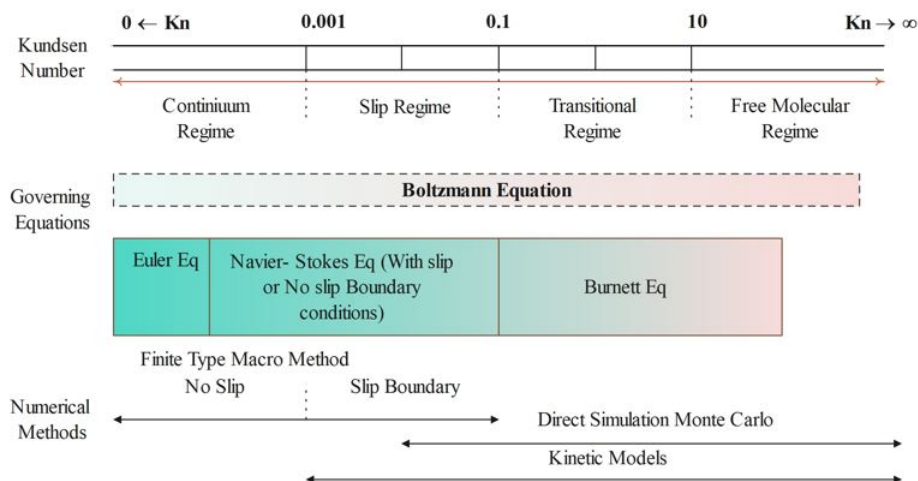


Figure III.9 – Gas flow regimes and main models according to the Knudsen number.

#### III.2.4.4 Thermal Accommodation Coefficient

One of the important parameters characterizing the interaction between gas molecules and the wall is the accommodation coefficient. The accommodation coefficient describes how a molecule is reflected from a wall upon collision. Several accommodations coefficients are used in the literature. In this thesis, the focus is on the Thermal Accommodation Coefficient (TAC), which is the fraction of energy exchanged with the wall. If a molecule collides with a wall, it will transfer a certain amount of its thermal energy to the wall. Based on this definition, the (TAC), also referred to as  $\alpha$ , can be expressed using the incident ( $T_i$ ) and reflected ( $T_r$ ) temperatures as [68] :

$$\alpha = \frac{T_i - T_r}{T_i - T_W} \quad (\text{III.24})$$

where  $T_W$  is the temperature of the wall . The (TAC) varies from 0 to 1, where a value of 0 corresponds to specular reflection (the molecule does not transfer any of its energy to the wall, or ( $T_r = T_i$ )). A value of 1 would mean that the reflection is diffuse, or the molecule fully accommodates to the energy of the wall . (TAC) values depend on several parameters, such as the wall material and its cleanliness, surface condition such as polishing, and the nature of the gas.

#### III.2.4.5 Temperature Jump

The temperature jump effect is shown visually in Figure III.10 If a solid is bounded on one side by a heater, and the other by gas, one can expect to see a temperature jump at the solidgas interface at low pressures. If the gas is not rarefied, then the temperature of the gas is the same as the temperature of the wall at the interface, and the temperature distribution in the solid will follow the dashed line. However, if the gas is rarefied (low pressure), there will be a discontinuity of temperature at the gas-solid interface, so that the gas temperature will be different from the wall temperature, as shown by the solid line in Figure III.10 This temperature discontinuity is called “temperature jump” and is defined as the difference between the gas and solid temperatures at their interface [68].

According to Smolan and Smoluchowski, the temperature jump can be written as [68] :

$$T_g - T_W = \zeta_t \lambda \left. \frac{\partial T}{\partial y} \right|_W \quad (\text{III.25})$$

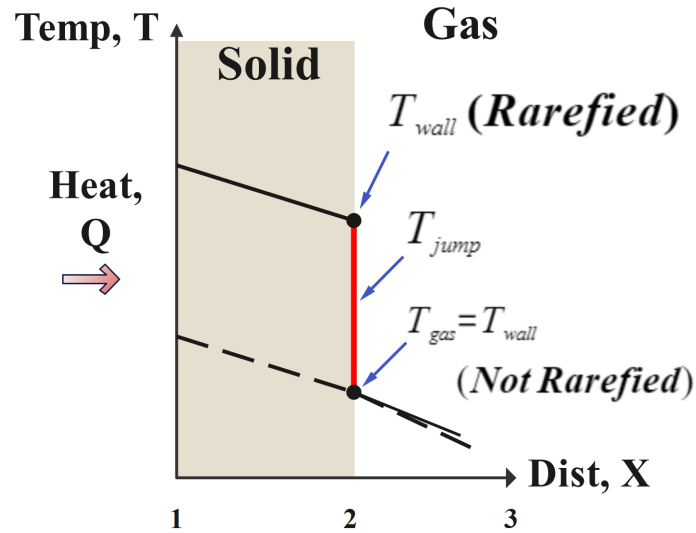


Figure III.10 – Temperature jump diagram.

where  $T_{\text{gas}}$  is the gas temperature, and  $\zeta_t$  in Eq III.25 is the temperature jump coefficient. The partial derivative term is the temperature distribution in the bulk of the gas.

### III.2.4.6 Slip flow regime

#### III.2.4.6.a Boundary conditions

Maxwell (Maxwell 1879) developed the theoretical basis for modeling the velocity slip at the wall. He postulated that when molecules collide with a surface, there are two possibilities [69] :

1. The molecules are reflected specularly and only change the direction of their normal velocity to the wall.
2. The molecules may have a more complex interaction with the surface and are reflected diffusely : the molecules leaving the surface scatter with an equilibrium Maxwellian distribution which is related to surface properties, such as the surface temperature and velocity.

Maxwell treated the reaction between molecules and surfaces as a combination of these two reflections. A fraction  $\alpha_\nu$  of the molecules reflects diffusely while the complementary fraction  $1 - \alpha_\nu$  of the molecules reflects specularly. The coefficient  $\alpha_\nu$  is generally called tangential momentum accommodation coefficient (TMAC), although Sharipov considers that the (TMAC) can be different from the fraction of the molecules reflected diffusely (Sharipov 2011). Based on a momentum balance, the famous Maxwell slip boundary was derived in the following form [69] :

$$u_{slip} = \frac{2 - \alpha_\nu}{\alpha_\nu} \lambda \left[ \frac{\partial u_s}{\partial n} - \frac{3}{2} \frac{\mu}{\rho T} \frac{\partial^2 T}{\partial s \partial n} \right]_{wall} + \frac{3}{4} \frac{\mu}{\rho T} \frac{\partial T}{\partial s} \Big|_{wall} \quad (\text{III.26})$$

where  $s$  and  $n$  denote the directions tangent and normal to the wall Figure III.11, respectively, and  $\rho$  is the gas density. The equation of Maxwell is generally cited in the literature under the form :

$$u_{slip} = \frac{2 - \alpha_\nu}{\alpha_\nu} \lambda \frac{\partial u_s}{\partial n} \Big|_{wall} + \frac{3}{4} \frac{\mu}{\rho T} \frac{\partial T}{\partial s} \Big|_{wall} \quad (\text{III.27})$$

The "no-slip" boundary condition is one of the cornerstones on which the mechanics of the linearly viscous liquid is built. In his original paper, Navier had proposed a slip boundary condition wherein the slip velocity depended linearly on the shear stress. Helmholtz and Pitrowski introduced the notion of the "coefficient of slip" (Gleitungskoeffizient) for the slip occurring adjacent to a wall. Kundt and Warburg studied the damping of a vibrating disk in a gas and found that the coefficient of slip was inversely proportional to the pressure.

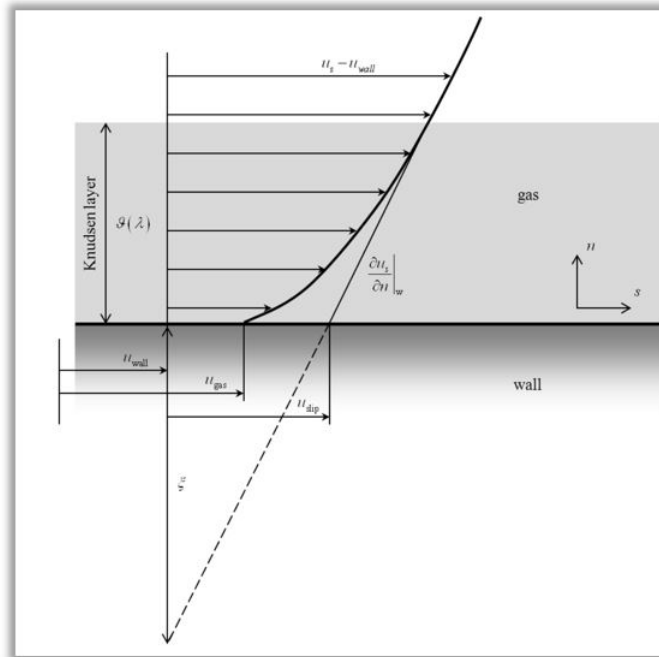


**Figure III.11** – Structure of the Knudsen layer and slip velocity [69].

The "no-slip" boundary condition is one of the cornerstones on which the mechanics of the linearly viscous liquid is built. In his original paper, Navier had proposed a slip boundary condition wherein the slip velocity depended linearly on the shear stress. Helmholtz and Pitrowski introduced the notion of the "coefficient of slip" (Gleitungskoeffizient) for the slip occurring adjacent to a wall. Kundt and Warburg studied the damping of a vibrating disk in a gas and

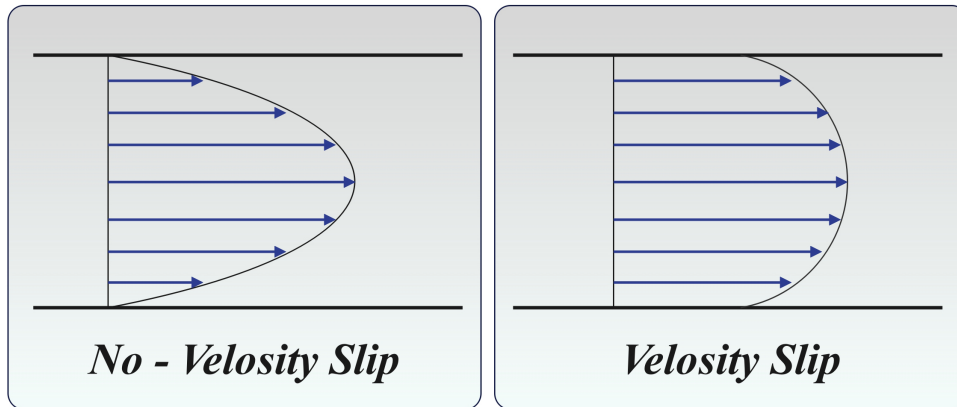


Figure III.12 – Velocity profile for Slip and No-slip.

found that the coefficient of slip was inversely proportional to the pressure [70].

### III.2.5 Configuration of optimized micro-channel heat sinks

Various types of copper foam fins were attached on a copper plate as optimized micro-channel heat sinks. The copper foam fins were glued to the copper plates with silicone grease. In this process, the contact area is very tight and the thermal resistance can be neglected under the working condition of heat sinks compared with brazed method and other assembly technology. Three types of copper foam fins were used here including the cube copper foam, column foam and strip copper foam, which are shown in Figure III.13. The bottom layer (gray) represents the copper plate. The upper layer (blue) represents the different copper foams. The colored arrows represent the various flow directions of air cooling [71].

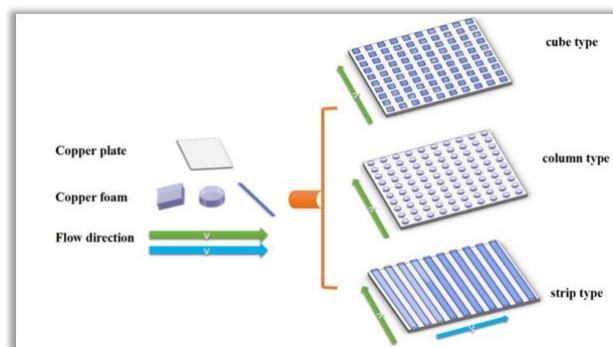


Figure III.13 – Configuration of different types of micro-channel heat sinks [71].

## III.3 Porous media and Magneto Hydrodynamics (MHD)

### III.3.1 Porous media

#### III.3.1.1 Introduction

By a porous medium we mean a material consisting of a solid matrix with an interconnected void. We suppose that the solid matrix is either rigid (the usual situation) or it undergoes small deformation. The interconnectedness of the void (the pores) allows the flow of one or more fluids through the material. In the simplest situation (single-phase flow) the void is saturated by a single fluid. In “two-phase flow” a liquid and a gas share the void space [72].

Forced convection heat transfer in porous media has many important applications such as geothermal energy extraction, catalytic and chemical particle beds, petroleum processing, transpiration cooling, solid matrix heat exchangers, packed-bed regenerators, and heat transfer enhancement. Therefore, fluid flow and convective heat transfer in porous media have received much attention for the past five decades.

There have been numerous investigations with experimental research, theoretical analysis, and numerical simulation of convection heat transfer in fluid saturated porous media. At the present time, the Darcy-Brinkman-Forchheimer model simultaneously considering the inertia and boundary effects is used in most numerical investigations of forced or mixed convection heat transfer in porous media [73].

#### III.3.1.2 Porosity

The volume fraction occupied by voids, i.e., the total void volume divided by the total volume occupied by the solid matrix and void volumes, is called the porosity. Each void is connected to more than one other pore (interconnected), connected only to one other pore (dead end), or not connected to any other pore (isolated). Fluid flows through the interconnected pores only. The volume fraction of the interconnected pores is called the effective porosity. In nonconsolidated media, e.g., particles loosely packed, the effective porosity and porosity are equal. In some consolidated media, the difference between the two can be substantial [74].

### III.3.1.3 Momentum Equation : Darcy's Law

We now discuss various forms of the momentum equation which is the porous medium analog of the Navier–Stokes equation. For the moment we neglect body forces such as gravity; the appropriate terms for these can be added easily at a later stage [72].

#### III.3.1.3.a Brinkman-Corrected Darcy's Law

Consider the simplest layout of flow in a parallel plate channel of length  $L$  and opening  $2H$ , filled with homogeneous isotropic porous media of permeability  $K$ , driven by an overall pressure difference. The governing equation for pressure reduces to :

$$\frac{d^2 p}{dx^2} = 0 \quad (\text{III.28})$$

The pressure variation is thus linear in the flow direction; using Darcy's law, the velocity components are evaluated as :

$$u = -\frac{K}{\mu} \frac{p_2 - p_1}{L}; \quad v=0 \quad (\text{III.29})$$

The velocity components predicted by Darcy's law are seen here to be independent of the axial coordinate and hence, fully developed. When the pressure difference changes with time, the x-component of velocity will change instantaneously, without any time lag. These results are not unexpected because the characteristic length scale that determines transient duration as well as the flow development is the pore diameter, which is a small quantity, relative to  $H$  and  $L$  [75].

#### III.3.1.3.b Forchheimer-Extended Darcy's Law

Darcy's law requires correction when the particle-diameter-based Reynolds number exceeds unity. Such a flow field is commonly encountered in high porosity systems where the fluid velocities are high. In gas flows, viscosity is low, and Reynolds numbers can once again exceed unity.

The immediate consequence of increasing Reynolds number is that form drag experienced by the particles of the solid phase becomes larger in relation to viscous drag. In the limiting case of high Reynolds numbers, form drag can be substantially larger than viscous drag [75].



III.3.1.4 Darcy’s Law : Permeability

Henry Darcy’s (1856) investigations into the hydrology of the water supply of Dijon and his experiments on steady-state unidirectional flow in a uniform medium revealed a proportionality between flow rate and the applied pressure difference. In modern notation this is expressed, in refined form, by Here  $\partial P/\partial x$  is the pressure gradient in the flow direction and  $\mu$  is the dynamic viscosity of the fluid. The coefficient  $K$  is independent of the nature of the fluid but it depends on the geometry of the medium. It has dimensions (length)<sup>2</sup> and is called the specific permeability or intrinsic permeability of the medium. In the case of single-phase flow, we abbreviate this to permeability [72].

$$u = -\frac{K}{\mu} \frac{\partial P}{\partial x} \tag{III.30}$$

III.3.1.5 Applications

The terms porous media refer to class of materials that contains connected, fluid-filled, pores within a solid matrix. Such a definition covers a wide range material used in a variety of engineering applications including, but not limited to, oil and gas exploration, fuel cells and batteries, soil and rock mechanics, and cardiovascular systems. The above applications rely on fluid flow, through the connected pores, often aided by heat and mass transfer phenomena. Understanding flow, heat, mass, and charge transfer through porous media, are, therefore, essential in the analysis of a variety of engineering applications Figure III.14 [75].

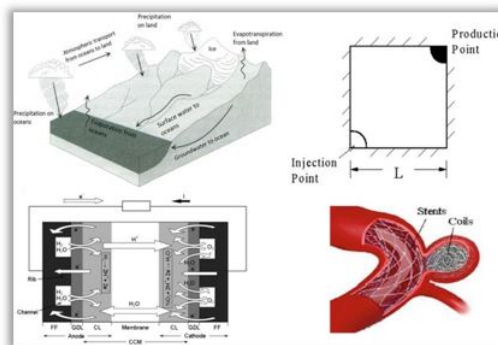


Figure III.14 – Schematic drawings of applications where porous media modeling is useful for analysis [75].

First row : left—groundwater flow ; right—immiscible displacement of oil by water ; second row : left—charge transfer in a fuel cell ; right—coils embolized in a cerebral artery.

### III.3.1.6 Thermal Equilibrium Model (LTE)

Many of the available research works on this topic have assumed Local Thermal Equilibrium LTE between the porous structure and the fluid inside it. In this case, only one heat equation would represent the thermal behavior of the porous medium and the fluid filling it. Employing the thermal equilibrium model of porous media, Basak et al. addressed different aspects of boundary conditions on the natural convection of a fluid-saturated porous medium in a cavity. Grosan et al. explored the effect of a magnetic field on the free convection heat transfer in an enclosure. Sun and Pop studied the natural convection in a triangular cavity. Very recently, Mehryan et al. considered the problem of free convection heat transfer of hybrid nanofluids in an enclosure filled with a porous medium using the LTE model of porous media [76].

### III.3.1.7 Thermal Non-equilibrium Model (LTNE)

The assumption of equal phase temperatures is equivalent to requiring the fluid and the solid media attain local thermal equilibrium quickly, in relation to the overall timescale of the transport process. This assumption is violated in several contexts and more so during rapid transients, namely when the timescale of the superimposed process is itself small [75].

An explicit treatment of individual phase temperatures is more general and will contain the approximation of thermal equilibrium as a special case. In view of this generality, the thermal non-equilibrium model is presented below. It is assumed that the porous medium has a solid phase coexisting with a single continuous fluid phase, leading to the two-equation model for temperature. These equations solve for the fluid and solid phase temperatures [75].

The respective equations will resemble the energy equations at the pure fluid and the pure solid limits with a point of difference. For the fluid medium, the solid particles at a distinct temperature will serve as an energy sink (or source, depending on the sign of the local temperature difference). One can imagine a hot fluid entering a cold porous region; a substantial part of the fluid energy will be spent in warming up the solid phase. This process requires a temperature difference and, clearly, a non-equilibrium model. The fluid–solid energy exchange term is thus central to the two-equation formalism. The fluid phase energy equation for temperature  $T^f$  is written as [75] :

$$\varepsilon(\rho C)_f \left( \frac{\partial T^f}{\partial t} + \frac{u}{\varepsilon} \cdot \nabla T^f \right) = k_f \nabla^2 T^f + Q_{f \leftarrow s} \quad (\text{III.31})$$

Similarly, the energy equation for the solid phase is written in terms of temperature  $T_s$  as :

$$(1 - \varepsilon)(\rho C)_s \left( \frac{\partial T^s}{\partial t} \right) = k_s \nabla^2 T^s + Q_{f \leftarrow s} \quad (\text{III.32})$$

### III.3.2 Magneto Hydrodynamics (MHD)

A MHD flow occurs, for instance when the Navier-Stokes governing equations are coupled with Maxwell ones and both electric conductivity and magnetization appear in the momentum and energy equations source terms, magnetic and electric fields are applied, perpendicularly to each other, across the height and width of a channel, a tube or even a micro-channel [77].

#### III.3.2.1 Magneto Hydrodynamics (MHD) Governing Equations

MHD governing equations are derived from the coupling between the Navier-Stokes equations and the Maxwell equations for electromagnetism. Assuming an incompressible and homogeneous flow, the Navier-Stokes continuity and momentum equations for a Newtonian fluid are [77] :

$$\frac{\partial \rho}{\partial t} + \rho(\nabla \cdot \mathbf{u}) = 0 \quad (\text{III.33})$$

$$\rho \frac{\partial \mathbf{u}}{\partial t} + \rho(\mathbf{u} \cdot \nabla) \mathbf{u} = \rho \mathbf{g} - \nabla p + \mu \nabla^2 \mathbf{u} + \mathbf{f} \quad (\text{III.34})$$

Introducing now the Maxwell equation :

$$\frac{\partial \mathbf{B}}{\partial t} = -\nabla \times \mathbf{E} \quad (\text{III.35})$$

The Low-frequency Maxwell equation :

$$\nabla \times \mathbf{B} = \mu_0 \mathbf{J} \quad (\text{III.36})$$

and the generalized Ohm's law for moving fluids :

$$\mathbf{J} \eta = (\mathbf{E} + \mathbf{u} \times \mathbf{B}) \quad (\text{III.37})$$

The set of MHD equations can be obtained.

In the MHD, the magnetic field acts through the Lorentz force ; which appears in the momentum equation [77] :

$$\rho \frac{\partial \mathbf{u}}{\partial t} + \rho(\mathbf{u} \cdot \nabla) \mathbf{u} = \rho \mathbf{g} - \nabla p + \mu \nabla^2 \mathbf{u} + \mathbf{f}_L \quad (\text{III.38})$$

$$\mathbf{f}_L = \mathbf{J} \times \mathbf{B} \quad (\text{III.39})$$

The Lorentz force expresses the action of the magnetic field on a moving charge ; therefore, if the fluid is electrically sensitive, the magnetic field generates a Lorentz force on it [77].

The current intensity  $\mathbf{J}$  is derived from the Ohm's law :

$$\mathbf{J} = \sigma(\mathbf{E} + \mathbf{u} \times \mathbf{B}) \quad (\text{III.40})$$

where  $\mathbf{B}$ , the magnetic flux density, satisfies the divergence-free constrain :

$$\nabla \cdot \mathbf{B} = 0 \quad (\text{III.41})$$

In absence of the electric field,  $\mathbf{E}$ , the current intensity  $\mathbf{J}$  is simplified as follow :

$$\mathbf{J} = \sigma(\mathbf{u} \times \mathbf{B}) \quad (\text{III.42})$$

And the Lorentz force becomes :

$$\mathbf{f}_L = (\mathbf{u} \times \mathbf{B}) \times \mathbf{B} \quad (\text{III.43})$$



# CHAPTER IV

## NUMERICAL PROCEDURE

- CFD
- Methodology CFD
- Ansys Presentation
- Mesh
- Simulation

## IV.1 Introduction

Computational fluid dynamics, usually abbreviated as **CFD**, is a branch of fluid mechanics that uses numerical analysis and data structures to solve and analyze problems related to fluid flows, heat transfer, and associated phenomena such as chemical reactions. **CFD** is an extremely powerful technique in the simulation that involves fluid flows which also spans a wide range of application areas including aerodynamics of aircraft and vehicles, electrical engineering, chemical process, marine engineering, environmental engineering, meteorology, biological engineering. There are many commercial **CFD** software used in engineering : **ANSYS-Fluent** is the most commonly used software [78].

**CFD** has been accepted as a design tool by many industrial users and is becoming a vital component in the design of industrial products. It was developed to provide a performance comparable to other Computer-aided Engineering **CAE** tools. **CFD** has been recognized as a common design tool in the wider industrial community since the 1990s with the availability of high-performance computing hardware and user-friendly interfaces (Versteeg and Malalasekera, 2007) [79].

**CFD** simulation can be set up easily and simulation can be done in far less time and expenses than that compared with the experimental work in the wind tunnel. In **CFD**, there is no limit on capacity and no limit on model scale. **CFD** offers several advantages over experimental approaches which are summarized as follows (Versteeg and Malalasekera, 2007) [78] :

- . Ability to do the simulation and study system where controlled experiments are difficult or impossible to perform e.g., very large system .
- . Reduction in the time and expense of design compared to experimental work.

- . Ability to assess a system under hazardous conditions e.g., safety studies and accident scenarios.
- . Gives unlimited level of detail of results.

## IV.2 Generalities on CFD

Computational Fluid Dynamics (CFD) is commonly assumed to be the complex science of predicting all parameters (thermal, mechanical, chemical and all related ones) of a fluid flow by computing a numerical solution of its governing equations, often called “Navier-Stokes” equations. The appearance of supercomputers and availability of strong and efficient CFD software such as ANSYS Fluent has led to its routine utilization in most engineering-related industries [80]. Such technology offers a wide range of advantages, among which [81] : A very low operating cost compared to experimental setups, constantly decreasing due to advancements in computer science.

- . Short computation time (varying from seconds to few days for more advanced problems).
- . Flexibility in physical modelling, allowing to extend focus on specific phenomena.
- . Comprehensive information within all parts of the simulated space. Despite this technology becoming more and more used in most engineering design industries involving fluid, few disadvantages can be noted, such as inaccuracies and instabilities due to the numerical modelling (discretization and physical models).

In practice, (CFD) simulation goes through several steps, listed as below [81] :

- Pre-processing (most critical for simulation success) where the solution domain is set, the mesh grid is generated, physical properties, models and boundary conditions are chosen and applied.
- Solving, where the software computes a solution.
- Post processing, where results are interpreted and displayed for easy use.

## IV.3 Areas of application of CFD

(CFD) analysis has applications in many sectors to design or improve systems or develop new products. Some of these are in [82] :

- . Automotive and aerospace industries.

- . Process and chemical industries.
- . Turbomachinery (fan, turbine, compressor, blowers and pumps, etc.).
- . Thermal and nuclear power plant.
- . Combustion, fire and environmental pollution.
- . Heating and ventilation of buildings, cars, buses and civil aircraft.
- . Weather forecasting.
- . Defense and space applications.
- . Biomedical applications.

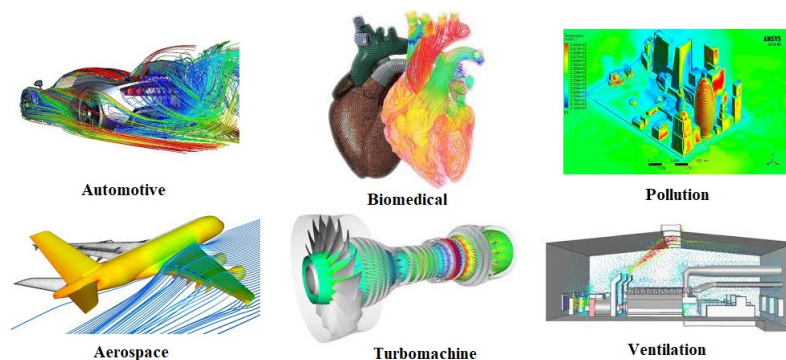


**Figure IV.1** – Some areas of application for CFD.

## IV.4 CFD simulation and meshing

### IV.4.1 Law of Fluid Motion

The (CFD) problems are stated in a set of mathematical equations and adequate boundary conditions and solved numerically. For the (CFD) problems related to fluid flow, these sets of mathematical equations are based on [78] :

- . **Conservation of Momentum** : the rate of change of momentum equals to the sum of forces on a fluid particle in (CFD), conservation of mass and conservation of momentum are expressed mathematically as a system of partial differential equations. These equations are the well-known Navier-Stokes equations together with the continuity equations (Drazin and Riley, 2006).
- . **Energy conservation equation** : The energy conservation equation is obtained from the first principle of thermodynamics [83].
- . **Conservation of mass** : the mass of the fluid is conserved.



### IV.4.2 Conservation of Momentum

Momentum conservation theory states that the rate of change of momentum of a fluid particle is equal to the sum of the forces on the fluid particle. The rate of change of momentum in x, y, and z-direction per unit volume i.e., force on each fluid particle is expressed as (Versteeg and Malalasekera, 2007) [78] :

$$\rho \frac{Du}{Dt}, \rho \frac{Dv}{Dt}, \rho \frac{D\omega}{Dt} \quad (\text{IV.1})$$

If we define the contribution of body force per unit volume by the term  $S_{mx}$ ,  $S_{my}$  and  $S_{mz}$  in x, y and z-direction respectively, then the momentum equations are given by (Versteeg and Malalasekera, 2007) :

$$\rho \frac{Du}{Dt} = \frac{\partial(-p + \tau_{xx})}{\partial x} + \frac{\partial(\tau_{yx})}{\partial y} + \frac{\partial(\tau_{zx})}{\partial z} + S_{mx} \quad (\text{IV.2})$$

$$\rho \frac{Dv}{Dt} = \frac{\partial(\tau_{xy})}{\partial x} + \frac{\partial(-p + \tau_{yy})}{\partial y} + \frac{\partial(\tau_{zy})}{\partial z} + S_{my} \quad (\text{IV.3})$$

$$\rho \frac{D\omega}{Dt} = + \frac{\partial(\tau_{xz})}{\partial y} + \frac{\partial(\tau_{yz})}{\partial x} + \frac{\partial(-p + \tau_{zz})}{\partial z} + S_{mz} \quad (\text{IV.4})$$

### IV.4.3 Energy conservation equation

The energy conservation equation is obtained from the first principle of thermodynamics and it can be written as [83] :

$$\underbrace{\frac{D(\rho c_p T)}{Dt}}_1 = \underbrace{\Delta(kT)}_2 + q + \underbrace{\beta T \frac{Dp}{DT}}_3 + \underbrace{\mu \phi}_4 = 0 \quad (\text{IV.5})$$

With :

- 1 : The total variation of energy (by accumulation and convection).
- 2 : The variation of energy by conduction.
- $q$  : Power density dissipated.
- 3 : The energy variation due to compressibility.
- 4 : Irreversible dissipation due to viscous friction.

$c_p$ ,  $k$ ,  $\beta$  are the heat capacity, the conductivity thermal and the isobaric coefficient of expansion of the fluid, respectively.

#### IV.4.4 Conservation of Mass

It states that the rate of increase of mass in an analytical space is equal to the net rate of flow of mass into that space [78].

The rate of increase of mass in the fluid element can be expressed as :

$$\frac{\partial}{\partial t} (\rho \delta x \delta y \delta z) = \frac{\partial \rho}{\partial t} (\rho \delta x \delta y \delta z) \quad (\text{IV.6})$$

Equating the rate of increase of mass in fluid element with the net rate of flow of mass into fluid element and dividing both sides by element volume ( $\delta x \delta y \delta z$ ) yields (Versteeg and Malalasekera, 2007) [78] :

$$\frac{\partial \rho}{\partial t} + \frac{\partial (\rho u)}{\partial t} + \frac{\partial (\rho v)}{\partial t} + \frac{\partial (\rho w)}{\partial t} = 0 \quad (\text{IV.7})$$

This relation can be expressed as the following mathematical form [78] :

$$\frac{\partial \rho}{\partial t} + \text{div} (\rho u) = 0 \quad (\text{IV.8})$$

This equation is the three-dimensional mass conservation or continuity equation for compressible fluid. The first term in the above equation is the rate of change of density, equal to zero in case of incompressible fluid ( $\rho$  constant) and the second term indicates the net flow of mass out of the element.

#### IV.4.5 Boussinesq approximation

The approximation of Boussinesq indicates an approximation of equations of Navier-Stokes for incompressible flows with free surface in which exists a gradient of density vertical resulting in the absence of hydrostatic equilibrium. This approximation is attributed to Boussinesq, but it was presented for the first time by Oberbeck [84].

Boussinesq's approximation consists of assuming that all the thermo-physical characteristics of fluids are constant and uniform, except in the density, it is assumed to vary linearly with temperature. The relation can be written as follows [83] :

$$\rho(T) = \rho_0 [1 - \alpha(T - T_0)] \quad (\text{IV.9})$$

This development in the first order is valid for many problems of natural and mixed convection since the temperature difference within the fluid always remains less than ten degrees,  $T$  represents the temperature of the fluid at a given point of the system,  $T_0$  is the reference temperature which generally corresponds to the mean value of the temperature of the system (operating temperature),  $\alpha$  is the coefficient of thermal expansion of the fluid and  $\rho_o$  is constant density of the fluid [83].

## IV.5 Methodology of CFD

(CFD) uses numerical methods and algorithms to solve and analyze problems related to fluid flow. Modeling in (CFD) is based on the fundamental law of fluid motion : conservation of mass and conservation of momentum. Commercial (CFD) packages are well structured with (CFD) codes and include a sophisticated user interface with the facility to provide problem parameters and to examine the results. All the codes in (CFD) contains three primary elements [78] :

1. pre-processor,
2. simulator or solver, and
3. post-processor,

At the preprocessor stage, the first step involved is to define a suitable geometry of the fluid problem. The fluid domain is then divided into smaller segments which are called as meshing of the fluid domain. The boundary condition of the fluid domain is then specified in this stage [78].

The solver stage is the calculation stage that leads to the solution of governing equations of fluid motion. Three techniques that are used to solve fluid problems are : finite difference method (FDM), finite element method (FEM), and finite volume method (FVM) [78].

After getting the results, the postprocessor stage is applied to analyze the results and provide with variety of plots. These include domain geometry and grid display, contour plot, vector plot, streamlines, 2D and 3D surface plots, animation for dynamic results, and so on [78].

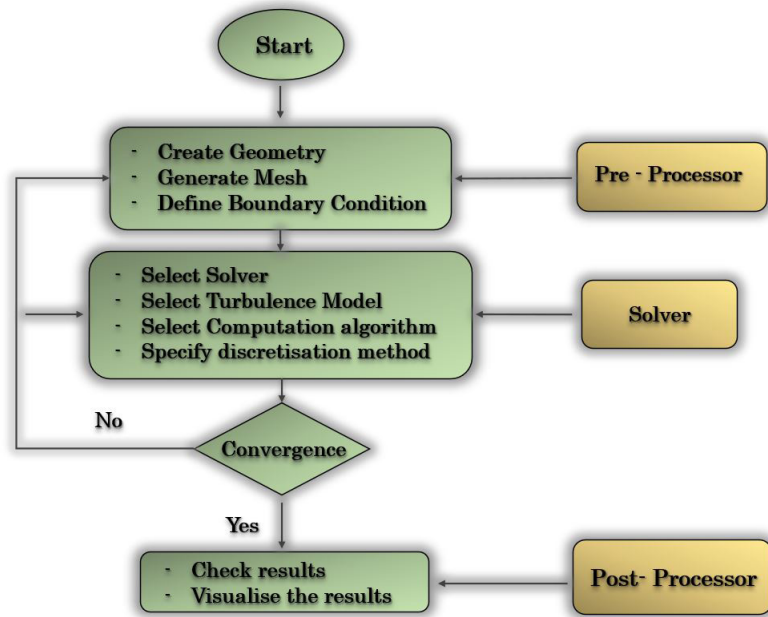


Figure IV.2 – Flow chart of CFD simulation

IV.5.1 The general method

A general overview of the followed procedure is seen in IV.3. The gradient of the cost function with respect to design variables, is computed when both a flow (Navies Stokes equations) and an adjoint simulation are fully converged. Based on the calculated sensitivity field, the morphing tool which modifies the boundary as well as the interior mesh inwards or outwards is applied. What follows, is the flow simulation of the morphed case and the loop of adjoint where the morphing tool iteratively runs until the optimum solution is obtained. Once the optimization is over, the boundary mesh is exported, wrapped and re-meshed in ANSA. This geometry is evaluated through a last flow simulation. The following Figure IV.3 illustrates the described methodology [79].

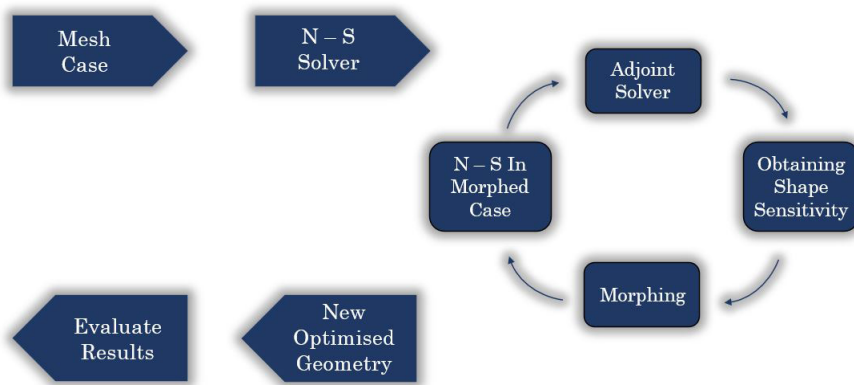


Figure IV.3 – Adjoint methodology.

The thesis is mainly focused on setting a robust loop procedure which results in a reliable adjoint solution. It is important that an adjoint loop is fed by an adequate mesh and flow solution which effect the loop iterations. For example, bad cell quality yield either in a diverged adjoint solution or in the appearance of negative volume cells during the initial and morphing loop step, respectively. In both cases, the loop breaks without providing any significant results. Moreover, the loop robustness is affected by adjoint and morphing setting that are presented on the upcoming pages [79].

### IV.5.2 Numerical methods

The objective of numerical methods is to provide a solution approach to the real behavior of physical phenomena. Among the most widely used numerical methods for solving partial differential equations numerically it can be mentioned as follows [83] :

- to finite difference method (FDM).
- to finite elements method (FEM).
- to finite volumes method (FVM).

The finite difference method presents a technic to solve partial differential equations, with approximating derivatives by finite differences. This method consists of subdividing the domain of study into a determined number of nodes and in representing the function searched in each of the nodes of the domain by a taylor series expansion. Thus, the differential equation is transformed into an algebraic equation for each node. On the other hand, the finite difference method (FDM) is simple and effective on structured grids and does not conserve momentum, energy, and mass on coarse grids. As for finite element method consists of transforming the differential equations into integral forms based on the concept of minimization of a quantity (such as energy...), leading to the exact solution. In other term, it is about finding a global function representing the mathematical model in the studied domain [83].

The fundamental principle of this method is consisted of [85] - subdividing the field of study into elementary regions (Finis Elements) and build the integral forms and also minimize the integral, then a matrix organization of calculations, in the last a resolution of the algebraic system. This method that helps for the resolution of partial differential equations especially in complex geometries. Its implementation, on the other hand, the finite element method (FEM) is used in structural analysis of solids, but is also applicable to fluids. It is the highest accuracy

on coarse grids. However, it is slow for large problems and not well suited for turbulent flow [83].

As for the finite volume method, it is widely used and is well suited to the resolution of conservation laws (mass, momentum, energy) also, it's a common approach used in (CFD) codes. One of its advantages is that the equations are calculated iteratively by imposing initial conditions and boundary conditions of the domain. The solver then seeks a solution of the fields of pressure, velocity, temperature, this method can be discussed in the next title [83].

#### IV.5.2.1 Finite volume method

The principle of the finite volume method is based on a discretization technique, whereby computation domain is divided into a finite number of elementary subdomains, called control volumes. In this method, it converts partial derivatives conservation equations into algebraic equations, which can subsequently be solved numerically [83].

The decisive advantage of this method over other methods is that it is distinguished by the reliability of its results and solution speed, its ability to deal with complex geometries, its guarantee for the conservation of mass and momentum, its adaptation to the physical problem. The technique of the control volumes consists of integration of partial derivatives equations on each control volume to obtain discretized equations. The different steps of the finite volume method is [83] :

- The discretization of the domain considered in control volume.
- Writing algebraic equations at the nodes of the mesh.
- Solving the algebraic system obtained.

An example of control volume is shown in the figure below [Figure IV.4](#). A point is positioned at the center of each and is called the control volume center, it will be denoted P (principal node), the nodes of neighboring volumes will be noted according to their positions [NSWET](#) and [B](#) (relating to the North, South, West, Top and Bottom directions respectively).

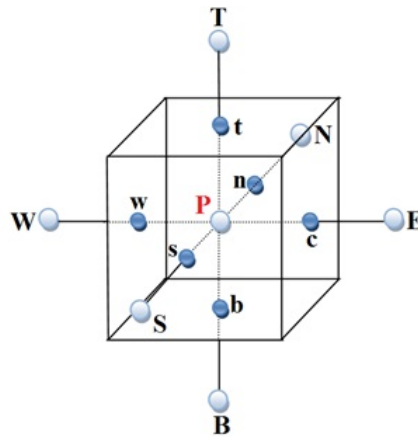


**Figure IV.4** – A cell or control volume in three dimensions [83].

#### IV.5.2.2 Finite Difference Method

The Finite Difference Method (FDM) was among the first methods and was utilized by Euler. It is directly applied to the differential equations using the Taylor series expansion to discretize the flow variables. The advantage of this method is its simplicity and ease to obtain high order approximations and hence accuracy [86].

The disadvantage is that it requires a structured grid and can-not be applied to body fitted grids which limits its applications. For more details on this method see the reference [87].

#### IV.5.2.3 Finite Element Method

The Finite Element Method (FEM) was originally developed for structural analysis, proposed in 1956 by Turner et al.. It can accommodate an unstructured mesh and the grid nodes are exclusively used to produce an arbitrarily high order of accuracy representation of the solution on smooth grids [87].

It works with an equivalent integral form of the governing equations, commonly accomplished based on the weak formulation. As this method uses an integral formulation and an unstructured grid, it is preferable for flows featuring complex geometry and is particularly suitable for non-Newtonian fluids. The finite element methods have a very rigorous mathematical foundation but can be shown to be mathematically equivalent to the finite volume method for certain cases and have a higher numerical expense [86].

## IV.6 Presentation of Ansys

ANSYS is a sophisticated and comprehensive finite element software package. It is useful in many different areas of physics, such as structural and thermal analysis, Ansys fluids, FLOTRAN and CFD. It can also be used to analyze coupled domains involving one or multiple type of these different kinds of physics. Ansys is an integrated program that allows all of these operations to be performed via a graphical user interface. Model creation and execution, as well as results postprocessing, can be done without leaving the Ansys environment. Because of its extremely fast, accurate and reliable numerical simulation tools, Ansys can be used to obtain accurate solutions to the problems encountered during the design and development of products. It allows organizations from all activity sectors to predict the performance of their products aftermarket launch. Ansys is a general-purpose software package for simulating interactions in all disciplines of physics, structural and vibrational analysis, and fluid dynamics, as well as heat transfer and electromagnetic analysis in engineering. Ansys allows designs to be tested in a virtual environment before a product prototype is manufactured. With Ansys, weaknesses can be identified and improved, the product lifetime can be computed, and likely issues can be predicted by conducting three-dimensional simulations in virtual environments [88].

Ansys is used by the following non-exhaustive list of industries : aerospace, automotive, biomedical, bridge and building engineering, electronics and appliances, heavy equipment and machinery, etc. It is important to note that the computer-Aided Design (CAD) aspect is not restricted to the finite element model itself, which is just a way of specifying to Ansys the positions of the nodes and the elements required to implement the finite element method. CAD consists of finding a mesh in order to create nodes and elements. The Finite Element Method (FEM) subdivides a structure into a number of elements (pieces of the structure), gives a simple description of the behavior of each individual element and then reconnects these elements together once again. This process is described by a set of simultaneous algebraic equations [88].

The key products associated with Ansys include [88] :

- **Ansys Structural** : this product allows mechanical simulations to be performed in order to compute structures. Its primary features are as follows :
  1. static analysis ;
  2. modal analysis ;
  3. harmonic analysis (forced response) ;



#### 4. temporal analysis ;

handling of various different nonlinear situations (contact, material plasticity, large displacements or deformations).

- **Ansys Mechanical** : this product has the same features as Ansys Structural with the addition of a thermal solver with radiation modeling.
- **Ansys CFX and Fluent** : these two software programs can be used to perform simulations in fluid mechanics. They bear the names of the companies that developed them, which were acquired by Ansys Inc. in **February 2003** and **February 2006**, respectively. Fluent is a solver : it does not include a mesher (the mesh must be constructed using meshing software, such as Gambit, which is also published by Ansys). The parameters of the model are configured using a graphical interface. A scripting interface is also available to automate the computation procedures. One of the advantages of this general-purpose simulation software is that it has a relatively large number of models that can be implemented to solve questions in fluid mechanics : diphasic flows (miscible, immiscible, cavitation, solidification), turbulence **LES, KE, Kw, SA, Reynolds stress**), combustion (premixed and non-premixed), particle transport, flows through porous media, mobile and dynamic meshes with mesh reconstruction and many others. The temporal and spatial numerical schemes of these models can be adjusted in order to improve their convergence. Fluent supports parallel processing and can take advantage of multiprocessor systems both on a single machine and over a network (cluster, dual core, multi-CPU platforms) [88] :
- **Gambit** : meshing software published by Ansys since **2006** (previously published by Fluent). This mesher allows custom geometries to be created with high levels of freedom and accuracy, or alternatively imported from a **CAD** file. It can also automatically mesh surfaces and volumes in parallel to the specification of boundary conditions. Gambit is often viewed as the gold standard for meshers by Fluent users.
- **Ansys AUTODYN and Ansys LS-DYNA** : these software packages have solvers that use explicit formulations for the equations to be solved, unlike the products listed above. Their scope of application is confined to models whose mechanics involve very large deformations.
- **Ansys Electromagnetics and Ansoft** : this product allows models involving electromagnetic phenomena to be solved.
- **Ansys Multiphysics** : this product combines all Ansys tools for implicit numerical simulations.
- Two software environments can be used to implement Ansys code :

- **Ansys Classic** : chronologically, this was the first software solution offered by the developers. It is designed for constructing finite element models with simple geometries that can easily be assembled from basic operations. Within this environment, the user directly builds finite element models using the scripting language i.e., Ansys Parametric Design Language (**APDL**). Ansys Classic is therefore oriented toward users with experience in numerical simulations.
- **Ansys Workbench** : this platform takes a different approach to model building by reusing the original Ansys code. It is particularly suitable for handling problems with complex geometries (many objects with pieces) and is accessible to users without experience in performing computations. In this environment, the user essentially works on the geometry of the model and not the model itself. The platform therefore fulfills the task of converting the commands specified by the user into Ansys code before launching the solving procedure. The finite element models generated in this way may, however, still be manipulated by inserting custom commands into the Ansys code.

#### IV.6.1 PERFORMING A SIMULATION IN ANSYS : FLUENT

**ANSYS** is a software suit that spans the entire range of physics, providing access to lots of fields of engineering simulation that a design process require. In particular, the module **FLUENT** is appropriate for this work. **FLUENT**'s models are focused on fluids flow and chemical reactions, including a very good model to run a first-approach simulations of combustion systems. In the next sections, it's explained the main characteristics of how to perform a simulation using **ANSYS FLUENT**. Starting, but not focusing, on the geometry and mesh creation, and continuing on how to set up the models and run the calculations. To perform a simulation in **ANSYS FLUENT**, the next steps are followed [79] :

- Design the geometry of the system.
- Discretise the geometry by generating an appropriated mesh.
- Set up the models to represent the reality adequately.
- Configure the calculation's parameters to run the simulation and obtain results.
- Results retrieval and visualization.

A summary of the fundamental methodology for building an **ANSYS FLUENT** solar **DASC** simulation is given in **Figure IV.6** below [89] :

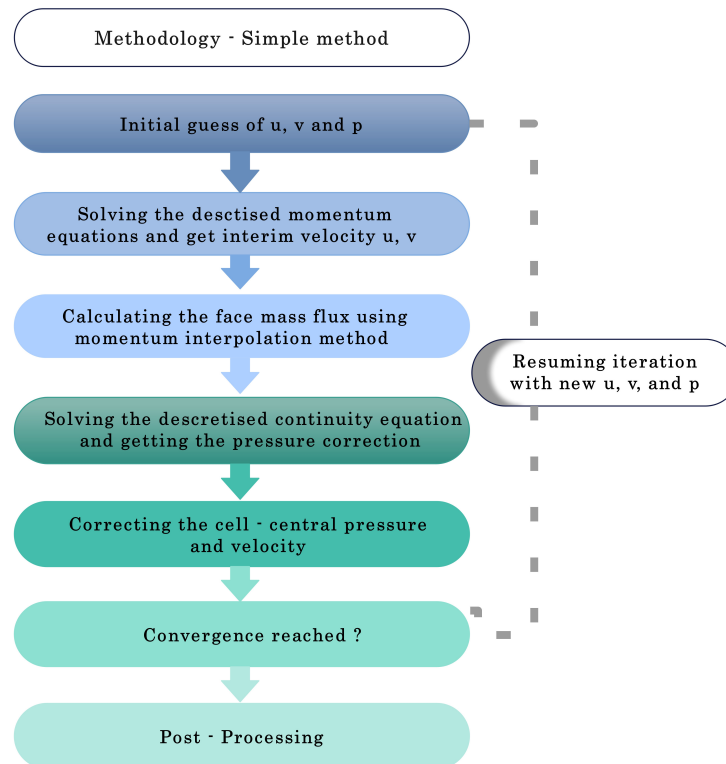


Figure IV.5 – Methodology of Simple Method.

## IV.6.2 Presentation of the GAMBIT software

The Gambit (Geometry and Mesh Building Intelligent Toolkit) software is a 2D/3D mesher ; a pre-processor that allows meshing of geometry domains of a CFD problem. It can generate a structured or unstructured mesh in Cartesian coordinates, polar, cylindrical or axisymmetric coordinates. It can produce complex meshes in two or three dimensions with rectangular or triangular meshes. Gambit's generation options offer flexibility of choice. The geometry can be broken down into several parts to generate a structured mesh. Alternatively, Gambit automatically generates an unstructured mesh that is suitable for the type of geometry being constructed. With the mesh verification tools, defects are easily detected.

It can be used to build a geometry and generate a mesh for it, or a geometry from another CAD software can be imported into this preprocessor. It generates .msh files for Fluent.



**Figure IV.6** – CFD ANSYS FLUENT Methodology for solving nanofluid DASC enclosure boundary value problem [89].

## IV.7 Mesh

The generation of the mesh (2D or 3D) is a very important phase in a CFD analysis, given its influence on the calculated solution. A very good quality mesh is essential for obtaining a precise, robust and meaningful calculation result. Good mesh quality is based on the minimization of elements with skewness, and on good "resolution" in regions with a strong gradient. In fact, the quality of the mesh has a serious effect on the convergence, the precision of the solution and especially on the computation time [83].

### IV.7.1 Mesh cell types

In CFD terminology, every control volume resulting from division of the domain is usually called a "cell". Many different types of cells have been developed, allowing for division of different type of geometries. Figure IV.7 below present the most common cell types used in CFD today. For commodity in the following parts of the thesis, tetrahedron and hexahedron shapes will be respectively referred to as "tetra" and "hexa" [80].

#### IV.7.1.1 Tetra Meshing

A Tetra mesher is an automatic tool used to directly mesh a CAD geometry without extra geometry manipulation and setup. The volume is then filled by tetra elements using one of many meshing algorithms. Smoothing tools are used to improve the mesh quality. Despite such mesh can be very convenient for complex geometries, it unfortunately does not perform very

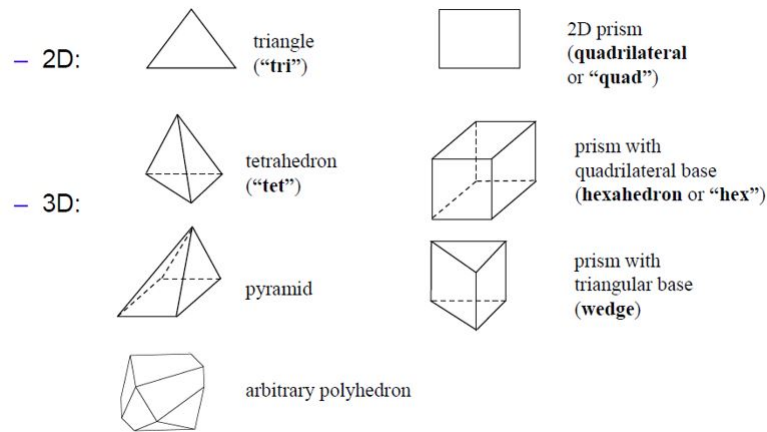


**Figure IV.7** – Main cell types used in CFD mesh generation software [80].

well to describe boundary layer physics and is very unstructured (one can even called “messy”) [80].

#### IV.7.1.2 Hexa Meshing

Hexa meshing is often considered as a more precise and efficient method, where only high quality hexa elements are used. This method is also more complex to use when the simulated space has unusual shapes [80].

#### IV.7.1.3 Hybrid Meshing

Compromise methods between tetra and hexa mesh exist, called (zonal) hybrid meshing. The goal is to use different methods in separate zones of the domain in order to compromise advantages of both tetra and hexa meshing. For example, in order to improve tetra mesher capabilities, some extra layers of prism or hexa cells can be generated close to the boundary layer in order to capture the physics of those flow parts [80].

The result is a hybrid Tetra / Prism mesh. Prism cells are generated or “inflated” from the triangular faces of the tetrahedral core.

After convergence, the solution must be independent of the density of the mesh to be sure of the realism of the solution [Figure IV.8](#). One must carry out a convergence test in mesh, by reporting the evolution of a variable, for example the temperature values (variable) according to the size of the mesh which one refines successively [83].

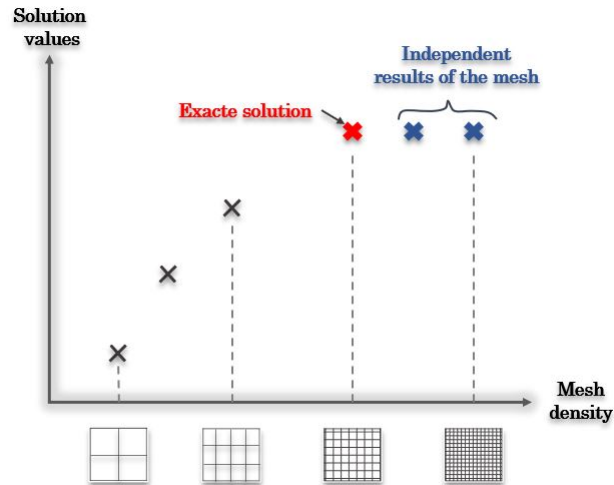


Figure IV.8 – Mesh convergence test.

## IV.8 Simulation

The main steps necessary to successfully simulate a problem in fluid mechanics using the Fluent software [83] :

1. Choice of solver.
2. Choice of laminar model.
3. Definition of the characteristics of the fluid.
4. Operating conditions.
5. Boundary conditions.
6. Choice of convergence criteria.
7. Initialization of calculations
8. Backups.
9. Starting of the simulation.

### IV.8.1 Defining boundary conditions

Boundary conditions of the fluid flow problem in CFD are used to define the limit of variable on the particular boundary, which implies that this condition is known. Defining the suitable boundary condition in CFD is almost close to the experiments. Naming of different boundaries has been done after the meshing of the solution domain and then boundary condition is applied to them. Users should define these boundary conditions correctly and understand their role in

the numerical analysis of the fluid flow problem. There are several boundary conditions as below [78] :

1. **Inlet boundary condition** : Flow variable distribution is specified at the inlet boundary. Uniform fluid flow velocity is known at the inlet of the solution domain, therefore it is specified as velocity inlet. Inlet is perpendicular to the x-direction. There are three velocity specification methods in ANSYS-Fluent : Magnitude (Normal to Boundary), Components, and Magnitude and direction. Apart from the velocity of the fluid, the specification of turbulence parameters is required at the inlet boundary condition.
2. **Outlet boundary condition** : If the location of the outlet is chosen far away from the geometrical disturbance, the flow eventually reaches a fully developed condition and pressure at the outlet is equal to atmospheric pressure. The outlet is specified as a pressure outlet.
3. **Wall boundary condition** : The wall is the most common boundary in the fluid flow problems. Free slip boundary condition is employed for the upper and lower wall and no-slip boundary condition is employed for the cylinder wall. Wall roughness is also defined in wall boundary condition. For the smooth wall, the roughness height is zero. For the rough wall, roughness is defined in terms of equivalent sand roughness and roughness constant.
4. **Symmetry boundary condition** : This boundary condition is a great tool to reduce the computational effort if the flow is symmetrical about a plane or pair of planes.
5. **The constant pressure boundary condition** : In the situations where exact details of the flow distribution is not known but the value of pressure at the boundary is known, this boundary condition is applied.
6. **Periodic or cyclic boundary condition** : This boundary condition is applied in the fluid flow problem in the presence of different types of symmetry and periodically repeating pattern of flow.

## IV.8.2 Convergence Criteria

Scaled residuals for momentum, continuity, turbulence, and volume fraction equations are monitored and our solution is considered converged when they all reach a value below  $10^{-5}$ . However, this criterion alone is not always reachable because it might never be fulfilled even though the solution is valid in some cases. Therefore, some parameters are being monitored besides the scaled residuals (for example local void fraction peak in the pipe, average velocities) and when both scaled residuals and our parameters reach constant values over a large number

of iterations, our solution can be considered converged [90].

#### IV.8.2.1 Evaluation Criteria

Results from a numerical simulation can be judged based on the following three different criteria [90] :

- **Accuracy** : it means how our different models succeeded in predicting some parameters like void fraction, phase velocities.
- **Computational time** : It evaluates how much time is needed by a certain model to converge.
- **Stability** : It measures how difficult it was to obtain a converged solution using a certain model.

#### IV.8.3 Solution Algorithms for Pressure-Velocity Coupling Equation

In solving the governing transport equations of fluid flow, the velocity component appearing in both momentum and continuity equation, and the pressure component appearing in the momentum equation are needed to be solved first. So, these momentum and continuity equations are intricately coupled with each other. If the pressure gradient is known, solving these equations would be easier, but in most of the cases, the pressure gradient is not normally known beforehand. In these cases, pressure and velocity are coupled with each other i.e., if the correct pressure field is applied in the momentum equations, the velocity obtained from that must satisfy the continuity equation. This pressure-velocity linkage can be solved by various iterative approaches : **SIMPLE** algorithm, **SIMPLER** algorithm, **SIMPLC** algorithm, **PISO** In these algorithms, the guessed pressure field is used to solve the momentum equation of fluid flow, then the continuity equation is solved to obtain the pressure correction field which is used to update the values of pressure and velocity fields. Initially, a certain value of velocity and pressure are assumed in these algorithms, which are continuously improved as the algorithm proceeds. This process continues until there is the convergence in velocity and pressure fields which yields the correct value of velocity and pressure at the end [78].



### IV.8.3.1 SIMPLE Algorithm

The **SIMPLE** algorithm was developed by Patankar and Spalding(1972) which stands for Semi-Implicit Method for Pressure-Linked Equations. In this method, a pressure field is initially guessed and that guessed value of pressure is used in the momentum equation of fluid flow to obtain the value of velocity. The pressure correction equation is solved and then the corrected value of pressure and velocities are obtained. These values are now used as an initial value and repeat the process. This process is continued until there is the convergence which yields the value of velocity that satisfies the continuity equation [78].

### IV.8.3.2 SIMPLER Algorithm

This algorithm is the improved version of the **SIMPLER** algorithm of Patankar (1980). In this method, the continuity equation is used directly to obtain an intermediate pressure field instead of using a pressure correction equation as in the **SIMPLE** algorithm. For the iteration, velocities are obtained from velocity correction equations. This algorithm is also continued until there is convergence [78].

### IV.8.3.3 SIMPLEC Algorithm

The **SIMPLEC** algorithm of Van Doormall and Raithby (1984) has the same steps as the **SIMPLE** algorithm. This method is different from the **SIMPLE** algorithm in the way that it manipulates the momentum equations where the less significant terms are omitted. The sequence of performance is the same as that of the **SIMPLE** algorithm [78].

### IV.8.3.4 PISO Algorithm

**PISO** algorithm is a pressure-velocity calculation procedure which was originally developed for non-iterative computation of unsteady compressible flows by Issa (1986). It has been improved for the iterative solution of steady-state problems as well. **PISO** means Pressure Implicit with Splitting of Operators and is the extended version of the **SIMPLE** algorithm. This algorithm has one predictor step and two corrector steps, unlike the **SIMPLE** algorithm which has one predictor and one corrector step. In the predictor step of **PISO**, momentum equations are solved with a guessed pressure field to get the velocity components. In the first corrector step of **PISO**, the velocity correction equation is used to calculate velocity components which are then used in the pressure correction equation that yields the pressure correction field. This is called the first

pressure correction equation. The new velocity components can be obtained using the calculated pressure correction field. These two steps are the same as the **SIMPLE** algorithm. The second corrector step is used in **PISO** to improve the **SIMPLE** algorithm. In the second corrector step, the second pressure correction equation is solved, and twice corrected value of pressure and velocity components are obtained. These values are now used as initial values and repeat the process. The pressure correction equation is solved twice in **PISO**, so it requires additional storage [78].

#### IV.8.4 Grid Resolution

A particular emphasis should be placed on choosing the best grid resolution in the numerical simulation. The spatial resolution must be sufficiently fine to ensure that the results are independent of the mesh quality, for limiting the grid resolution influences the accuracy and reliability of the predicted results. As a result of the independence grid study, the grid resolution of  $400 \times 200$  gridpoints in the axial and radial directions **Figure IV.9**, respectively, turns out to be adequate grid resolution over the abovementioned conditions. This mesh is considered a suitable grid resolution and a good compromise between the required precision and **CPU** time.

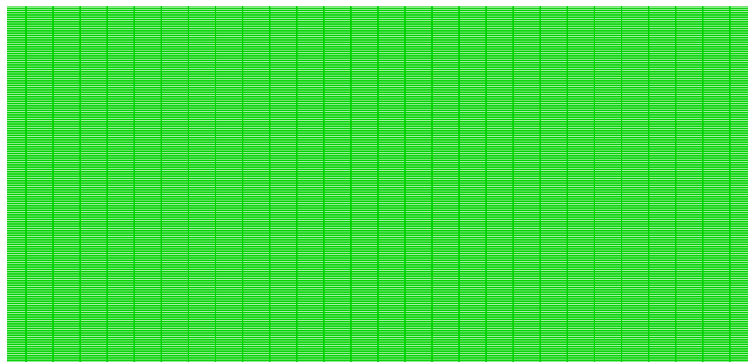


**Figure IV.9** – The Grid Resolution.

A person wearing a white turban is shown from the chest up, with a blue glow effect applied to the image. The person's face is partially visible, looking slightly to the right. The background is dark, and the overall aesthetic is modern and artistic.

# CHAPTER V

## RESULTS AND DISCUSSIONS

# RESULTS AND DISCUSSIONS



## V.1 Introduction

Microchannels are used in several industries and equipment, such as the cooling of electronic packages, microchannel heat sinks, microchannel heat exchangers, microchannel fabrication, and different device cooling and heating. In recent years, research on characteristics of flow and heat transfer behaviour in microchannels has gotten great attention Sing et al. [35](2012), Akbari et al. [37](2016). More recently, Magnetism and microfluidics have been combined in an amazing variety of ways by using magnetic fields, which are usually applied from outside the channel Afrand et al. [50] (2016), Karimipour et al. [51] (2016), Madhu et al. [54] (2019). Magnetohydrodynamic MHD is the mutual interaction between the magnetic fields and electrically conducting fluids flow used for pumping, controlling and mixing fluids, as well as incorporating switches and valves into lab-on-a-chip devices. The flow behaviour of non-Newtonian fluid is of high interest in many areas of science and technology. The fluid rheological behaviour must be considered in practical applications for electroosmosis, such as sample collection, detection, mixing, and separation of various biological and chemical species on a chip integrated with fluidic pumps and valves. Non-Newtonian fluids' relevance in predicting the rheological behaviour of many naturally occurring processes can't be ignored. At present, a rich amount of literature is available on flow characteristics of non-Newtonian fluids in microchannels Shamsi et al. [56] (2017), Javidi Sarafan et al. [59] (2020). The primary purposes of the present investigation are to look for the best heat transfer efficiency configuration of the heat sink microchannel. This research also seeks to determine and reveal the effects of heater length, Knudsen number, Darcy number, medium porosity, flow behaviour index, Hartmann numbers, and magnetic field inclination angle on the momentum and heat transfer characteristics via offering and discussing the different statistical quantities such as the local and average Nusselt numbers, velocity profiles, and temperature profiles carefully.

The primary purposes of the present investigation are to look for the best heat transfer efficiency configuration of the heat sink microchannel. This research also seeks to determine and reveal the effects of heater length, Knudsen number, Darcy number, medium porosity, flow behaviour index, Hartmann numbers, and magnetic field inclination angle on the momentum and heat transfer characteristics via offering and discussing the different statistical quantities such as the local and average Nusselt numbers, velocity profiles, and temperature profiles carefully.

## V.2 Problem description

The present investigation is devoted to analysing momentum and heat transfer characteristics of a two-dimensional steady laminar incompressible flow MHD forced convection heat transfer of Cu- $Al_2O_3$ / hybrid water nanofluid and power-law fluid. The considered geometry of the studied problem is a porous rectangular microchannel of length (L) and height (H) subjected to a uniform external magnetic field  $B_0$  applied along the x-axis inclined by an angle of  $\alpha$  from the x-axis. Furthermore, the induced magnetic field is ignored since this magnetic Reynolds number is considered low compared to the applied magnetic field. The porous medium is modelled by employing the Brinkman-Darcy model with a local thermal equilibrium (LTE) approach between the working fluid and the porous matrix for energy transfer.

As shown in Figure V.1, the heat source attached to the upper and lower enclosure walls is parameterised with length (B) values of 5, 10, 20, and 30, and it is subjected to constant heat flux (q) and the remaining parts of the walls are thermally insulated. The first configuration is a fully saturated metal foam occupied by a Cu- $Al_2O_3$ / hybrid water nanofluid with a concentration of 1%. In the second configuration Figure V.2, the multi-layered is used to enhance the heat transfer mechanism; the power-law fluid occupies the upper layer without a porous medium, and the power-law fluid saturates the lower layer through porous media with flow behaviour index of (0.2, 0.4, 0.6, 0.8, 1, 1.2, 1.4, 1.6, and 1.8). A slip velocity boundary condition is also imposed on the walls.

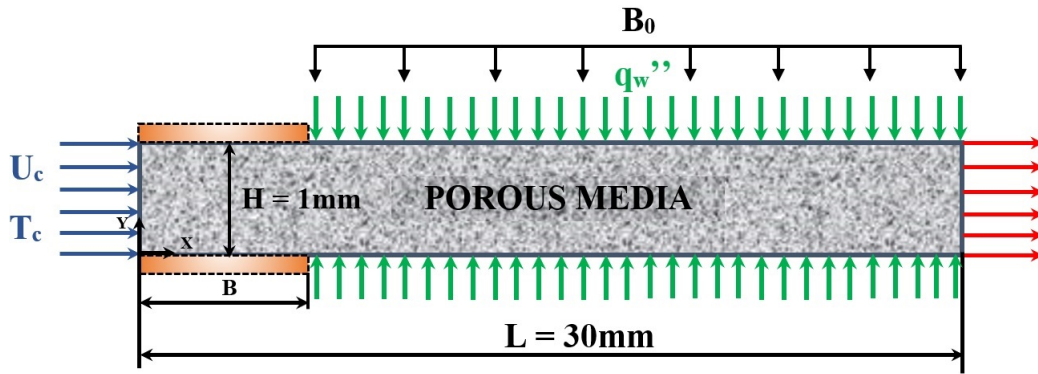


Figure V.1 – The schematic of the studied microchannel.

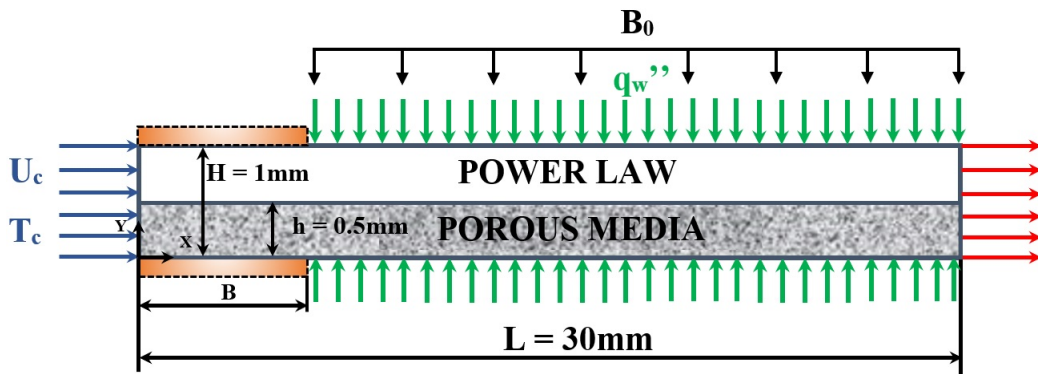


Figure V.2 – The schematic of the studied microchannel of power law.

## V.3 Governing Equations

### V.3.1 Fundamental flow equations

The Navier–Stokes equations were applied as the governing equations for the studied flow region. The effect of the porous material was included as loss terms in the momentum equation. The physical properties of the porous material were considered as a function of porosity, fluid properties and solid material properties. The fluid flow was expressed via three equations : the continuity equation, the Navier–Stokes momentum equations and the energy equation.

### V.3.2 Continuity equation

The continuity equation is based on the conservation of mass principle. According to this equation, the mass entering a control volume equals that exiting that control volume. The final form of the continuity equation applied to any control volume within a two-dimensional steady-state flow field with constant fluid density is obtained as :

$$\frac{\partial}{\partial x} (\rho_n f u) + \frac{\partial}{\partial y} (\rho_n f v) = 0 \quad (\text{V.1})$$

### V.3.3 Momentum equations

The second principal law of mechanics is Newton's second law. Two types of forces can be applied to a fluid : body forces which are proportional to the fluid volume and surface forces which are proportional to the fluid surface. The general form of Newton's second law for an arbitrary control volume is :

$$\frac{\partial}{\partial x} (\rho_{nf} u u) + \frac{\partial}{\partial y} (\rho_{nf} u v) = -\frac{\partial p}{\partial x} + \frac{\partial}{\partial x} \left( \mu_{nf} \frac{\partial u}{\partial x} \right) + \frac{\partial}{\partial y} \left( \mu_{nf} \frac{\partial u}{\partial y} \right) - \frac{\mu_{nf} u}{K} + \frac{\sigma_{nf} \sin \alpha B_0^2}{\rho_{nf}} u \quad (\text{V.2})$$

$$\frac{\partial}{\partial x} (\rho_{nf} u v) + \frac{\partial}{\partial y} (\rho_{nf} v v) = -\frac{\partial p}{\partial y} + \frac{\partial}{\partial x} \left( \mu_{nf} \frac{\partial v}{\partial x} \right) + \frac{\partial}{\partial y} \left( \mu_{nf} \frac{\partial v}{\partial y} \right) - \frac{\mu_{nf} v}{K} - \frac{\sigma_{nf} \cos \alpha B_0^2}{\rho_{nf}} v \quad (\text{V.3})$$

### V.3.4 Energy equation

The energy equation can be used to obtain the temperature distribution for a given flow field. According to the first law of thermodynamics, the net energy change in a given control volume is always equal to the (algebraic sum of) the energy transferred across that control volume boundaries in the form of heat and work :

$$\frac{\partial}{\partial x} (\rho_{nf} c_{nf} u T) + \frac{\partial}{\partial y} (\rho_{nf} c_{nf} v T) = \frac{\partial}{\partial x} \left( k_{nf} \frac{\partial T}{\partial x} \right) + \frac{\partial}{\partial y} \left( k_{nf} \frac{\partial T}{\partial y} \right) \quad (\text{V.4})$$

The above equations form a system of nonlinear differential equations with four unknowns, namely, P, v, u and T. The pressure field P is not directly observed in the continuity equation, but indirectly affects this equation because the velocity obtained from the pressure field must satisfy the continuity equation. Eq V.1 to Eq V.4 are written in dimensionless forms as follows to examine the results :

$$\frac{\partial}{\partial X} (U) + \frac{\partial}{\partial Y} (V) = 0 \quad (\text{V.5})$$

$$\frac{\partial}{\partial X} (UU) + \frac{\partial}{\partial Y} (VU) = \frac{\partial P}{\partial X} + \frac{\partial}{\partial X} \left( \frac{\partial U}{\partial X} \right) + \frac{\partial}{\partial Y} \left( \frac{\partial U}{\partial Y} \right) - \frac{U}{Da \text{ Re}} + \frac{\sin \alpha Ha^2}{\text{Re}} U \quad (\text{V.6})$$

$$\frac{\partial}{\partial X} (UV) + \frac{\partial}{\partial Y} (VV) = \frac{\partial P}{\partial Y} + \frac{\partial}{\partial X} \left( \frac{\partial V}{\partial X} \right) + \frac{\partial}{\partial Y} \left( \frac{\partial V}{\partial Y} \right) - \frac{V}{Da \text{ Re}} - \frac{\cos \alpha Ha^2}{\text{Re}} V \quad (\text{V.7})$$

$$\frac{\partial}{\partial X} (U\theta) + \frac{\partial}{\partial Y} (V\theta) = \frac{1}{\text{Re Pr}} \left( \frac{\partial^2 \theta}{\partial x^2} \right) + \frac{1}{\text{Re Pr}} \frac{\partial}{\partial Y} \left( \frac{\partial \theta}{\partial Y} \right) \quad (\text{V.8})$$

In Eq V.5 – Eq V.8, the dimensionless numbers are all written with respect to the properties of the nanofluid, i.e.,  $Re = \frac{\rho_{bf} u_b h}{\mu_{bf}}$   $Pr = \frac{v_{bf}}{\alpha_{bf}}$   $Ha = B_0 h \left( \frac{\sigma_{bf}}{\mu_{bf}} \right)^{0.5}$  The following dimensionless parameters are also used in Eqs. (5–8).

$$X = \frac{x}{h} \quad Y = \frac{y}{h} \quad U = \frac{u}{u_b} \quad V = \frac{v}{u_b} \quad P = \frac{p}{\rho_{bf} u_b^2} \quad \theta = \frac{T - T_C}{\Delta T} \quad \Delta T = \frac{q''_0 h}{K_{bf}} \quad (V.9)$$

## V.4 Thermophysical properties of hybrid nanofluid

In the dimensionless governing Eq V.5 Eq V.8,  $U$  and  $V$  are the velocity components in dimensionless coordinates in  $X$  and  $Y$  directions,  $\theta$  is nondimensional temperature,  $P$  is non-dimensional fluid pressure,  $\varepsilon$  is the porosity of porous media, and  $g$  is the acceleration due to gravity. The thermophysical properties are presented by the subscript  $hnf$  for the hybrid nanofluid. All these properties are estimated on the basis of a mixture of  $Cu$  and  $Al_2O_3$  hybrid nanoparticles volumetric concentration ( $\varphi$ ) in the pure fluid, so that :

$$\varphi = \varphi_{Al_2} + \varphi_{Cu} \quad (V.10)$$

The subscripts  $f$  and  $s$  are utilized for denoting the thermophysical properties for the pure fluid and the solid nanoparticles, respectively.

The effective density  $\rho_{hnf}$ , specific heat capacity  $(cp)_{hnf}$ , thermal expansion coefficient of the hybrid nanofluid are expressed by :

$$\rho_{hnf} = (1 - \phi) \rho_f + \phi_{Al_2O_3} \rho_{Al_2O_3} + \phi_{Cu} \rho_{Cu} \quad (V.11)$$

$$(\rho cp)_{hnf} = (1 - \phi) (\rho cp)_f + \phi_{Al_2O_3} (\rho cp)_{Al_2O_3} + \phi_{Cu} (\rho cp)_{Cu} \quad (V.12)$$

$$(\rho \beta)_{hnf} = (1 - \phi) (\rho \beta)_f + \phi_{Al_2O_3} (\rho \beta)_{Al_2O_3} + \phi_{Cu} (\rho \beta)_{Cu} \quad (V.13)$$

The hybrid nanofluid thermal diffusivity is expressed as :

$$\alpha_{hnf} = \frac{k_{hnf}}{(\rho cp)_{hnf}} \quad (V.14)$$

The effective dynamic viscosity of the hybrid nanofluid is expressed following the classical Brinkman model as :



$$\mu_{hnf} = \frac{\mu_f}{(1 - \phi)^{2.5}} \quad (V.15)$$

Furthermore, the effective electrical conductivity of the hybrid nanofluid is calculated following the Maxwell model

$$\sigma_{hnf} = \sigma_f \left[ 1 + \frac{3 \left( \frac{\sigma_s}{\sigma_f - 1} \right) \phi}{\left( \frac{\sigma_s}{\sigma_f + 2} \right) - \left( \frac{\sigma_s}{\sigma_f - 1} \right) \phi} \right] \quad (V.16)$$

Where :

$$\phi \sigma_s = \phi_{Cu} \sigma_{Cu} + \phi_{Al_2O_3} \sigma_{Al_2O_3} \quad (V.17)$$

The effective thermal conductivity could be obtained by the Maxwell model as :

$$k_{hnf} = k_f \left[ \frac{(k_s + 2k_f) - 2\phi(k_f - k_s)}{(k_s + 2k_f) + \phi(k_f - k_s)} \right] \quad (V.18)$$

where

$$\phi k_s = \phi_{Cu} k_{Cu} + \phi_{Al_2O_3} k_{Al_2O_3} \quad (V.19)$$

In the above equations, the thermal conductivities of Cu and  $Al_2O_3$  and the pure fluid nanoparticles are expressed  $k_{Cu}$ ,  $k_{Al_2O_3}$ , and  $k_f$ , respectively. Such expressions have been used by many researchers as reported in the published literature. However, in reality, such classical models fail to accurately estimate the thermal conductivity (Maxwell model) as well as viscosity (Brinkman model) of the  $CuAl_2O_3$ /water hybrid nanofluid. In order to get the correct effective thermal conductivity and viscosity for the hybrid nanofluid, the available experimental data are utilized in the present study, which are tabulated in Table V.1 for  $\phi = 0.001, 0.02$ . However, for extending the present numerical study, we have extrapolated the data little bit for a range of hybrid nanoparticles volume fraction  $\phi = 0.03, 0.05$ , which are indicated in the last three rows of Table V.1. The overall heat transfer characteristics, the quantity of physical interest, are evaluated by calculating the average Nusselt number (Nu) at the bottom heated wall, which can be written as :

$$Nu = \frac{k_{hnf}}{k_f} \int_0^1 \left( -\frac{\partial \theta}{\partial Y} \Big|_{Y=0} \right) dX \quad (V.20)$$

## V.5 Boundary conditions

It is clear that the non-slip boundary condition should be used at the macroscopic level. However, the slip boundary condition must be used in the slip flow regime in a microchannel which indicates the presence of slippage (slip velocity) in the fluid particles on the microchannel wall. The slip velocity value is estimated by the following equation :

$$u_c = \pm\beta \left( \frac{\partial u}{\partial y} \right)_{y=0,h} \quad (\text{V.21})$$

where,  $\beta$  represents the slip coefficient. The dimensionless form of the Eq V.11 on the wall is :

$$u_c = \pm\beta^* \left( \frac{\partial U}{\partial Y} \right)_{y=0,1} \quad (\text{V.22})$$

where,  $\beta^* = \frac{\beta}{h}$  is the dimensionless slip coefficient. Other dimensionless boundary conditions are as follows :

$$U = 1 \quad , \quad V = \theta = 0 \quad \text{at} \quad X = 0 \quad , \quad 0 \leq Y \leq 1 \quad (\text{V.23})$$

$$V = 0 \quad , \quad \frac{\partial U}{\partial X} = 0 \quad \text{at} \quad X = 30 \quad , \quad 0 \leq Y \leq 1 \quad (\text{V.24})$$

$$V = 0 \quad , \quad U = U_S \quad , \quad \frac{\partial \theta}{\partial Y} = 0 \quad \text{at} \quad Y = 0 \quad , \quad 0 \leq X \leq 30 \quad (\text{V.25})$$

$$V = 0 \quad , \quad U = U_S \quad , \quad \frac{\partial \theta}{\partial Y} = 0 \quad \text{or} \quad \frac{\partial \theta}{\partial Y} = \frac{k_f}{k_{nf}} \quad \text{at} \quad Y = 1 \quad , \quad 0 \leq X \leq 30 \quad (\text{V.26})$$

$\varphi/\%$	$\varphi_{Cu}/\%$	$\varphi_{Al_2O_3}/\%$	$k_{hnf}/W m^{-1} K^{-1}$	$\mu_{hnf}/kg m^{-1} s^{-1}$
0.1	0.0038	0.0962	0.619982	0.000972
0.33	0.0125	0.03175	0.630980	0.001098
0.75	0.0285	0.7215	0.649004	0.001386
1.0	0.0380	0.9620	0.657008	0.001602
2.0	0.0759	1.9241	0.684992	0.001935
3.0	0.1138	2.8862	0.712976	0.002268
4.0	0.1517	3.8483	0.712976	0.002268
5.0	0.1896	4.8104	0.740960	0.002601

**Table V.1** – Effective thermal conductivity and dynamic viscosity of Cu- $Al_2O_3$ /water hybrid nanofluid [91].

## V.6 Results and Discussions

The primary purposes of the present investigation are to look for the best heat transfer efficiency configuration of the heat sink microchannel. This research also seeks to determine and reveal the effects of heater length ( $B$ ), Knudsen number ( $Kn$ ), Darcy number ( $Da$ ), medium porosity ( $\varepsilon$ ), flow behaviour index ( $n$ ), Hartmann numbers ( $Ha$ ), and magnetic field inclination angle ( $\alpha$ ) on the momentum and heat transfer characteristics via offering and discussing the different statistical quantities such as the local and average Nusselt numbers, velocity profiles, streamline and isotherm distributions carefully. A series of computations are carried out on the steady laminar MHD forced convection heat transfer of  $Cu-Al_2O_3/water$  hybrid nanofluid and power-law fluids inside a fully and partially porous heat sink microchannel. The present study consists of a set of simulations for wide ranges of heat source length ( $5 \leq B \leq 30$ ), Knudsen numbers (0.001, 0.05, 0.01, 0.05, and 0.1), flow behaviour indices (0.2, 0.4, 0.6, 0.8, 1, 1.2, 1.4, 1.6, and 1.8), the Darcy numbers ( $10^{-5} \leq Da \leq 10^{-2}$ ), medium porosities ( $0.1 \leq \varepsilon \leq 0.9$ ), the Hartmann numbers ( $0 \leq Ha \leq 160$ ), and magnetic field inclination angles ( $0^\circ \leq \alpha \leq 90^\circ$ ) for the following fixed parameters : Reynolds number,  $Re=50$  ; nanofluid concentration,  $\varphi = 1\%$  ; porous thermal conductivity ratio,  $Ks=0.613$ . The porous medium is modelled by employing the Brinkman-Darcy model with a local thermal equilibrium LTE approach between the working fluid and the porous matrix for energy transfer

## V.7 Validation

The accuracy and reliability of the predicted results and numerical method have been ascertained and confirmed decisively by comparing the current prediction findings to those found in the literature. The results of a laminar forced convection and slip flow inside a microchannel in the presence of a magnetic field have been compared reasonably well with those of Afrand et al. [50] for various slip coefficients of 0.005 and 0.05 with fixed Reynolds number  $Re=20$ , and with those of Karimipour et al. [51] for different slip coefficients  $\beta$  (0, 0.04, 0.05, 0.08) at Reynolds number of  $Re=10$  . As shown in Figure V.3, Figure V.4, Figure V.5, and Figure V.6, the axial velocity and temperature profiles are in excellent agreement with the results of Afrand et al. [50] such as Karimipour et al. [51] , where no significant differences were found between them for all compared cases.

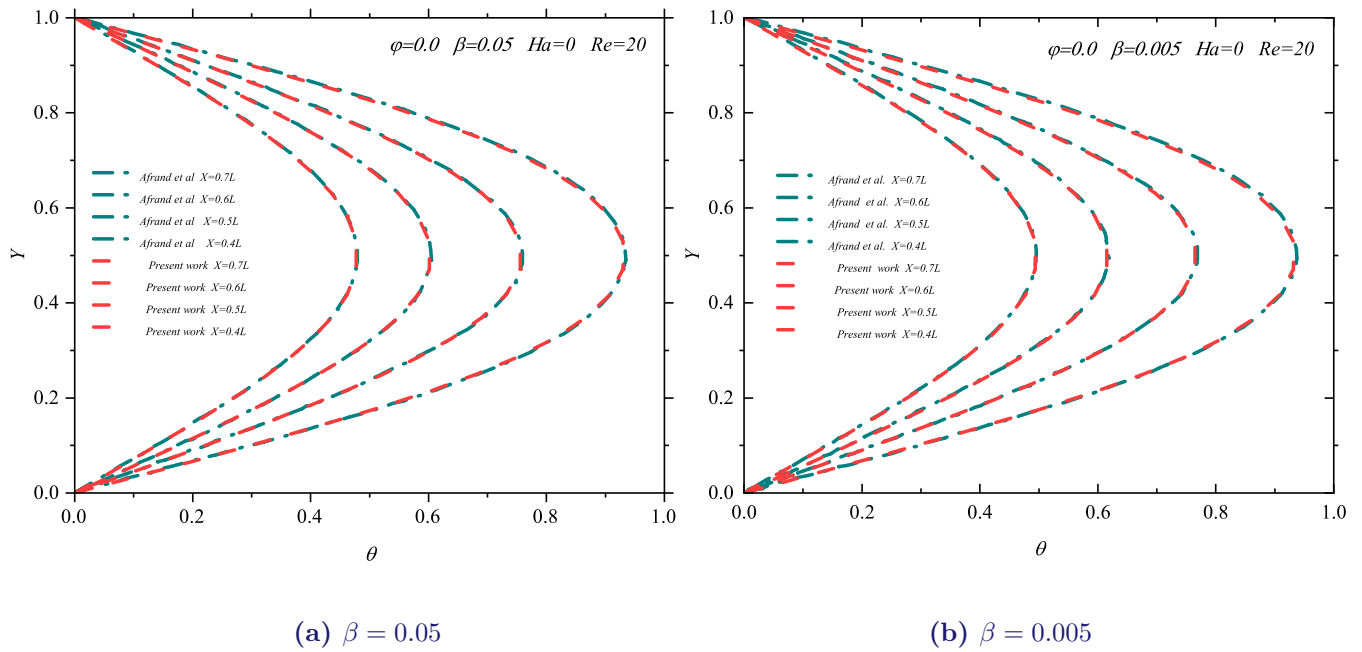


Figure V.3 – Temperature profiles of  $\theta$  at  $\varphi = 0.0$ ,  $Re = 20$ ,  $Ha = 0$ ,  $\beta = 0.05$  and  $\beta = 0.005$  for different cross sections of the micro-channel.

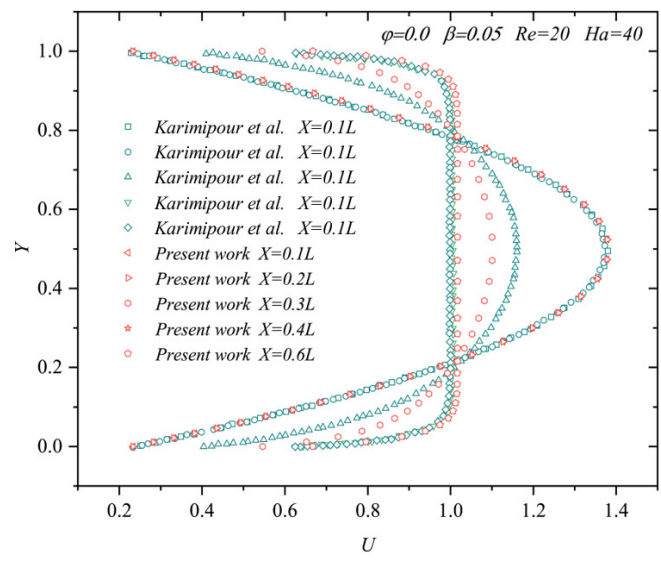
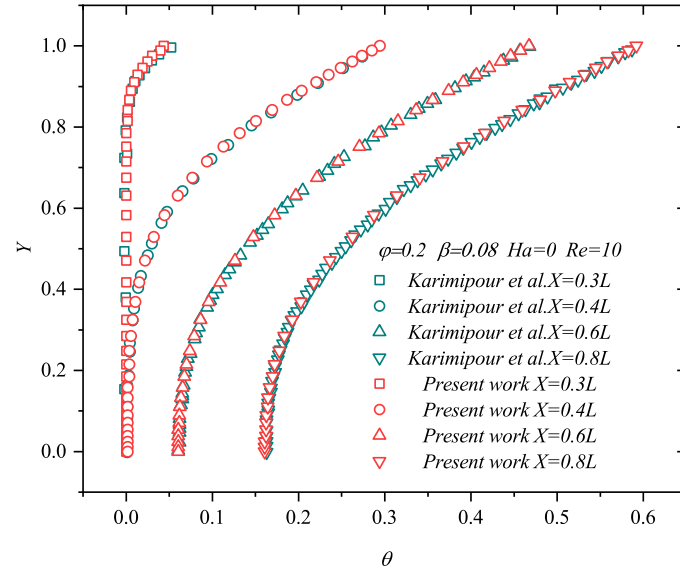
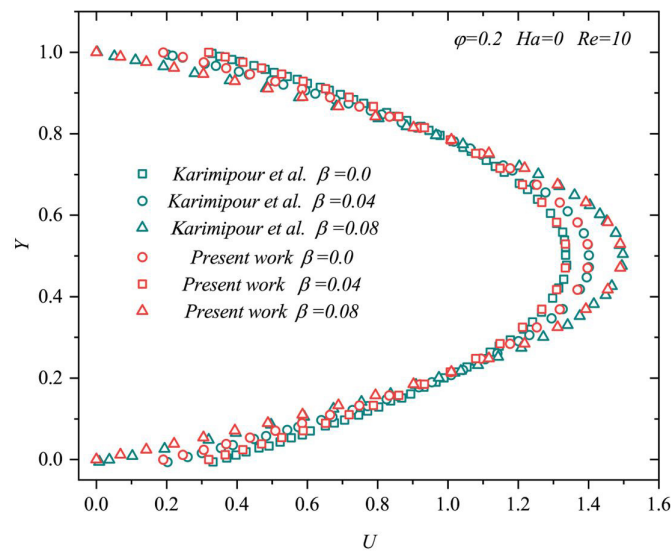


Figure V.4 – Velocity profile of  $U$  at  $\varphi = 0.0$ ,  $Re = 20$ ,  $Ha = 40$ ,  $\beta = 0.05$  for different cross sections of the microchannel.



**Figure V.5** – Temperature profile of  $\theta$  at  $\phi = 0.2$ ,  $Re=10$ ,  $Ha=0$ ,  $\beta = 0.08$  for different cross sections of the micro-channel.



**Figure V.6** – Velocity profile of  $U$  at  $\phi = 0.2$ ,  $Re=10$ ,  $Ha=0$ , for  $\beta = 0.0, \beta = 0.04, \beta = 0.08$ .

## V.8 Hybrid Nanofluid

### V.8.1 Effects of heat source length B

#### V.8.1.1 The Local Nusselt profile

The effect of the heat source length on the local Nusselt number is analysed and discussed in the following paragraphs. Figure V.7 depicts the local Nusselt number evolution along the heat source against the axial direction ( $x$ ) normalised by the microchannel length ( $L$ ). These simulations were conducted over various heat source lengths (5, 10, and 20) for a fixed Darcy number of  $10^{-1}$ , Knudsen number of 0.01, and Reynolds number of 50. As shown in Figure V.7, the local Nusselt number decreases gradually with axial distance for each heat source length; these profiles seem linear and remain constant along the heat source.

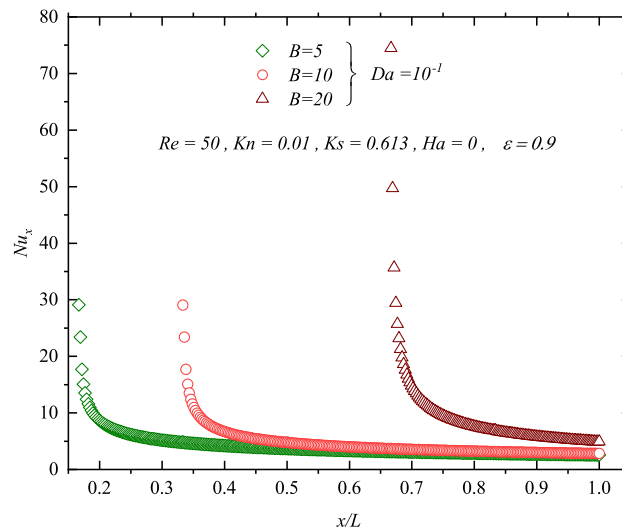


**Figure V.7** – Variations of local Nusselt number along the microchannel wall at different values of heat source length  $B=5$ ,  $B=10$ ,  $B=20$  at fixed Darcy number  $Da = 10^{-1}$  and Reynolds number  $Re=50$  for  $Kn=0.01$ ,  $Ha=0$ ,  $\varepsilon = 0.9$ .

#### V.8.1.2 The Average Nusselt profile

The following subsection reveals the influence of the heat source length, Darcy number, and magnetic field inclination angle on the thermal characteristics and the heat transfer mechanism inside the microchannel. That is via analysing and discussing the average Nusselt number.

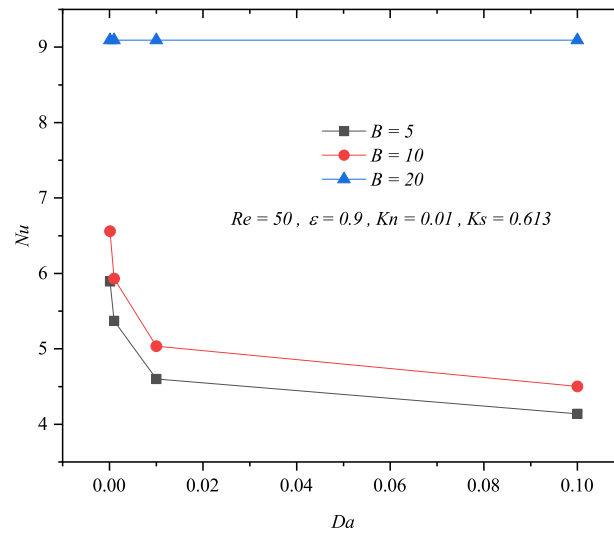


**Figure V.8** – Variations of Average Nusselt number at different values of heat source length  $B=5$ ,  $B=10$ ,  $B=20$  at fixed Reynolds number  $Re=50$  for  $Kn=0.01$ ,  $\varepsilon = 0.9$ .

Figure V.8 demonstrates the average Nusselt number evolutions against Darcy number for various values of heat source lengths  $B$  (5, 10, and 20) at Reynolds number  $Re=50$ , Knudsen number  $Kn=0.01$ . The heat transfer mechanism of the nanofluid inside the microchannel depends on the geometry effects and Darcy number; the heat source length significantly affects the average Nusselt number over the conditions mentioned above. The heat source length induces a noticeable improvement in the average Nusselt numbers, which is more significant when the heat source length increases. The average Nusselt number increases markedly with the increasing length of the heat source for each Darcy number. On the other hand, the average Nusselt number exhibits a noticeable reduction with increasing Darcy number and this trend is more obvious as the heat source length decreases.

### V.8.2 Effects of dimensionless slip coefficient $Kn$

The present research focuses on enhancing the heat transfer mechanism by looking for the best heat transfer performance in the considered configuration. The parametric effects of the heat source length ( $B$ ) and Darcy number ( $Da$ ) on the momentum and heat transfer characteristics are investigated in the present section by analysing and discussing the mean axial velocity, temperature profiles, and local and average Nusselt numbers.

### V.8.2.1 Velocity profiles

Figure V.9 illustrates the evaluation of the axial velocity profiles normalised by the bulk velocity ( $U_b$ ) against the radial direction ( $y$ ) normalised by the microchannel high ( $H$ ) along the normal wall direction located at an axial position of  $X=1$  inside a microchannel with heat source size of 20. These simulations were conducted over a wide range of Knudsen numbers (0, 0.001, 0.05, 0.01, 0.5, and 0.1) for a fixed Darcy number of  $10^{-1}$ .

In the no-slip flow  $Kn=0$ , the viscous force considerably influences the axial velocity along the radial direction when approaching the microchannel wall, where this effect seems stronger at the wall. It should be noted that the mean axial velocity equals zero value at the microchannel wall where the shear rate reached the maximum value in this flow region due to the no-slip condition imposed on the wall. As shown in Figure V.9, the axial velocity increases further away from the microchannel wall towards the centreline and reaches its maximum value at the microchannel centre; the axial velocity in the microchannel centreline is 1.5 of the mean bulk velocity, where the axial velocity profile is characterised by the parabolic shape for the case of  $Kn=0$ .

It can be seen from Figure V.9 that the slip flow considerably influences the hydrodynamic characteristics, a stronger dependence of the axial velocity profiles on Knudsen number along the radial coordinates in the fully developed region for all considered Darcy numbers. As shown in Figure V.9, the axial velocity profiles exhibit a pronounced redistribution along the radial direction as the Knudsen number varies; these profiles differ from each other with increasing Knudsen number. The axial velocity profile of the no-slip flow seems higher than those of slip flow in the microchannel centreline, denoting that the shear rate of the no-slip flow is lower than those of slip-flow in the microchannel centreline. On the contrary, the axial velocity profiles of the slip flow marked positive values at the microchannel wall; the axial velocity of the slip flow marked a high value at the microchannel wall compared with that of no-slip flow, where the axial velocity reaches 0.9 for  $Kn=0.5$  and equals to zero for  $Kn=0$ .

Further away from the microchannel wall, the velocity profiles of the slip flow seem more flattened in the microchannel centreline. This trend is more pronounced as the Knudsen number increases due to the imposed slip condition on the microchannel wall.



The increased Knudsen number results in a pronounced increase of the axial velocity and a reduction in the shear rate at the wall, resulting in a noticeable decrease of the velocity in the microchannel centre and a marked increase of the axial velocity at the microchannel wall. It should be noted that the axial velocity profile redistribution is caused by the jump velocity induced by the slip flow. This trend is more evident as the Knudsen number increases.

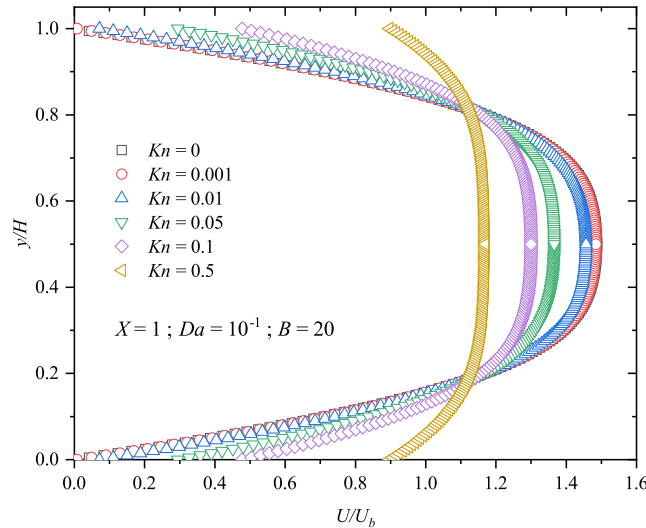


**Figure V.9** – Velocity profile of  $U/U_b$  for different values of Knudsen numbers at fixed Darcy number  $Da = 10^{-1}$  and  $B=20$ , for  $X=20$

The Figure V.10 depicts the evaluation of the axial velocity profiles normalised by the bulk velocity ( $U_b$ ) against the radial direction ( $y$ ) normalised by the microchannel high ( $H$ ) at three axial positions ( $X=0.1, 0.5$ , and  $1$ ), for ( $Kn=0.05, 0.1$ ) at a fixed Darcy number  $Da = 10^{-1}$ , and a heat source length ( $B=20$ ). The axial velocity profile of the increased Knudsen number ( $Kn=0.1$ ) is lower and seems more flattened than that of decreased Knudsen number ( $Kn=0.05$ ) in the microchannel centreline at every axial position ( $X=0.1, 0.5$ , and  $1$ ). In the fully developed flow region, the axial velocity profile becomes progressively parabolic further away from the microchannel inlet for the Knudsen number equals  $0.05$ . As for  $Kn=0.1$ , the axial velocity profile flattens apparently in microchannel centreline and this trend is more pronounced in the fully developed region.

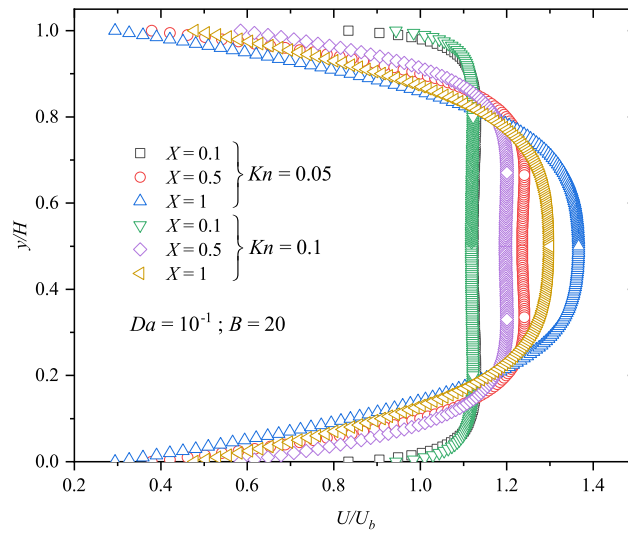


**Figure V.10** – Velocity profile of  $U/U_b$  for  $Kn=0.05$ ,  $Kn=0.1$  at fixed Darcy number  $Da = 10^{-1}$  and  $B=20$ , for different cross sections of the micro-channel.

### V.8.2.2 Temperature profiles

Figure V.11 demonstrates the evaluation of the dimensionless temperature against the radial direction ( $y$ ) normalised by the microchannel high ( $H$ ) along the normal wall direction located at an axial position of  $X=21$ ,  $25$ , and  $30$ , for Knudsen number of  $0$  and  $0.1$ . As shown in Figure V.11, the heat slip flow considerably affects the heat transfer mechanism; the temperature profile exhibits a significant redistribution along the radial direction as the Knudsen number varies.

The temperature profile develops progressively further away from the entrance region towards the developed region flow for all considered cases; these profiles seem to be more flattened in the entrance region for both Knudsen numbers. It can be seen from Figure V.11 that the temperature distributions are nearly independent of the Knudsen number; these profiles are consistent with each other along the radial direction.

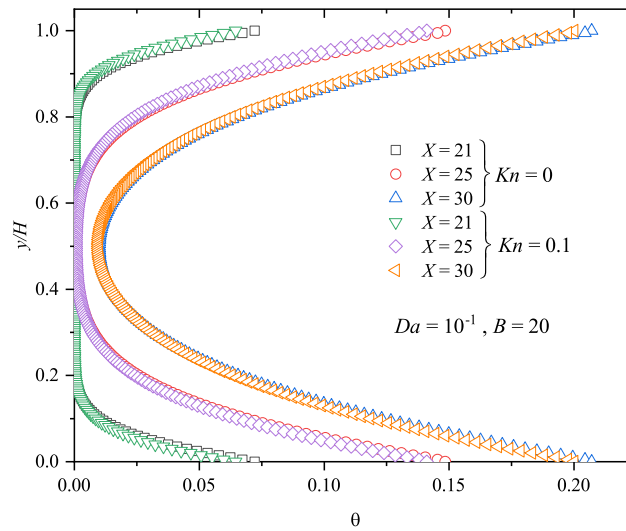


**Figure V.11** – Temperature profile of  $\theta$  for  $Kn=0$ ,  $Kn=0.1$  at fixed Darcy number  $Da = 10^{-1}$  and  $B=20$  for different cross sections of the micro-channel.

### V.8.2.3 Local Nusselt number

The present subsection reveals the influence of the dimensionless slip coefficient  $Kn$  on the heat transfer mechanism. That is via analysing and discussing the local Nusselt number along the heat source. The Figure V.12 describes the local Nusselt profiles along the microchannel wall normalised by the axial direction ( $x$ ) normalised by the microchannel length ( $L$ ) for several values of Knudsen numbers  $Kn$  (0, 0.05, and 0.1) at fixed heat source length  $B=5$ , and one Darcy number  $Da = 10^{-1}$ . As shown in Figure V.12, the Knudsen number appears to have a limited effect on the local Nusselt number ; the local Nusselt number profiles are almost identical and coincide along the heat source with varying Knudsen numbers as (0, 0.05, and 0.1) in the considered configurations. As shown in Figure V.12, the local Nusselt number decreases gradually with axial distance ( $X$ ), and the local Nusselt number remains constant and equal to 5 beyond  $X/L=0.5$  for all Knudsen numbers.

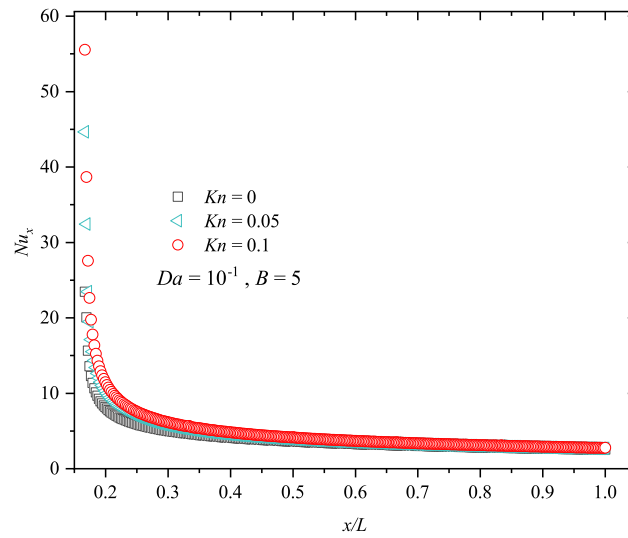


**Figure V.12** – Variations of local Nusselt number along the microchannel wall at different values of Knudsen numbers  $Kn=0$ ,  $Kn=0.05$ , and  $Kn=0.1$  at fixed Darcy number  $Da = 10^{-1}$  and  $B=5$ .

#### V.8.2.4 Average Nusselt number

As shown in Figure V.13, the average Nusselt number seems affected by the Knudsen number with varying heat source length and Darcy number. The heat transfer mechanism enhances significantly under the slip flow condition; the Nusselt number increases markedly as the Knudsen number increases and this trend is more pronounced as the Knudsen number and heat source length increase for all Darcy numbers.

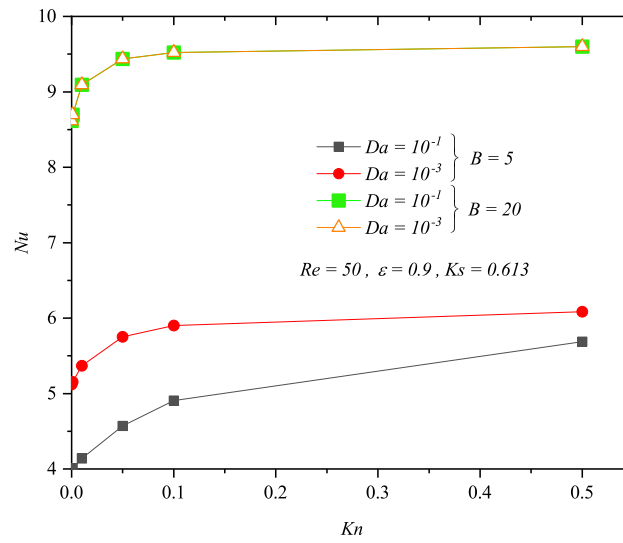


**Figure V.13** – Variations of Average Nusselt number at two values of Darcy numbers  $Da = 10^{-1}$ ,  $Da = 10^{-3}$  for  $B=5$ ,  $B=20$  at fixed Reynolds number  $Re=50$ ,  $\varepsilon = 0.9$ .

### V.8.3 Effects of $Ha$ and $\alpha$

The present section concerns a steady-state laminar flow magnetohydrodynamic (MHD) forced convection natural convective inside a fully porous horizontal microchannel occupied with  $Cu-Al_2O_3$ /water hybrid nanofluid; the thermal conductivity and nanofluid viscosity are correlated experimentally. The Darcy-Brinkmann model is adopted to model the flow through the porous medium foam with a local thermal-equilibrium (LTE) approach between the working fluid and the porous matrix for energy transfer. A uniform transverse magnetic field permeates the nanofluid ( $B_0$ ) inclined by an angle ( $\alpha$ ) over a wide range of the Hartmann numbers ( $0 \leq Ha \leq 160$ ) and magnetic field inclination angles ( $0^\circ \leq \alpha \leq 90^\circ$ ) for the following fixed parameters : heat source length,  $B=20$ ; Knudsen number,  $Kn=0.01$ ; medium porosity,  $\varepsilon = 0.9$ ; Reynolds number,  $Re=50$ ; Darcy number,  $Da = 10^{-1}$ ; and porous thermal conductivity ratio,  $Ks=0.613$ ). The present analysis reveals the dependency of the average Nusselt number, streamline and isotherm contours on the externally imposed magnetic field ( $B_0$ ) and its different orientations.

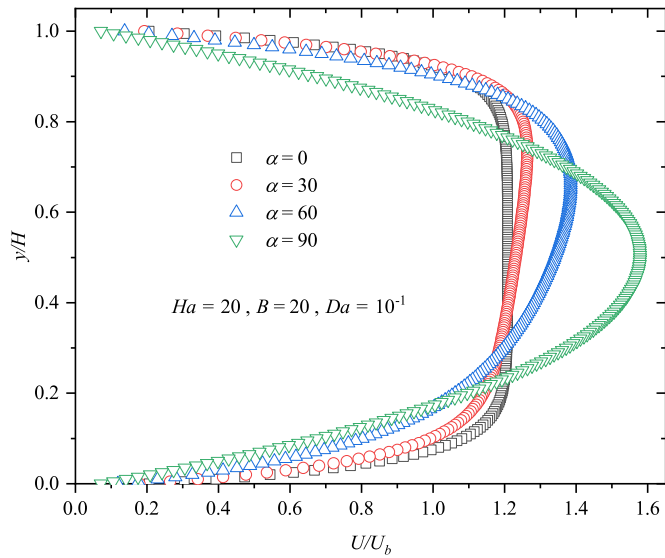
### V.8.3.1 Velocity profile

The velocity profiles are analysed and discussed in the following paragraphs to examine the effects of the Hartmann number and magnetic field inclination angles on the heat transfer inside the considered geometry.

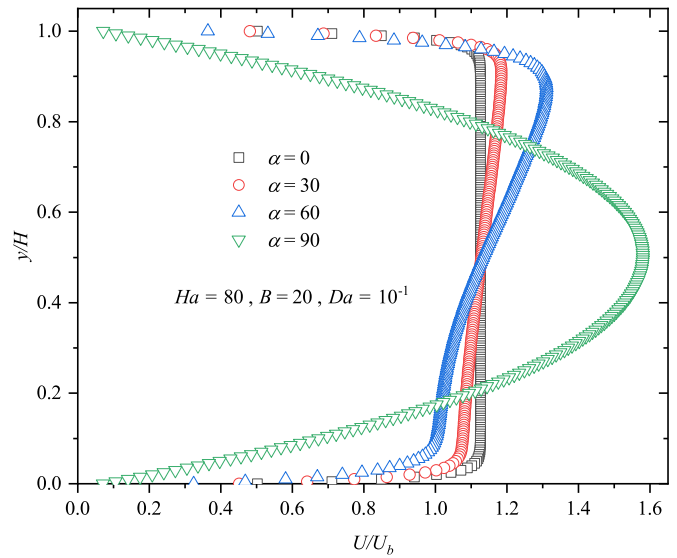
Figure V.14a, Figure V.14b, Figure V.14c illustrate the evaluation of the axial velocity profiles normalised by the bulk velocity ( $U_b$ ) against the radial direction ( $y$ ) normalised by the microchannel high ( $H$ ) along the normal wall direction located at an axial position of  $X=30$  inside a microchannel with heat source size of 20. These simulations were conducted over wide ranges of Hartmann numbers (20, 80, 160) and magnetic field inclination angles ( $0^\circ$ ,  $30^\circ$ ,  $60^\circ$ , and  $90^\circ$ ) at a fixed Darcy number of  $10^{-1}$ . The Hartmann number and magnetic field inclination angle considerably affect the momentum characteristics; the mean axial velocity profiles differ from each other with varying Hartmann numbers and magnetic field inclination angles for all considered configurations.

As shown in Figure V.14a, Figure V.14b, Figure V.14c, the velocity profiles exhibit a significant redistribution along the radial direction by varying the magnetic field inclination angle for all Hartmann numbers. The axial velocity increases gradually further away from the microchannel pipe towards the centreline, where the axial velocity profile is characterised by the parabolic shape for the case of magnetic field inclination angle of  $\alpha = 90^\circ$  for all Hartmann numbers. The axial velocity profile of  $90^\circ$  seems higher than those of  $0^\circ$ ,  $30^\circ$ , and  $60^\circ$  along the normal-wall direction. As shown in Figure V.14a, Figure V.14b, Figure V.14c, the axial velocity in the microchannel centreline is 1.6 of the mean bulk velocity for the case of  $90^\circ$ . It is worth noting that the decreased magnetic field inclination angle reduces the axial velocity profile along the radial direction. For all Hartmann numbers, these profiles seem more flattened in the microchannel centre as the magnetic field inclination angle decreases.

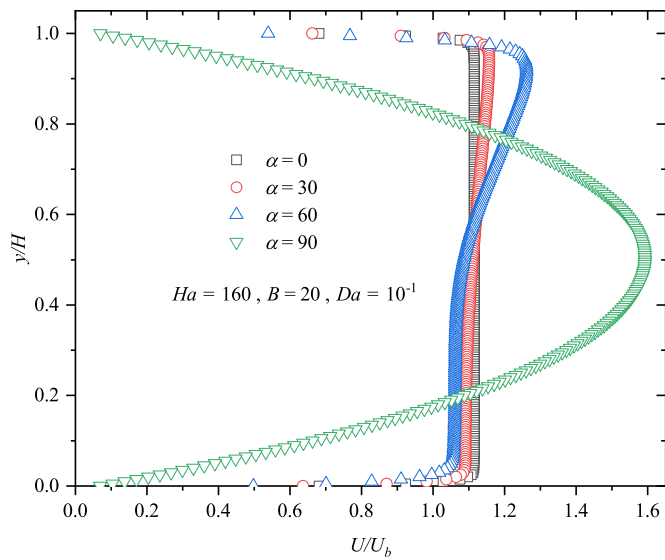
On the other hand, the mean axial velocity profiles are strongly affected by the Hartmann number for each magnetic field inclination angle. As shown in Figure V.14d, the axial profiles exhibit a noticeable redistribution along the radial direction, the profiles of the Hartmann number 160 lie down those of 20 and 80 along the radial direction for all magnetic field inclination angles.



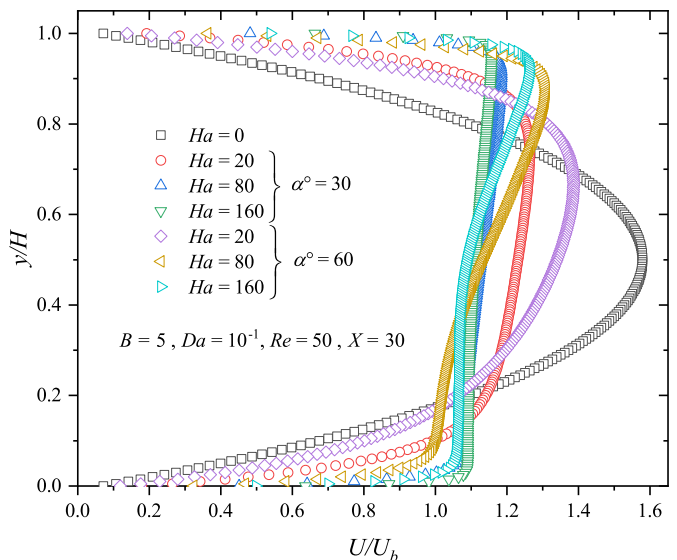
(a)



(b)



(c)



(d)

**Figure V.14** – Velocity profile of  $U/U_b$  for different magnetic field inclination angles and Hartmann numbers at fixed Darcy number  $Da = 10^{-1}$  and  $B=20$ .

The axial velocity profiles are flattened near the lower microchannel wall, and the maximum velocity value deviates significantly towards the upper microchannel wall with varying Hartmann numbers. It can be said that the increased Hartmann number results in a marked deviation in the maximum axial velocity profile when approaching the magnetic field, resulting in a marked decrease in the axial velocity profile further away from the magnetic field.

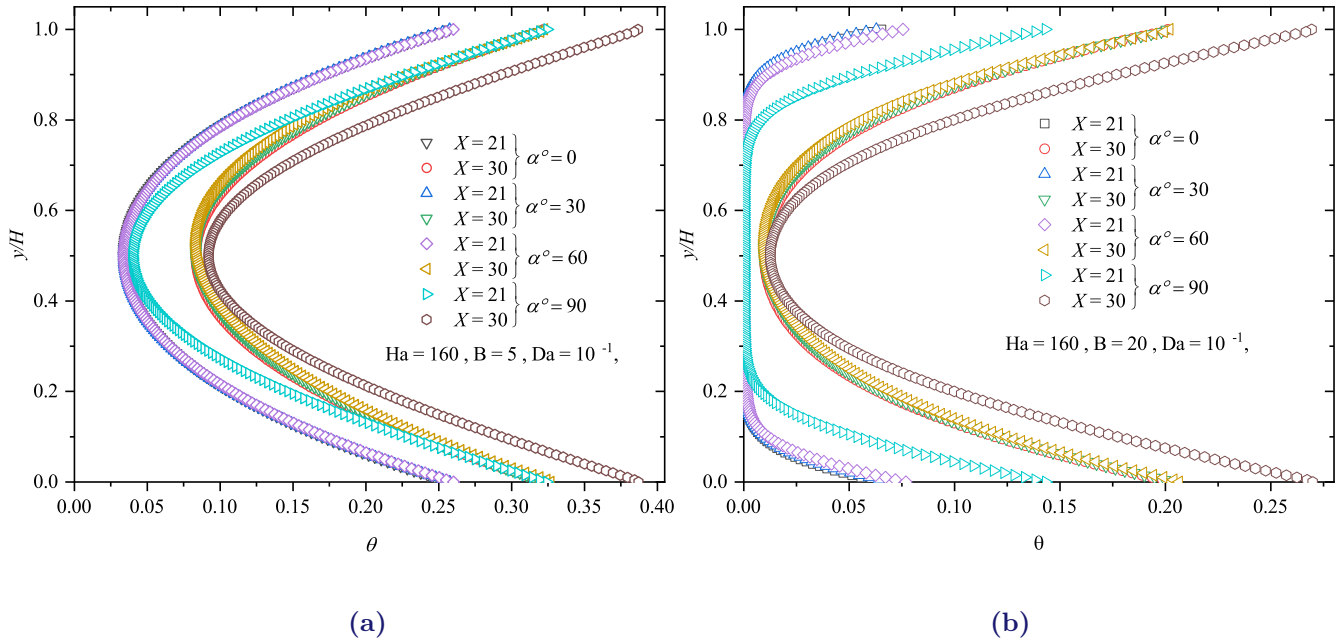
### V.8.3.2 Temperature profile

Figure V.15 shows the evaluation of the temperature profiles normalised by  $\theta$  versus the radial direction ( $y$ ) normalised by the microchannel high ( $H$ ) along the heat source. This subsection demonstrates the effects of Hartmann number ( $Ha$ ) as well as the axial positions on the temperature profiles under various values of magnetic field inclination angles  $\alpha$  ( $0^\circ$ ,  $30^\circ$ ,  $60^\circ$ ,  $90^\circ$ ) at different cross sections ( $X=21, 30$ ) of microchannel for the considered fluid, at  $\varphi = 0.01$ ,  $Re=50$ ,  $B=5$ ,  $Da = 10^{-1}$ , with fixed slip coefficient  $Kn=0.01$ . Where,  $Ha=20$  and  $Ha=160$  in Figure V.15a Figure V.15b respectively. It can be seen that the fluid temperature profile exhibits a significant redistribution along the heat source by varying the magnetic field inclination angle for all axial positions and Hartmann numbers. The results suggest that the magnetic field inclination angle affects the fluid temperature significantly for all considered cases. The parabolic shape for all magnetic field inclination angles characterises the fluid temperature profile. As shown in Figure V.15, the temperature decreases significantly as the magnetic field inclination angle increases; the highest temperature is marked in the case of the magnetic field inclination angle equal to  $0$  for all considered cases.

### V.8.3.3 Average Nusselt number

As shown in Figure V.16, The Nusselt number seems affected by the Hartmann number and the magnetic field inclination angle. The average Nusselt number of  $90$  seems independent of the Hartmann number for both heat source lengths  $5$  and  $20$ . The Nusselt number varies significantly as the magnetic field inclines, the Nusselt number increases markedly magnetic field inclination angle decreases for all considered cases and this trend is more obvious for Hartmann number equals  $20$ . On the other hand, the increased Hartmann number results in a pronounced increase in the average Nusselt number for all magnetic field inclination angles.





**Figure V.15** – Temperature profile of  $\theta$  for two values of heat source length ( $B=5$ ,  $B=20$ ) at fixed Darcy number  $Da = 10^{-1}$  and Hartmann number  $B=160$  for different cross sections of the micro-channel.

#### V.8.4 Effects of porosity $\varepsilon$

The Darcy-Brinkmann model is adopted to model the flow through the porous medium foam with a local thermal-equilibrium (LTE) approach between the working fluid and the porous matrix for energy transfer. The present section focuses on enhancing the heat transfer efficiency and improving the forced convection heat transfer mechanism by looking for the best heat transfer performance in the considered configuration. This section investigates the parametric effects of the medium porosity and the Darcy number on the momentum and heat transfer fields of the  $\text{Cu-Al}_2\text{O}_3$ /water hybrid nanofluid inside a heat sink microchannel. That is via analysing and discussing the axial velocity and local and average Nusselt numbers in detail.

This analysis is conducted over wide ranges of porosities (0.1, 0.2, 0.3, 0.4, 0.5, 0.6, 0.7, 0.8, and 0.9), Darcy numbers ( $10^{-4}$ ,  $10^{-3}$ ,  $10^{-2}$ , and  $10^{-1}$ ), for the fixed following parameters : heat source length,  $B=20$ ; Knudsen number,  $\text{Kn}=0.01$ ; Reynolds number,  $\text{Re}=50$ , and porous thermal conductivity ratio,  $\text{Ks}=0.613$ .

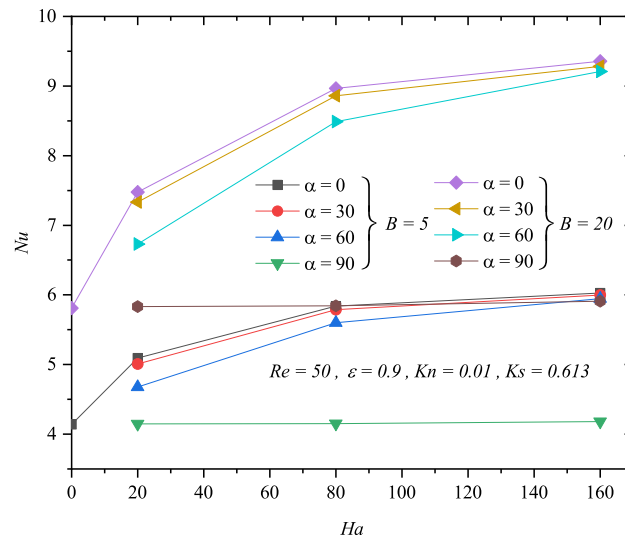


**Figure V.16** – Variations of Average Nusselt number at two heat source length  $B=5$ ,  $B=20$  with fixed Reynolds number  $Re=50$ ,  $\varepsilon = 0.9$  for different magnetic field inclination angles.

#### V.8.4.1 Velocity profiles

Figure V.17 illustrates the evaluation of the axial velocity profiles normalised by the bulk velocity ( $U_b$ ) against the radial direction ( $y$ ) normalised by the microchannel high ( $H$ ) along the normal wall direction located at an axial position of  $X=1$  inside a microchannel with heat source size of 20. These simulations were conducted over various porosities (0.1, 0.2, 0.3, 0.4, 0.5, 0.6, 0.7, 0.8, and 0.9) for a fixed Darcy number of  $10^{-3}$  and  $10^{-1}$ .

The parametric study indicates that the momentum characteristics and heat transfer mechanism strongly depend on the media porosity; the axial velocity distributions seem to be strongly influenced by the porosity in the considered geometry. As shown in Figure V.17, the velocity evolutions are similar along the radial direction; these profiles seem more distinct with the varying media porosity for all Darcy numbers.

As shown in Figure V.17a and Figure V.17b, the axial velocity increases further away from the microchannel wall towards the centreline and reaches its maximum value at the microchannel centre; the axial velocity in the microchannel centreline is 1.5 of the mean bulk velocity, where the axial velocity profile is characterised by the parabolic shape for the case porosity of 0.9. The axial velocity profiles change gradually with varying medium porosity; these profiles exhibit a notable increase further away from the microchannel wall towards the microchannel centre for both Darcy numbers. It can be said that the decreased medium porosity results in a marked

increase in the axial velocity profiles along the radial direction, especially in the microchannel centre. It should be noted that the maximum axial velocity reaches 11 of the mean bulk velocity microchannel centrelines for the case of porosity of 0.1. Moreover, as the porosity decreases, the microchannel centreline’s axial velocity profiles seem more flattened. This trend is more pronounced as the media porosity decreases due to the decrease in the gap between the porous matrix. It can be said that decreased porosity leads to reduce the gap between the porous matrix, resulting in pronounced increases in the axial velocity of the nanofluid through the microchannel, and this trend is more pronounced as the porosity decreases for all Darcy numbers.

As for the position effect, the axial velocity profile develops progressively far away from the entrance region towards the fully developed region for all porosities. As shown in Figure V.18a and Figure V.18b, the decreased porosity leads to an increase and flatten the axial velocity profiles, especially in the microchannel centre. This trend is more obvious in the developed region for both Darcy numbers.

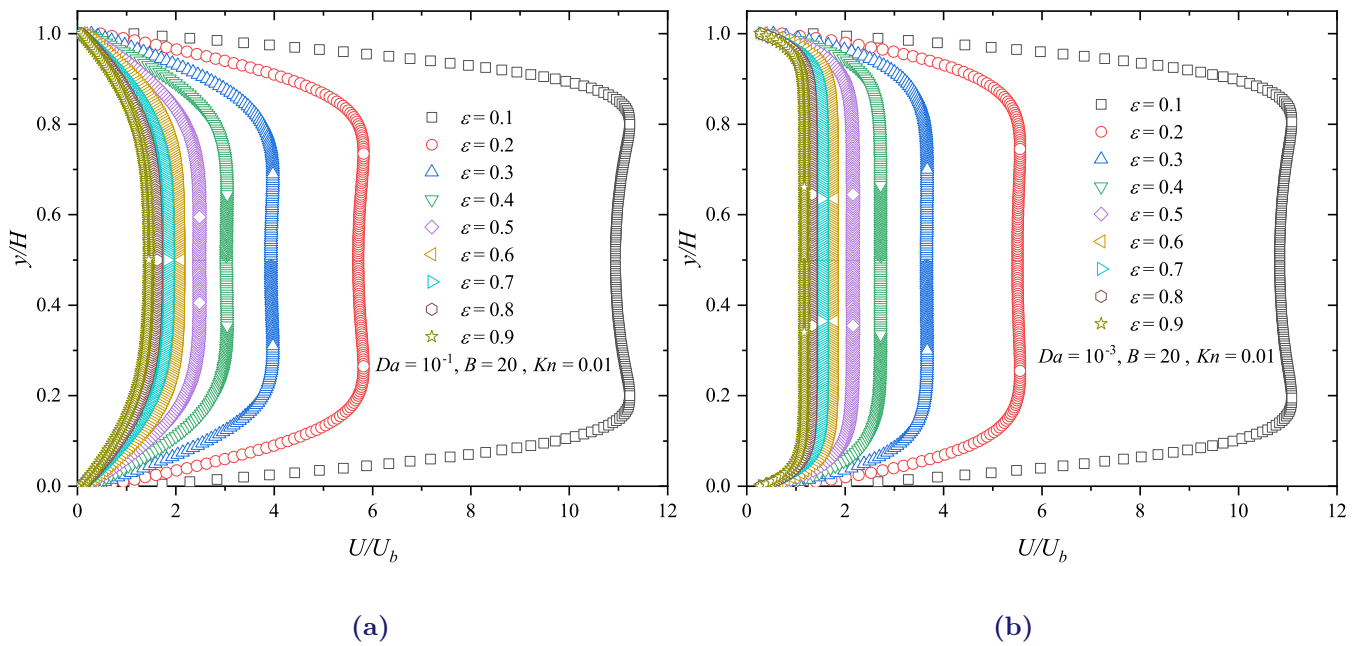


**Figure V.17** – Velocity profile of  $U/U_b$  for different values of porosities at two Darcy number  $Da = 10^{-1}$ ,  $Da = 10^{-3}$  for fixed heat source length  $B=20$  and  $Kn=0.01$ .

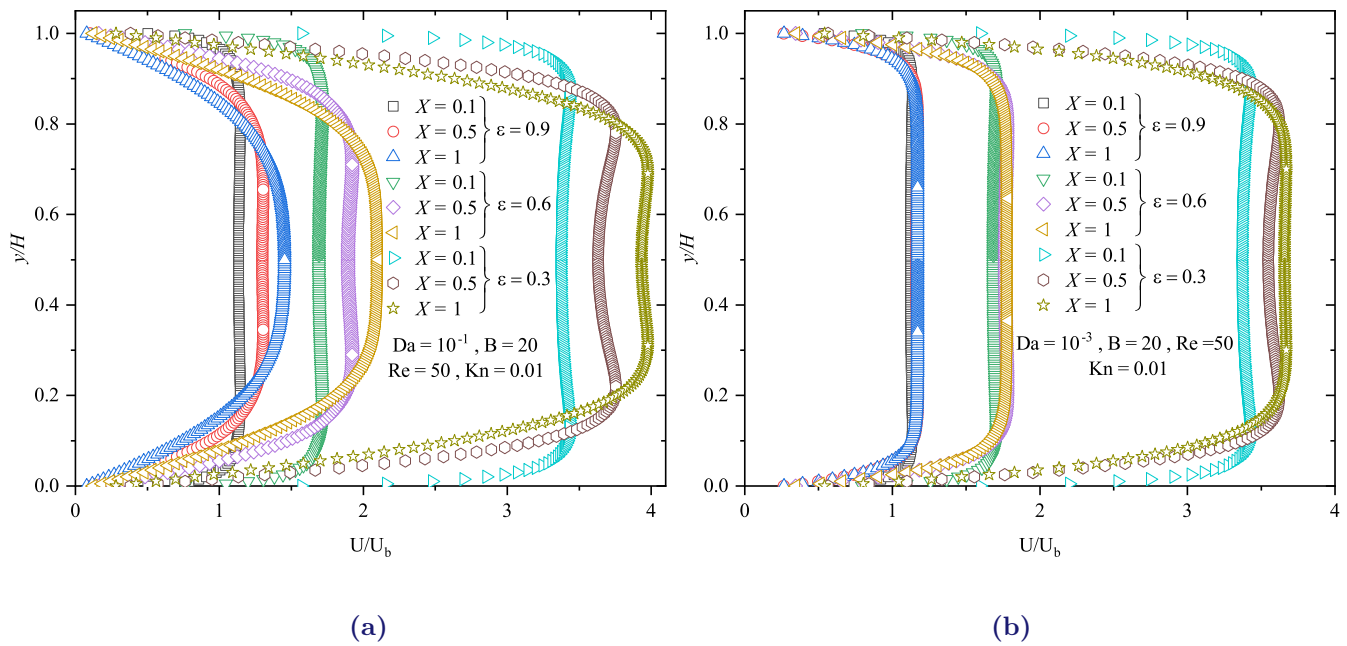


**Figure V.18** – Velocity profile of  $U/U_b$  for three values of porosities at two Darcy number  $Da = 10^{-1}$ ,  $Da = 10^{-3}$  for fixed heat source length  $B=20$ ,  $Kn=0.01$ ,  $Re=20$ .

#### V.8.4.2 Average Nusselt number

Figure V.19 shows the average Nusselt Distributions against the medium porosity for several values of Darcy number  $Da = 10^{-1}$ ,  $Da = 10^{-3}$  with various values of heat source length  $B=5$  and  $B=20$ . The heat transfer characteristics of the nanofluid seem to be more dependent on the medium porosity; the average Nusselt numbers are affected strongly by the medium porosity for all Darcy numbers and heat sink lengths. It can be seen from Figure V.19 that the Nusselt number increase significantly with decreased Darcy number for all heat source lengths, this trend is more obvious as the medium porosity increases.

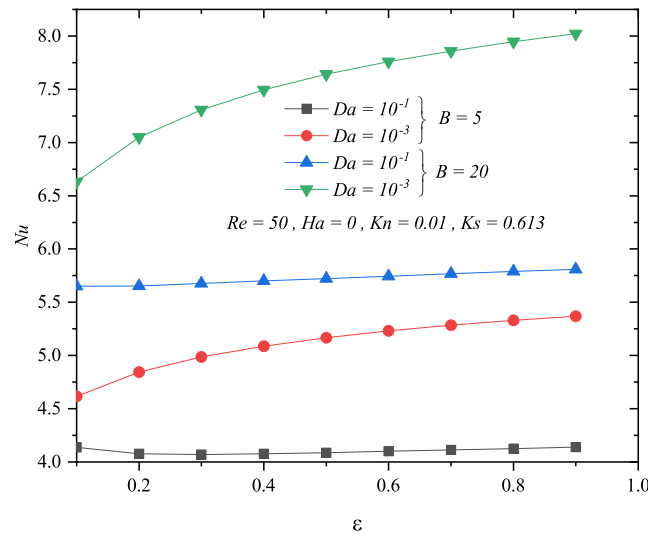


**Figure V.19** – Variations of Average Nusselt number at two Darcy numbers  $Da = 10^{-1}$ ,  $Da = 10^{-3}$  with fixed Reynolds number  $Re=50$ ,  $Kn=0.01$ ,  $Ha=0$  at two heat source length  $B=5$ ,  $B=20$ .

## V.9 Power law fluid

The present part gives special consideration to examining the effects of the rheological properties of the Ostwald de Waele fluid on heat transfer characteristics and rheological and hydrodynamic behaviour. This section focuses on analysing the slip flow and non-Newtonian fluid through a porous metal foam. The current investigation deals numerically with a two-dimensional steady laminar flow forced convection heat transfer of Ostwald de Waele fluid through a microchannel heat sink. The considered geometry of the studied problem is a multi-layered microchannel heat sink, the lower layered is filled with porous metal foam with a medium porosity of 0.5, occupied by Ostwald de Waele fluid over a wide flow behaviour index range (0.2, 0.4, 0.6, 0.8, 1, 1.2, 1.4, 1.6, and 1.7). This investigation is performed over wide ranges of Reynolds numbers (10, 25, 50, 75, 100), Knudsen numbers (0, 0.001, 0.05, 0.01, 0.1), Darcy numbers ( $10^{-1}$ ,  $10^{-3}$ ), for the following fixed parameters : Hartmann number,  $Ha=0$ , and porous thermal conductivity ratio,  $Ks = 0.613$ .

## V.9.1 Effects of behaviour index $n$

### V.9.1.1 Velocity profiles

To demonstrate the effect of the flow behaviour index on the momentum, flow pattern, and rheological behaviour, the following present subsection examines the effect of the flow behaviour index on the axial velocity distributions along the radial direction for various configurations. Figure V.20 illustrates the evaluation of the dimensionless velocity profiles against the radial direction ( $y$ ) normalised by the microchannel high ( $H$ ) along the normal wall direction at the axial position of  $X=30$ . This subsection consists of a set of simulations for various values of flow behaviour index ((0.2, 0.4, 0.6, 0.8, 1, 1.2, 1.4, 1.6, and 1.7), with high Reynolds number  $Re=100$ , the porosity of the solid matrix of 0.5, Darcy number of  $10^{-1}$ , at fixed Knudsen number of  $Kn = 0.1$ .

## V.9.2 Effects of behaviour index $n$

The momentum characteristics seem more dependent on the flow behaviour index in all considered cases; the axial velocity profiles of the Ostwald de Waele fluid inside the microchannel exhibit a significant deviation with varying flow behaviour index in all axial positions. As shown in Figure V.20, the axial velocity profile marked a pronounced deviation in the lower microchannel half with varying flow behaviour index due to the apparent viscosity of the Ostwald de Waele fluid and porous medium. The axial velocity profile increases gradually further away from the microchannel pipe towards the centreline, where the axial velocity profile is characterised by the parabolic shape for a flow behaviour index of 1. It can be seen from Figure V.20 that the velocity profiles of the dilatant fluid with flow behaviour index of 1.2, 1.4, and 1.6 are higher than on the Newtonian fluid ( $n = 1$ ) along the microchannel high for all axial positions. It should be noted the increased flow behaviour index results in the apparent deviation in the shear rate distribution of the dilatant fluid along the radial coordinates, resulting in a marked variation in the apparent fluid viscosity, which leads to an increase in the axial velocity distributions along the microchannel high.

On the other hand, the axial velocity profiles of the pseudoplastic ( $n < 1$ ) exhibit a noticeable reduction with varying the flow behaviour index, these profiles seem also flattened in the upper microchannel half with varying the flow behaviour index. It can be said that the decreased flow behaviour index of the pseudoplastic results in marked deviation in the shear rate and apparent

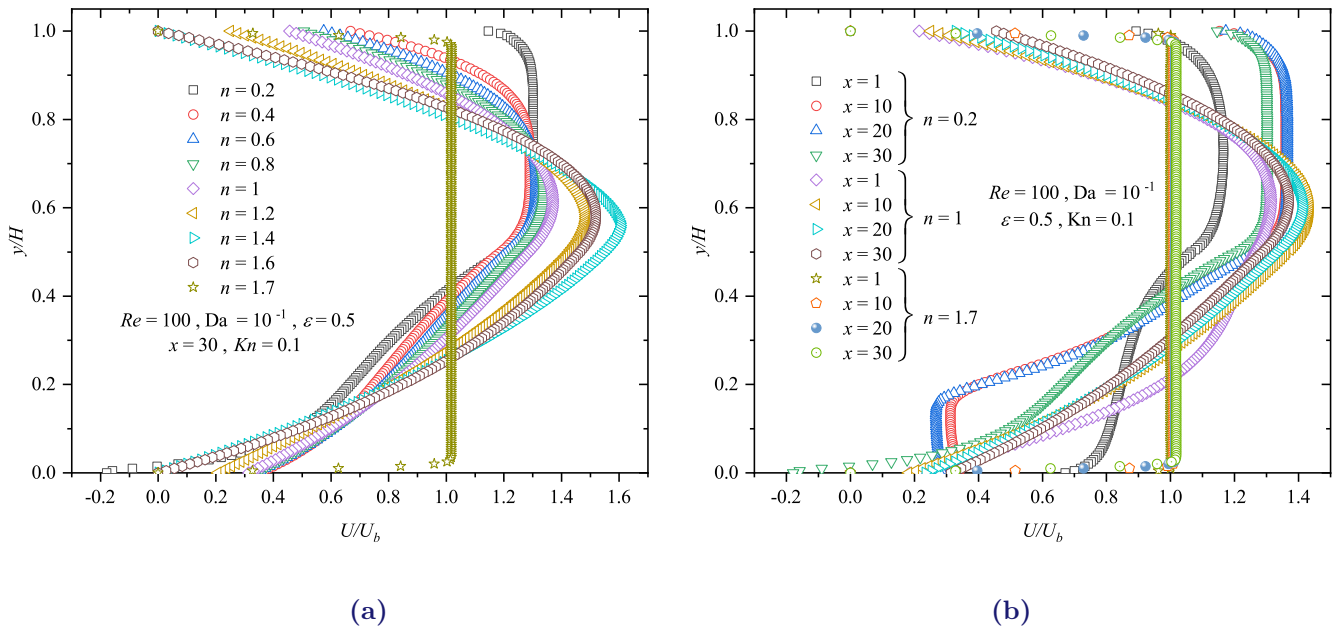


**Figure V.20** – Velocity profile of  $U/U_b$  for different values of flow behaviour index at Darcy number  $Da = 10^{-1}$ , for fixed Knudsen number  $Kn=0.1$ ,  $Re=100$ ,  $\varepsilon = 0.5$ .

fluid viscosity, resulting in a significant reduction in the axial velocity profile. The decreased flow behaviour index of the pseudoplastic also leads to moving the axial velocity’s maximum value (peak value) toward the upper microchannel wall.

As for the flow behaviour index of 1.7, the axial velocity profile is flattened along the radial coordinate because of the high apparent viscosity of the dilatant fluid, where the inertia force is less than the viscous force which affected the development of the velocity profile along the microchannel high.

### V.9.3 Effects of Reynolds number Re

The momentum characteristic and rheological behaviour of the Ostwald de Waele seem more dependent on the Reynolds number and flow behaviour index in the considered configuration ; the axial velocity profiles of the Ostwald de Waele fluid inside the microchannel exhibit a significant deviation with varying Reynolds number. Figure V.21 illustrates the evaluation of the dimensionless velocity profiles against the radial direction ( $y$ ) normalised by the microchannel high ( $H$ ) along the normal wall direction at the axial position of  $X=30$ . This subsection consists

of a set of simulations for various values of Reynolds number (10, 25, 50, 75, and 100), with porosity of the solid matrix of 0.5, Darcy number of  $Da = 10^{-1}$ , at fixed Knudsen number of  $Kn = 0.1$ .

As shown in Figure V.21, the axial velocity of the dilatant fluid ( $n=1.7$ ) increases further away from the microchannel wall towards the centreline and reaches its maximum value at the microchannel centre; the axial velocity in the microchannel centreline is 1.5 of the mean bulk velocity, where the axial velocity profile is characterised by the parabolic shape for the case of  $Re=10$ . Further away from the microchannel wall, the velocity profiles of the slip flow seem more flattened in the microchannel centreline. This trend is more pronounced as the Reynolds number increases.

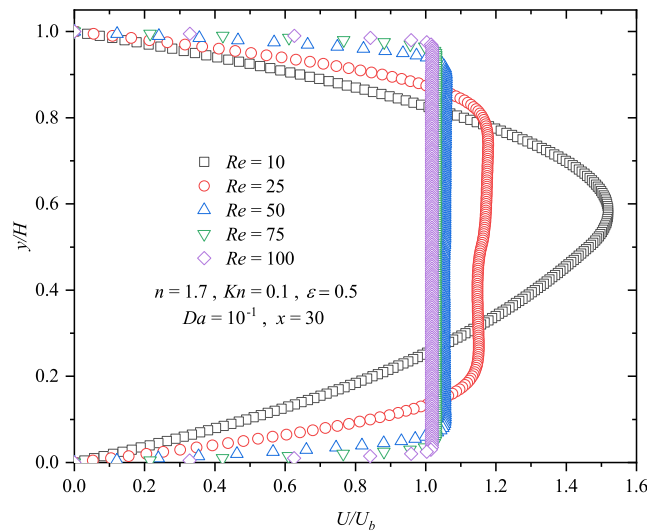


**Figure V.21** – Velocity profile of  $U/U_b$  for different Reynolds numbers at flow behaviour index  $n=1.7$ , Darcy number  $Da = 10^{-1}$ , for fixed Knudsen number  $Kn=0.1$ ,  $Re=100$ ,  $\varepsilon = 0.5$ .

## V.9.4 Effects of Knudsen number $Kn$

### V.9.4.1 Velocity profile

Figure V.22 illustrates the evaluation of the axial velocity profiles of pseudoplastic fluid ( $n=0.2$ ) normalised by the bulk velocity ( $U_b$ ) against the radial direction ( $y$ ) normalised by the microchannel high ( $H$ ) along the normal wall direction located at an axial position of  $X=30$  inside a microchannel with heat source size of 20. These simulations were conducted over a wide range of Knudsen numbers (0, 0.001, 0.05, 0.01, 0.5, and 0.1) for a fixed Darcy number



of  $10^{-1}$ . It can be seen from Figure V.22 that the axial velocity profiles seem more dependent on the flow behaviour index and Knudsen number in all considered cases; the axial velocity profiles of the pseudoplastic fluid inside the microchannel exhibit a significant deviation with varying Knudsen numbers. The effect of the Knudsen number on the axial velocity profile is more pronounced in the lower layer. On the other hand, the velocity profiles seem flattened in the upper layer for each Knudsen number due to the influence of the apparent fluid viscosity on the axial velocity distributions further away from the microchannel walls. It can be said that the decreased flow behaviour index of the pseudoplastic results in marked deviation in the shear rate and apparent fluid viscosity, resulting in a significant reduction in the axial velocity profile. The decreased flow behaviour index of the pseudoplastic also leads to moving the axial velocity's maximum value (peak value) toward the upper microchannel wall.

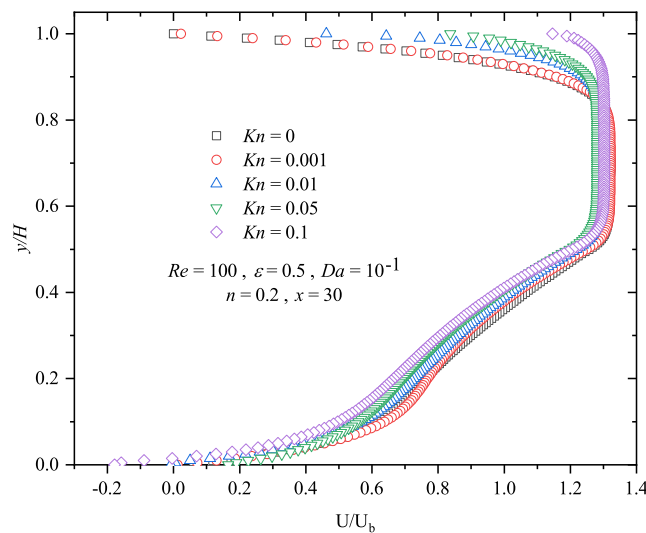


**Figure V.22** – Velocity profile of  $U/U_b$  for different Knudsen numbers at flow behaviour index  $n=0.2$ , Darcy number  $Da = 10^{-1}$ ,  $Re=100$ ,  $\epsilon = 0.5$ .

#### V.9.4.2 Temperature profile

Figure V.23 illustrates the evaluation of the dimensionless temperature of the pseudoplastic fluid ( $n=0.2$ ) against the radial direction ( $y$ ) normalised by the microchannel high ( $H$ ) along the heat source at an axial position of  $X=20$  inside a microchannel with a heat source size of 20. These simulations were conducted over a wide range of Knudsen numbers (0, 0.001, 0.05, 0.01, 0.5, and 0.1) for a fixed Darcy number of  $10^{-1}$ . The effect of the Knudsen number on the temperature distribution is limited along the radial coordinate. The temperature profiles

are similar along the heat source ; these profiles seem more distinct with the varying Knudsen numbers in the lower microchannel wall.

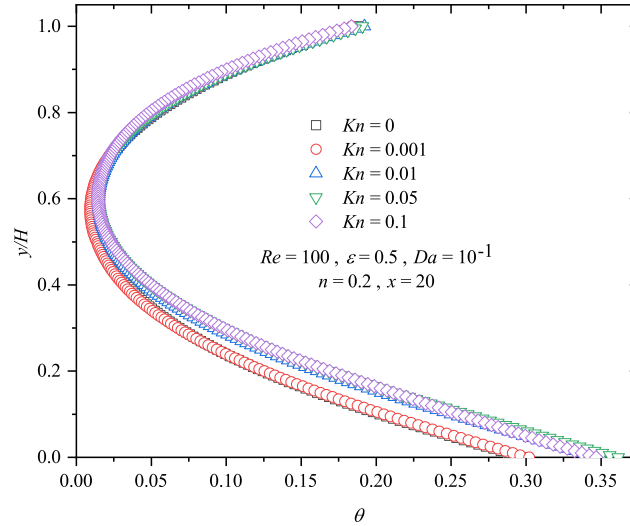


**Figure V.23** – Temperature profile of  $U/U_b$  for different Knudsen numbers at flow behaviour index  $n=0.2$  , Darcy number  $Da = 10^{-1}$ ,  $Re=100$ ,  $\varepsilon = 0.5$ .

## V.10 Conclusion

The present investigation was devoted to a numerical analysis of a two-dimensional steady laminar flow (MHD) forced convection heat transfer within a fully and partially porous medium heat sink rectangular microchannel subjected to a uniform transverse magnetic field ( $B_0$ ) inclined by an angle ( $\alpha$ ). Cu- $Al_2O_3$ /hybrid water nanofluid, pseudoplastic and dilatant fluids occupied the pores with a nanofluid concentration of  $\varphi = 1\%$  and flow behaviour index of (0.2, 0.4, 0.6, 0.8, 1, 1.2, 1.4, 1.6, and 1.8). The porous medium is modelled by employing the Brinkman-Darcy model with a local thermal equilibrium (LTE) approach between the working fluid and the porous matrix for energy transfer. The present investigation consisted of a set of simulations for wide ranges of heat source length ( $5 \leq B \leq 30$ ), Knudsen numbers ( $0.001 \leq Kn \leq 0.1$ ), Darcy numbers ( $10^{-5} \leq Da \leq 10^{-2}$ ), medium porosities ( $0.1 \leq \varepsilon \leq 0.9$ ), Hartmann numbers ( $0 \leq Ha \leq 160$ ), and magnetic field inclination angles ( $0^\circ \leq a \leq 90^\circ$ ) for the following fixed parameters : Reynolds number,  $Re=50$ ; porous thermal conductivity ratio,  $Ks=0.613$ . Furthermore, the predicted results showed an excellent agreement with the available literature results for validation. The evolution of the average Nusselt number, velocity profiles, and temperature profiles were analysed and discussed carefully. Furthermore, the predicted

results showed an excellent agreement with the available literature results for validation.

The major conclusions of this research will be summarised :

- The magnetic field and inclination angle considerably affected the momentum and thermal characteristics with varying Hartmann numbers and magnetic field inclination angles for all considered configurations.
- The heat transfer mechanism between the working fluid and the microchannel walls significantly affected the heat source length; the average Nusselt number increases markedly with the increasing length of the heat source for each Darcy number. On the other hand, the average Nusselt number exhibited a noticeable reduction with increasing Darcy number, and this trend was more evident as the heat source length decreased.
- The heat transfer seemed affected strongly by the slip flows from the microchannel wall towards the centre; the average Nusselt number seems affected by the Knudsen number with varying heat source length and Darcy number. The heat transfer mechanism enhanced significantly under the slip flow condition; the Nusselt number increased markedly as the Knudsen number increased, and this trend was more pronounced as the Knudsen number and heat source length increased for all Darcy numbers.
- The decreased flow behaviour index of the pseudoplastic resulted in marked deviation in the shear rate and apparent fluid viscosity, resulting in a significant reduction in the axial velocity profile. The decreased flow behaviour index of the pseudoplastic also led to moving the axial velocity's maximum value (peak value) toward the upper microchannel wall.



# GENERAL CONCLUSION

# GENERAL CONCLUSION

---

The present investigations aimed to determine the best heat transfer efficiency configuration of the heat sink microchannel. This study also sought to determine and reveal the effects of heater length, Knudsen number, flow behaviour index, Darcy number, medium porosity, flow behaviour index, Hartmann numbers, and magnetic field inclination angle on the rheological behaviour, momentum and heat transfer characteristics via offering and discussing the different statistical quantities such as the local and average Nusselt numbers, velocity profiles, and temperature profiles carefully. The present study concerned a steady-state laminar magnetohydrodynamic (MHD) flow forced convection heat transfer inside a fully and partially filled microchannel occupied by Cu- $Al_2O_3$ / water hybrid, pseudoplastic and dilatant fluids permeated by a uniform transverse magnetic field ( $B_0$ ) and inclined by an angle ( $\alpha$ ). The present investigation consisted of a set of simulations for wide ranges of heat source length ( $5 \leq B \leq 30$ ), Knudsen numbers ( $0.001 \leq Kn \leq 0.1$ ), flow behaviour indices ( $0.2 \leq n \leq 1.8$ ), Darcy numbers ( $10^{-5} \leq Da \leq 10^{-2}$ ), medium porosities ( $0.1 \leq \varepsilon \leq 0.9$ ), Hartmann numbers ( $0 \leq Ha \leq 160$ ), and magnetic field inclination angles ( $0^\circ \leq \alpha \leq 90^\circ$ ) for the following fixed parameters : Reynolds number,  $Re=50$ ; nanofluid concentration,  $\varphi = 1\%$ ; porous thermal conductivity ratio,  $Ks = 0.613$ . The porous medium was modelled by employing the Brinkman-Darcy model with a local thermal equilibrium (LTE) approach between the working fluid and the porous matrix for energy transfer. The predicted results showed an excellent agreement with the available literature results for validation.

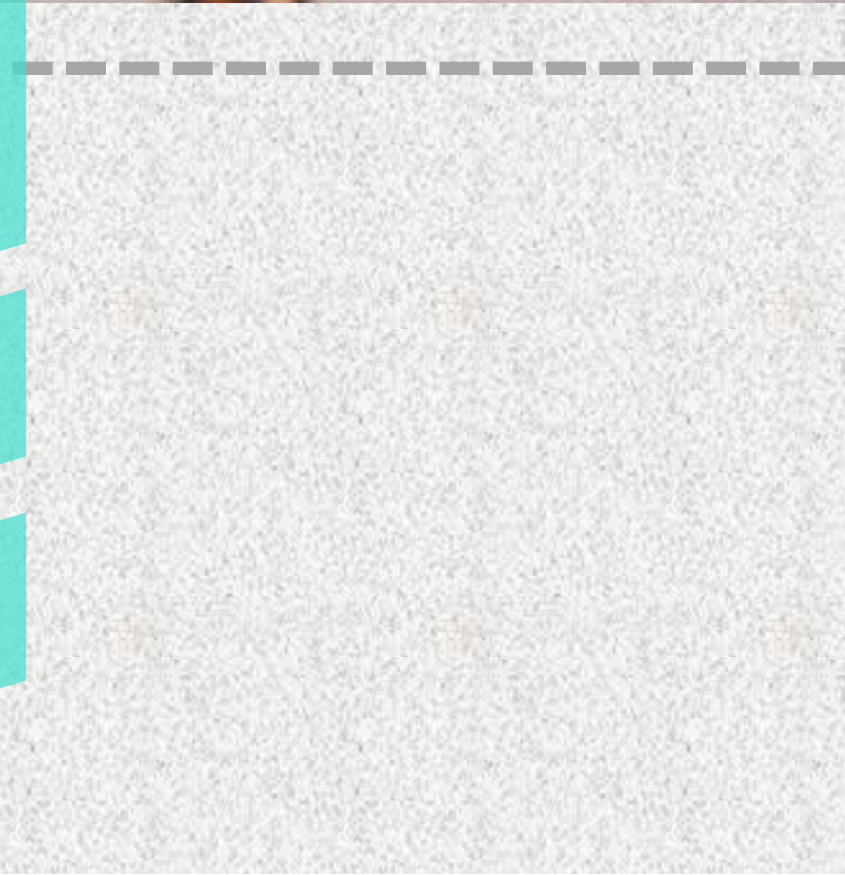
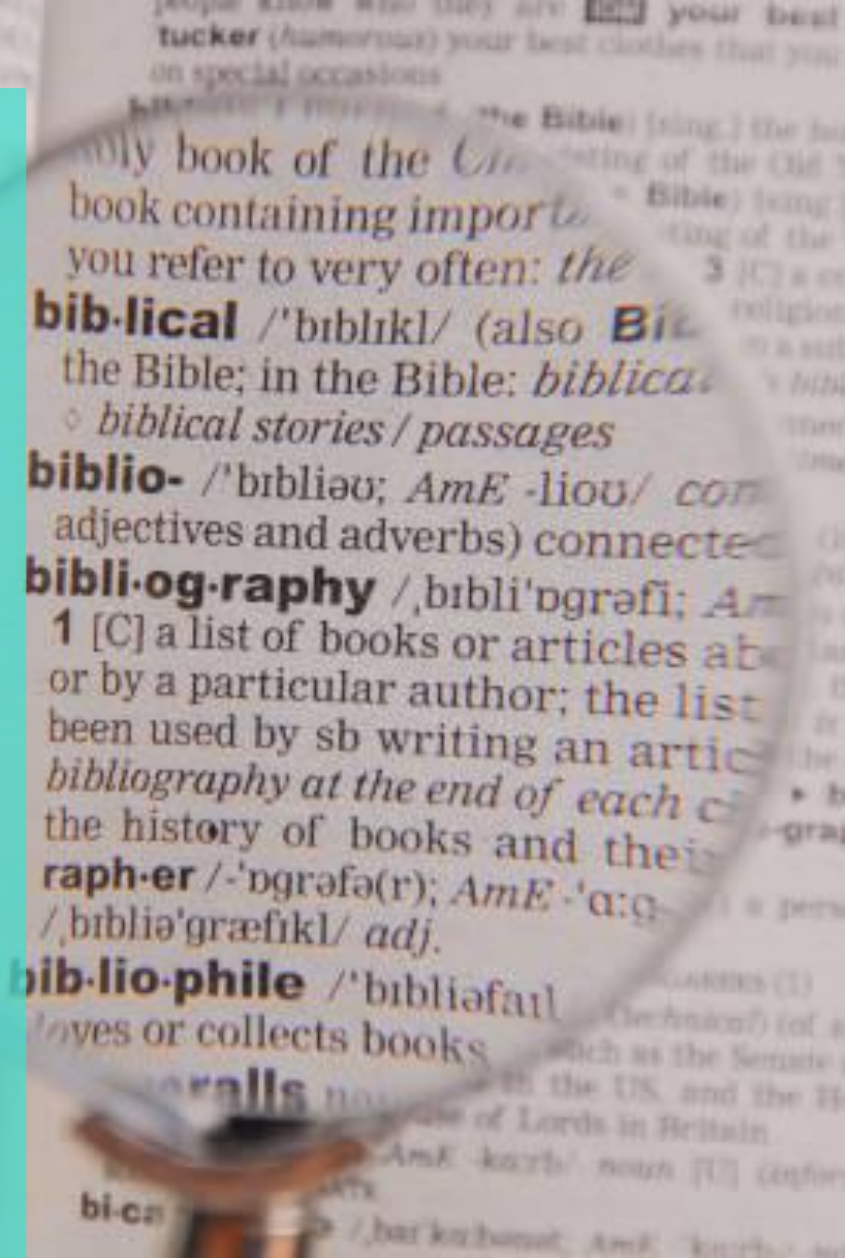
The major conclusions of this research will be summarised as follows :

- The increased Knudsen number resulted in a pronounced increase of the axial velocity and a reduction in the shear rate at the wall, resulting in a noticeable decrease of the velocity

in the microchannel centre and a marked increase of the axial velocity at the microchannel wall; the axial velocity profile redistribution was caused by the jump velocity induced by the slip flow, and this trend was more evident as the Knudsen number increased. The heat transfer mechanism improved significantly under the slip flow condition; the Nusselt number increased markedly as the Knudsen number increased, and this trend was more pronounced as the Knudsen number increased.

- The heat transfer characteristics of the hybrid nanofluid seemed to be more dependent on the strength of the applying Lorentz force; the momentum and heat transfer characteristics were affected strongly by the magnetic field and the magnetic inclination angle. The increased Hartmann number resulted in a marked deviation in the maximum axial velocity profile when approaching the magnetic field, resulting in a significant decrease in the axial velocity profile further away from the magnetic field. On the other hand, the decreased magnetic field inclination angle reduced the axial velocity profile along the radial direction. These profiles seemed more flattened in the microchannel centre for all Hartmann numbers as the magnetic field inclination angle decreased.
- The parametric study indicated that the momentum characteristics and heat transfer mechanism strongly depend on the media porosity; the axial velocity distributions seemed to be strongly influenced by the porosity in the considered geometry. The decreased porosity reduced the gap between the porous matrix, resulting in pronounced increases in the axial velocity of the nanofluid through the microchannel, and this trend was more apparent as the porosity decreased for all Darcy numbers. On the other hand, the Nusselt number increased significantly with decreased Darcy number for all heat source lengths; this trend was more obvious as the medium porosity increased.
- The momentum characteristics seemed more dependent on the flow behaviour index; the axial velocity profiles of the Ostwald de Waele fluid inside the microchannel exhibited a significant deviation with varying flow behaviour index. The increased flow behaviour index resulted in the apparent deviation in the shear rate distribution of the dilatant fluid along the radial coordinates, resulting in a marked variation in the apparent fluid viscosity, which leads to an increase in the axial velocity distributions along the microchannel high. The decreased flow behaviour index of the pseudoplastic also led to moving the axial velocity's maximum value (peak value) toward the upper microchannel wall.

# BIBLIOGRAPHY



# BIBLIOGRAPHY

---

- [1] Fridtjov Irgens. *Rheology and non-newtonian fluids*, volume 1. Springer, 2014.
- [2] Thomas Mezger. *The rheology handbook : for users of rotational and oscillatory rheometers*. European Coatings, 2020.
- [3] Howard A Barnes. *A handbook of elementary rheology*, volume 1. University of Wales, Institute of Non-Newtonian Fluid Mechanics Aberystwyth, 2000.
- [4] Eseosa M Ekanem. *Rheology and adsorption of hydrolysed polyacrylamide polymer in complex geometries*. PhD thesis, Imperial College London, 2021.
- [5] Albert Ibarz, Elena Castell-Perez, and Gustavo V Barbosa-Cánovas. Newtonian and non-newtonian flow. *Food Eng*, 2 :11, 2009.
- [6] Christophe Ancey. Introduction to fluid rheology. *LHE École Polytechnique Fédérale de Lausanne*, 2005.
- [7] Muhammad Sultan. *Towards a high pressure piezoelectric axial vibrator rheometer*. PhD thesis, Pau, 2012.
- [8] Mohamed Abdi. *Simulation numérique à grande échelle (LES) de l'écoulement turbulent pleinement développé d'un fluide non newtonien dans une conduite cylindrique en rotation*. PhD thesis, University of Science and Technology of Oran Mohamed Boudiaf, 2020.
- [9] Aroon Shenoy. *Heat Transfer to Non-Newtonian Fluids : Fundamentals and Analytical Expressions*. John Wiley & Sons, 2018.
- [10] Maureen Dinkgreve. *The rheology of jamming*. 2018.
- [11] Emile Van Den Heever. *Rheological model influence on pipe flow predictions for homogeneous non-Newtonian fluids*. PhD thesis, Cape Peninsula University of Technology, 2013.



- [12] Taha Sochi. Non-newtonian flow in porous media. *Polymer*, 51(22) :5007–5023, 2010.
- [13] J Murali Krishnan, Abhijit P Deshpande, and PB Sunil Kumar. *Rheology of complex fluids*. Springer, 2010.
- [14] Raj P Chhabra and John Francis Richardson. *Non-Newtonian flow and applied rheology : engineering applications*. Butterworth-Heinemann, 2011.
- [15] ABM Islam. Experimental investigation of material functions of eor polymer solutions. Master’s thesis, University of Stavanger, Norway, 2019.
- [16] NJ Alderman. Non-newtonian fluids : guide to classification and characteristics. *London : ESDU*, 1997.
- [17] Alexander Y Malkin and Avraam I Isayev. *Rheology : concepts, methods, and applications*. Elsevier, 2022.
- [18] Devdatta Prakash Kulkarni. *Experimental Investigations Of Fluid Dynamic And Thermal Performance Of Nanofluids*. PhD thesis, 2007.
- [19] Samah Hamze. *Graphene based nanofluids : development, characterization and application for heat and energy systems*. PhD thesis, Université Rennes 1, 2020.
- [20] Nader Nikkam. *Engineering nanofluids for heat transfer applications*. PhD thesis, KTH Royal Institute of Technology, 2014.
- [21] Mourad Rebay, Sadik Kakac, and Renato M Cotta. *Microscale and Nanoscale Heat Transfer : Analysis, Design, and Application*. CRC Press, 2016.
- [22] L Syam Sundar, KV Sharma, MT Naik, and Manoj K Singh. Empirical and theoretical correlations on viscosity of nanofluids : a review. *Renewable and sustainable energy reviews*, 25 :670–686, 2013.
- [23] G Paul, M Chopkar, I Manna, and PK Das. Techniques for measuring the thermal conductivity of nanofluids : a review. *Renewable and Sustainable Energy Reviews*, 14(7) :1913–1924, 2010.
- [24] R.L Hamilton and OK Crosser. Thermal conductivity of heterogeneous two-component systems. *Industrial & Engineering chemistry fundamentals*, 1(3) :187–191, 1962.
- [25] Ismail Ozan Sert, Nilay Sezer-Uzol, and Sadik Kakac. Numerical analysis of nanofluids convective heat transfer with mixture model approaches. In *Proceedings of CONV-14 : International Symposium on Convective Heat and Mass Transfer*. Begel House Inc., 2014.
- [26] C Boutin. Taking the heat off : Nanofluids promise efficient heat transfer. *logos*, 19(2), 2001.

- [27] Caiyan Qin, Kyeonghwan Kang, Ikjin Lee, and Bong Jae Lee. Optimization of a direct absorption solar collector with blended plasmonic nanofluids. *Solar Energy*, 150 :512–520, 2017.
- [28] R Turcu, AL Darabont, A Nan, N Aldea, D Macovei, D Bica, L Vekas, O Pana, ML Soran, AA Koos, et al. New polypyrrole-multiwall carbon nanotubes hybrid materials. *Journal of optoelectronics and advanced materials*, 8(2) :643–647, 2006.
- [29] Furqan Jamil and Hafiz Muhammad Ali. Applications of hybrid nanofluids in different fields. In *Hybrid nanofluids for convection heat transfer*, pages 215–254. Elsevier, 2020.
- [30] Eiyad Abu-Nada and Hakan F Oztop. Effects of inclination angle on natural convection in enclosures filled with cu–water nanofluid. *International Journal of Heat and Fluid Flow*, 30(4) : 669–678, 2009.
- [31] S Lee, SU-S Choi, S Li, , and JA Eastman. Measuring thermal conductivity of fluids containing oxide nanoparticles. 1999.
- [32] S US Choi and Jeffrey A Eastman. Enhancing thermal conductivity of fluids with nanoparticles. Technical report, Argonne National Lab.(ANL), Argonne, IL (United States), 1995.
- [33] Hussam Jouhara, Vladimir Anastasov, and Ibrahim Khamis. Potential of heat pipe technology in nuclear seawater desalination. *Desalination*, 249(3) :1055–1061, 2009.
- [34] Mujid S Kazimi. Introduction to the annular fuel special issue. *Nuclear Technology*, 160(1) :1–1, 2007.
- [35] Pawan K Singh, PV Harikrishna, T Sundararajan, and Sarit K Das. Experimental and numerical investigation into the hydrodynamics of nanofluids in microchannels. *Experimental Thermal and Fluid Science*, 42 :174–186, 2012.
- [36] Zahra Nikkhah, Arash Karimipour, Mohammad Reza Safaei, Pezhman Forghani-Tehrani, Marjan Goodarzi, Mahidzal Dahari, and Somchai Wongwises. Forced convective heat transfer of water/-functionalized multi-walled carbon nanotube nanofluids in a microchannel with oscillating heat flux and slip boundary condition. *International Communications in Heat and Mass Transfer*, 68 : 69–77, 2015.
- [37] Omid Ali Akbari, Davood Toghraie, Arash Karimipour, Mohammad Reza Safaei, Marjan Goodarzi, Habibollah Alipour, and Mahidzal Dahari. Investigation of rib’s height effect on heat transfer and flow parameters of laminar water–al<sub>2</sub>o<sub>3</sub> nanofluid in a rib-microchannel. *Applied Mathematics and Computation*, 290 :135–153, 2016.

- [38] Hamed Bazdar, Davood Toghraie, Farzad Pourfattah, Omid Ali Akbari, Hoang Minh Nguyen, and Amin Asadi. Numerical investigation of turbulent flow and heat transfer of nanofluid inside a wavy microchannel with different wavelengths. *Journal of Thermal Analysis and calorimetry*, 139(3) :2365–2380, 2020.
- [39] Liu Yang and Kai Du. Numerical simulation of nanofluid flow and heat transfer in a microchannel : the effect of changing the injection layout arrangement. *International Journal of Mechanical Sciences*, 172 :105415, 2020.
- [40] Arash Karimipour, Alireza Hossein Nezhad, Annunziata D’Orazio, and Ebrahim Shirani. Investigation of the gravity effects on the mixed convection heat transfer in a microchannel using lattice boltzmann method. *International Journal of Thermal Sciences*, 54 :142–152, 2012.
- [41] Mohammad Reza Tavakoli, Omid Ali Akbari, Anoushiravan Mohammadian, Erfan Khodabandeh, and Farzad Pourfattah. Numerical study of mixed convection heat transfer inside a vertical microchannel with two-phase approach. *Journal of Thermal Analysis and Calorimetry*, 135 : 1119–1134, 2019.
- [42] Annunziata D’Orazio and Arash Karimipour. A useful case study to develop lattice boltzmann method performance : gravity effects on slip velocity and temperature profiles of an air flow inside a microchannel under a constant heat flux boundary condition. *International Journal of Heat and Mass Transfer*, 136 :1017–1029, 2019.
- [43] MR Thansekhar and C Anbumeenakshi. Experimental investigation of thermal performance of microchannel heat sink with nanofluids al<sub>2</sub>o<sub>3</sub>/water and sio<sub>2</sub>/water. *Experimental Techniques*, 41 :399–406, 2017.
- [44] C Anbumeenakshi and MR Thansekhar. On the effectiveness of a nanofluid cooled microchannel heat sink under non-uniform heating condition. *Applied Thermal Engineering*, 113 :1437–1443, 2017.
- [45] Abedin Arabpour, Arash Karimipour, and Davood Toghraie. The study of heat transfer and laminar flow of kerosene/multi-walled carbon nanotubes (mwcnts) nanofluid in the microchannel heat sink with slip boundary condition. *Journal of Thermal Analysis and Calorimetry*, 131 : 1553–1566, 2018.
- [46] CJ Ho, Yu-Wei Guo, Tien-Fu Yang, Saman Rashidi, and Wei-Mon Yan. Numerical study on forced convection of water-based suspensions of nanoencapsulated pcm particles/al<sub>2</sub>o<sub>3</sub> nanoparticles in a mini-channel heat sink. *International Journal of Heat and Mass Transfer*, 157 :119965, 2020.

- [47] Mohammad Ghazvini and Hossein Shokouhmand. Investigation of a nanofluid-cooled microchannel heat sink using fin and porous media approaches. *Energy conversion and management*, 50(9) :2373–2380, 2009.
- [48] Mehdi Nojoomizadeh, Arash Karimipour, Masoumeh Firouzi, and Masoud Afrand. Investigation of permeability and porosity effects on the slip velocity and convection heat transfer rate of  $Fe_3O_4$ /water nanofluid flow in a microchannel while its lower half filled by a porous medium. *International Journal of Heat and Mass Transfer*, 119 :891–906, 2018.
- [49] Ehsan Gholamalizadeh, Farzad Pahlevanzadeh, Kamal Ghani, Arash Karimipour, Truong Khang Nguyen, and Mohammad Reza Safaei. Simulation of water/fmwcnt nanofluid forced convection in a microchannel filled with porous material under slip velocity and temperature jump boundary conditions. *International Journal of Numerical Methods for Heat & Fluid Flow*, 30(5) :2329–2349, 2020.
- [50] Masoud Afrand, Arash Karimipour, Afshin Ahmadi Nadooshan, and Mohammad Akbari. The variations of heat transfer and slip velocity of fmwnt-water nano-fluid along the micro-channel in the lack and presence of a magnetic field. *Physica E : Low-Dimensional Systems and Nanostructures*, 84 :474–481, 2016.
- [51] Arash Karimipour, Abdolmajid Taghipour, and Amir Malvandi. Developing the laminar mhd forced convection flow of water/fmwnt carbon nanotubes in a microchannel imposed the uniform heat flux. *Journal of Magnetism and Magnetic Materials*, 419 :420–428, 2016.
- [52] Arash Karimipour, Annunziata D’Orazio, and Mostafa Safdari Shadloo. The effects of different nano particles of  $Al_2O_3$  and  $Ag$  on the mhd nano fluid flow and heat transfer in a microchannel including slip velocity and temperature jump. *Physica E : Low-Dimensional Systems and Nanostructures*, 86 :146–153, 2017.
- [53] Ali Alipour Lalami, Hamid Hassanzadeh Afrouzi, and Abouzar Moshfegh. Investigation of mhd effect on nanofluid heat transfer in microchannels : an incompressible lattice boltzmann approach. *Journal of Thermal Analysis and Calorimetry*, 136 :1959–1975, 2019.
- [54] M Madhu, NS Shashikumar, B Mahanthesh, BJ Gireesha, and N Kishan. Heat transfer and entropy generation analysis of non-newtonian flu flow through vertical microchannel with convective boundary condition. *Applied Mathematics and Mechanics*, 40 :1285–1300, 2019.
- [55] Si-Ning Li, Hong-Na Zhang, Xiao-Bin Li, Qian Li, Feng-Chen Li, Shizhi Qian, and Sang Woo Joo. Numerical study on the heat transfer performance of non-newtonian fluid flow in a manifold microchannel heat sink. *Applied Thermal Engineering*, 115 :1213–1225, 2017.

- [56] Mohammad Reza Shamsi, Omid Ali Akbari, Ali Marzban, Davood Toghraie, and Ramin Mashayekhi. Increasing heat transfer of non-newtonian nanofluid in rectangular microchannel with triangular ribs. *Physica E : Low-Dimensional Systems and Nanostructures*, 93 :167–178, 2017.
- [57] Mehdi Kiyasatfar. Convective heat transfer and entropy generation analysis of non-newtonian power-law fluid flows in parallel-plate and circular microchannels under slip boundary conditions. *International Journal of Thermal Sciences*, 128 :15–27, 2018.
- [58] Anum Tanveer, Taimoor Salahuddin, Mair Khan, Muhammad Yousaf Malik, and MS32066045 Alqarni. Theoretical analysis of non-newtonian blood flow in a microchannel. *Computer Methods and Programs in Biomedicine*, 191 :105280, 2020.
- [59] Mahnaz Javidi Sarafan, Rasool Alizadeh, Abolfazl Fattahi, Mostafa Valizadeh Ardalan, and Nader Karimi. Heat and mass transfer and thermodynamic analysis of power-law fluid flow in a porous microchannel. *Journal of Thermal Analysis and Calorimetry*, 141 :2145–2164, 2020.
- [60] Xin Dong and Xiaomin Liu. Multi-objective optimization of heat transfer in microchannel for non-newtonian fluid. *Chemical Engineering Journal*, 412 :128594, 2021.
- [61] SA Shehzad, Macha Madhu, NS Shashikumar, BJ Giresha, and B Mahanthesh. Thermal and entropy generation of non-newtonian magneto-carreau fluid flow in microchannel. *Journal of Thermal Analysis and Calorimetry*, 143 :2717–2727, 2021.
- [62] Davood Domairry Ganji and Amir Malvandi. *Heat transfer enhancement using nanofluid flow in microchannels : simulation of heat and mass transfer*. William Andrew, 2016.
- [63] Satish Kandlikar, Srinivas Garimella, Dongqing Li, Stephane Colin, and Michael R King. *Heat transfer and fluid flow in minichannels and microchannels*. elsevier, 2005.
- [64] MAYANK KUMAR GUPTA. *CFD ANALYSIS OF MICROCHANNEL HEAT SINK WITH PILLARS*. PhD thesis, 2018.
- [65] K Naga Ramesh, T Karthikeya Sharma, and G Amba Prasad Rao. Latest advancements in heat transfer enhancement in the micro-channel heat sinks : a review. *Archives of Computational Methods in Engineering*, 28 :3135–3165, 2021.
- [66] Richard J Phillips et al. Microchannel heat sinks. *The Lincoln Laboratory Journal*, 1(1) :31–48, 1988.
- [67] Daxiang Deng, Long Zeng, and Wei Sun. A review on flow boiling enhancement and fabrication of enhanced microchannels of microchannel heat sinks. *International Journal of Heat and Mass Transfer*, 175 :121332, 2021.

- [68] Cody S Zampella. *Experimental Determination of the Thermal Accommodation Coefficient for Helium on a Stainless Steel Surface Using a Concentric Cylinders Apparatus*. PhD thesis, University of Nevada, Reno, 2019.
- [69] Jie Chen. *Numerical and experimental analysis of flows generated by temperature fields in rarefied gas : application to the design of Knudsen micropumps*. PhD thesis, Toulouse, INSA, 2016.
- [70] Khan Rehan Wasim. *Slip flow in microchannels*. PhD thesis, 2013.
- [71] Zhaoda Zhong, Like Meng, Xixi Li, Guoqing Zhang, Yanrou Xu, and Jian Deng. Enhanced heat transfer performance of optimized micro-channel heat sink via forced convection in cooling metal foam attached on copper plate. *Journal of Energy Storage*, 30 :101501, 2020.
- [72] Donald A Nield, Adrian Bejan, et al. *Convection in porous media*, volume 3. Springer, 2006.
- [73] Pei-Xue Jiang. Numerical simulation of forced convection heat transfer in porous plate channels using thermal equilibrium and nonthermal equilibrium models. *Numerical Heat Transfer : Part A : Applications*, 35(1) :99–113, 1999.
- [74] Maasoud Kaviany. *Principles of heat transfer in porous media*. Springer Science & Business Media, 2012.
- [75] Malay K Das, Partha P Mukherjee, and Krishnamurthy Muralidhar. *Modeling transport phenomena in porous media with applications*, volume 241. Springer, 2018.
- [76] JM Alhumoud. Non-equilibrium natural convection flow through a porous medium. *Mathematical Modelling of Engineering Problems*, 6(2) :163–169, 2019.
- [77] PIETRO SCIENZA. Numerical investigation of non-newtonian biomagnetic fluid flows in presence of localised magnetic field. 2015.
- [78] Dwaipayyan Sharma. *CFD Simulation of Vortex-Induced Vibration of Ice Accreted Stay Cable Using ANSYS-Fluent*. PhD thesis, The University of Toledo, 2020.
- [79] Athanasios Tzanakis. Duct optimization using cfd software ‘ansys fluent adjoint solver’. *Master’s thesis in Automotive Engineering. Department of Applied Mechanics. Division of Vehicle Engineering and Autonomous Systems. Chalmers University of Technology. Goteborg, Sweden*, 2014.
- [80] PAUL JACQUEMARD. Fluid field analysis on a flexible combustor for a hybrid solar/brayton system : A numerical study, 2020.
- [81] Herbert Spiegel. The hypnotic induction profile (hip) : A review of its development. *Annals of the New York Academy of Sciences*, 296(1) :129–142, 1977.

- [82] I Ansys. Fluent theory guide. *ANSYS Inc, USA [(accessed on 27 March 2020)]*, 2013.
- [83] Kamel CHADI. *Modélisation et simulation du refroidissement des éléments à base de composants électroniques par des nanofluides*. PhD thesis, Université Mohamed Khider–Biskra, 2020.
- [84] Anton Oberbeck. Über die wärmeleitung der flüssigkeiten bei berücksichtigung der strömungen infolge von temperaturdifferenzen. *Annalen der Physik*, 243(6) :271–292, 1879.
- [85] Mohamed Rachid Mekideche. *Contribution à la modélisation numérique de torches à plasma d'induction*. PhD thesis, Nantes, 1993.
- [86] Benjamin Michael Carver Johnson. *Computational Fluid Dynamics (CFD) modelling of renewable energy turbine wake interactions*. PhD thesis, University of Central Lancashire, 2015.
- [87] J Blazek. Boundary conditions. *Computational Fluid Dynamics : Principles and Applications, 1st ed., Elsevier Science, UK*, page 270, 2001.
- [88] Abdelkhalak El Hami and Bouchaïb Radi. *Fluid-structure interactions and uncertainties : ansys and fluent tools*, volume 6. John Wiley & Sons, 2017.
- [89] Sireetorn Kuharat. *Numerical study of nanofluid-based direct absorber solar collector systems with metallic/carbon nanoparticles, multiple geometries and multi-mode heat transfer*. University of Salford (United Kingdom), 2021.
- [90] Omar Ahmed Mohamed Abdelhamid Elshawarby. Computational fluid dynamics of multiphase flow using ansys fluent. 2021.
- [91] Nirmalendu Biswas, UK Sarkar, Ali J Chamkha, and Nirmal Kumar Manna. Magneto-hydrodynamic thermal convection of cu–al 2 o 3/water hybrid nanofluid saturated with porous media subjected to half-sinusoidal nonuniform heating. *Journal of Thermal Analysis and Calorimetry*, 143 :1727–1753, 2021.